Joint PhD Programme in Fusion Science and Engineering

Università degli Studi di Padova

Ghent University

Cycle XXXV

Modelling of helically self-organized plasmas with 3D nonlinear magnetohydrodynamics: dimensionless parameters and transport studies

Supervisor: Dr. Marco Veranda
Supervisor: Dr. Daniele Bonfiglio
Supervisor: Prof. Geert Verdoolaege

PhD student: Nicholas Vivenzi

Contents

List of Tables

List of Figures

Acknowledgements

Having reached the end of this course of study, I would like to thank the people who have supported me in all the difficulties up to the achievement of this important goal.
First of all, I would like to thank my family for always giving me unconditional support and help, especially in the most difficult moments, allowing me to freely make my choices and overcome many obstacles, even the most demanding ones.
I will always be sincerely grateful to my supervisor Dr. Marco Veranda, for everything he taught me, for having introduced me to the world of research and having followed the development of this work step by step.
I particularly thank my supervisor Dr. Daniele Bonfiglio for his teachings and for the availability he has shown me during this research project.
I specially acknowledge Dr. Gianluca Spizzo, for his his availability and the decisive support in the analysis of the experimental data of the RFX-mod device.
Furthermore, I would like to express gratitude to Dr. Susanna Cappello, head of the theory and simulation group of Consorzio RFX for the valuable advice and discussions, without whom this work would not have been possible.
I would like to thank Prof. Dr. Geert Verdoolaege and the fusion data science research group of Ghent University, for having hosted me during the exchange period in Belgium and for collaborating profitably on this research.
I thank Dr. V Igochine and Dr. W JT Bos for carefully reading this manuscript and for the useful suggestions provided to improve this work.
Finally, I am grateful to all the members of Consorzio RFX team that I have had the pleasure of meeting over these three years. It has been really a pleasure working with you all!

Padova,
15^{th} March 2023

Nicholas Vivenzi

Abstract

This Thesis summarizes the activity of about three years I spent at Consorzio RFX, located in the C.N.R. Padova research area, in Italy (between October 2019 and September 2022) and at the Ghent University, in Belgium (between October 2022 and December 2022), as part of the Joint PhD Programme in Fusion Science and Engineering.
Fusion science research is aimed at the study of nuclear fusion as a future energy source able to sustain the growing energy demand, CO_2 free, expected to be safer than the actual exploitation of nuclear energy (based on nuclear fission), based on more easily available fuels and independent on weather conditions at variance with other renewable energy sources. The future exploitation of nuclear fusion needs the confinement of the plasma, which is a state of matter characterized by a consistent degree of particles ionization. According to the plasma confinement method adopted, different research lines exist, among which the inertial and the magnetic confinement should be mentioned. The European research program is strongly engaged on the magnetic confinement, where the plasma is confined in toroidal devices by means of strong magnetic fields. Magnetic confinement fusion represents the working environment of this Thesis.
Since a magnetically confined fusion plasma is a complex system, different approaches (each with its pros and cons) can be adopted in order to model its dynamical evolution, which span from the microscopic single particle description to the macroscopic magneto-fluid description. The latter is the one considered in this work, which considers the plasma as a single fluid immersed in a magnetic field by means of 3D nonlinear magnetohydrodynamics model and which relates two magnetic configurations: the alternative reversed field pinch and the principal tokamak configurations. The flows of physical relevant quantities (like electric charge, momentum and energy) between different regions of non-equilibrium plasmas, give rise to transport phenomena. In this Thesis I address the problem of the experimental evaluation of **transport parameters**, which usually appear as input free parameters in the numerical implementations solving the magnetohydrodynamics model equations. These parameters rule the transition between qualitatively different dynamical regimes of the equations. On the other hand, transport parameters can be written in the context of transport theory as function of plasma measurable parameters, allowing their experimental evaluation.
It has been highlighted in the past a relation between such dynamical transitions and the density limits manifested in the Reversed Field Pinch. One of the **main target** of this work, among the other described in the following list, is to achieve a better understanding and description of the density limit, which are ruled by transport parameters in the reversed-field pinch. This can be achieved in three distinct steps:

- Studying the action of dimensionless transport parameters in numerical simulations of current carrying fusion plasmas with specific focus on: the role of time-dependent and non-uniform profiles of visco-resistive coefficients on RFP helical regimes (Chp. 5) and the role of dissipation parameters in ruling the sawtooth oscillations regime in tokamak configuration (Chp. 6).

- Assessing a kinematic viscosity coefficient evaluation in RFP fusion plasmas, Chp. 8, evaluating the main contribution to the viscosity, comparing the evaluations due to different transport theories: classical Braginskii, Ion Temperature Gradient and Finn. This is motivated, since the assessment of a viscosity estimate still represents one of the main difficulties in applying MHD predictions to laboratory plasma, as stated in Ref. Montgomery [1992].
- Exploring the physical insights of the density limit in RFP plasmas, describing its phenomenology in terms of fluid dimensionless parameters derived from fundamental MHD equations, Chp. 9. Indeed, despite its crucial role for the realization of fusion, the density limit is still lacking a satisfactory explanation in terms of idealized equations, see Ref. Hawryluk and Zohm [2019].

In the development of the research several **results** are obtained, a strict summary is as follows:

- In RFP MHD simulations, Braginskii-like viscosity profiles (higher at the edge with respect to uniform profile) produce a damp of the kinetic energy of the modes resonating at the edge, allowing a slight enhancement of the magnetic energy of the correspondent modes. A preliminary time-dependent experimental-like visco-resistive dissipation is tested, mainly resulting in the slow-down of the sawtooth dynamics.
  In tokamak MHD simulations with fixed helicity and non-zero pressure the sawtooth oscillation regimes are ruled by the visco-resistive dissipation, while the isotropic heat conductivity rules the core plasma temperature.
- The perpendicular Braginskii viscosity is found out to be the main contribution to the viscosity term able to maximize the agreement between visco-resistive magnetohydrodynamics numerical simulations and experimental data.
- A description of the RFP density limit is developed in the context of nonlinear magnetohydrodynamics, highlighting the role of the Hartmann number (which represents the visco-resistive dissipation) in triggering the growth of edge $m = 0$ instabilities and in the MARFE (Multifaceted Asymmetric Radiation From the Edge) onset, precursor of the discharge termination.

The main matter of this Thesis is organized into 9 Chapters. The Chp. 1 - 3 constitute the introductory part (Part I), while Chp. 4 - 9 present the original part of this work, focusing on numerical simulations (Part II) and experimental data analysis (Part III). Conclusions follow in Part IV.
Chp. 1 is devoted to the introduction of nuclear fusion as a future energy source, contextualizing its potential role in long term energy scenarios. The basics of nuclear fusion reactions and plasma confinement methods are introduced, with specific focus on the magnetic one, to which the European Fusion Roadmap is devoted. Finally, the main features and physics related problems of a future fusion reactor are presented.
Chp. 2 deals with reversed-field pinch configuration, the most studied in this work. The main features and scientific achievements of this configuration are briefly described, following the historical development of the scientific work carried on at Consorzio RFX in the last decades. A summarized perspective of future applications is also provided.
Chp. 3 represents the more mathematical related part of this work. The specific aim of the Chapter is to report the main steps which allow to derive the formulas of transport coefficients (resistivity, viscosity and heat conductivity) as function of plasma measurable quantities. The derivation is developed in the closure scheme of magnetohydrodynamics equations for the classical transport. Specific hints related to turbulent transport are also provided. Finally, the visco-resistive MHD model, representing the main theoretical framework of this work, is presented.

Chp. 4 presents the numerical tools used in this work (SpeCyl and PIXIE3D codes), briefly describing the models simulated and the numerical schemes adopted by the two codes. The second part of the Chapter summarizes the state of art of the research in visco-resistive magnetohydrodynamics modelling of toroidal pinches, with reference to the role of boundary conditions and transport dimensionless parameters. The final part presents the database of simulations available and the prediction they can provide for the comparison with the experimental data.
Chp. 5 investigates the role of spatial profiles and time dependence of resistivity and viscosity in SpeCyl simulations and their influence on velocity and magnetic fields perturbations. Since the viscosity represents the major uncertainty parameter, the analysis is mainly a sensitivity study to assess the effect of non-uniform viscosity profiles in different RFP regimes (Single Helicity, Quasi Single Helicity and Multiple Helicity). However, even slight variations of the (more consolidated) resistivity profile are tested. As final result, a preliminary experimental-like self-consistent evolution of the core visco-resistive coefficients is tested.
Chp. 6 is devoted to the modelling of tokamak sawtooth oscillations in the context of 3D nonlinear magnetohydrodynamics. As a first step, the effect of finite pressure and Spitzer-like resistivity is tested in 1D axisymmetric simulations. Then, a set of finite pressure PIXIE3D numerical simulations with helical symmetry, performed systematically varying the dimensionless transport coefficients (resistivity, viscosity and isotropic heat conductivity), is analyzed, studying the role of the latter in triggering the sawtooth instability, limited to this simplified framework. Additional studies related to this topic can be considered for future works, e. g. exploiting a Spitzer-like self-consistently evolved resistivity even for non axisymmetric simulations.
Chp. 7 presents the RFX-mod experiment and the database of shots considered for this work. In particular, the previous studies, conducting using these data, are summarized. Moreover, some preliminary analysis of the database is presented, including the evaluation of transport dimensionless parameters, exploiting the results from Chp. 3.
Chp. 8 is specifically devoted to the problem of the viscosity estimate on the basis of RFX-mod experimental data. Since different evaluations, depending on the transport theory considered, display orders of magnitude differences, a comparison with numerical simulations, based on the scaling of edge magnetic field instabilities as function of the visco-resistive dissipation has been considered. This analysis has been refined using Bayesian model comparison to asses the viscosity estimate which maximizes the agreement between simulations and experimental data.
Chp. 9 briefly summarizes the state of art of reversed-field pinch density limit, contextualizing it in the main framework of toroidal pinches density limit. Then, the Multifaceted Asymmetric Radiation From the Edge (MARFE) phenomenology in the reversed field pinch is introduced, discussing its rise (in terms of edge $m = 0$ magnetic field instabilities) and its role as precursor of the density limit. As final step, the analysis of RFX-mod shots is presented, showing the role of the visco-resistive coefficient (i. e. the Hartmann number derived from first principles magnetohydrodynamics equations) in triggering the MARFE onset and rise, finally allowing the description of the physics insights of the RFP density limit in terms of a theory-based parameter.

Prefazione

Questa Tesi riassume l'attività di ricerca della durata di circa tre anni trascorsi presso il Consorzio RFX, sito nell'Area di Ricerca di Padova, in Italia (tra Ottobre 2019 e Settembre 2022) e presso l'Università di Ghent, in Belgio (tra Ottobre 2022 e Dicembre 2022), nell'ambito del Programma di Dottorato Congiunto in Scienza e Ingegneria della Fusione.
La ricerca scientifica in tale ambito è finalizzata allo studio della fusione nucleare come futura fonte di energia in grado di sostenere la crescente domanda di quest'ultima, libera dall'emissione di CO_2, prevista più sicura della fissione nucleare (su cui si basa l'attuale sfruttamento dell'energia nucleare), dipendente da combustibili più facilmente reperibili e indipendente dalle condizioni meteorologiche, diversamente da altre fonti di energia rinnovabile. Il futuro sfruttamento della fusione nucleare necessita del confinamento del plasma, uno stato della materia caratterizzato da un elevato grado di ionizzazione delle particelle. A seconda del metodo di confinamento del plasma adottato, esistono diverse linee di ricerca, tra cui è doveroso menzionare quella a confinamento inerziale e quella a confinamento magnetico. Il programma di ricerca europeo è fortemente dedicato al confinamento magnetico, il quale prevede che il plasma sia confinato in dispositivi di forma toroidali attraverso la generazione di forti campi magnetici. La fusione a confinamento magnetico rappresenta l'ambito di lavoro di questa Tesi.
Dal momento che un plasma da fusione confinato magneticamente è un sistema complesso, diversi approcci (ciascuno con i propri vantaggi e svantaggi) possono essere adottati per modellizzare la sua evoluzione dinamica, spaziando dalla descrizione microscopica di singola particella fino alla descrizione macroscopica di magnetofluido. Quest'ultimo approccio è quello considerato in questo lavoro, dove il plasma viene considerato come un fluido unico immerso in un campo magnetico e descritto attraverso un modello magnetoidrodinamico non lineare 3D, relativamente a due configurazioni magnetiche: il Reversed Field Pinch (alternativo) e il tokamak (configurazione principale). I flussi di grandezze fisiche rilevanti (come carica elettrica, quantità di moto ed energia) tra diverse regioni di plasmi non in equilibrio danno luogo a fenomeni di trasporto. In questa Tesi affronto il problema della valutazione sperimentale dei **parametri di trasporto**, i quali appaiono di solito come input nelle implementazioni numeriche che risolvono le equazioni del modello magnetoidrodinamico (MHD). Tali parametri regolano la transizione tra regimi dinamici delle equazioni qualitativamente diversi. D'altra parte, i parametri di trasporto possono essere scritti nel contesto della teoria del trasporto come funzione delle quantità misurabili del plasma, consentendone la valutazione sperimentale.
In passato, è stata evidenziata una relazione tra tali transizioni dinamiche ed i limiti di densità manifestati nel RFP. Uno degli **obiettivi principali** di questo lavoro, tra l'altro descritto nell'elenco che segue, è quello di ottenere una migliore comprensione e descrizione del limite di densità, mostrando come entrambi siano regolati dai parametri di trasporto nel Reversed Field Pinch. È possibile raggiungere questo risultato in tre passaggi intermedi:

- Studio dell'azione dei parametri di trasporto adimensionali nelle simulazioni numeriche di plasmi da fusione con particolare attenzione: al ruolo della dipendenza temporale e di profili non uniformi dei coefficienti viscoresistivi sui regimi elicoidali della configurazione

RFP (Cap. 5) e al ruolo dei parametri di dissipazione nel governare il regime di oscillazione sawtooth nella configurazione tokamak (Cap. 6).

- Stima del coefficiente di viscosità cinematica nei plasmi da fusione RFP, Cap. 8, valutandone il contributo principale sulla base delle valutazioni prodotte in accordo a differenti teorie del trasporto: classica secondo Braginskii, basata sul gradiente di temperatura ionica e secondo Finn. Questo è motivato dal fatto che la valutazione di una stima della viscosità rappresenti una delle principali difficoltà nell'applicare le previsioni del modello MHD ai plasma di laboratorio, come affermato in Ref. Montgomery [1992].

- Studio delle motivazioni fisiche del limite di densità nei plasmi RFP, descrivendone la fenomenologia in termini di parametri fluidi adimensionali derivati dalle equazioni fondamentali del modello MHD, Cap. 9. Infatti, nonostante il suo ruolo cruciale per la realizzazione della fusione, il limite di densità manca ancora di una spiegazione soddisfacente in termini di equazioni idealizzate, Ref. Hawryluk and Zohm [2019].

Nello sviluppo di questa ricerca sono stati ottenuti diversi **risultati**, brevemente riassunti nei seguenti punti:

- Nelle simulazioni MHD in configurazione RFP, i profili di viscosità ispirati alla teoria Braginskii (più alti al bordo rispetto al profilo uniforme) producono uno smorzamento dell'energia cinetica dei modi risonanti al bordo, consentendo un leggero aumento dell'energia magnetica dei modi corrispondenti. Inoltre, è stata testata in maniera preliminare una dissipazione visco-resistiva dipendente dal tempo, similmente alla condizione sperimentale, avente come risultato principale il rallentamento della dinamica sawtooth. Nelle simulazioni MHD in configurazione tokamak con elicità fissa e pressione diversa da zero, i regimi dell'oscillazione sawtooth sono governati dalla dissipazione visco-resistiva, mentre la conduttività termica isotropa regola la temperatura interna del plasma.

- La viscosità di Braginskii perpendicolare risulta essere il principale contributo al termine di viscosità in grado di massimizzare l'accordo tra simulazioni numeriche del modello visco-resistivo MHD e dati sperimentali.

- Viene sviluppata una descrizione del limite di densità RFP nel contesto della magnetoidrodinamica non lineare, evidenziando il ruolo del numero di Hartmann (che rappresenta la dissipazione visco-resistiva) nell'innescare la crescita delle instabilità di bordo $m = 0$ e l'insorgenza della cosiddetta MARFE (Multifaceted Asymmetric Radiation From the Edge), precursore della terminazione della scarica.

Il materiale presentato in questa Tesi è organizzato in 9 Capitoli. I Cap. 1 - 3 costituiscono la parte introduttiva (Parte I), mentre i Cap. 4 - 9 presentano la parte originale di questo lavoro, concentrandosi su simulazioni numeriche (Parte II) e analisi di dati sperimentali (Parte III). Seguono le conclusioni nella Parte IV.
Il Cap. 1 è dedicato all'introduzione della fusione nucleare come futura fonte di energia, contestualizzata analizzando il suo potenziale ruolo in scenari energetici di lungo termine. Vengono introdotti le basi delle reazioni di fusione nucleare e i metodi di confinamento del plasma, con particolare attenzione a quello magnetico, a cui è dedicata la Roadmap europea per la fusione. Infine, vengono presentati le caratteristiche principali e i problemi relativi alla fisica di un futuro reattore a fusione.
Il Cap. 2 si occupa della configurazione reversed-field pinch, la più studiata in questo lavoro. Le principali caratteristiche ed i risultati scientifici di questa configurazione vengono descritti brevemente, seguendo lo sviluppo storico del lavoro scientifico svolto presso il Consorzio RFX negli ultimi decenni. Viene inoltre fornita una prospettiva riassuntiva delle future applicazioni di questa configurazione.

Il Cap. 3 rappresenta la parte più matematica di questo lavoro. Lo scopo specifico del capitolo consiste nel riportare i passaggi principali che consentono di ricavare le formule dei coefficienti di trasporto (resistività, viscosità e conducibilità termica) in funzione delle grandezze misurabili del plasma. La derivazione è sviluppata nello schema di chiusura delle equazioni magnetoidrodinamiche per il trasporto classico. Sono inoltre fornite informazioni specifiche relative al trasporto turbolento. Infine, viene presentato il modello MHD viscoresistivo, che rappresenta il principale quadro teorico di questo lavoro.
Il Cap. 4 presenta gli strumenti numerici utilizzati in questo lavoro (codici SpeCyl e PIXIE3D), descrivendo brevemente i modelli simulati e gli schemi numerici adottati dai due codici. La seconda parte del capitolo riassume lo stato dell'arte della ricerca nella modellizzazione magnetoidrodinamica visco-resistiva dei pinch toroidali, con riferimento al ruolo delle condizioni al contorno e parametri di trasporto adimensionali. La parte finale presenta il database delle simulazioni disponibili e la previsione che possono fornire per il confronto con i dati sperimentali.
Il Cap. 5 indaga il ruolo dei profili spaziali e la dipendenza dal tempo della resistività e della viscosità nelle simulazioni SpeCyl e la loro influenza sulla velocità e sulle perturbazioni dei campi magnetici. Dal momento che la viscosità rappresenta il principale parametro di incertezza, l'analisi è principalmente uno studio di sensibilità per valutare l'effetto di profili di viscosità non uniformi in diversi regimi RFP (singola elicità, quasi singola elicità ed elicità multipla). Tuttavia, vengono testate anche lievi variazioni del profilo di resistività (il cui andamento è però conosciuto con maggiore sicurezza). Come risultato finale, viene testata una preliminare evoluzione auto-consistente, ispirata ai dati sperimentali, dei coefficienti visco-resistivi a centro plasma.
Il Cap. 6 è dedicato alla modellizzazione delle oscillazioni sawtooth del tokamak nel contesto della magnetoidrodinamica 3D non lineare. Come primo passo, vengono testati l'effetto di una pressione finita e di una resistività di 'tipo Spitzer' in simulazioni 1D assialsimmetriche. Successivamente, viene analizzato un insieme di simulazioni numeriche PIXIE3D con pressioni finite e simmetria elicoidale, variando sistematicamente i coefficienti di trasporto adimensionali (resistività, viscosità e conducibilità termica isotropa), al fine di studiare il ruolo di quest'ultimi nell'innescare l'instabilità sawtooth, limitatamente a questo quadro semplificato. Ulteriori studi relativi a questo argomento possono essere presi in considerazione per lavori futuri, ad es. sfruttando una resistività evoluta in modo autoconsistente di tipo Spitzer anche per simulazioni non assialsimmetriche.
Il Cap. 7 presenta l'esperimento RFX-mod e il database di spari considerato per questo lavoro. In particolare, vengono riassunti gli studi precedenti, condotti utilizzando questi dati. Inoltre, vengono presentate alcune analisi preliminari del database, compresa la valutazione dei parametri di trasporto adimensionali, sfruttando i risultati del Cap. 3.
Il Cap. 8 è specificamente dedicato al problema della stima della viscosità sulla base dei dati sperimentali di RFX-mod. Poiché valutazioni diverse, a seconda della teoria del trasporto considerata, mostrano differenze di ordini di grandezza, è stato considerato un confronto con simulazioni numeriche, basato sugli scaling delle instabilità del campo magnetico al bordo in funzione della dissipazione visco-resistiva. Questa analisi è stata perfezionata, utilizzando il confronto di modelli bayesiano per determinare la stima della viscosità che massimizzi l'accordo tra simulazioni e dati sperimentali.
Il Cap. 9 riassume brevemente lo stato dell'arte del limite di densità in configurazione RFP, contestualizzandolo nel quadro principale del limite di densità dei pinch toroidali. Viene introdotta la fenomenologia della MARFE (Multifaceted Radiation Radiation From the Edge) nel RFP, discutendo la sua crescita (in termini di instabilità del campo magnetico di bordo $m = 0$) e il suo ruolo di precursore del limite di densità. Come passaggio finale, viene presentata l'analisi degli spari di RFX-mod, mostrando il ruolo del coefficiente viscoresistivo (cioè il numero di Hartmann derivato dalle equazioni MHD basate su principi primi) nell'innescare l'inizio e la crescita della MARFE, permettendo infine la descrizione del significato fisico del limite di densità RFP in

termini di un singolo parametro derivato dalla teoria.

Voorwoord

Dit proefschrift vat de activiteit samen van ongeveer drie jaar die ik heb doorgebracht bij Consorzio RFX, gevestigd in de C.N.R. Onderzoeksgebied Padua, in Italië (tussen Oktober 2019 en September 2022) en aan de Universiteit Gent, in België (tussen Oktober 2022 en December 2022), als onderdeel van het Joint PhD Programme in Fusion Science and Engineering.
Fusie wetenschap onderzoek is gericht op de studie van kernfusie als een toekomstige energiebron die in staat is om de groeiende vraag naar energie te ondersteunen, CO2-vrij, naar verwachting veiliger dan de daadwerkelijke exploitatie van kernenergie (gebaseerd op kernsplijting), gebaseerd op gemakkelijker beschikbare brandstoffen en onafhankelijk van weersomstandigheden in strijd met andere hernieuwbare energiebronnen. De toekomstige exploitatie van kernfusie vereist de opsluiting van het plasma, een toestand van materie die wordt gekenmerkt door een consistente mate van deeltjes ionisatie. Volgens de toegepaste plasma opsluiting methode bestaan er verschillende onderzoekslijnen, waaronder de traagheids- en de magnetische opsluiting. Het Europese onderzoeksprogramma zet sterk in op de magnetische opsluiting, waarbij het plasma door middel van sterke magnetische velden wordt opgesloten in toroïdale apparaten. Magnetische opsluitingsfusie vertegenwoordigt de werkomgeving van dit proefschrift. Magnetische opsluiting fusie vertegenwoordigt de werkomgeving van dit proefschrift.
Aangezien een magnetisch opgesloten fusieplasma een complex systeem is, kunnen verschillende benaderingen (elk met zijn voor- en nadelen) worden toegepast om de dynamische evolutie ervan te modelleren, die zich uitstrekken van de microscopische beschrijving van een enkel deeltje tot de macroscopische magneto-vloeistofbeschrijving. Dit laatste wordt beschouwd in dit werk, dat het plasma beschouwt als een enkele vloeistof ondergedompeld in een magnetisch veld door middel van een 3D niet-lineair magnetohydrodynamisch model en dat twee magnetische configuraties met elkaar in verband brengt: de alternatieve reversed field pinch en de belangrijkste tokamak-configuraties. De stromen van fysisch relevante grootheden (zoals elektrische lading, momentum en energie) tussen verschillende gebieden van plasma's die niet in evenwicht zijn, leiden tot transport verschijnselen.
In dit proefschrift behandel ik het probleem van de experimentele evaluatie van **transport parameters**, die meestal verschijnen als invoer vrije parameters in de numerieke implementaties die de magnetohydrodynamica-modelvergelijkingen oplossen. Deze parameters bepalen de overgang tussen kwalitatief verschillende dynamische regimes van de vergelijkingen. Aan de andere kant kunnen transport parameters worden geschreven in de context van transport theorie als functie van plasma meetbare parameters, waardoor hun experimentele evaluatie mogelijk wordt. In het verleden is gewezen op een relatie tussen dergelijke dynamische overgangen en de dichtheidslimieten die zich manifesteren in de Reversed Field Pinch. Een van de belangrijkste doelen van dit werk, naast de andere beschreven in de volgende lijst, is om een beter begrip en beschrijving te krijgen van de dichtheidslimiet, die wordt bepaald door transport parameters in de reversed-field pinch. Dit kan in drie verschillende stappen worden bereikt:

- Bestudering van de werking van dimensieloze transport parameters in numerieke simulaties van stroomvoerende fusieplasma's met specifieke focus op: de rol van tijdsafhankelijke en

niet-uniforme profielen van visco-resistieve coëfficiënten op RFP-helixregimes (Hoofdstuk 4) en de rol van dissipatie parameters bij het beheersen van het zaagtandoscillatieregime in tokamak-configuratie (Hoofdstuk 6).

- Beoordeling van een kinematische viscositeitscoëfficiëntevaluatie in RFP-fusieplasma's, Hoofdstuck 8, evaluatie van de belangrijkste bijdrage aan de viscositeit, vergelijking van de evaluaties als gevolg van verschillende transporttheorieën: klassieke Braginskii, ionentemperatuurgradiënt en Finn. Dit is gemotiveerd, aangezien de beoordeling van een viscositeitsschatting nog steeds een van de belangrijkste moeilijkheden vormt bij het toepassen van MHD-voorspellingen op laboratoriumplasma, zoals vermeld in Ref. Montgomery [1992].

- Onderzoek naar de fysische inzichten van de dichtheidslimiet in RFP-plasma's, waarbij de fenomenologie wordt beschreven in termen van dimensieloze vloeistofparameters afgeleid van fundamentele MHD-vergelijkingen, Hoofdstuck 9. Ondanks zijn cruciale rol voor de realisatie van fusie, ontbreekt er inderdaad nog steeds een bevredigende verklaring voor de dichtheidslimiet in termen van geïdealiseerde vergelijkingen, zie Ref. Hawryluk and Zohm [2019].

Bij de ontwikkeling van het onderzoek worden verschillende **resultaten** verkregen, een strikte samenvatting is als volgt:

- In RFP MHD-simulaties produceren Braginskii-achtige viscositeitsprofielen (hoger aan de rand ten opzichte van uniform profiel) een demping van de kinetische energie van de modi die resoneren aan de rand, waardoor een lichte verbetering van de magnetische energie van de corresponderende modi mogelijk is. Er wordt een voorlopige tijdsafhankelijke, experimenteel-achtige visco-resistieve dissipatie getest, die voornamelijk resulteert in een vertraging van de zaagtanddynamiek.
  In tokamak MHD-simulaties met vaste heliciteit en niet-nuldruk worden de zaagtandoscillatieregimes bepaald door de visco-resistieve dissipatie, terwijl de isotrope warmtegeleiding de kernplasmatemperatuur regelt.

- De loodrechte Braginskii-viscositeit blijkt de belangrijkste bijdrage te zijn aan de viscositeitsterm die in staat is om de overeenkomst tussen visco-resistieve magnetohydrodynamica numerieke simulaties en experimentele gegevens te maximaliseren.

- Een beschrijving van de RFP-dichtheidslimiet is ontwikkeld in de context van niet-lineaire magnetohydrodynamica, waarbij de rol wordt benadrukt van het Hartmann-getal (dat de visco-resistieve dissipatie vertegenwoordigt) bij het veroorzaken van de groei van rand $m = 0$ instabiliteiten en in de MARFE (Multifaceted Asymmetric Radiation From the Edge) begin, voorloper van de ontladingsbeëindiging.

De kern van dit proefschrift is onderverdeeld in 9 Hoofdstukken. De Hoofdstukken 1 - 3 vormen het inleidende deel (Deel I), terwijl Hoofdstukken 4 - 9 presenteren het originele deel van dit werk, gericht op numerieke simulaties (Deel II) en experimentele data-analyse (Deel III). Conclusies volgen in Deel IV.
Hoofdstuk 1 is gewijd aan de introductie van kernfusie als toekomstige energiebron, waarbij de potentiële rol ervan in energiescenario's op de lange termijn wordt gecontextualiseerd. De basisprincipes van kernfusiereacties en plasma-opsluitingsmethoden worden geïntroduceerd, met specifieke aandacht voor de magnetische, waaraan de European Fusion Roadmap is gewijd. Ten slotte worden de belangrijkste kenmerken en fysische problemen van een toekomstige fusiereactor gepresenteerd.
Hoofdstuk 2 gaat over reversed-field pinch configuratie, de meest bestudeerde in dit werk. De belangrijkste kenmerken en wetenschappelijke prestaties van deze configuratie worden kort

beschreven, in navolging van de historische ontwikkeling van het wetenschappelijke werk dat de afgelopen decennia bij Consorzio RFX is verricht. Er wordt ook een samenvattend perspectief van toekomstige toepassingen gegeven.
Hoofdstuk 3 vertegenwoordigt het meer wiskundig gerelateerde deel van dit werk. Het specifieke doel van het hoofdstuk is om de belangrijkste stappen te rapporteren die het mogelijk maken de formules van transportcoëfficiënten (weerstand, viscositeit en warmtegeleiding) af te leiden als functie van meetbare plasmagrootheden. De afleiding is ontwikkeld in het sluitingsschema van magnetohydrodynamische vergelijkingen voor het klassieke transport. Er worden ook specifieke tips gegeven met betrekking tot turbulent transport. Ten slotte wordt het visco-resistieve MHD-model gepresenteerd, dat het belangrijkste theoretische kader van dit werk vertegenwoordigt.
Hoofdstuk 4 presenteert de numerieke hulpmiddelen die in dit werk worden gebruikt (SpeCyl- en PIXIE3D-codes), waarbij een korte beschrijving wordt gegeven van de gesimuleerde modellen en de numerieke schema's die door de twee codes zijn gebruikt. Het tweede deel van het hoofdstuk vat de stand van zaken samen van het onderzoek in visco-resistieve magnetohydrodynamica modellering van toroïdale kneepjes, met verwijzing naar de rol van randvoorwaarden en dimensieloze transportparameters. Het laatste deel presenteert de database met beschikbare simulaties en de voorspelling die ze kunnen geven voor de vergelijking met de experimentele gegevens.
Hoofdstuk 5 onderzoekt de rol van ruimtelijke profielen en tijdsafhankelijkheid van soortelijke weerstand en viscositeit in SpeCyl-simulaties en hun invloed op snelheid en verstoringen van magnetische velden. Aangezien de viscositeit de belangrijkste onzekerheidsparameter vertegenwoordigt, is de analyse voornamelijk een gevoeligheidsstudie om het effect te beoordelen van niet-uniforme viscositeitsprofielen in verschillende RFP-regimes (Single Helicity, Quasi Single Helicity en Multiple Helicity). Er worden echter zelfs kleine variaties van het (meer geconsolideerde) soortelijke weerstandsprofiel getest. Als eindresultaat wordt een voorlopige experimenteel-achtige zelfconsistente evolutie van de visco-resistieve coëfficiënten van de kern getest.
Hoofdstuk 6 is gewijd aan het modelleren van tokamak-zaagtandoscillaties in de context van 3D niet-lineaire magnetohydrodynamica. Als eerste stap wordt het effect van eindige druk en Spitzer-achtige soortelijke weerstand getest in 1D assymmetrische simulaties. Vervolgens wordt een reeks PIXIE3D-numerieke simulaties met eindige druk met spiraalsymmetrie, uitgevoerd door systematisch de dimensieloze transportcoëfficiënten (weerstand, viscositeit en isotrope warmtegeleiding) te variëren, geanalyseerd, waarbij de rol van laatstgenoemde bij het veroorzaken van de zaagtandinstabiliteit wordt bestudeerd, beperkt tot deze vereenvoudigde kader. Aanvullende studies met betrekking tot dit onderwerp kunnen worden overwogen voor toekomstige werken, bijv gebruikmakend van een Spitzer-achtige zelfconsistent ontwikkelde soortelijke weerstand, zelfs voor niet-assymmetrische simulaties.
Hoofdstuk 7 presenteert het RFX-mod-experiment en de database met opnamen die voor dit werk zijn overwogen. In het bijzonder worden de eerdere onderzoeken, uitgevoerd met behulp van deze gegevens, samengevat. Bovendien wordt enige voorlopige analyse van de database gepresenteerd, inclusief de evaluatie van transportdimensieloze parameters, gebruikmakend van de resultaten van Hoofdstuk 3.
Hoofdstuk 8 is specifiek gewijd aan het probleem van de viscositeitsschatting op basis van RFX-mod experimentele gegevens. Aangezien verschillende evaluaties, afhankelijk van de beschouwde transporttheorie, ordegrootteverschillen vertonen, is een vergelijking overwogen met numerieke simulaties, gebaseerd op de schaling van randmagnetische veldinstabiliteiten als functie van de visco-resistieve dissipatie. Deze analyse is verfijnd met behulp van Bayesiaanse modelvergelijking om de viscositeitsschatting te beoordelen die de overeenkomst tussen simulaties en experimentele gegevens maximaliseert.
Hoofdstuk 9 geeft een korte samenvatting van de stand van de techniek van de dichtheidslimiet van reversed-field pinch, en contextualiseert deze in het hoofdkader van de dichtheidslimiet van ringkernen. Vervolgens wordt de Multifaceted Asymmetric Radiation from the Edge (MARFE)-

fenomenologie in de reversed field pinch geïntroduceerd, waarbij de stijging ervan wordt besproken (in termen van instabiliteiten van het magnetische veld van de rand $m = 0$) en zijn rol als voorloper van de dichtheidslimiet. Als laatste stap wordt de analyse van RFX-mod-opnamen gepresenteerd, waarbij de rol van de visco-resistieve coëfficiënt (d.w.z. het Hartmann-getal afgeleid van de eerste beginselen van de magnetohydrodynamica-vergelijkingen) bij het triggeren van het begin en de stijging van MARFE, waardoor uiteindelijk de fysische inzichten van de RFP-dichtheidslimiet kunnen worden beschreven in termen van een op theorie gebaseerde parameter.

Part I

Introduction

Chapter 1

Magnetic confinement nuclear fusion

This Chapter introduces nuclear fusion as a potential energy source for long term energy scenarios, describing the basic physics of the process, the different plasma confinement methods studied so far and the most important constraints on a future 'fusion reactor' imposed by plasma physics. The focus is mainly on the magnetic confinement, according to the European Union program study on controlled nuclear fusion energy.
In Sec. 1.1, the problem of the world energy supply is introduced, presenting the causes and the options elaborated by the UN to overcome it.
In Sec. 1.2, we analyze the potential role of nuclear fusion in the future production of energy, presenting the EUROfusion program to make nuclear fusion energy a reality, in terms of scientific, technological and economic feasibility.
Sec. 1.3 deals with the physics of nuclear fusion reactions, explaining the basic features of nuclear energy processes and discussing which among the known nuclear reactions could better satisfy the requirements of a future reactor.
Sec. 1.4 concerns the basic physical features of fusion plasmas, with a particular focus on the plasma confinement. Three different methods of confinement are described: gravitational, inertial and magnetic. For the latter case, the main magnetic configurations in toroidal geometry (tokamak, stellarator and reversed-field pinch) are analyzed in terms pros and cons in future a reactor perspective.
In Sec. 1.5 we discuss the power balance of a fusion reactor, deriving the main requirements for such a device in terms of fusion performance.
The next two sections describe the main obstacle to realize fusion energy, in the field of plasma physics. Sec. 1.6 introduces the formalism of the energy principle, according to which the pressure and current driven instabilities are derived and discussed.
Finally, in Sec. 1.7, the main limits (on the edge safety factor, the line averaged density and the β parameter) imposed by plasma instabilities on experimental devices are briefly depicted.
Summary and final remarks follow in Sec. 1.8.

1.1 The problem of world energy supply

Nowadays, energy services (like industrial production, transportation, heating, cooling and lighting of the buildings, ...) are indispensable to guarantee an accettable standard of living. It is a well established evidence that the energy availability plays a key role in determining the life quality in a country. To quantify the latter, United Nations introduced in 1990 the HDI (Human Development Index), mainly considering the life expectation, the average educational level and economic condition of a population, Ref. UNDP (United Nations Development Programme) [1990]. Fig. 1.1 (b) shows that the HDI is correlated to the energy consumption per capita: in particular a minimum threshold consumption of about 80 GJ per capita turns out to be necessary in order to reach full development level (HDI $\geqslant 0.8$).

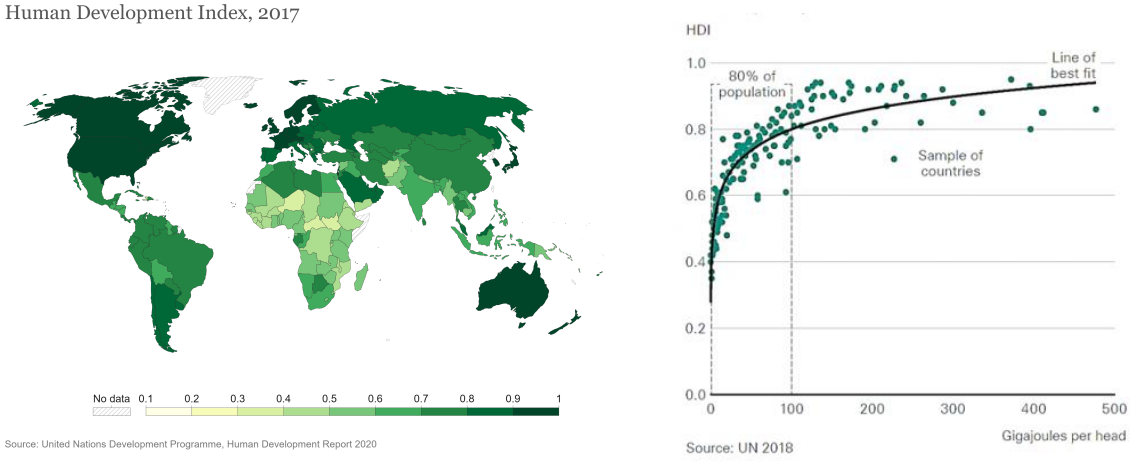

(a) (b)

Figure 1.1: Nations classification in terms of HDI (a). The HDI as function of the energy consumption per capita, according to United Nations data (b).

In the last decades the energy demand has increased and it is expected to maintain this growing trend in the future because of the world population increase and the development of rapidly industrializing countries. Unfortunately, the increase of energy need and production can seriously jeopardize the global environmental stability, due to the use of fossil fuel in energy production and to the consequent emission of Green House Gases (GHGs).
In October 2018, the IPCC (Intergovernmental Panel for Climate Change) published a report about the impacts of a 1.5 °C average temperature increase with respect to the pre-industrial level (Ref. Masson-Delmotte et al. [2018]). The study of the Earth temperature change suggests that the latter scenario is likely to be reached within the 2030-2052 years, because a 1.0°C global warming with respect to pre-industrial levels has already taken place, as shown in Fig 1.2 (a). As a consequence, GHGs emissions must be drastically reduced, in order to avoid further long-terms climate changes, in addition to the already existing ones. To this aim, very ambitious scenarios with absence or limited overshot of the 1.5 °C threshold increase are studied, implying drastic reduction of GHGs (and especially CO_2) starting from the present days to reach zero global CO_2 emissions within the next decades (Fig. 1.2 (b)).
Those scenarios try to predict the long terms trends related to population, economic growth and hypothesize the development and introduction of new technologies in the energy field. In particular, the latest report of the International Energy Agency (Ref. IEA (International Energy Agency) [2020]) provides as desirable power production scenario (Fig. 1.3):

- to more than double the actual amount of power generation by the 2070,
- to shut down (almost completely) the power generating plants based on fossil fuels (coal,

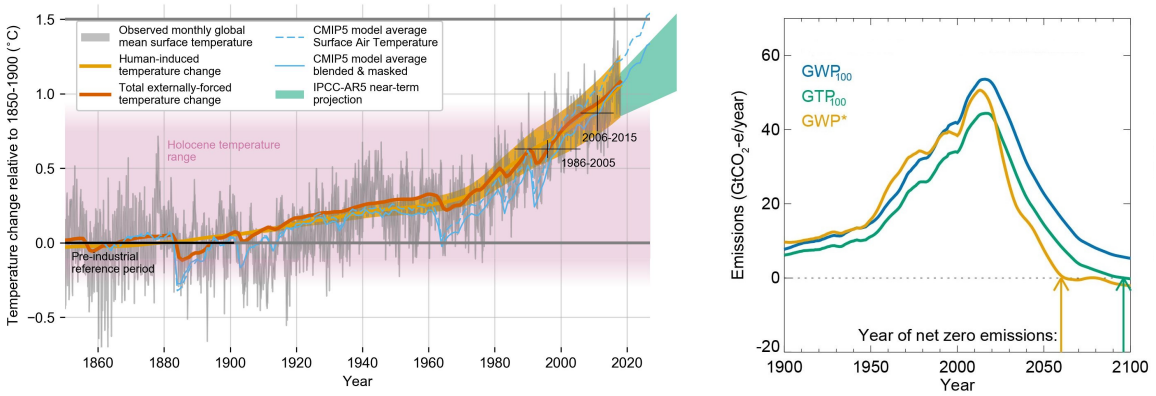

(a) (b)

Figure 1.2: Earth temperature change (1850 - 2018) with respect to the average temperature in the pre-industrial period 1850-1900 (a). CO_2 emission measurements and scenario to avoid 1.5 °C overshoot (b). Images from Ref. Masson-Delmotte et al. [2018].

oil and natural gas),

- to reach an energy production mix mainly based on renewable energy sources (wind, hydroelectric and solar plants),
- to maintain and increase a significant amount of power generation by nuclear plants.

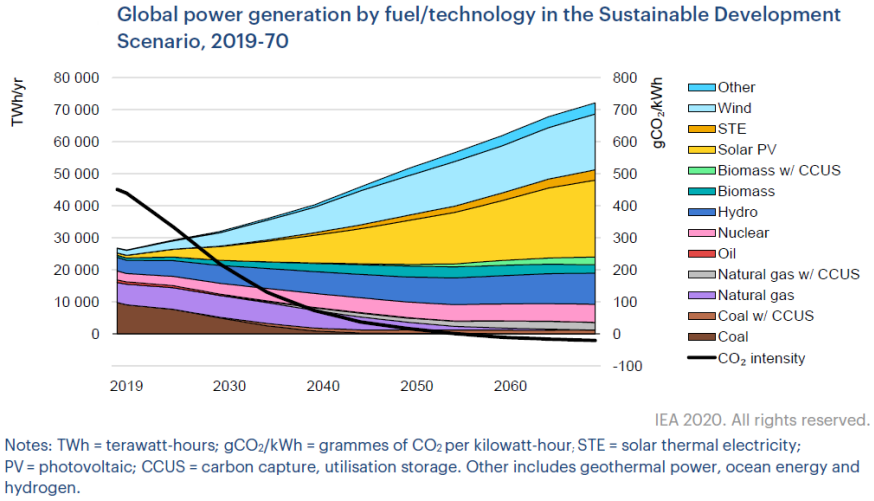

Figure 1.3: Image from Ref. IEA (International Energy Agency) [2020].

In the long term, other carbon free energy sources, based on the development of new technologies are expected to contribute to the future energy mix. One of the most promising energy source is probably nuclear fusion, to which many efforts and international projects are devoted.

1.2 The role of fusion in long term energy scenarios

Nuclear fusion is a promising energy source for long term energy scenarios, with a potential benefits with respect to the other energy sources available in the present energy mix. Unlike fossil fuels, fusion is a CO_2 free energy source and it would require largely available fuels. Unlike

renewable energy sources, fusion does not depend on weather conditions and does not require huge energy storage systems. Fusion is a nuclear technology (like nuclear fission), but it does not produce long lasting nuclear waste and, more importantly, fusion reactors are safe because they are not based on a chain reaction, so that in case of an accident the nuclear reactions are no more sustained from the outside and the reactor automatically turns off, without damaging the external environment.
Despite the huge efforts that have been put in fusion research by the international scientific community for many decades (Ref. Barbarino [2020]), the goal of an operating fusion reactor is still far away. The long series of studies historically began just after World War II, at the "Second United Nations International Conference on the Peaceful uses of Atomic Energy", better known as the "Atoms for Peace" conference (1-13 September 1958, Geneve) and it is predicted to last for many decades. In this context, the European Union has developed a reactor-oriented fusion development program (summarized in the so called Power Plant Conceptual Study, described in Ref. Maisonnier et al. [2007]) aimed at the successive demonstration of the scientific, the technological and the economic feasibility of fusion power. The main steps towards this ambitious goal are summarized in Ref. EUROfusion Consortium [2018], that constitutes the European research roadmap, illustrated in Fig. 1.4.

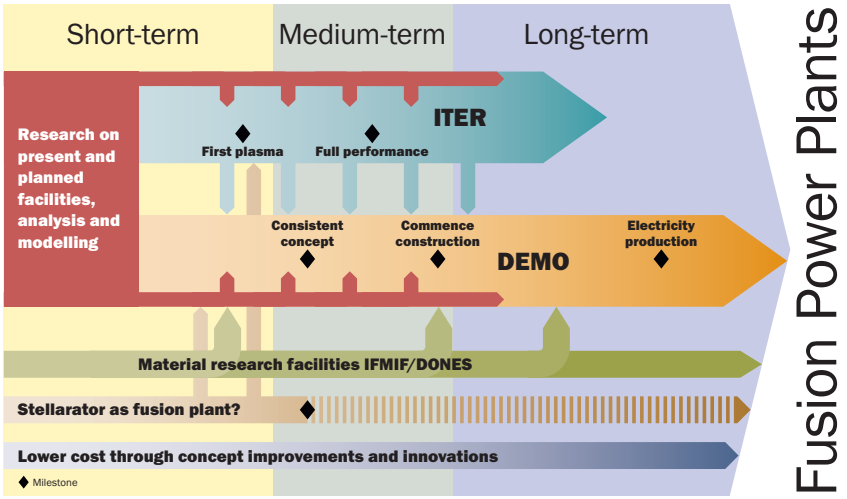

Figure 1.4: The EUROfusion program, aimed at the realization of Fusion Power Plants, image taken from Ref. EUROfusion Consortium [2018].

The European fusion research project mainly relies on the magnetic confinement, focusing on the tokamak configuration, but considering also other alternatives, like the stellarator, see Sec. 1.4. The ITER project (International Thermonuclear Experimental Reactor), currently under construction in Cadarache (France) represents the next major step in fusion research, aimed at demonstrating the scientific feasibility of fusion. It is a tokamak configuration device and it si predicted to begin the operations within the end of the decade and to the reach the full performance in the 2040's. Parallel to ITER, different projects aimed at solving technological problems in material research will be operated. The final step will consist of the construction of the European DEMO (DEMOnstrative reactor), which will prove the technological feasibility of fusion energy directly producing electrical power for the grid, opening the way to the exploitation of fusion energy during the second part half of this century.
Despite the very long and challenging roadmap, nuclear fusion energy still represents one of the

main hopes to solve the problem of world energy supply, at least in a long term scenario, thanks to its intrinsic safety and to the huge amount of energy producible with a small amount of fuel.

1.3 Nuclear fusion reactions

The atomic nucleus is composed by protons and neutrons hold together by the nuclear force in a very small region of space, of the order of $1 - 10$ fm (depending on the nucleus considered). This quantum binding state is characterized by a mass lower than the sum of the masses of its smaller constituents: the difference in mass Δm is directly related to the binding energy thanks to the famous Einstein formula $E = \Delta mc^2$.
For a nucleus with mass M atomic number Z and mass number A, the binding energy per nucleon B is given by the following formula (in natural units):

$$M(A, Z) = Zm_p + (A - Z)\, m_n - AB(A, Z). \tag{1.1}$$

Each nucleus is characterized by its own binding energy: the behaviour of the latter (deduced from the experimental measures of the masses) with respect to the mass number can be estimated in the context of the liquid drop model for nuclei and it is shown in Fig. 1.5.

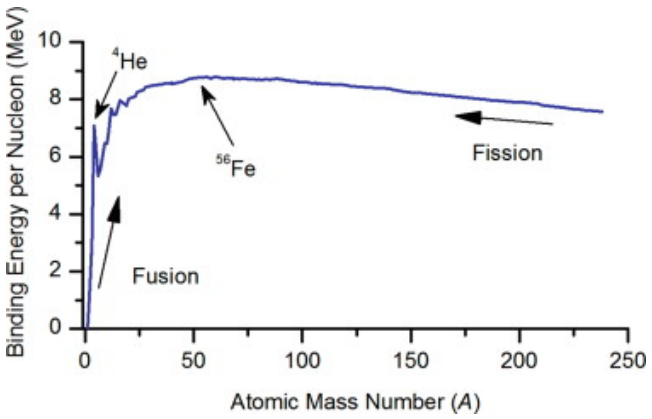

Figure 1.5: Trend of the binding energy per nucleon as function of the atomic mass number.

As a consequence, in the nuclei a vast amount of energy is stored, exploitable by means of nuclear reactions. Indeed, in a nuclear reaction, a certain amount of energy can be released (as products kinetic energy) when the mass of the products is lower than the mass of the reactants, that corresponds to the case in which the products have a higher binding energy than the reactants. Since the binding energy trend shows a maximum correspondent to $A = 56$ (iron peak), two very different types of reactions are available to get energy: fission and fusion.
The reactions of nuclear fission consist of the subdivision of a heavy nucleus into two or more lighter nuclei and fragments. Such a reaction can be spontaneous or induced by an external projectile (like proton, neutron and γ photon), as in the following reaction (from Ref. Freidberg [2007]):

$$^{235}_{92}\mathrm{U} + {}^{1}_{0}\mathrm{n} \longrightarrow {}^{140}_{58}\mathrm{Ce} + {}^{94}_{40}\mathrm{Zr} + 2\,{}^{1}_{0}\mathrm{n} + 6\,\mathrm{e}^{-} + 206\,\mathrm{MeV}. \tag{1.2}$$

Nuclear fission has been regularly exploited as a controlled energy source in nuclear power plants since several decades, during which it has shown the potential to develop enormous amounts of energy. However, there are also disadvantages in the exploitation of nuclear fission: the production of long-lasting radioactive waste which requires special storage for a practically infinite time and the awful accidents that can occur when the chain reaction control fails (Černobyl' 1986) or the cooling system does not work properly (Fukushima 2011).
Nuclear fusion is the opposite process: two light nuclei merge together and give rise to a heavier

nucleus. It is the type of reaction powering stars and sustaining their structure against the gravitational force that, otherwise, would cause them to collapse. Nuclear fusion is also responsible for the generation of the chemical elements with $Z \leqslant 26$.
The exploitation of nuclear fusion turned out to be much more difficult than in the case of fission and, despite the efforts made, it does not exist yet a prototype reactor similar to the "Fermi pile" (described in Ref. Fermi [1946]) able to produce electric power from fusion for commercial purposes: this is mainly due to the fact that nuclei are positively charged and their fusion requires the overcoming of the Coulomb potential barrier generated by the nuclei themselves. To build a machine able to exploit controlled nuclear fusion, the reactions mostly taken into account are the following:

$$^2\mathrm{D} + {}^2\mathrm{D} \longrightarrow {}^3\mathrm{T}(1.01\,\mathrm{MeV}) + \mathrm{p}(3.02\,\mathrm{MeV}), \tag{1.3}$$

$$^2\mathrm{D} + {}^2\mathrm{D} \longrightarrow {}^3\mathrm{He}(0.82\,\mathrm{MeV}) + \mathrm{n}(2.45\,\mathrm{MeV}), \tag{1.4}$$

$$^2\mathrm{D} + {}^3\mathrm{T} \longrightarrow {}^4\mathrm{He}(3.5\,\mathrm{MeV}) + \mathrm{n}(14.1\,\mathrm{MeV}), \tag{1.5}$$

$$^2\mathrm{D} + {}^3\mathrm{He} \longrightarrow {}^4\mathrm{He}(3.6\,\mathrm{MeV}) + \mathrm{p}(14.7\,\mathrm{MeV}), \tag{1.6}$$

where the energy released by the reactions can be found in Ref. Kikuchi et al. [2012]. As anticipated in Sec. 1.2, the energy obtained by means of a nuclear fusion reaction is of the order of $1 - 10$ MeV, one million times the typical value of $1 - 10$ eV that can be obtained by means of chemical combustion of fossil fuels, showing that, if carried out, fusion could be a promising energy source for the future.
To determine the future reactor basic features, one among the reactions has to be chosen, with the goal of maximizing the reaction cross section (and consequently the reaction rate of the system) at the reactor operating temperature. Cross section detailed values for the reactions (1.3) - (1.6) are reported in Ref. Bosch and Hale [1992]. Nowadays, the reaction candidate is (1.5) because it is the one that largely maximizes the cross section (that means the probability of realizing it) at the lowest value of the scattering energy, as it is evident from Fig. 1.6.

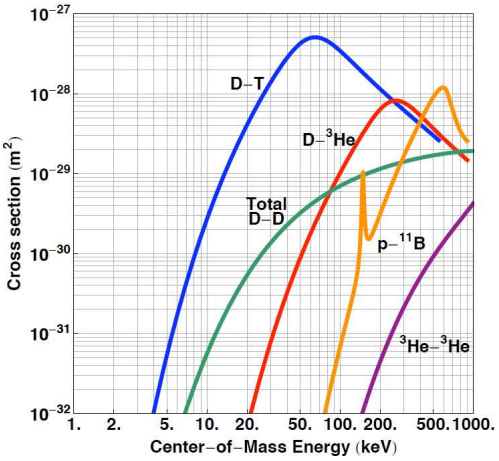

Figure 1.6: Fusion reactions cross section, as function of the center of mass energy.

However, there are also critical aspects related to it, because a radioactive isotope not present in nature like tritium is involved and a high energy neutron is produced. The first drawback would require to perform on site tritium breeding, using lithium, while to overcome the second drawback, a long-term scientific research program is on course (as anticipated in Sec. 1.2) with the goal of managing the effects of high energy neutron fluxes on materials. In any case,

also the other reactions are not completely discarded at least for second generation reactors, because they can overcome the limit given by the finite lithium availability. The disadvantages in exploiting nuclear fusion are in any case minor than in the case of nuclear fission because developing uncontrolled chain reactions is physically impossible and the maximum life-time of the radioactive waste produced is about 100 years, with respect to 10^5-10^6 years of fission.

1.4 Plasma: methods of confinement

The relatively high collision energies that are required to achieve the values of the cross sections in Fig. 1.6 imply working with matter in the state of plasma. The latter (defined for the first time in Ref. Langmuir [1928]), is a state of matter characterized by a considerable degree of ionization so that the charged particles that make it up are able to display a collective behaviour. In this ionized gas, the encounter of a deuterium and tritium nuclei not always gives rise to a fusion reaction because the largely dominant outcome of the collision is Coulomb scattering, since its cross section is approximately two orders of magnitude greater (see Fig. 1.7).

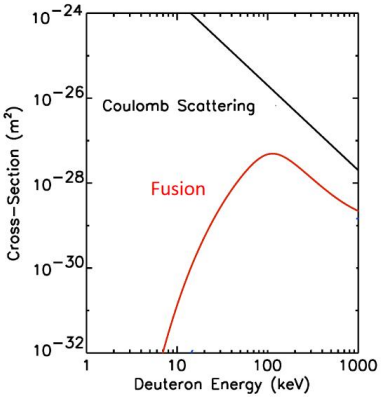

Figure 1.7: Comparison between Coulomb scattering and deuterium-tritium fusion cross sections: Coulomb scattering is the largely dominant process.

To realize a sufficient number of fusion reactions (i.e to guarantee a sufficient rate of energy production), plasma needs to be confined in a finite region of space for a relatively long time: in this way, each deuterium/tritium particle is forced to undergo multiple collisions with the opposite species, till it fuses into a helium nucleus.
Different plasma confinement methods are known (as shown in Fig 1.8) that exploit respectively: gravity (gravitational confinement, Fig 1.8 (a)), compression (inertial confinement, Fig 1.8 (b)) and , magnetic field (magnetic confinement, Fig 1.8 (c)).

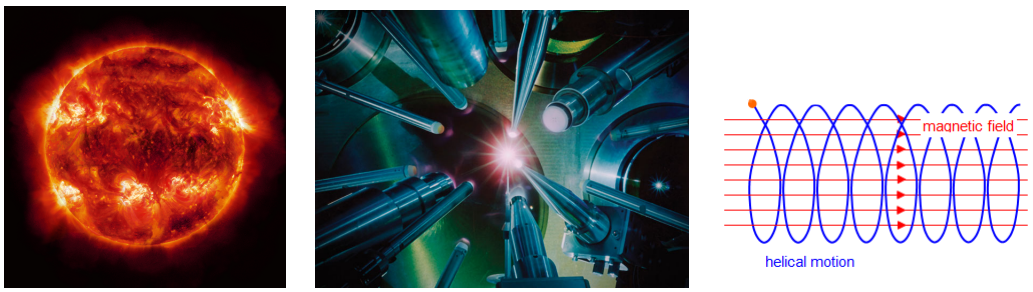

(a) (b) (c)

Figure 1.8: Plasma confinement methods: gravitational confinement (a), inertial confinement (b) and magnetic confinement (c).

1.4.1 Gravitational confinement

The gravitational confinement represents the 'natural' way of confining plasma in stars. A star is indeed a massive celestial object, made up of plasma held together by its self-gravitational interaction. The star life-cycle is ruled by the balance of gravitational force (generating the star collapse) and pressure force (generating the star expansion) sustained by the large amount of fusion reactions that power the star.
It is worth noticing that the reaction selected to power the future fusion reactor (1.5) is different with respect to the reactions occurring in the stars (described, e.g. in Ref. Iliadis [2015]). This is not a surprise, since the plasma conditions of the future reactor are expected to be different with respect to the stellar ones (especially in terms of density and pressure). The main nuclear astrophysics reactions of hydrogen burning (and helium synthesis) are the following:

$$\mathrm{p} + \mathrm{p} + \mathrm{e}^{-} \longrightarrow {}^{2}\mathrm{D} + \nu_{\mathrm{e}} + 1.4\,\mathrm{MeV}, \tag{1.7}$$

$${}^{2}\mathrm{D} + \mathrm{p} \longrightarrow {}^{3}\mathrm{He} + \gamma + 5.5\,\mathrm{MeV}, \tag{1.8}$$

$${}^{3}\mathrm{He} + {}^{3}\mathrm{He} \longrightarrow {}^{4}\mathrm{He} + 2\,\mathrm{p} + 12.9\,\mathrm{MeV}. \tag{1.9}$$

As it is evident, in stellar hydrogen burning no tritium is involved and no neutrons are produced.

1.4.2 Inertial confinement

A possibility of plasma confinement for nuclear fusion research is the so-called inertial confinement fusion, Ref. Atzeni and Meyer-ter Vehn [2004]. This method basically consists of rapidly heating the deuterium-tritium solid target surface with high power laser beams, generating a plasma that surrounds the fuel envelope. Then, the evaporation of the surface material compresses the fuel up to very high temperatures ($\sim 10\,\mathrm{keV}$) and particle densities ($\sim 10^{32}\,\mathrm{m}^{-3}$), causing the capsule implosion, resulting in the thermonuclear burn of the fuel (shown in Fig. 1.9). The energy is released in very short time intervals ($\sim 10^{-10}\,\mathrm{s}$).

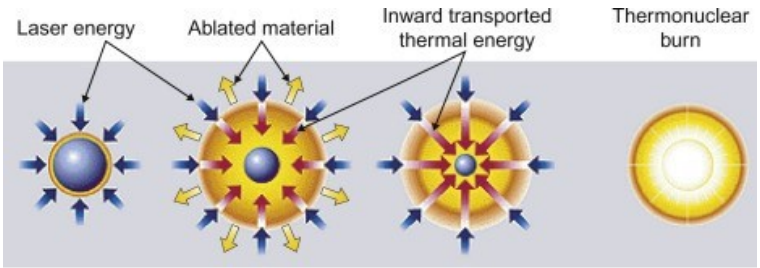

Figure 1.9: Main phases of inertial confinement fusion: target heating, target surface evaporation and fuel compression, implosion and thermonuclear burn.

The difficulties of the inertial confinement are mainly related to: the extremely high power laser required to initiate the reaction, the low percentage of the laser energy that ends up in the fuel target and the high power management generated by the experiment.
The largest inertial fusion experiment is the National Ignition Facility (NIF), located at Lawrence Livermore National Laboratory (LLNL) in Livermore, California, USA and it is composed by a system of 192 high power laser beams. In 2021 this device made a significant step forward in the field of inertial confinement fusion, realizing a 1.37 MJ fusion yield during an inertial fusion implosion (described in Ref. Zylstra et al. [2022]), overcoming the previous record by a factor ~ 8.

1.4.3 Magnetic confinement

The most promising confining method on which the European research project is centered (and on which this work is focused) is the magnetic one, summarized in Ref. Ongena et al. [2016]. The idea at the basis of magnetic confinement is quite easy: since no material surface able to support direct contact with high temperature plasma exists, a magnetic field distribution has to be generated in order to confine the plasma, exploiting its composition of charged particles. In fact an electric $\mathbf{E}$ and magnetic field $\mathbf{B}$ affect the motion of a q charged particle with velocity $\mathbf{v}$ by means of a force $\mathbf{F}$, whose expression is given by the Lorentz formula:

$$\mathbf{F} = q\left(\mathbf{E} + \mathbf{v} \times \mathbf{B}\right). \tag{1.10}$$

A complete treatment of charged particles dynamics (including drifts) in presence of an electromagnetic field can be found in Chapters 2 and 3 of Ref. Goldston and Rutherford [1995]. The motion can be typically divided into two contributions: a uniform velocity gyro-motion with radius given by the *Larmor radius* r_L and angular frequency given by *cyclotron frequency* ω_c and a guide-center motion that follows magnetic field lines:

$$r_L = \frac{mv_\perp}{qB}, \qquad \omega_c = \frac{qB}{m}. \tag{1.11}$$

Using this basic idea, the early linear fusion devices were built exploiting a cylindrical symmetry magnetic field; the main defects of such a configuration was the lost of particles at the extremes that could be reduced but not cancelled by magnetic field intensification ("mirrors", Ref. Post [1987]).
To overcome this difficulty, toroidal geometry was introduced. This type of geometry can be represented by the toroidal solenoid model: a toroidal magnetic field is generated by a series of equally spaced, torus concatenated magnetic field coils, the so called 'toroidal field coils'. This solution definitively solves the problem of particle loss at the extremes, but introduces unavoidable deflections of particle trajectories with respect to the magnetic field line, known as "drifts". Drifts can be due to magnetic field gradients and curvature and can be almost completely cancelled (at least for thermal particles) with the introduction of a poloidal component of the magnetic field, introducing the so called 'magnetic field rotational transform'.
Depending on how the latter is generated, toroidal plasma configurations are classified in: pinches (like the tokamak and the reversed-field pinch) and stellarators. In the first case a plasma current is imposed, which generates the poloidal magnetic field (Faraday's law). In the second one, the rotational transform is generated exploiting a specific design of the magnetic field coils, that are able to produce a magnetic field with both toroidal and poloidal components. The main toroidal plasmas magnetic configurations are summarized in the next paragraphs.

The tokamak configuration

The best known magnetic configuration is the tokamak, Ref. Wesson and Campbell [2011]. It was invented in the USSR in the early 1950's, by Sakahrov and Tamm. The details of their work (Ref. Tamm [1957], Sakharov [1958]) became known in western countries only some years later during the "Atoms for Peace" conference. Soon, the tokamak became the leading configuration in controlled nuclear fusion research after the achievement of a 1 keV core plasma temperature in 1968 on the T3 tokamak, as reported in Ref. Peacock et al. [1969], which represented an undisputed record for the time. Since then, a lot of progresses have been made in this research field and the tokamak still represents the favorite configuration to approach reactor conditions, as the construction of ITER proves.
In a tokamak (sketched out in Fig. 1.10), the toroidal component of the magnetic field is obtained thanks to toroidal magnetic field coils, while the poloidal one is guaranteed by the plasma

current flowing in toroidal direction triggered by the central solenoid. Vertical field coils are instead used to control shape and positioning of the plasma inside the vacuum chamber. In the tokamak the poloidal field B_θ is smaller than the toroidal B_ϕ, $B_\theta/B_\phi << 1$.

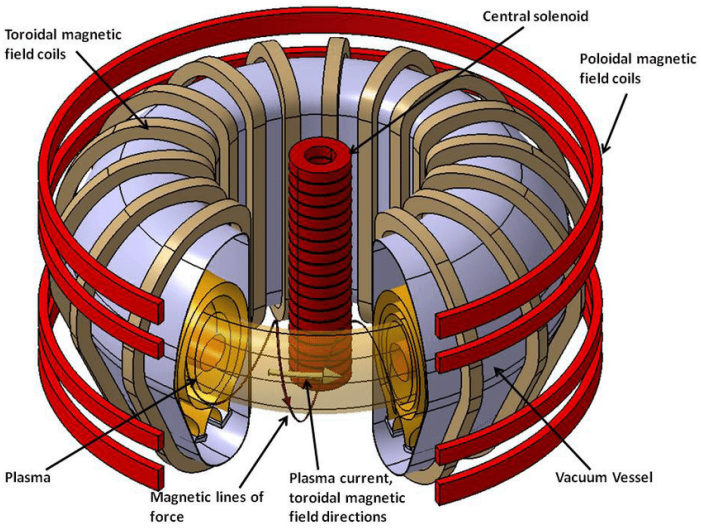

Figure 1.10: Schematic representation of the tokamak configuration.

Nowadays, the main drawback of tokamak physics is the presence of many plasma instabilities, summarized in Sec. 1.6, that significantly restrict the operational space of tokamak devices.

The stellarator configuration

According to the EUROfusion roadmap, stellarators (described in Ref. Wakatani [1998]) represent the alternative configuration to be considered for the future reactor. The stellarator was invented in the 1950's by Lyman Spitzer in the USA, Ref. Spitzer [1958].
The main characteristic of the stellarator is the absence of a significant plasma current and the presence of specially designed magnetic field coils able to generate both the components of the field, shown in Fig. 1.11. This characteristic has both benefits and drawbacks: the absence of the current prevents the development of current driven instabilities and makes the stellarator intrinsically capable to sustain a plasma steady-state while the overall experiment design becomes much more complicated because of the magnetic field coils and the massive use of additional heating systems, necessary to compensate the absence of ohmic heating effect, guaranteed (in tokamaks) by the plasma current.

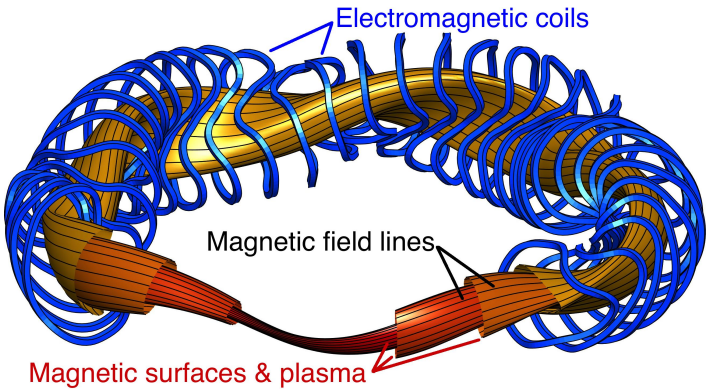

Figure 1.11: Schematic representation of the stellarator configuration.

The largest experiment of this configuration is the optimized superconducting stellarator device Wendelstein 7-X (with major radius $R_0 = 5.5\,\mathrm{m}$ and minor radius $a = 0.5\,\mathrm{m}$). It is located in Greifswald, Germany and operates since 2015. Before entering the present shut down phase, very promising results have been obtained during the first high performance operations, described in Ref. Klinger et al. [2019].

The Reversed-Field Pinch (RFP) configuration

The reversed-field pinch (RFP) configuration is the less known among the three configurations and it is characterized by high values of the plasma current (even an order of magnitude larger than those of a tokamak with the same on axis magnetic field), and reversed sign of the toroidal magnetic field in the external region. In the RFP the ordering of the magnetic field is $B_\theta \approx B_\phi$. The exploitation of such a high plasma current has both benefits and drawbacks (the opposites with respect to the stellarator configuration). In particular, the design of a RFP device is simplified, since the need for additional heating systems and superconducting magnetic field coils is reduced thanks to the high self-organization level displayed by RFP plasmas. However, the RFP displays a lot of current driven instabilities, whose non linear interaction usually generates magnetic chaos and lack of confinement.
Since this is the configuration on which the major part of this work is focused, a more detailed description is referred to Chp. 2.

1.5 Fusion reactor power balance: present and future experiments

A fusion reactor is a device able to generate a positive energy output by means of fusion reactions. Taking into account the main sources of gain and loss of energy, it is possible to predict approximately the operational conditions of future reactors. This type of analysis was carried on for the first time by Lawson, obtaining the homonym criterion described in Ref. Lawson [1957]. Since that time, additional heating systems have been introduced and slightly different power balance analysis have become more common. In this Section, the analysis considered in Chapter 1 of Ref. Wesson and Campbell [2011] is followed.
The main factors that contribute to the change of the plasma energy density w are: the power heating input p_H which can be injected from outside, the α particles power heating p_α produced by fusion reactions, the power loss related to transport p_L and to radiation p_R. In one formula (all the powers involved are expressed per unit of volume):

$$\frac{dw}{dt} = p_H + p_\alpha - p_L - p_R. \tag{1.12}$$

Considering the simplifying hypotheses of quasi-neutrality ($n_e \approx n_i \approx n$), equal ion and electron temperature ($T_e \approx T_i \approx T$) and that the plasma can be treated as a monoatomic gas one gets:

$$w = 3nT, \tag{1.13}$$

where the temperature T indicates the associated energy (by means of the Boltzmann constant k_B).
While neutrons cannot be held in the plasma by the magnetic field, alpha particles in principle should remain trapped thanks to their electric charge and consequently contribute to plasma heating. In particular, their contribution is proportional to the energy brought by each single particle ($E_\alpha = 3.5\,\mathrm{MeV}$) and to the number of reactions realized per unit of time and volume (reaction rate). Here, an optimized case in which deuterium and tritium have the same density $n/2$ is considered:

$$p_\alpha = \frac{1}{4} n^2 \langle \sigma v \rangle E_\alpha, \tag{1.14}$$

where the symbol $\langle\rangle$ denotes that the average is computed over the velocity components of the phase space.
The difficulty in modeling transport phenomena in fusion plasmas is also reflected in the estimate of the relative losses. Typically, the power loss is expressed using a phenomenological parameter, called *energy confinement time* τ_E, that can be estimated experimentally or by means of scaling formulas:

$$p_L = \frac{w}{\tau_E}. \tag{1.15}$$

Three different phenomena contribute instead to radiation losses: cyclotron radiation, line spectroscopic emission and bremsstrahlung. Cyclotron radiation is to be attributed to the helical trajectory followed by a charged particle in presence of a magnetic field: its contribution is not relevant because plasma is able to reabsorb radiation at those frequencies. Also the line spectroscopic emission can be neglected if one considers that its main sources are impurity atoms not completely ionized, whose concentration should be reduced at the minimum possible level. Finally, the only contribution to the radiation losses that can not be neglected or reduced is the one related to bremsstrahlung: this phenomenon consists of the radiation emission due to acceleration that the charged particles undergo in a magnetized plasma. The power density associated to bremsstrahlung is usually calculated thanks to the following formula:

$$p_b = \alpha_b n^2 T^{1/2} \mathrm{W m^{-3}}, \tag{1.16}$$

where the constant $\alpha_b = 5.35 \times 10^{-37}\,\mathrm{W m^3 keV^{-1/2}}$.
The ideal condition to be achieved by a fusion reactor is called *ignition*: in such a situation, the system has a positive power balance exploiting the energy generated by α particles, without the addition of external heating. This condition can be equivalently expressed by the following inequality:

$$n\tau_E > \frac{12T}{\langle \sigma v \rangle E_\alpha - 4\alpha_b T^{1/2}}. \tag{1.17}$$

However, ignition remains a very difficult target to be achieved because it requires very high temperatures (about 25 keV) well beyond the predicted operating temperature of future reactors (about 10 - 15 keV). In this range the reactivity $\langle \sigma v \rangle$ is well described by the scaling formula:

$$\langle \sigma v \rangle = 1.1 \times 10^{-24} T^2 \mathrm{m^3 s^{-1}} \tag{1.18}$$

that implies the achievement of the final condition, that represents the 'figure of merit', known as *triple product*:

$$nT\tau_E > 5 \times 10^{21}\,\mathrm{m^{-3} keV s}. \tag{1.19}$$

This value can provide an idea of the target values for each quantity in magnetic confinement fusion research: $n \approx 10^{20}\,\mathrm{m^{-3}}$, $T \approx 10 - 15\,\mathrm{keV}$ and $\tau_E \approx 3 - 5\,\mathrm{s}$. In Fig. 1.12 the best results achieved by tokamaks in terms of triple product ($nT\tau_E$) are plotted.
Since additional external heating is thought to be unavoidable for the next generation of devices it is customary to define another parameter Q as the ratio between the power produced via thermonuclear reactions and the external power provided to the plasma. In this way, ignition would correspond to $Q = \infty$. A value of $Q = 1$ (*break-even* condition) indicates a balance of the powers related to the plasma, but to build a reactor able to exploit fusion for commercial purposes a value of $Q \sim 50$ is required, to guarantee a positive balance, according to an engineering point of view.

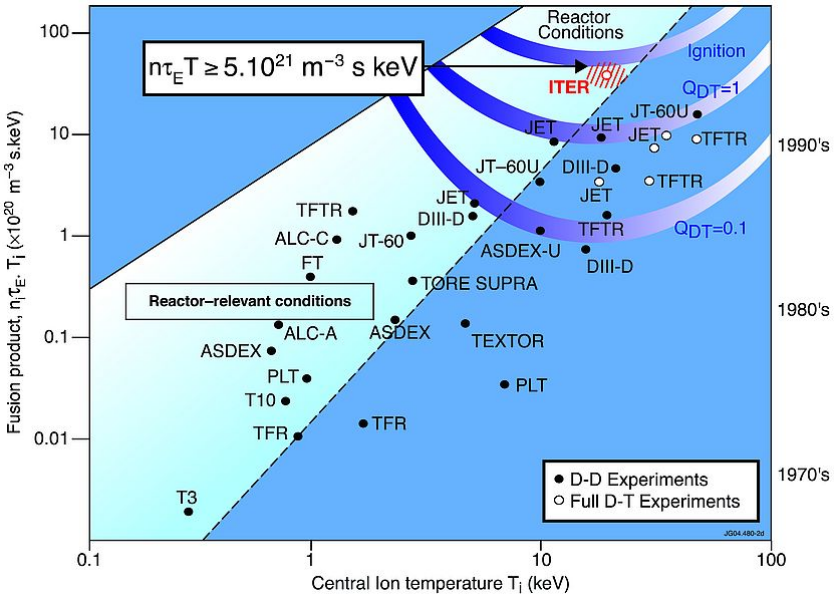

Figure 1.12: Achievements of the main fusion devices in terms of triple product.

The most important performances in terms of the Q parameter have been achieved during the 1990's by the experiments: TFTR (Tokamak Fusion Test Reactor) in 1994 at Princeton, USA with a $Q \sim 0.27$ and by JET (Joint European Torus) in 1997 at Culham, UK with a $Q \sim 0.65$, during their deuterium tritium (DT) campaigns. A detailed overview of the two experimental operations can be found in Ref. Bell et al. [1995] and Keilhacker et al. [1999]). The JET '97 record has not yet been beaten by any other device so far because, since the 90s, no more performing experiments have been built. However, during the recent JET DT campaign aimed at studying ITER relevant physics, the record of a single shot energy production has been obtained (59 MJ), although using a higher input power than in '97, resulting in a factor $Q \sim 0.3$, Ref. Banks [2022].

The next years are predicted to be a period of great advances in fusion research, since new experimental facilities, capable of DT operations are under construction.

The ITER project (International Thermonuclear Experimental Reactor) will be the largest fusion device ever built ($R_0 = 6.2$ m and $a = 2.0$ m), with operational parameters near the ones needed to reach the condition in Eq. (1.19), a value of $Q \sim 10$ and a 500 MW fusion power output. It is currently under construction at Cadarache, France (Ref. Bigot [2021]). Its first plasma is temporarily scheduled for 2025, while the DT operations are scheduled for 2037-2042, even though these dates are currently undergoing to a process of re-evaluation, due to the impact Covid-19 pandemic.

Another ambitious project is the compact, high-field, tokamak SPARC (Ref. Creely et al. [2020]), currently under construction in Devens, Massachusetts, USA, aiming at a Q value comparable to the ITER one and at 100 MW of fusion power. Dealing with a compact device, this project does not rely on the plasma volume (as ITER), but on the generation of high magnetic fields: indeed an on axis magnetic field $B_0 = 12.2$ T is expected for SPARC, in comparison to the $B_0 = 5.3$ T of ITER. This result can be obtained exploiting the technology of High Temperature Superconductors (HTS), which has recently proved to be successful, with the development of the first extremely high field magnetic coil for fusion, reported in Ref. Molodyk et al. [2021].

Other important future devices but not capable of DT operations are: JT-60SA and DTT. JT-60SA (upgrade of JT-60U), whose construction has been completed in Japan (Ref. Kamada et al. [2022]) will operate to contribute to the ITER physics development, while DTT (Divertor Test Tokamak), will be built in Italy (Ref. Albanese and all [2016]) to investigate different divertor configurations in view of DEMO.

1.6 Plasma instabilities

The major physics related problem affecting magnetic confinement machines is related to plasma instabilities. In fact, when an equilibrium configuration is explored, the development of instabilities generally has deleterious effects, depending on the magnetic configuration considered and on the type of the instability developed. For the tokamak configuration one should mention: harmless saturated instabilities, ELM (Edge Localized Modes described in Ref. Zohm [1996]) and disruptions (described in Ref. Wesson et al. [1989]). The latter are dangerous events which lead to premature discharge termination: in this case the energy accumulated in the plasma is released in a very small time, and, consequently it is absorbed by the walls delimiting the plasma, causing damage to them in addition to the generation of high stresses on the external coils.
In this Section, we briefly review the main tokamak plasma instabilities, following Ref. Zohm [2014]: this would bring us to outline the main operational constraints imposed by plasma physics instability to a tokamak configuration device in Sec. 1.7. The starting point for any linear stability analysis is the equilibrium configuration. This can be easily derived from the magnetohydrodynamics equations (see Chp. 3):

$$\mathbf{j}_0 \times \mathbf{B}_0 = \nabla p_0, \qquad \nabla \cdot \mathbf{B}_0 = 0, \qquad \nabla \times \mathbf{B}_0 = \mu_0 \mathbf{j}_0, \quad \mathbf{v}_0 = 0, \tag{1.20}$$

with $\mathbf{j}$, $\mathbf{B}$, $\mathbf{v}$ representing respectively the current density, the magnetic field and the plasma velocity field. The second step consists of rewriting each quantity X as sum of an equilibrium term $X_0(\mathbf{r})$ and a small time dependent pertubative term $X_1(\mathbf{r},t)$: $X(\mathbf{r},t) = X_0(\mathbf{r}) + X_1(\mathbf{r},t)$, $|X_1| << |X_0|$. If one introduces the *Lagrangian displacement vector* $\boldsymbol{\xi}(\mathbf{r},t)$ of a plasma element from its equilibrium state:

$$\mathbf{v} := \frac{d\boldsymbol{\xi}}{dt} \quad \rightarrow \quad \mathbf{v}_1 \approx \frac{\partial \boldsymbol{\xi}}{\partial t}, \tag{1.21}$$

the first ordering of the equation of motion results in:

$$\rho_0 \frac{\partial \mathbf{v}_1}{\partial t} = \mathbf{j}_1 \times \mathbf{B}_0 + \mathbf{j}_0 \times \mathbf{B}_1 - \nabla p_1 := \mathbf{F}(\mathbf{r},t) \quad \rightarrow \quad \rho_0 \frac{\partial^2 \boldsymbol{\xi}}{\partial t^2} = \mathbf{F}, \tag{1.22}$$

where $\mathbf{F}$ is the first force per unit of volume acting on the plasma. Since Eq. (1.22) resembles Newton's dynamics equation, it can be treated exploiting the *energy principle* (introduced in the magnetohydrodynamics field in Ref. Bernstein et al. [1958]). The latter consists of the evaluation of the potential energy difference δW introduced by the displacement $\boldsymbol{\xi}$:

$$\delta W = -\frac{1}{2} \int \boldsymbol{\xi} \cdot \mathbf{F}(\boldsymbol{\xi}) dV. \tag{1.23}$$

If δW is positive, the system is stable, otherwise it's unstable. The solution of the eigenvalue Eq. 1.23 highlights the existence of two distinct main causes for plasma instabilities: pressure gradient and magnetic field curvature (for the *pressure driven* modes, Fig. 1.13 (a)) and the current density parallel to the equilibrium field (for the *current driven* modes, Fig. 1.13 (b)). Despite this classification, it is worth noting that the majority of plasma instabilities jointly involves pressure and current driven modes.
The pressure driven modes can often be analyzed using the β parameter, defined as the ratio between kinetic and magnetic pressure, quantifying the effectiveness of plasma confinement, given a determined magnetic field:

$$\beta = \frac{p}{B^2/2\mu_0}. \tag{1.24}$$

Their stabilization depends on the balance of the contributions coming from plasma regions with good or bad magnetic field curvature.

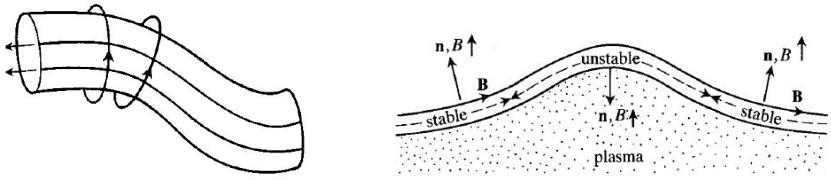

(a) (b)

Figure 1.13: Schematic representation of the linear stability analysis modes: current driven (a), pressure driven (b).

To analyze the current driven modes the *safety factor* q is introduced. This factor is a parameter (dependent on the magnetic surface ψ considered) defined as the toroidal angle $\Delta\phi$ necessary to complete an entire poloidal lap (2π) along a magnetic field line, that is usually computed in cylindrical geometry:

$$q := \frac{\Delta\phi}{2\pi} = \frac{1}{2\pi}\oint_{\psi}\frac{B_\phi}{R_0 B_\theta}ds \quad \rightarrow \quad q(r) = \frac{rB_z(r)}{R_0 B_\theta(r)}. \tag{1.25}$$

Current driven modes can be further classified in *resistive* and *ideal modes*, depending on the effect of the resistivity η in the instability development. In particular, in fusion plasmas a non negligible resistivity causes the formation of regions called *current sheets* characterized by a very strong convexity of the magnetic field (high $\nabla^2 B$). In this case, Alfvén theorem does not hold anymore and the topology of the magnetic field lines can vary during the so called *magnetic reconnection* events (see Ref. Yamada et al. [2010]). Resistive instabilities cause the breaking up of the current sheet in different regions with separated magnetic topology called *magnetic islands* (see Fig. 1.14).

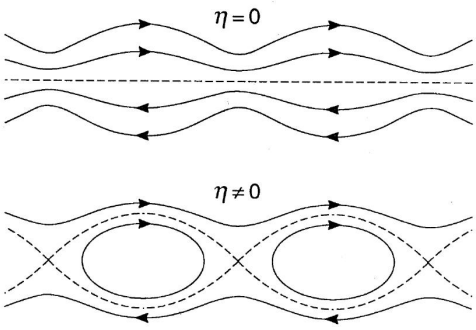

Figure 1.14: Magnetic field lines comparison in case of ideal and resistive instabilities.

For the sake of completeness, we mention that resistive modes can be further classified in: *tearing modes* (with a mode growth rate scaling comparable to the Sweet Parker reconnection, Ref. Parker [1957]) and *resistive kink* (with a faster growth than in the Sweet Parker model). For a large aspect ratio ($R_0/a >> 1$), low β tokamak the exact energy contribution δW due to current driven kink, can be calculated:

$$\delta W = \frac{2\pi^2 B_z^2}{\mu_0 R_0} \int_0^a \left[\left(r\frac{d\xi}{dr} \right)^2 + \left(m^2 - 1 \right) \xi^2 \right] \left(\frac{n}{m} + \frac{1}{q} \right)^2 r dr + \frac{2\pi^2 B_z^2}{\mu_0 R_0} \xi_a^2 a^2 \left[\frac{n^2}{m^2} - \frac{1}{q_a^2} + \Lambda m \left(\frac{1}{q_a} + \frac{n}{m} \right)^2 \right], \quad (1.26)$$

where Λ represent the stabilizing effect of a perfectly conducting wall and m and n represent the poloidal and toroidal wave number of the perturbation ($\boldsymbol{\xi} \propto \exp\left[i\left(m\theta + n\phi\right)\right]$).
Eq. (1.26) highlights the main causes of current driven instabilities in tokamak plasmas: the presence of a real wall (giving rise to *resistive wall* modes) and the presence of a resonant surface, a magnetic surface where the condition:

$$q = -\frac{m}{n} \quad (1.27)$$

holds, giving rise to a *resonant* kink. It is worth noting that, according to the Fourier expansion used in this Thesis (see App. B.3), the harmonic argument of a perturbation is $m\theta + n\phi$, and therefore the resonant condition holds a minus sign, $-m/n$. If the condition (1.27) is satisfied by a perturbation, it means that there is a resonant magnetic surface where the perturbation matches exactly the spatial periodicity of the magnetic field lying on that surface, neutralizing the the stabilizing action of the magnetic tension (justified by the Alfvén theorem in hot conductive plasmas) and allowing the growth of the instability.
The most dangerous instabilities of this type are those characterized by low integer wave numbers value: in particular, for the tokamak configuration, the conditions to avoid are $q(a) = 2$ (satisfied by the perturbations with $m = 2$, $n = -1$ and its harmonics), $q(a) = 3$, and more generally $q(a) = m/n$ with low m, n: in this case the working parameters are chosen in order to obtain $3 < q(a) < 4$. Another requirement for the tokamak stability is represented by the condition: $q(r) > 1$ (Kruskal-Shafranov limit). In particular the value $q \sim 1$ is reached for tokamak only on the magnetic axis ($r = 0$), thanks to a phenomenon called sawtooth oscillations (see Chp. 6) that consists in an oscillation of the central temperature values connected precisely to a resistive instability, while for the RFP configuration $q(0) << 1$.

1.7 The operational limits of a fusion reactor

There are three important limits that significantly restrict the tokamak operational space: the $q(a) = 2$ *limit*, the *density limit* and the β *limit*.
The first one is related to the *resonant kink* instabilities (already cited in Sec. 1.6). The value of the safety factor to avoid all this type of instabilities are summarized in Ref. Wesson [1978]. The most important constraints involve the edge safety factor and is given by the condition $q(a) > 2$, necessary to avoid the disruption caused by the $m = 2$, $n = -1$ mode destabilization. From the operative point of view, the most common choice for tokamak devices is to operate in the range: $3 < q(a) < 4$. This requirement constraints the maximum achievable plasma current (if we consider the toroidal magnetic field determined by technological constraints on the magnetic field coils).
The second instability summarized in this Section is the *Greenwald density limit*: it consists of a limit related to the number density above which plasma discharges are no more sustained. This limit (disruptive for the tokamak) affects all the three magnetic configurations and will be discussed in details in Chp. 9. According to a theoretical point of view, a completely satisfying explanation of this limit is not yet available and the physical origin of the density limit is not fully understood. However, a phenomenological law based on experimental data-sets was found by Greenwald (Ref. Greenwald et al. [1988]). It states that stability (with respect to the density limit) is obtained for line-averaged value of density $\bar{n}$, such that:

$$\bar{n}\left(10^{20}\,\mathrm{m}^{-3}\right) < \frac{I\,(\mathrm{MA})}{\pi a^2\,(\mathrm{m}^2)}, \tag{1.28}$$

in which the right hand side is called *Greenwald density* n_G. This operative parameter represents the maximum achievable density, once the plasma current has been fixed. One of the most accredited explanation of the phenomenon suggests the density limit to be linked with the high concentration of not entirely ionized impurities in the plasma edge: the latter increase the irradiated power and consequently cause the cooling of the plasma external region and the increase of the resistivity (because it will be shown in the Chp. 3 that $\eta \propto T^{-3/2}$). As a final result, the decrease of current causes a contraction of the plasma column that brings to the loss of stability. Also for the density limit a strong relationship with resonant mode is believed, in particular for the mode $m = 2$, $n = -1$ in the tokamak configuration and $m = 0$ $n = -1$ in the RFP configuration.
The operational parameters with respect to the current driven instabilities are well summarized in the so called Greenwald plot (see Fig. 1.15).

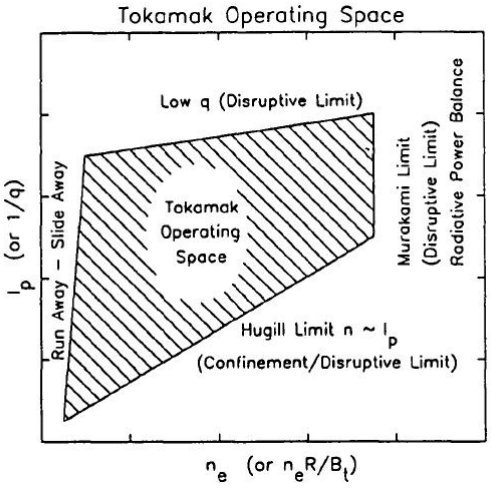

Figure 1.15: Tokamak operating space on the Greenwald plane: picture from Ref. Greenwald et al. [1988].

In this plot, four important limits imposed on the tokamak operating space mainly by the current driven instabilities are sketched out:

- the low q limit ($q(a) > 2$), that constraints the maximum value of the plasma current,
- the Murakami limit that constraints the maximum value of density at high currents (being mainly radiative, the latter can be relaxed injecting power to the plasma),
- the Hugill limit, that constraints the maximum achievable density to n_G,
- the limit associated to the run away electrons, that imposed a minimum density threshold below which a consistent fraction of electrons (on the high temperature of the Maxwellian distribution) become non-collisional, providing damage to the device. This argument has been recently reviewed in Ref. Breizman et al. [2019].

In this work we will provide an interpretation of the density limit (in the case of RFP magnetic configuration), trying to connect it with dimensionless fluid-dynamical numbers defined in the context of MHD models and with the analysis of experimental data related to measures of the magnetic turbulence in then edge of RFX-mod plasmas, see Chp. 9.

The β *limit* involves pressure driven instabilities. Since $nT\tau_E \propto B^2\beta\tau_E$, it is desirable to increase the value of β as much as possible, however the maximum values achievable are strongly limited by the existence of a limit above which, pressure driven instabilities development is found, called *Troyon limit* (presented in Ref. Troyon et al. [1984]):

$$\beta\,(\%) < g\frac{I(\mathrm{MA})}{a(\mathrm{m})B_\phi(\mathrm{T})}, \tag{1.29}$$

where a, B_ϕ, I are respectively minor radius, toroidal magnetic field and plasma current, while the constant g is called Troyon factor (its value is betweeen 2.8 and 3.5).
Due to this restriction in β, a lot of efforts should be put in improving the technology of the magnetic field coils and increasing the energy confinement time τ_E.

1.8 Summary and final remarks

Because of the world population increase and the rapid industrialization of developing nations, the global energy demand is expected to increase in the medium and long term scenario. On the other side, the clear link between fossil fuels energy production, the consequent emission of green house gases and the average Earth temperature increase imposes a complete revision of the future energy mix production.
In this context, nuclear fusion represents a promising energy source for long term energy scenarios, being: based on abundant fuels, carbon-free, intrinsically safe and producing only short term radioactive wastes. For this reason, an ambitious program to prove the scientific (ITER experiment), technological (DEMO reactor) and economic (first fusion power plant) feasibility of fusion energy exists.
The key feature of nuclear fusion energy is the vast amount of energy stored in the atomic nuclei, that can be exploited during fusion reactions. The reaction that maximizes the rate of energy production is the fusion of deuterium and tritium nuclei into a helium nucleus and a neutron. To force the merging of positively charged nuclei, it is necessary to achieve very high temperatures ($\sim 10\,\mathrm{keV}$), condition at which the matter exists at the plasma state, requiring the confinement of the latter. There are three different options for plasma confinement: gravitational, inertial and magnetic. Magnetic confinement relies on the generation of high magnetic field that confine the charged particles composing the plasma.
The target for a magnetic confinement fusion reactor is to confine the plasma at a sufficiently high density and temperature and for a sufficiently long time to overcome the triple product threshold: $nT\tau_E > 5 \times 10^{21}\,\mathrm{m}^{-3}\mathrm{keVs}$.
However, there are some important plasma physics related obstacles (typically ending up in the plasma loss) that could prevent the next generation of fusion devices to achieve this goal. These obstacles, studied in the context of magnetohydrodynamics linear stability analysis, are the plasma instabilities that can be driven by pressure gradient and plasma current density. The pressure driven modes mainly contribute to the Troyon limit, that limits the effectiveness of the confinement. The current driven modes impose an important constraint on the safety factor profile $q(a) > 2$, which implies a restriction on the maximum plasma current. The latter determines, according to the Greenwald phenomenological scaling, a threshold for the maximum achievable density (density limit).
At the present research status, the physical understanding of these processes represents a crucial point to guarantee safe operations in the next generation of nuclear fusion devices.

Chapter 2

The Reversed-Field Pinch (RFP) configuration

This Chapter is devoted to the presentation of the reversed-field pinch (RFP) configuration, because a substantial part of the work will be devoted to phenomena concerning such magnetic configuration. The main goal is to provide the physics basic features of the RFP plasmas with particular reference to the Research work carried on in Padova (Italy) in the last decades by Consorzio RFX, in the C.N.R. research area.
In Sec. 2.1 the basic properties of the RFP configuration, with specific focus on the plasma physics point of view.
Sec. 2.2 is a brief review of the evolution in RFP science in both theoretical and experimental fields and of the experimental devices operating in Padova in the context of the reversed-field pinch fusion research activity.
The next two Sections retrace the main goals achieved in the field of theoretical modeling of RFP plasmas. In Sec. 2.3, the Taylor's theory is presented, describing its comparison to the experimental data and why it has become necessary to go beyond this theory in recent decades. In Sec. 2.4 we present the subsequent advances to the Taylor's theory, mainly sustained by the modelling activity, based on magnetohydrodynamics numerical simulations.
Sec. 2.5 analyzes the typical safety profile displayed by a RFP plasma and the related MHD instabilities, which can develop as result of the resonance of a magnetic field perturbation.
Sec. 2.6 deals with the main experimental features observed in helical self-organized states, trying to point out the role played by the latter in a future fusion reactor that exploits RFP plasmas.
To conclude, in Sec. 2.7 the possible exploitation of the RFP configuration for a future fusion reactor is described. At the current research state, the properties of the RFP seem to fit very well the requirements needed by hybrid fission-fusion reactors, that are analyzed in the Section. Summary and final remarks follow in Sec. 2.8.

2.1 Basic features of the RFP

As anticipated in Sec. 1.4, reversed field-pinch is one of the three main toroidal configurations for the magnetic confinement of fusion relevant plasmas. In this Section, its most relevant features are summarized.
The reversed-field pinch magnetic configuration is experimentally induced in a toroidal plasma, generating a very intense plasma current, flowing in the toroidal direction, which can reach values up to an order of magnitude larger with respect to a tokamak discharge current, with the same on-axis toroidal field B_0. According to the Ampére's law, the high toroidal current induces a high poloidal magnetic field, much more intense than in an analogous tokamak plasma.
Indeed, for the latter configuration, the toroidal magnetic field is one order of magnitude larger than the poloidal one: $B_\theta << B_\phi$. On the contrary, in the RFP the toroidal and poloidal components are of comparable amplitude: $B_\theta \approx B_\phi$. Moreover, in the outer region of the plasma, the poloidal field is dominant, because the toroidal component decreases as one approaches the plasma edge, and reverses its sign in the outermost region, as shown in Fig. 2.1. This non-trivial phenomenon is discussed in Sec 2.3, 2.4 and names the configuration.

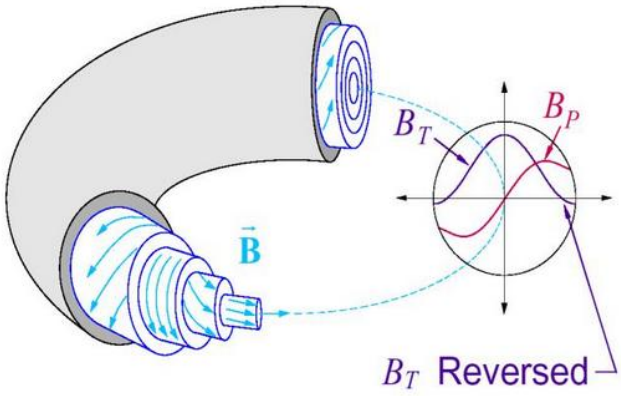

Figure 2.1: Toroidal and poloidal magnetic fields for RFP configuration. Figure from Ref. Sarff [2011].

Because less performing than the tokamak, the reversed-field pinch is not a favourite candidate for the construction of the first fusion demonstrative reactor, but it is still of interest, according to the current state of the research, for a second generation of fusion devices (see Sec. 2.7).
The potential advantages obtained exploiting the RFP configuration consist of limiting:

- the need for superconducting coils, because the majority of the magnetic field is generated by the plasma current,
- need for additional heating systems (e. g. neutral beam injection and radio-frequency wave heating) thanks to the relatively high plasma resistivity (with respect to the tokamak configuration) that could allow the entirely ohmic heating of the plasma.

It should be mentioned that limiting the additional heating systems has important consequences on the current drive, requiring additional operational constraints on the central solenoid, increased by the high level of operating plasma current.
On balance, in a reactor perspective, the choice of the RFP configuration could globally improve the device reliability and allow for a simpler reactor design.
However, there are also important disadvantages in exploiting the RFP, that are related to the magnetohydrodynamics instabilities (presented in Sec. 2.5) and the confinement. This is highlighted by the value of the energy confinement time τ_E: the latter is lower by orders of

magnitude in the RFP with respect to the tokamak, as consequence of the more disordered magnetic topology (represented in Fig. 2.2), which is characterized by the overlap of magnetic islands generated by tearing mode instabilities) that enhances the transport from the central region to the edge, prohibiting optimal confinement and heating of the center of the plasma.

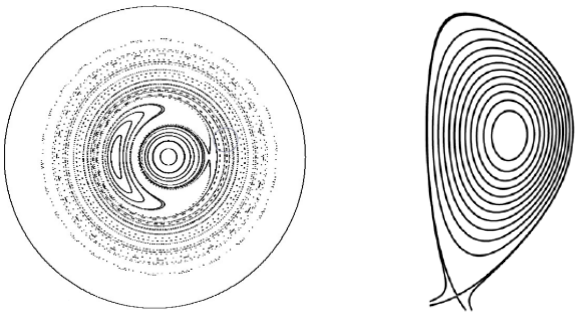

(a) (b)

Figure 2.2: Poloidal projection of RFP (a) and tokamak (b) magnetic field lines: while in RFP plasmas magnetic islands and chaos arise, in tokamak plasmas a more ordered magnetic topology is observed.

Despite this, both numerical and experimental studies show the possibility (which will be discussed further in Sec. 2.6) of reaching, under favourable conditions, a high level of self-organization, in which the plasma column spontaneously assumes a helical shape (Fig. 2.3), transport barriers are created and also an improved magnetic topology is reached, with beneficial effects on plasma confinement. As consequence of it, RFP plasmas still represent an important research field for physics and engineering studies in magnetic confinement fusion.

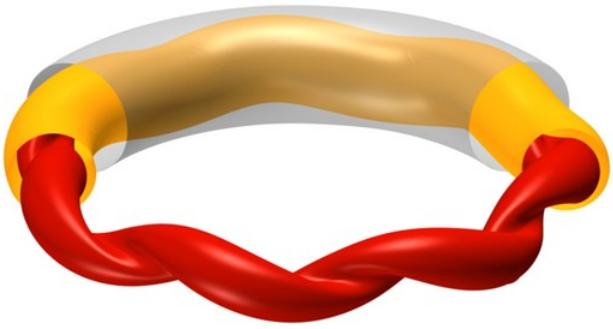

Figure 2.3: Plasma column self-organization in RFP configuration: the assumes a helical shape and confinement is improved. Figure from Ref. Lorenzini et al. [2009b].

There are many experiments devoted to the study of the RFP configuration, generally of smaller size if compared with the largest tokamaks or stellarators. The main are RFX-mod (Reversed-Field eXperiment) located in Padova (Italy), the MST (Madison Symmetric Torus) located in Madison, Wisconsin (USA) (see Ref. Dexter et al. [1991]), the KTX (Keda Torus eXperiment) in Hefei, China (see Ref. Liu et al. [2019]), EXTRAP T2R in Stockholm Sweden (see Ref. Brunsell et al. [2001]), TPE-RX (see Ref. Koguchi et al. [2009]) and RELAX (see Ref. Masamune et al. [2007]), both operated in Japan.

2.2 Brief history of RFP research in Padova

In the last decades, a lot of progresses have been made carrying on research in reversed-field pinch fusion plasmas, periodically reviewed in Ref. Bodin and Newton [1980], Bodin [1990], Marrelli et al. [2021]. In particular, significant steps have been made in increasing the value of the plasma current (reaching the record of 2 MA on RFX-mod) and improving the feedback control system of MHD instabilities. These advancements have allowed the possibility of creating and studying helically self-organized plasma states, basically resulting in an improvement of the fusion performance (see Sec. 2.6). In Fig. 2.4, the main scientific advancements and the experimental devices succeeded in Padova are sketched out.

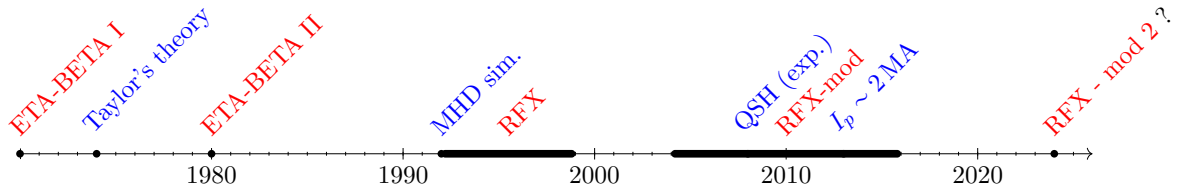

Figure 2.4: Time line of RFP research activity: devices operating in Padova (red), scientific milestones in RFP science (blue).

The first pioneering experiments operating in Padova in '70s and '80s were ETA-BETA I and ETA-BETA II, described respectively in Ref. Buffa et al. [1975] and Antoni and Ortolani [1983]. In the same decades, the origin of the edge toroidal magnetic field reversal was studied, resulting in the relaxation theory, by J. B. Taylor, summarized in Sec. 2.3. Despite qualitatively predicting the reversal, it soon became clear that, in order to get a quantitative match with the experimental data, it was necessary to proceed with more refined techniques. This activity started in the early '90s and it is carried on also nowadays: it consists of the numerical simulations of the RFP plasma using magnetohydrodynamic models, summarized in Chp. 3 and 4. The MHD contribution to this research mainly resulted in the prediction of the helical self organized states existence and in the modelling of the physical properties of the latter.
In the same years, the RFX (Reversed-Field eXperiment) device started its experimental activity, as the largest operating RFP device, presented in Ref. Rostagni [1995]. The main limitations of RFX were the mode control and the low current operations. The RFX experimental activity ended in 1999, due to a fire that considerably damaged the experimental device.
The RFX device (upgraded to RFX-mod, described in Sec. 7.1) was back in production in 2004. Endowed with a system of saddle coils able to suppress many MHD modes, this device has been able to prove the existence of helical self organized states, reaching operating currents of 2 MA. Now the RFX is facing again a shut-down phase, currently predicted to end in 2024, with the launch of the new upgrade RFX-mod 2, that thanks to the removal of the vessel is expected to provide a further limitation of the instabilities caused by the wall resistivity. More details on the upgrade will be given in Sec 7.2.

2.3 Taylor's relaxation theory

The theoretical explanation of the reversed-field pinch has been developed over the last few decades. The first milestone in this field is undoubtedly the Taylor's theory of plasma relaxation that was enunciated for the first time in Ref. Taylor [1974].
To develop it, two requirements (derived in Ref. Woltjer [1958]) are essential. These two statements regard a physical quantity related to the magnetic topology, called *magnetic helicity* $\mathcal{H}$ which is defined as:

$$\mathcal{H} := \int \mathbf{A} \cdot \mathbf{B} dV, \tag{2.1}$$

where the integral is calculated over the volume of the magneto-fluid system considered and $\mathbf{A}$ is the vector potential defined by the relation: $\mathbf{B} = \nabla \times \mathbf{A}$. Although the vector potential depends on the choice of the gauge, it can be shown that helicity is gauge invariant, that means it is a good physical quantity. The two Woltjer's theorems are now enunciated:

First Woltjer's theorem. *If a magneto-fluid has zero resistivity ($\eta = 0$), than helicity $\mathcal{H}$ is conserved in time:*

$$\frac{d\mathcal{H}}{dt} = 0. \tag{2.2}$$

Second Woltjer's theorem. *In a system in which the magnetic helicity $\mathcal{H}$ is kept constant, the minimization of the magnetic energy $W = \int B^2/2\mu_0 dV$ is obtained for a force-free field defined by the condition:*

$$\nabla \times \boldsymbol{B} = \mu \boldsymbol{B}, \tag{2.3}$$

with μ constant.

The proof of the two theorems is summarized in App A.1, following the approach of Choudhuri [1998].
J. B. Taylor considered a magneto-fluid with a small departure from perfect conductivity (the effect of the resistivity η is not negligible) in toroidal symmetry. When this system is characterized by a high Θ parameter, also known as "pinch" parameter, defined as the normalized edge poloidal field B_θ:

$$\Theta := \frac{B_\theta(r = a)}{\langle B_\phi \rangle} = \frac{\mu_0 I_p}{2\pi a \langle B_\phi \rangle}. \tag{2.4}$$

The initial condition (out of equilibrium) relaxes towards a "quiescent" state that is largely stable. In Eq. (2.4), $\langle\rangle$ indicates the average along the radial coordinate.
To analyze the phenomenon from a more quantitative point of view, Taylor made the hypothesis that, although the resistivity is non negligible, the total helicity is conserved, which seems in contradiction with first Woltjer's theorem. Actually, the presence of resistivity implies that each magnetic field line is not frozen inside the fluid flux tube and so the helicity is not anymore constant along each line of force. However, if the departure from the perfect conduction is slight, the global helicity (evaluated on the whole fluid volume) is expected to remain approximately constant, because the dissipation, while changing the magnetic topology, does not significantly alter the value of the field. For this reason the effect of the topological change consists merely in a redistribution of the helicity contributions among all magnetic field lines (see Ref. Taylor [1974] for more details).
Since helicity is conserved, the second Woltjer's theorem can be applied and so one can state that the system will minimize its magnetic energy in the condition of force-free field. This final state results to be a 'quiescent' state because if the minimization of the magnetic energy implies that no magnetic force can act on the magneto-fluid.
To describe this final state of equilibrium (reached after the relaxation) Eq. (2.3) is solved in cylindrical geometry with periodic boundary conditions. Using the coordinates r, θ and z all the physical quantities result constant with respect to θ and z because of the symmetry, and the remaining non trivial equation components are:

$$-\frac{dB_z}{dr} = \mu B_\theta, \qquad \frac{1}{r}\frac{d}{dr}(rB_\theta) = \mu B_z. \tag{2.5}$$

If one replaces the first Eq. in (2.5) in the second one, after some algebra steps, it is readily obtained:

$$r^2\frac{d^2B_z}{dr^2} + r\frac{dB_z}{dr} + \mu^2 r^2 B_z = 0, \tag{2.6}$$

which is a Bessel equation with variable μr and order $\alpha = 0$ and therefore it is solve by the Bessel function of the first kind J_0:

$$B_z = B_0 J_0(\mu r), \tag{2.7}$$

with B_0 magnetic field on axis. Since $J_1 = -\frac{1}{\mu}\frac{dJ_0}{dr}$, from (2.5) one can readily obtain:

$$B_\theta = B_0 J_1(\mu r). \tag{2.8}$$

Eq.s (2.5) are solved by the lowest order Bessel functions ($J_0(\mu r)$, $J_1(\mu r)$) that are combinations of sine and cosine with modulated amplitude (shown in Fig. 2.5).

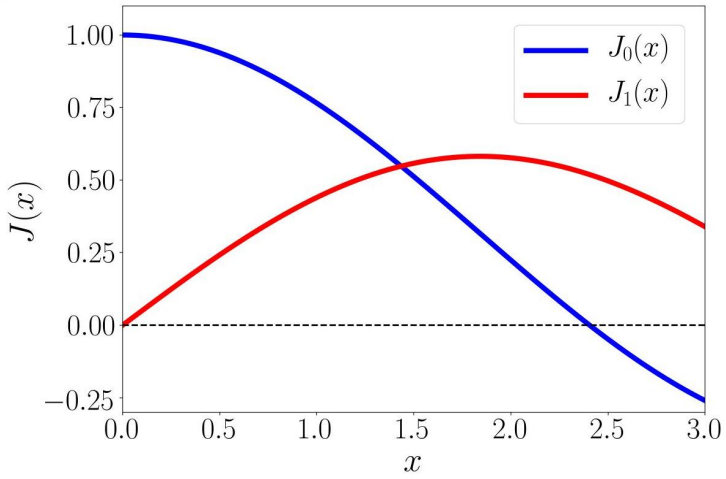

Figure 2.5: Lowest order Bessel function, corresponding to the equilibrium current and fields in the Bessel Function Model (BFM).

The resulting model is called Bessel Function Model (BFM) and it is still routinely used, in a slightly modified version, for calculating the equilibrium fields, in the RFX-mod device (see Ref. Ortolani [1983]).
Bessel functions are largely able to reproduce the behaviour of the magnetic field and, in particular, the reversal of the toroidal magnetic field in the external region. The first experimental measurements seemed to confirm the BFM predictions, especially those coming from the experiment ZETA, one of the first to work in the RFP configuration, Ref. Robinson and King. [1969]. An experimental comparison can be made with measurements of the magnetic field profile and introducing the parameter F, defined as:

$$F := \frac{B_\phi\,(r = a)}{\langle B_\phi \rangle}, \tag{2.9}$$

that represents the edge toroidal magnetic field normalized to its average. The condition that data should satisfy (in order to confirm Taylor's relaxation theory) is the following:

$$\frac{F}{\Theta} = \frac{B_\phi(a)}{B_\theta(a)} = \frac{J_0(\mu a)}{J_1(\mu a)}. \tag{2.10}$$

The plot of F as a function of Θ is shown in Fig. 2.6 with the comparison to the experimental data. It is worth noting that, in the BFM, reversal of the toroidal field happens when the pinch parameters $\Theta > 1.2$.

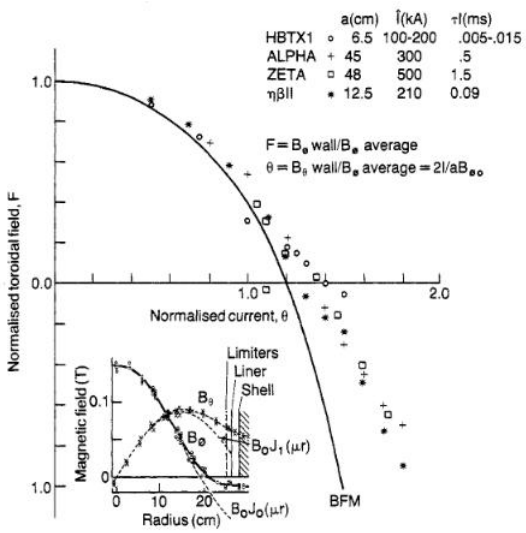

Figure 2.6: Comparison between Taylor's prediction and experimental data in the (Θ, F) plane. Figure adapted from Ref. Bodin [1988].

In this picture, although Taylor's theory predicts quite well the trend shown by the data, there is still something missing, since quantitative agreement is not perfect especially at large Θ values (bottom right corner of Fig. 2.6). Allowing for a variation of μ along the radius (the so called "μ & p" model, presented in Ref. Ortolani [1983]), helps in fitting data better, although for a more accurate description of the relaxation mechanism it is necessary to use a more modern MHD approach through numerical simulations.

2.4 Beyond Taylor's relaxation theory

The understanding of the RFP configuration has greatly improved since 1990s thanks to numerical simulations and to the growing experimental activity in this field.
In particular, thanks to the high computational power it is possible to predict many features of the reversed-field pinch by numerically simulating magnetohydrodynamics models (see Chp. 3, 4), accounting for specific hypothesis to study this phenomenon. A detailed summary regarding the evolution of RFP configuration during the years is found in Cappello et al. [2008], that is broadly followed in the contents of this Section, moving from Taylor's theory to the modern interpretation of RFP self-organization, based on MHD models.

2.4.1 The wire model

The wire model consists of a really simplified representation ('toy model') of the reversed-field pinch, explained in Ref. Escande et al. [2000]. The initial configuration considered (Fig. 2.7 (a)) has a cylindrical symmetry and is composed by an external ideal shell that guarantees, thanks to a uniform azimuthal current I_{shell}, the presence of an axial magnetic flux $\Phi(\mathbf{B})$ and by an axial wire, in which the current I is flowing. The ideal shell current I_{shell} is flowing keeping $\Phi(\mathbf{B})$ constant, so that this system results in a *magnetic flux conservator*.
Imaging for simplicity the development of a kink helical perturbation on the wire (Fig. 2.7 (b)): this perturbation can bring the wire current to flow parallel with respect to the shell one or anti-parallel with respect to it. Since parallel currents attract, this type of perturbation is enhanced, while the opposite one is reduced.
At this point, a perturbation of the 'parallel' type will be increased and will generate an additional magnetic field $\mathbf{B}'$ that is parallel to the original one. To compensate the increase of

magnetic field flux it is necessary to have a decrease or even a sign inversion of the magnetic field in the edge region not interested by the wire perturbation (Fig. 2.7 (c)), so that the global magnetic flux is conserved.

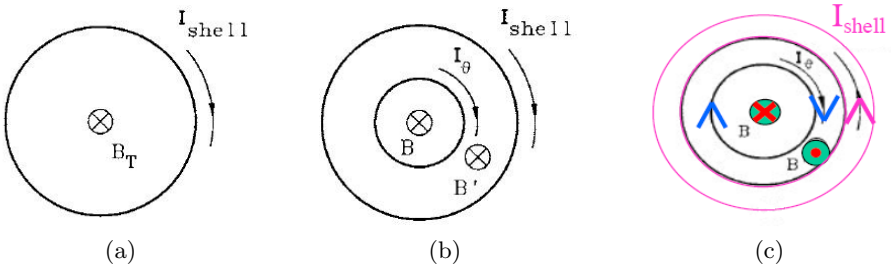

Figure 2.7: Graphic representation of the wire model: current carrying wire in a magnetic flux conservator (a), rise of a kink perturbation (b), development of the perturbation edge magnetic field sign reverse (c). Picture adapted from Ref. Escande et al. [2000].

2.4.2 Magnetohydrodynamics modelling of RFP

In order to provide quantitative predictions, the wire model needs to be upgraded in the context of magnetohydrodynamic model by means of numerical simulations of the differential equations involved. Limited to the reversed-field pinch configuration the visco-resistive model solution is of particular interest (see Chp. 4 for more details about this topic).
Solving 3D nonlinear MHD equations gives rise to qualitatively different solutions, on the basis of the composition of the spectrum of active plasma instabilities (more details about the Fourier spectrum will be given in Chp. 4, especially devoted to numerical solutions of the MHD model). In fact, there are cases in which there is no clear dominant mode in the Fourier spectrum. They are defined as turbulent or *multiple helicity* (MH) regime. In others, instead, the plasma can reach, after a phase transition, an entirely different state, characterized by the total dominance of one Fourier mode over all the others. This regime is defined as laminar or *single helicity* (SH). Also an intermediate situation exists featured by the presence of a dominant mode end other modes whose contribution is smaller but not negligible with respect to the dominant one: this regime is defined as *quasi single helicity* (QSH).
The different phases are not only predicted by solving the equations, but they are verified during the experiment in the geometry of the plasma *self-organization* (see Fig. 2.8) and in the magnetic topology (see Fig. 2.9).
An evident difference in the magnetic field configurations is present among the different regimes: in particular the transition towards the laminar regime is featured with a strong reduction of the magnetic chaos (see frames (c) and (d) in Fig. 2.8), that consists of the disappearance of the magnetic islands and of the formation of an ordered geometry that entails benefits (described in Sec. 2.6) also for transport, allowing the formation of a hot plasma helical core.

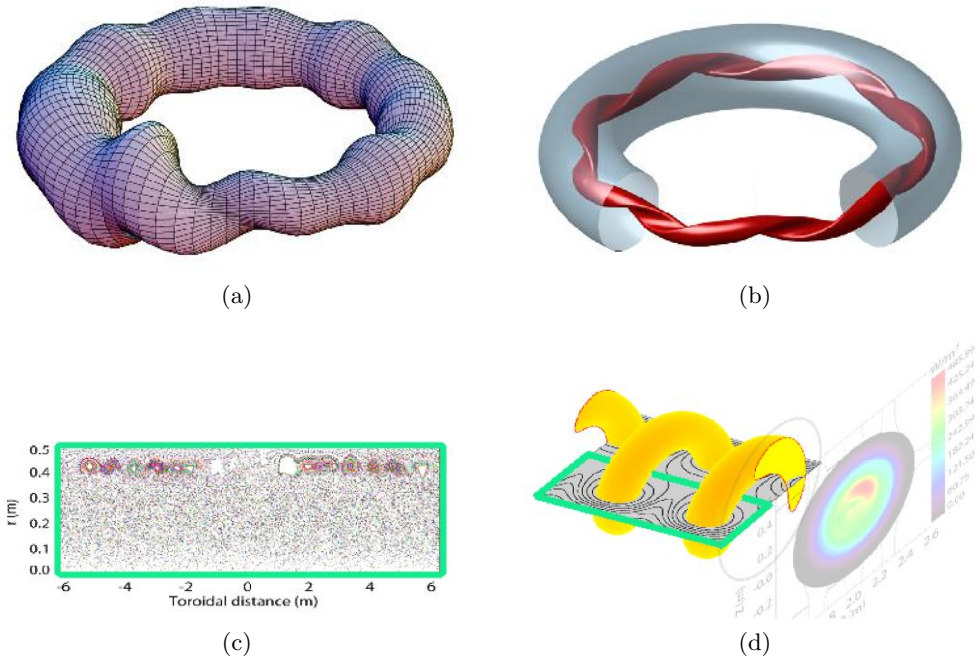

(a) (b)

(c) (d)

Figure 2.8: Bifurcation dominating RFP plasmas: (a) - (c) is the MH state, while (b) - (d) is the QSH helical state. (a) and (b) are reconstructions of the plasma shape, while (c) and (d) show the inner magnetic topology, adapted from Ref. Spizzo et al. [2012].

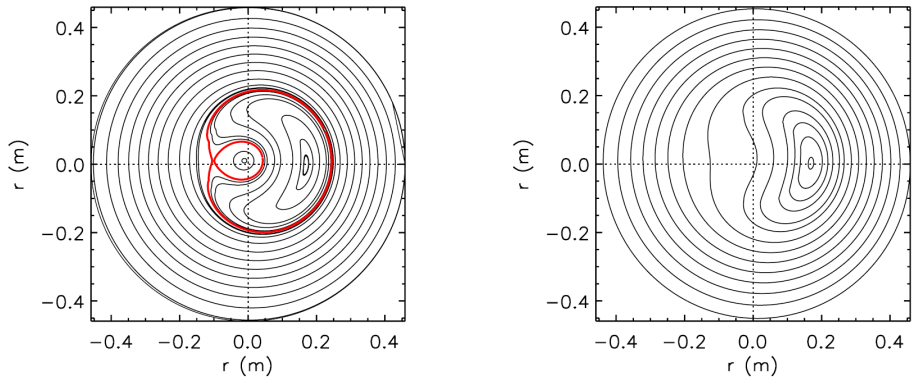

(a) (b)

Figure 2.9: Magnetic topology reconstructed comparison in RFX-mod: QSH (a) which displays a magnetic island and SH (b) regimes. Ref. Lorenzini et al. [2009a]

2.5 MHD instabilities of the RFP configuration

The high level plasma current characterizing the reversed-field pinch, induces a high poloidal magnetic field and the reversal of edge toroidal magnetic field. This results in a monotonically decreasing safety factor profile, represented for the case of a low aspect ratio RFP in Fig. 2.10.

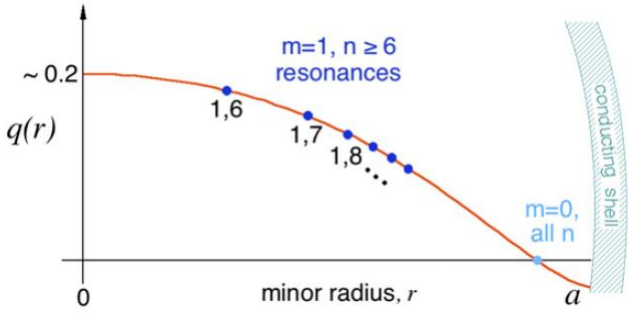

Figure 2.10: Low aspect ratio RFP safety factor profile $q(r)$. The main resonances of $m = 1$ and $m = 0$ modes are highlighted. Picture from Ref. Marrelli et al. [2021].

The precise value of the safety factor profile at the center $q(0)$ depends on the torus aspect ratio: for RFX-mod $q(0) \sim 0.15$. This makes the mode $m = 1$ $n = -7$ the first internal resonant kink, often resulting to be the dominant on this device. The wave numbers $m = 1$, $n \leqslant -8$ produce the secondary instabilities. As the poloidal wave number n is decreased, the instabilities become tearing modes and their resonant positions move towards the reversal.
The latter represents a peculiar propriety of the RFP and in this precise position all the $m = 0$ instabilities resonate. As it will be shown in Chp. 9, the development of the $m = 0$ instabilities plays a key role in the theories that study the reversed-field pinch density limit in a magneto-hydrodynamic framework. The $m = 1$ $n = -6$ is an externally resonant mode and its growth is linked to the finite resistivity of the conducting shell (resistive wall mode). As shown in Sec. 2.4, the instabilities briefly reviewed in this Section determine the helical shaping and magnetic topology of the plasma column. The latter having direct consequences on the temperature and confinement level achieved during the shot.

2.6 Helical self-organized states in RFP plasmas

The existence of helical self-organized states in RFP plasmas has been described for the first time during the '90s by means of numerical simulations, presented in Ref. Cappello and Paccagnella [1992] and Finn et al. [1992b]. In the last decade the numerical predictive capability has largely improved reaching a satisfying level of quantitative agreement, as explained in Chp. 4.
This section deals with the basic properties displayed by these states, from the experimental point of view. First of all, it is necessary to point out that in order to achieve the QSH, high plasma current operations are required ($I_p \sim 1.5 - 2\,\mathrm{MA}$), as the magnetic feedback control of magnetohydrodynamic instabilities. For this reason, the QSH has been studied on RFX-mod only in the late 2000's and presented in Ref. Lorenzini et al. [2009b] and Piovesan et al. [2009]. It is observed that increasing the plasma current, the ratio of the dominant mode over the secondary ones increases and the plasma spontaneously assess a self-organized helical state. In particular, if the edge normalized magnetic field instabilities are considered, the systematic repetition of $m = 1$ $n = -7$ mode dominance is observed, interspersed with periods during which the reconnection takes place, also known as *crashes*, dominated by magnetic turbulence, as shown in Fig. 2.11. Such succession of relatively long helically ordered phases and short chaos dominated periods is called *RFP sawtooth acitivity*.
The helical self organization level can be even increased in QSH states with a single helical axis

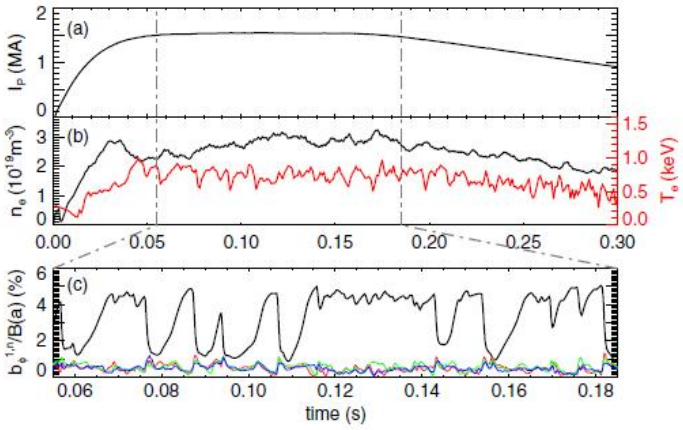

Figure 2.11: Waveform of # 24063 of RFX-mod, in quasi-single helicity phase. Plasma current, panel (a). Core density and electron temperature, panel (b). Edge normalized magnetic field perturbations: dominant ($m = 1$, $n = -7$) mode (black) and secondary ($m = 1$, $n = -8, -9, -10$) modes (coloured), panel (c). Picture from Ref. Piovesan et al. [2009].

(SHAx): in these states the magnetic axis coincides with the O-point of the magnetic island associated with the dominant mode.
During the helical self-organization of RFP fusion plasmas a remarkable improvement of the 'fusion performance' is observed. In particular, in SHax the ordered magnetic topology induces the formation of a high temperature helical core (Fig. 2.12 (a)), causing a doubling of the central electron temperature with respect to MH states (Fig. 2.12 (b)); in this case the helical symmetry of the topology is reflected by the difference on the temperature gradient profiles, depending on the radial side considered. In addition, SHax displays an increase of the confinement time up to a factor 4 with respect to turbulent MH states (Fig. 2.12 (c))

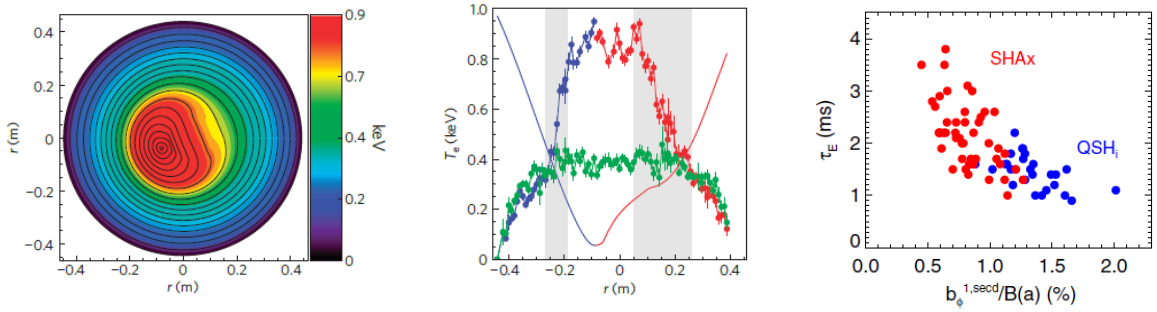

(a) (b) (c)

Figure 2.12: Fusion relevant properties of helical self-organized states measurements. Temperature field contour-plot, highlighting the rise of a hot helical core in SHax (a). Comparison of the temperature profiles in MH (green dots) and SHax on two different sides (red and blue dots) (b). Pictures from Ref. Lorenzini et al. [2009b]. Energy confinement time τ_E increases as the secondary $m = 1$ modes are decreased (i. e. increasing the helical order). Picture from Ref. Piovesan et al. [2009] (c).

The achievement of the QSH regime, keeps RFP configuration of interest for fusion purposes, at least for a future second generation fusion reactor. The main difficulty to this goal is the achievement and the maintenance of the quasi single helicity that MHD simulations show to be obtained in plasmas with an Hartmann number above a determined threshold or stimulating it with particular external perturbations called seed magnetic perturbations (these problems are

addressed in Chp. 4). Anyhow, the existence of a spontaneous QSH regime shows that RFP can be described as a self-organized helical state that displays magnetic order.

2.7 RFP application for future fusion reactors

Despite the progresses in RFP studies summarized in Sec. 2.6, a future purely fusion reactor remains a distant goal. However, there are interesting studies (see Ref. Piovan et al. [2020] and Bustreo et al. [2019]) that investigate the future applications of the RFP configuration to fusion-fission hybrid reactors. These type of reactors can provide several benefits, in addition to the electric power production, among which we should mention the treatment of radioactive waste and the production of radioisotopes of medical interest, both of which are obtained irradiating fissile fuel by neutrons produced in fusion reactions.
Three main parts constitute a fusion-fission hybrid reactor: the core neutron source, the breeding blanket and the irradiation region. The first part is devoted to the production of neutrons and it is supposed to be power by D-T reactions. The second part is devoted to the production of tritium (to get a self-powered reactor) and to the slow down of the neutrons. In fact high energy neutrons by fusion reactions ($\sim 14\,\mathrm{MeV}$), needs to be slow down at lower energy ($\sim 1\,\mathrm{MeV}$) to be of interest for fission applications. Finally, the irradiation zone constitutes the 'fission based part' of the reactor, where the treatment of nuclear waste or radioactive isotopes takes place, producing a net energy gain.
Reversed-field pinch configuration features fit quite well the requirements for a fusion based core neutron source in a hybrid reactor and it could perform better than tokamak and stellarators in playing this role. In fact, this type of source needs to be as simple as possible, to limit the required maintenance (requirement satisfied by the absence of superconductive coils and additional heating systems in the RFP), while the constraint on energy production nedd to be less strict than in a usual fusion reactor, since an energy gain $Q \sim 1$ is required.
We conclude just mentioning the main physical properties of a future hybrid reactor, based on the RFP configuration: $R_0 \sim 4-6\,\mathrm{m}$, $a \sim 1\,\mathrm{m}$, $I_p \sim 20\,\mathrm{MA}$, $T \sim 10\,\mathrm{keV}$, resulting in a final fusion $Q \sim 0.5-1$, which makes the project of a future hybrid reactor interesting and deserving of future studies.

2.8 Summary and final remarks

In this Chapter, we have described the main features of reversed-field pinch plasmas. Despite less performing than tokamak and stellarator, such configuration remains of interest for the fusion research community and several studies and efforts have been devoted to it, during the last decades.
The RFP is characterized by large values of the plasma current, which causes the edge toroidal magnetic field to reverse. This combination gives rise to a considerable amount of MHD instabilities, resulting in reduced energy confinement time. On the other side, exploiting high plasma current operations and MHD modes feedback control systems, fusion scientists have shown the possibility of achieving highly self-organized states, with helical shape. The latter displayed an increase of the core temperature and the confinement time.
The high plasma current values (and the consequent plasma self-organization) also contribute in achieving a relatively simple reactor design, with limited need for superconductive coils and additional heating systems.
The rise of helical states have been described in the last decades by increasingly refined numerical simulations of MHD models, which definitely contribute in the search and the optimization of this phenomenon. For this reason, the next two Chapters are devoted to introduce the magnetohydrodynamics models (Chp. 3) and the numerical codes (Chp. 4) of interest for this Thesis.

Chapter 3

Magnetohydrodynamics (MHD) models

This Chapter deals with the mathematical derivation of magnetohydrodynamics (MHD) models to describe magnetically confined fusion plasmas. The aim is to sketch out the first principle derivation of transport coefficients formulas as function of plasma parameters, necessarily introduced in order to close the system of equations which constitute any fluid model.
In Sec. 3.1, the plasma kinetic theory is introduced, which, as solid theory of statistical mechanics, represents the starting point of the mathematical derivation of fluid models.
In Sec. 3.2, the focus moves from the kinetic theory to the macroscopic level, by means of the calculations of the moments of the kinetic equation.
Sec. 3.3 is devoted to the derivation of the Braginskii equations for a magnetically confined plasma and to the problem of the equations incompleteness, solved following the procedure introduced by Chapmann-Enskog and Balescu, that results in the modelling of transport physics.
In Sec. 3.4, the transport coefficient formulas from classical transport theory are reported and discussed, concerning the transport of electric charge, momentum and heat, originated by (mainly binary) Coulomb collisions.
Sec. 3.5 deals with anomalous transport. In particular, alternative microscopic mechanism able to origin transport (like magnetic field stochasticity) are analyzed.
Sec. 3.6 is devoted to introduce the assumptions and the equations that constitute the single fluid MHD model.
In Sec. 3.7, some further assumptions are made to develop the visco-resistive MHD model. This is a key model for this work, since an important part of the Thesis is devoted to the visco-resistive MHD modelling of RFP plasmas. In this context, also the main fluid dimensionless numbers (Lundquist, viscous Lundquist, magnetic Prandtl and Hartmann) are introduced.
Summary and final remarks follow in Sec. 3.8.

3.1 Plasma kinetic theory

To achieve the comprehension of a complex system by means of a physical model it is necessary to choose the right 'level of description' of the physical system, considering: the specific phenomenon of interest, the physical quantities that can be measured experimentally and that should be predicted by the model and, finally, the possibility of formulating useful forecasts by means of analytical calculations or, more likely, numerical simulations requiring an acceptable computing power.
To describe complex systems like fluids and plasmas four different levels of the description can be adopted (see Ref. Choudhuri [1998]):

- the microscopic quantum approach (solving the many body system Schrödinger equation)
- the microscopic classical approach (solving the Newton/Hamilton equation for the set classical particles composing the system)
- the kinetic approach (solving the Boltzmann/Vlasov equations)
- the macroscopic (magneto)fluid approach (solving the (magneto)hydrodynamics equations).

Since fusion plasmas are physical systems composed by a huge number of particles ($N \approx N_{av}$), we will work on the derivation of the macroscopic magneto-fluid model, on the basis of the kinetic plasma theory, without developing the microscopic approaches (at quantum or classical level), according to which it is particularly difficult to draw interesting conclusions for our purposes. This derivation is described in many advanced textbooks on magnetohydrodynamics, like Ref. Goedbloed et al. [2019] and Fitzpatrick [2014]. For convenience reasons, the notation of the latter is followed.
The physical macroscopic system under analysis is supposed to be such that it can contain a sufficiently high number of small volumes (to allow a macroscopic treatment based on differential equations) and that each small volume contains an enormous number of particles: this hypothesis is satisfied by all the systems that can be studied at a thermodynamic level.
Let $\rho_s\left(\mathbf{x}_1, \mathbf{u}_1, \ldots, \mathbf{x}_N, \mathbf{u}_N, t\right)$ be the microscopic phase space density of N classical particles of the species s with positions $\mathbf{x}_1$, ..., $\mathbf{x}_N$ and velocities $\mathbf{u}_1$, ..., $\mathbf{u}_N$ in the Γ phase space. Than, using Liouville theorem:

$$\frac{d\rho_s}{dt}\left(\mathbf{x}_1, \mathbf{u}_1, \ldots, \mathbf{x}_N, \mathbf{u}_N, t\right) = 0, \tag{3.1}$$

where d/dt denotes the total lagrangian derivative. Liouville theorem expresses the phase space conservation in Γ space. Equation (3.1) is easily rewritten as:

$$\frac{\partial \rho_s}{\partial t} + \sum_{i=1}^{N} \mathbf{u}_i \cdot \nabla_{\mathbf{x}_i} \rho_s + \sum_{i=1}^{N} \frac{\mathbf{F}_{i,s}}{m_s} \cdot \nabla_{\mathbf{u}_i} \rho_s = 0, \tag{3.2}$$

in which the symbols $\nabla_{\mathbf{x}_i}$ and $\nabla_{\mathbf{u}_i}$ denote the gradients calculated with respect to the spatial coordinates and to the velocities of the i-th particle and the variables m_s and $\mathbf{F}_{i,s}$ are respectively the mass and the force exerted on the i-th particle of the s species. Equation (3.2) is easily derived but needs a very difficult solution. In fact the ensemble density ρ_s contains in its argument a dependence on the trajectories of all the particles considered, whose determination is equivalent to the solution of the many-body problem.
In order to simplify this problem, the ensemble average of ρ_s can be calculated, giving rise to the single particle distribution function f_s:

$$f_s\left(\mathbf{r}, \mathbf{u}, t\right) := \left\langle \rho_s\left(\mathbf{x}_1, \mathbf{u}_1, \ldots, \mathbf{x}_N, \mathbf{u}_N, t\right)\right\rangle_{ens}, \tag{3.3}$$

that has the physical meaning of number of particles with position between $\mathbf{r}$ and $\mathbf{r}+d\mathbf{r}$, velocity between $\mathbf{u}$ and $\mathbf{u}+d\mathbf{u}$ at the time t, per unit of phase space volume. To find an equation that rules the evolution of f_s, equation (3.2) can be averaged: the only non trivial term is the third contribution because the expression of $\mathbf{F}_{i,s}$ is given by the Lorentz force (in the case of plasmas) where a velocity dependence is contained, so that a correlation between the two factors is generated and the product average can not be trivially factorized. In other words, a correlation term $C_s(f)$ has to be introduced:

$$\left\langle \sum_{i=1}^{N} \frac{\mathbf{F}_{i,s}}{m_s} \cdot \nabla_{\mathbf{u}_i} \rho_s \right\rangle_{ens} = \frac{\mathbf{F}_s}{m_s} \cdot \nabla_{\mathbf{u}} f_s - C_s(f), \tag{3.4}$$

where $\mathbf{F}_s$ represents an averaged force due to smooth electromagnetic fields generated by all the particles contribution. The final kinetic (Boltzmann) equation obtained is:

$$\frac{\partial f_s}{\partial t} + \mathbf{u} \cdot \nabla f_s + \frac{\mathbf{F}_s}{m_s} \cdot \nabla_{\mathbf{u}} f_s = C_s\left(f\right). \tag{3.5}$$

$C_s(f)$ is usually called collision operator because collisions are the main physical mechanism that generates non zero correlation terms and it is a very difficult term to be evaluated: this is the reason why, such term is neglected (Vlasov limit), whenever it is possible. However, in literature, expressions for $C_s(f)$ exist: in the case of neutral gases the operator was calculated by Boltzmann (with the hypotheses of binary collisions) and it can be found, for example in Ref. Huang [2008], while for the case of plasmas an expression was found by Landau under strict hypotheses, including the existence of only two species (ions and electrons), conservation of particle number for each species (absence of fusion, recombination, charge exchange, ...) and the dependence only on the one particle distribution function (absence of higher order correlation), see the original paper in Ref. Landau [1937]. For the aim of this work it is sufficient to know that the collisional processes conserve number of particles, momentum and energy at each point, without entering in the details of collisions modelling.
The kinetic approach has two important drawbacks: from one side the distribution function f_s has a seven dimensional dependence that makes computer simulations more difficult to implement, on the other side it is not easily measurable experimentally. In the past, these disadvantages have brought scientists to develop the macroscopic fluid approach. However, in the present days, thanks to advancements in computational power, the kinetic approach is widely used to simulate plasma turbulence and transport in the so-called gyrokinetic codes (see Ref. Catto [2019] for more details): these codes typically analyze small-scale structures on fast timescales, and the magnetic field is generally not evolved self-consistently in the code. Modern supercomputers allow for obtaining more and more efficient gyrokinetic simulations and presently much effort is devoted in this field of research.

3.2 Moments of the kinetic equation

An approach complementary to the one used in gyrokinetic codes is to take the moments of the distribution function: this approach gives rise to the second, large family of codes used in plasma physics, namely the Magnetohydrodynamic (MHD) codes. The k-th moment of the ensemble averaged distribution function $f_s\left(\mathbf{r},\mathbf{u},t\right)$ is defined as follows:

$$\mathbf{M}_k\left(\mathbf{r},t\right) := \int \mathbf{u} \cdot ... \cdot \mathbf{u} f_s\left(\mathbf{r},\mathbf{u},t\right) d^3\mathbf{u}, \tag{3.6}$$

repeating the $\mathbf{u}$ factors k times. Moments connect the distribution function to easily measurable physical quantities. In particular, number density $n_s(\mathbf{r},t)$, flux density $n_s\mathbf{v}_s$, stress tensor $\mathbf{P}_s$ and energy flux density $\mathbf{Q}_s$ can be defined using the moments of the first orders:

$$n_s(\mathbf{r},t) := \int f_s(\mathbf{r},\mathbf{u},t)\, d^3\mathbf{u}, \tag{3.7}$$

$$n_s\mathbf{v}_s(\mathbf{r},t) := \int \mathbf{u} f_s(\mathbf{r},\mathbf{u},t)\, d^3\mathbf{u}, \tag{3.8}$$

$$\mathbf{P}_s(\mathbf{r},t) := \int m_s\mathbf{u}\mathbf{u} f_s(\mathbf{r},\mathbf{u},t)\, d^3\mathbf{u}, \tag{3.9}$$

$$\mathbf{Q}_s(\mathbf{r},t) := \int \frac{1}{2} m_s u^2 \mathbf{u} f_s(\mathbf{r},\mathbf{u},t)\, d^3\mathbf{u}. \tag{3.10}$$

In the definition (3.8), a new quantity called flow velocity $\mathbf{v}_s$ is introduced. Defining also the relative velocity $\mathbf{w}_s := \mathbf{u} - \mathbf{v}_s$, pressure tensor $\mathbf{p}_s$ and heat flux density $\mathbf{q}_s$ are consequently introduced:

$$\mathbf{p}_s(\mathbf{r},t) := \int m_s\mathbf{w}\mathbf{w} f_s(\mathbf{r},\mathbf{u},t)\, d^3\mathbf{u} \tag{3.11}$$

$$\mathbf{q}_s(\mathbf{r},t) := \int \frac{1}{2} m_s w^2 \mathbf{w} f_s(\mathbf{r},\mathbf{u},t)\, d^3\mathbf{u} \tag{3.12}$$

A scalar quantity (scalar pressure p_s) can be associated to the tensor in Eq. (3.11) as $p_s := \frac{1}{3}Tr(\mathbf{p}_s)$ and, finally, it is natural to define as kinetic temperature of equilibrium the variable $T_s := \frac{p_s}{n_s}$. To compute the moments of the kinetic equation, also the moments of the collision operator have to be found.
To find the moments of the collision operator it is necessary to hypothesize its bilinearity with respect to the single particle distribution function:

$$C_s(f) = \sum_{s'} C_{ss'}(f_s, f_{s'}), \tag{3.13}$$

with $C_{ss'}(f_s, f_{s'})$ bilinear in both its arguments. In this way, it is possible to introduce the friction force exerted on the species s by the species s' ($\mathbf{F}_{ss'}$), the total force experienced by the species s ($\mathbf{F}_s$) and, similarly, the difference in kinetic energy of the species s due to s' ($W_{ss'}$) and the total change in energy of the species s (W_s).
The final steps to get fluid macroscopic equations of the considered system consist of the calculation of the first three orders moments of the Eq. (3.5), applying the procedure indicated in the definition (3.6). Avoiding repeating all the algebraic steps, only the main ideas to get the final result are exposed. First of all, flow in the velocity space of the Lorentz force $\mathbf{F}$ is incompressible:

$$\nabla_{\mathbf{u}} \cdot \mathbf{F} = q\nabla_{\mathbf{u}} \cdot (\mathbf{E} + \mathbf{u} \times \mathbf{B}) = q\left[(\nabla_{\mathbf{u}} \times \mathbf{u}) \cdot \mathbf{B} - \mathbf{u} \cdot (\nabla_{\mathbf{u}} \times \mathbf{B})\right] = 0, \tag{3.14}$$

so that the Eq. (3.5) can be rearranged and the moments calculus ($k = 0, 1, 2$) can be set up:

$$\int \frac{m_s}{k!}\mathbf{u} \cdot ... \cdot \mathbf{u} \left(\frac{\partial f_s}{\partial t} + \nabla \cdot (\mathbf{u} f_s) + \nabla_{\mathbf{u}} \cdot \left(\frac{\mathbf{F}_s}{m_s} f_s \right) \right) d^3\mathbf{u} = \int \frac{m_s}{k!}\mathbf{u} \cdot ... \cdot \mathbf{u} C_s(f)\, d^3\mathbf{u}. \tag{3.15}$$

Performing the integration, using the Gauss theorem (with the hypothesis that fields vanish as $r \to \infty$) and making use of the definition introduced in this section one finds the continuity equation ($k = 0$):

$$\frac{\partial n_s}{\partial t} + \nabla \cdot (n_s \mathbf{v}_s) = 0, \tag{3.16}$$

the momentum conservation equation ($k = 1$):

$$\frac{\partial\left(m_s n_s \mathbf{v}_s\right)}{\partial t} + \nabla \cdot \mathbf{P}_s - e_s n_s \left(\mathbf{E} + \mathbf{v}_s \times \mathbf{B}\right) = \mathbf{F}_s, \tag{3.17}$$

and, finally, the energy conservation equation ($k = 2$):

$$\frac{\partial}{\partial t}\left(\frac{3}{2} p_s + \frac{1}{2} m_s n_s v_s^2\right) + \nabla \cdot \mathbf{Q}_s - e_s n_s \mathbf{E} \cdot \mathbf{v}_s = W_s + \mathbf{v}_s \cdot \mathbf{F}_s. \tag{3.18}$$

The main concept expressed by these equations is the conservation of a physical quantity (at a macroscopic) level as consequence of the conservation at the microscopic interaction level: in particular, it is evident that the time variation of one of these conserved quantities inside a volume has to be balanced by its flow through the volume surface or by the interaction with other species (terms containing $\mathbf{F}_s, W_s$) and with the electromagnetic field (terms containing $\mathbf{E}$ and $\mathbf{B}$).

3.3 The problem of Braginskii equations incompleteness

Eq. (3.16), (3.17) and (3.18) can be rewritten in a more manageable form, performing some tensor algebra, introducing the convective derivative d/dt and the tensor operator $: \nabla$ that are defined in the following way:

$$\frac{d}{dt} := \frac{\partial}{\partial t} + \mathbf{v}_s \cdot \nabla, \qquad \mathbf{S} : \nabla \mathbf{T} = (S)_{ij} \frac{\partial T_j}{\partial x_i}, \tag{3.19}$$

where $\mathbf{S}$, $\mathbf{T}$ are rank two tensors and Einstein convention is used. The equations thus turn out to be rewritten in the following form, assuming the name of *Braginskii equations*:

$$\frac{dn}{dt} + n \nabla \cdot \mathbf{v}_e = 0, \tag{3.20}$$

$$m_e n \frac{d\mathbf{v}_e}{dt} + \nabla p_e + \nabla \cdot \mathbf{\Pi}_e + en \left(\mathbf{E} + \mathbf{v}_e \times \mathbf{B}\right) = \mathbf{F}, \tag{3.21}$$

$$\frac{3}{2}\frac{dp_e}{dt} + \frac{5}{2} p_e \nabla \cdot \mathbf{v}_e + \mathbf{\Pi}_e : \nabla \mathbf{v}_e + \nabla \cdot \mathbf{q}_e = W_e, \tag{3.22}$$

for the electrons and similarly for the ions:

$$\frac{dn}{dt} + n \nabla \cdot \mathbf{v}_i = 0, \tag{3.23}$$

$$m_i n \frac{d\mathbf{v}_i}{dt} + \nabla p_i + \nabla \cdot \mathbf{\Pi}_i - en \left(\mathbf{E} + \mathbf{v}_i \times \mathbf{B}\right) = -\mathbf{F}, \tag{3.24}$$

$$\frac{3}{2}\frac{dp_i}{dt} + \frac{5}{2} p_i \nabla \cdot \mathbf{v}_i + \mathbf{\Pi}_i : \nabla \mathbf{v}_i + \nabla \cdot \mathbf{q}_i = W_i, \tag{3.25}$$

in both cases the pressure tensor is written as a sum of a diagonal part that models the effect of the isotropic pressure, and an off-diagonal part related to viscous stresses:

$$\mathbf{p}_s = p_s \mathbb{1}_3 + \mathbf{\Pi}_s. \tag{3.26}$$

Moreover, the quasi-neutrality of the plasma is assumed: $n_e \approx Z n_i \approx n$. In other words, on the macroscopic scale considered to describe the plasma bulk, the charge unbalance and the consequent formation of electric fields is neglected. In fact, if an imbalance of charges develops, the corresponding electric field would move the plasma charges (which are free to move in the plasma) in order to eliminate the imbalance itself, on a very short time scale. Eq. (3.20)-(3.25) were introduced for the first time by Braginskii in Ref. Braginskii [1965].

Braginskii equations present a fundamental defect (also common to the case of neutral fluids): the incompleteness. The number of unknowns largely exceeds the number of available equations, because moving from the kinetic approach to the magneto-fluid approach only three moments of the kinetic equations are calculated: closure could be restored calculating all of the moments in the kinetic equation. Such an approach is clearly impractical because the higher order moments have not an evident physical meaning and the solution of all the equations involved is equivalent to the many body problem solution.
In order to solve this problem, a mathematically formal *closure procedure* is needed. This topic is developed in depth in two monographs by Chapmann-Enskog (for neutral fluids, Ref. Chapman et al. [1990]) and Balescu (for fully ionized plasmas in booth cylindrical, Ref. Balescu [1988a] vol. 1 and toroidal geometry, Ref. Balescu [1988b] vol. 2). The closure is based on an expansion of the single particle distribution function $f(\mathbf{r}, \mathbf{u}, t)$ as sum of an equilibrium term (typically Maxwell-Boltzmann distribution) $f_0(\mathbf{r}, \mathbf{u})$ and a small perturbation one:

$$f(\mathbf{r}, \mathbf{u}, t) \approx f_0(\mathbf{r}, \mathbf{u}) + \epsilon f_1(\mathbf{r}, \mathbf{u}, t), \tag{3.27}$$

$$f_0(\mathbf{r}, \mathbf{u}) = n(\mathbf{r}) \left(\frac{m}{2\pi T(\mathbf{r})} \right)^{3/2} \exp \frac{m(\mathbf{u} - \mathbf{v})^2}{2T(\mathbf{r})}, \tag{3.28}$$

with f_0 and f_1 of the same order and ϵ is a small parameter expansion. The f_1 perturbation term allows the modelling of transport, that otherwise would be set to zero in the case of equilibrium distribution functions. The choice of the ϵ parameter strongly depends on the fluid considered: in the case of magnetically confined fusion plasma ϵ can be chosen as the ratio between Larmor radius r_L and the macroscopic scale length of the device L, because in this case the following condition is satisfied:

$$\epsilon = \frac{r_L}{L} << 1. \tag{3.29}$$

In particular, in this limit confinement phenomena are dominating over collisional phenomena, being the Larmor gyro-radius smaller than the mean free path, or, equivalently defining the collisional time for ions and electrons τ_i, τ_e:

$$\omega_i \tau_i, \quad \omega_e \tau_e << 1. \tag{3.30}$$

Assuming the hypotheses of bi-linearity (in Eq. (3.13)) of the collision operator, the closure procedure can be performed expanding f_1 with a polynomial expansion in the velocity space by means of Laguerre polynomials (as Chapmann-Enskog did) or Hermite polynomials (as Balescu did). It was shown by Balescu that the relative difference between its method and the Chapmann-Enskog one is below 1%. Such expansions are fairly prohibitive from the point of view of the calculations because they involve terms that are tensors of increasing dimension by the term considered. For this reason, in this work the mathematical steps are not repeated but only the procedure and the final results. Truncating the f_1 expansion at the second order, replacing it in the moments of the kinetic equation and solving the simplified form for the moments, one can get the laws that rule transport with its relative coefficients. The transport laws resulting from the closure procedure are summarized in Sec. 3.4.

3.4 Transport coefficients in classical theory

In this Section, the fundamental laws of transport are written for a magnetized plasma, outlining the dependence of transport coefficients on plasma measurable parameters and focusing on the physical meaning of the dependence. Three cases are considered, corresponding to the determination of *electrical conductivity/resistivity* (quantifying electric charge transport), *heat*

conductivity (quantifying heat transport), *viscosity* (quantifying momentum transport).
In classical theory, the relaxation mechanism of the distribution function towards the Maxwell equilibrium f_0 is guaranteed by Coulomb collisions. As consequence of it, the first step consists of finding an expression for the collisional time for electron-ion collisions τ_{ei} and ion-ion collisions τ_{ii}. In an ionized plasma, a long range (Coulomb) interaction is present, so the definition of a collision event is not trivial at all, contrary to what happens in the case of fluids. According to the preferred definition, a collision is a particles encounter that produces a considerable trajectory deflection of at least one of the particles: this implies the momentum exchanged during the collision to be of the same order of the initial momentum of the particles. Thanks to this consideration it is possible to obtain the most important physical dependencies of the collisional time.
In fact, considering a particle with charge e, mass m and thermal velocity v, the distance of closest approach r_0 is easily found, evaluating the momentum exchanged Δp:

$$\Delta p \approx F\Delta t \approx \frac{e^2}{4\pi\epsilon_0 r_0^2}\frac{r_0}{v}, \qquad \Delta p \approx mv \qquad \rightarrow \qquad r_0 \approx \frac{e^2}{4\pi\epsilon_0 m v^2}. \tag{3.31}$$

The number of collisions per unit of time (collisional frequency ν_c) is given counting the number of encounters for a particle traversing a collisional cylinder with radius r_0:

$$\nu_c \approx n\pi r_0^2 v \approx \frac{ne^4}{16\pi\epsilon_0^2 m^2 v^3} \propto \frac{ne^4}{m^{1/2}T^{3/2}}. \tag{3.32}$$

This simple reasoning for evaluating the trend of the collisional time, whose exact formulas can be found carrying out all of the specific calculations:

$$\tau_{ei} = \frac{6\sqrt{2}\pi^{3/2}\epsilon_0^2 m_e^{1/2}T_e^{3/2}}{n_i Z^2 e^4 \ln\Lambda}, \qquad \tau_{ii} = \frac{6\sqrt{2}\pi^{3/2}\epsilon_0^2 m_i^{1/2}T_i^{3/2}}{n_i Z^4 e^4 \ln\Lambda}, \tag{3.33}$$

where $\ln\Lambda$ represents the Coulomb logarithm, defined as $\ln\Lambda := \ln(r_{max}/r_{min})$, being r_{max} and r_{min} the Debye length and the distance of closest approach during particle collisions at the average velocity, see Ref. Richardson [2019].

3.4.1 Electric charge transport

The strong anisotropy introduced by the magnetic field makes sure that transport physics strictly depends on its direction with respect to the latter. From the closure procedures, we can derive the electrical conductivity σ (the reciprocal of the resistivity η). This coefficient assumes different values depending on the direction of electric current with respect to the magnetic field:

$$\sigma_\parallel = 1.96\frac{ne^2\tau_{ie}}{m_e}, \qquad \sigma_\perp = 0.51\sigma_\parallel = \frac{ne^2\tau_{ie}}{m_e}. \tag{3.34}$$

The dependence in equation (3.34) is explained by the following consideration: since $\mathbf{F}$ is a friction force per unit of volume, it will be increased by the momentum lost by the electrons (the species that originate the current) in favour of ions:

$$\mathbf{F} \propto \frac{nm_e(\mathbf{v}_e - \mathbf{v}_i)}{\tau_{ie}} = \frac{n^2e^2(\mathbf{v}_e - \mathbf{v}_i)}{ne^2\tau_{ie}/m_e} \propto \frac{ne\mathbf{j}}{\sigma}, \tag{3.35}$$

that justifies the dependencies in (3.34). Using Eq. (3.34), parallel and perpendicular resistivity is determined:

$$\eta_\parallel = 0.51\frac{m_e}{n_e e^2\tau_{ei}} = \frac{0.06}{\pi^{3/2}}\frac{m_e^{1/2}e^2}{\epsilon_0^2}\frac{Z\ln\Lambda}{T_e^{3/2}}, \qquad \eta_\perp = \frac{m_e}{n_e e^2\tau_{ei}} = \frac{0.118}{\pi^{3/2}}\frac{m_e^{1/2}e^2}{\epsilon_0^2}\frac{Z\ln\Lambda}{T_e^{3/2}}. \tag{3.36}$$

It is worth noting the dependence of the resistivity on the electron temperature $\eta \propto T_e^{-3/2}$, which takes the name of Spitzer resistivity, see Ref. Spitzer [1956].

3.4.2 Heat transport

In the context of heat transport, the closure procedure shows the following formulas in which the heat flux $\mathbf{q}$ is evaluated for both the species considered:

$$\mathbf{q}_e = -k_{\parallel}^e \nabla_{\parallel} T_e - k_{\perp}^e \nabla_{\perp} T_e - k_{\times}^e \mathbf{b} \times \nabla_{\perp} T_e - 0.71 \frac{T_e \mathbf{j}_{\parallel}}{e} - \frac{3T_e}{2\left|\omega_e\right| \tau_{ie} e} \mathbf{b} \times \mathbf{j}_{\perp}, \tag{3.37}$$

$$\mathbf{q}_i = -k_{\parallel}^i \nabla_{\parallel} T_i - k_{\perp}^i \nabla_{\perp} T_i + k_{\times}^i \mathbf{b} \times \nabla_{\perp} T_i, \tag{3.38}$$

where $\mathbf{b}$ denotes the unitary vector parallel to the magnetic field and the the sub-indices $\parallel$ and $\perp$ refer to the magnetic field direction: $\nabla_{\parallel} = \mathbf{b}\,(\mathbf{b} \cdot \nabla)$, $\nabla_{\perp} = \nabla - \nabla_{\parallel}$. As in the previous case, we can provide the 'physical insights' of Eq. (3.37) and (3.38). The first two terms in both the equations are quite easy: in fact, they simply quantify the usual heat diffusion due to microscopic collisions in presence of a gradient in temperature and, as expected, this phenomenon is influenced by the anisotropy introduced by the magnetic field. The proportionality coefficient is defined as thermal conductivity and it depends on the species and on the direction considered:

$$k_{\parallel}^e = 3.2 \frac{n \tau_{ei} T_e}{m_e}, \qquad k_{\parallel}^i = 3.9 \frac{n \tau_{ii} T_i}{m_i}, \qquad k_{\perp}^e = 4.7 \frac{n T_e}{m_e \omega_e^2 \tau_{ei}}, \qquad k_{\perp}^i = 2 \frac{n T_i}{m_i \omega_i^2 \tau_{ii}}. \tag{3.39}$$

They are calculated, assuming that the typical length and time scales on which collisions happen at microscopic level are the mean free path l and the collisional time τ in the case of parallel transport:

$$\mathbf{q} \propto \frac{n l^2 \nabla T}{\tau} = \frac{n T \tau}{m} \nabla T, \tag{3.40}$$

while in the case of perpendicular transport, the mean free path is replaced by the Larmor radius r_L:

$$\mathbf{q} \propto \frac{n r_L^2 \nabla T}{\tau} = \frac{n v^2 \nabla T}{\omega^2 \tau} = \frac{n T}{m \omega^2 \tau} \nabla T, \tag{3.41}$$

The third term on the right hand side of Eq. (3.37), (3.38) is a combined effect of the magnetic field and of a temperature gradient with a non zero component perpendicular to the field. Analyzing the case of the electrons the unidirectional heat flux (nTv) will have an unbalanced component in the direction $-\mathbf{b} \times \nabla_{\perp} T_e$ (for the ions the term holds the opposite sign): the reason is similar to the one that brings to the rise of gyro-viscosity (see Sec. 3.4.3) and also the physical configuration is analogous (Fig. 3.1). In fact:

$$\mathbf{q} \propto n T v \left(\frac{r_L}{T}\right) \mathbf{b} \times \nabla_{\perp} T = n v r_L \mathbf{b} \times \nabla_{\perp} T \propto \frac{n T}{m \left|\omega\right|} \nabla_{\perp} T, \tag{3.42}$$

that allows the introduction of the cross thermal conductivity for electrons and ions, that, using the right calculation of the closure procedure results:

$$k_{\times}^e = \frac{5 n T_e}{2 m_e \left|\omega_e\right|}, \qquad k_{\times}^i = \frac{5 n T_i}{2 m_i \omega_i}. \tag{3.43}$$

The last two terms of Eq. (3.37) affect only the transport of the electrons, because they are the only ones governing the current: they consist of heat fluxes that are strictly connected with the friction force contributions.

The combination of Eq. (3.39), (3.43) and Eq. (3.33) allows to determine parallel, perpendicular and cross thermal conductivity both for the species of ions and electrons:

$$k_{\parallel}^{e} = 3.2\frac{n\tau_{ei}T_e}{m_e} = 27.2\pi^{3/2}\frac{\epsilon_0^2}{m_e^{1/2}e^4}\frac{T_e^{5/2}}{Z\ln\Lambda}, \tag{3.44}$$

$$k_{\parallel}^{i} = 3.9\frac{n\tau_{ii}T_i}{m_i} = 46.8\pi^{3/2}\frac{\epsilon_0^2}{m_p^{1/2}e^4}\frac{T_i^{5/2}}{Z^4\gamma^{1/2}\ln\Lambda}, \tag{3.45}$$

$$k_{\perp}^{e} = 4.7\frac{nT_e}{m_e\omega_e^2\tau_e} = \frac{0.544}{\pi^{3/2}}\frac{m_e^{1/2}e^2}{\epsilon_0^2}\frac{Z^3n_i^2\ln\Lambda}{T_e^{1/2}B^2}, \tag{3.46}$$

$$k_{\perp}^{i} = 2\frac{nT_i}{m_i\omega_i^2\tau_i} = \frac{0.167}{\pi^{3/2}}\frac{m_p^{1/2}e^2}{\epsilon_0^2}\frac{\gamma^{1/2}Z^2n_i^2\ln\Lambda}{T_i^{1/2}B^2}, \tag{3.47}$$

$$k_{\times}^{e} = \frac{5nT_e}{2m_e\left|\omega_e\right|} = 2.5\frac{1}{e}\frac{n_eT_e}{B}, \qquad k_{\times}^{i} = \frac{5nT_i}{2m_i\omega_i} = 2.5\frac{1}{e}\frac{n_iT_i}{ZB}. \tag{3.48}$$

To conclude, we mention that the heat conductivity is usually normalized to the particle density n, giving rise to the *heat diffusivity*, denoted in this Thesis with χ. The latter represents the heat diffusion coefficient (with unit of measure $\left[\mathrm{m}^2/\mathrm{s}\right]$)

3.4.3 Momentum transport

The case of momentum transport with its relative coefficients (viscosity) is more complex than the previous cases, since the quantity transported is now a vector (no longer a scalar as in the cases of electric charge and heat). In the simpler case of neutral fluids or, in general, in the case of short range interactions with a faster decrease than the electromagnetic one, the phenomenon can be described using a rate of strain tensor W that is symmetric and traceless:

$$W_{i,j} = \frac{\partial v_i}{\partial r_j} + \frac{\partial v_j}{\partial r_i} - \frac{2}{3}\nabla\cdot\mathbf{v}\delta_{i,j}. \tag{3.49}$$

Instead, in a magnetized plasma where the main force on action is the Coulomb interaction, the best description is given by a tensor that can be split into five different components:

$$\mathbf{\Pi} = \sum_{n=0}^{4}\mathbf{\Pi}_n. \tag{3.50}$$

The first one is related to parallel transport of momentum components parallel to the magnetic field lines:

$$\mathbf{\Pi}_0 = -3\mu_0\left(\mathbf{bb} - \frac{1}{3}\mathbb{1}\right)\left(\mathbf{bb} - \frac{1}{3}\mathbb{1}\right) : \nabla\mathbf{v}, \tag{3.51}$$

where the coefficient μ_0 is found to be:

$$\mu_0^e = 0.73n\tau_{ei}T_e, \qquad \mu_0^i = 0.96n\tau_{ii}T_i. \tag{3.52}$$

In the perpendicular direction the transport of perpendicular momentum components is ruled by the sum of two tensors:

$$\mathbf{\Pi}_1 = -\mu_1\left[\mathbb{1}_\perp\cdot\mathbf{W}\cdot\mathbb{1}_\perp + \frac{1}{2}\mathbb{1}_\perp\left(\mathbf{b}\cdot\mathbf{W}\cdot\mathbf{b}\right)\right], \tag{3.53}$$

$$\mathbf{\Pi}_2 = -4\mu_1\left[\mathbb{1}_\perp\cdot\mathbf{W}\cdot\mathbf{bb} + \mathbf{bb}\cdot\mathbf{W}\cdot\mathbb{1}_\perp\right], \tag{3.54}$$

where $\mathbb{1}_\perp$ is defined as $\mathbb{1}_\perp := \mathbb{1} - \mathbf{bb}$ and the perpendicular viscosity results to be reduced of a factor $(r_L/l)^2$ by the magnetic confinement:

$$\mu_1^e = 0.51\frac{nT_e}{\omega_e^2\tau_{ei}}, \qquad \mu_1^i = \frac{3nT_i}{10\omega_i^2\tau_{ii}}. \tag{3.55}$$

The last contribution comes from the so called *gyro-viscosity* and it describes the transport in a direction perpendicular to the momentum component transported; it is given by a sum of two components:

$$\mathbf{\Pi}_3 = \frac{\mu_3}{2}\left[\mathbf{b}\times\mathbf{W}\cdot\mathbf{bb} - \mathbb{1}_\perp\cdot\mathbf{W}\times\mathbf{b}\right], \tag{3.56}$$

$$\mathbf{\Pi}_4 = 2\mu_3\left[\mathbf{b}\times\mathbf{W}\cdot\mathbf{bb} - \mathbf{bb}\cdot\mathbf{W}\times\mathbf{b}\right], \tag{3.57}$$

where the μ_3 coefficient is given by:

$$\mu_3^e = -\frac{nT_e}{2\left|\omega_e\right|}, \qquad \mu_3^i = \frac{nT_i}{2\omega_i}. \tag{3.58}$$

A detailed analysis on the theory of gyro-viscosity can be found in Ref. Ramos [2005]. In this work, the main concern is to provide a physical intuition of gyro-viscosity contribution rises. The origins of the giro-viscosity (see Fig. 3.1) can be explained in terms of combined effects of the magnetic field and the presence of a component of the temperature gradient perpendicular to the magnetic field, due to which particles with a different kinetic energy have to face each other, generating a friction in the direction perpendicular to both $\mathbf{B}$ and ∇T_e.

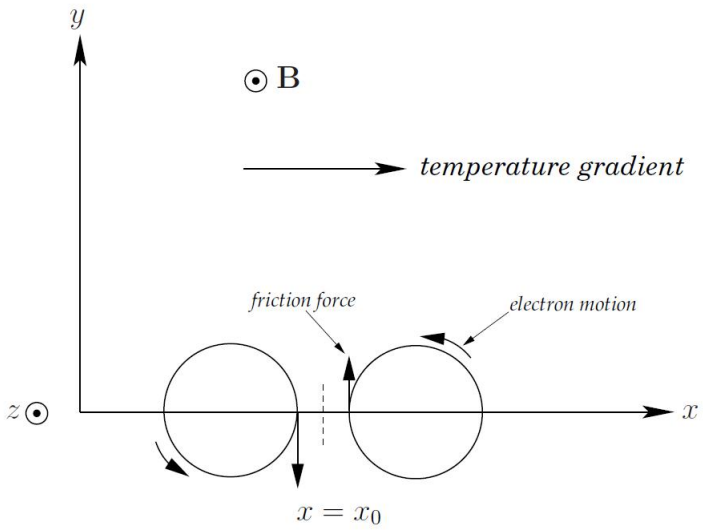

Figure 3.1: Origin of the gyroviscosity, due to the presence of a gradient in temperature perpendicular to the magnetic field: Picture from Ref. Fitzpatrick [2014].

The higher values for the viscosity coefficients are related to ion species, because these particles are determinant in momentum transport mechanism, thanks to their larger mass that allows a longer collisional time and a smaller cyclotron frequency with respect to the electrons. It can be seen that each viscosity coefficient has a positive scaling with the mass of the species involved and this justifies the dominance of the ions, since the ratio between the two masses (m_e/m_i) is at least of the order 10^{-3}, that makes the approximation in which electrons contribution is neglected reasonable. To conclude, we define, the *parallel* $\mu_\parallel$, the *perpendicular* $\mu_\perp$ and *gyro-viscosity* $\mu_\times$, in terms of μ_0, μ_1 and μ_3.

$$\mu_{\parallel}^{i} = 3\mu_0 = 34.6\pi^{3/2}\frac{\epsilon_0^2 m_p^{1/2}}{e^4}\frac{\gamma^{1/2}T_i^{5/2}}{Z^4\ln\Lambda}, \tag{3.59}$$

$$\mu_{\perp}^{i} := \mu_1 + 4\mu_1 = \frac{3}{2}\frac{n_i T_i}{\omega_i^2\tau_{ii}} = \frac{1}{8\pi^{3/2}}\frac{m_p^{3/2}e^2}{\epsilon_0^2}\frac{\gamma^{3/2}n_e^2\ln\Lambda}{T_i^{1/2}B^2}, \tag{3.60}$$

$$\mu_{\times}^{i} := \frac{1}{2}\mu_3 + 2\mu_3 = \frac{5}{4}\frac{n_i T_i}{\omega_i} = 1.25\frac{m_p}{e}\frac{\gamma n_i T_i}{ZB}. \tag{3.61}$$

As for the heat conduction case, it is possible to normalize the viscosity coefficient to the mass density, getting the so called *kinematic viscosity*, usually denoted with ν. This quantity has the unit of measure of a diffusivity coefficient $\left[\mathrm{m}^2/\mathrm{s}\right]$, revealing the role of momentum diffusion coefficient for the kinematic viscosity.
In App. B.1 we summarize the fundamental formulas for the transport coefficients for charge, heat and momentum transport.

3.5 Beyond classical theory: anomalous transport

The main hypothesis of classical transport is that Coulomb (mainly binary) collisions represent the driving microscopic mechanism of transport. In magnetically confined fusion plasmas, the classical prediction of transport coefficient has often turned out to underestimate the experimental measurements even by orders of magnitude. This has resulted in the search for alternative transport mechanism (also known as *anomalous transport*), summarized in Ref. Balescu [2000]. To confirm this we mention that Coulomb interaction is a long range interaction (which makes binary collisions unlikely) and particles are strongly constrained by the magnetic field (making the evolution of the latter a key plasma feature to understand transport).
The main features of the magnetic field that influence transport in fusion plasmas are: the toroidal geometry (*neoclassical transport*), and the stochastic nature due to plasma instabilities (*stochastic or turbulent transport*). Indeed the nonlinear interaction between plasma instabilities, gives rise to magnetic chaos and stochasticity, which are able to deeply modify the topology of the magnetic field, making the magnetic diffusivity the main mechanism to trigger transport in the case of uniformly chaotic systems, Ref. Rechester and Rosenbluth [1978].
As it will be discussed in Chp. 8, the presence of an anomaly in transport coefficients evaluation is particularly evident in the case of the viscosity for RFP plasmas. About this, two important theories should be mentioned:

- The *ion temperature gradient (ITG) viscosity* (see Ref. Guo et al. [1994]) caused by an ion temperature gradient driven mode that damps the velocity fluctuations (associated to the tearing modes) originating an anomalous ion heating (i. e. anomalous viscosity effect), quantified by the formula:

$$\nu_{ITG} = 1.08\times 10^{-4}\frac{\gamma^{1/2}T_e T_i^{1/2}}{Z_{eff}a_T^{3/4}a_B^{1/4}B^2}, \tag{3.62}$$

  where T_i and T_e are expressed in eV and a_T and a_B represents the typical decay length of temperature and magnetic field: $a_T^{-1} := -d/dr\,(\ln T/T_0)$, $a_B^{-1} := -d/dr\,(\ln B/B_0)$.

- The *Finn anomalous viscosity* (see Ref. Finn et al. [1992a]) models the momentum transport in a stochastic magnetic field by sound waves propagation, considering a stochastic magnetic diffusion coefficient according to the Rechester-Rosenbluth model. This can be evaluated as function of plasma measurable parameters using the formula from Ref. Fridström et al. [2018]:

$$\nu_{Finn} = c_s L_C \sum_{m,n} \left(\frac{b^r_{m,n}}{B} \right)^2 \tag{3.63}$$

evaluating the sound speed $c_s = \sqrt{\frac{\gamma_e Z T_e + \gamma_i T_i}{M_i}}$ with $\gamma_e = 1$, $\gamma_i = 3$ and with L_c representing the auto-correlation length.

These formulas are reported in App. B.1.

3.6 Single fluid MHD equations

A further approximation to the model consisting of Eq. (3.20) - (3.25) is given by the *single fluid model*. This model is valid only if the plasma is studied on a sufficiently large space-time scale so that no charge unbalance can be detected experimentally on that macroscopic scale. From a more quantitative point of view, it means that the space scale L and the time scale t must satisfy the following relations:

$$L >> \lambda_D, \qquad t >> \omega_p^{-1}, \tag{3.64}$$

where the Debye length λ_D and the plasma frequency ω_p are defined as follows:

$$\lambda_D := \sqrt{\frac{\epsilon_0 T_e}{n e^2}}, \qquad \omega_p := \sqrt{\frac{n e^2}{\epsilon_0 m_e}}. \tag{3.65}$$

Since fusion plasmas satisfy these hypotheses, it is possible to define a single fluid mass density ρ, velocity $\mathbf{v}$, scalar pressure p, viscous stress tensor $\mathbf{\Pi}$ and the density current $\mathbf{j}$ (the latter has already been encountered in the previous paragraph):

$$\rho := (m_i + m_e)\, n, \qquad \mathbf{v} := \frac{m_i \mathbf{v}_i + m_e \mathbf{v}_e}{m_i + m_e}, \qquad p := p_i + p_e, \qquad \mathbf{\Pi} := \mathbf{\Pi}_i + \mathbf{\Pi}_e. \tag{3.66}$$

The single fluid equations are easily found in terms of linear combinations of the Eq. (3.20) - (3.25) with any further simplification hypotheses. They are simply found using simple algebra steps but, in any case, the explicit derivation is carried out in Ref. Fitzpatrick [2014] and Ref. Choudhuri [1998].
The *continuity equation* is obtained by means of the combination $m_e\,(3.20) + m_i\,(3.23)$ which returns:

$$\frac{\partial \rho}{\partial t} + \nabla \cdot (\rho \mathbf{v}) = 0. \tag{3.67}$$

The single fluid *motion equation* is instead obtained by means of the sum of the two equations for the two species ((3.21) + (3.24)):

$$\rho \left(\frac{\partial \mathbf{v}}{\partial t} + (\mathbf{v} \cdot \nabla)\, \mathbf{v} \right) = \mathbf{j} \times \mathbf{B} - \nabla p - \nabla \cdot \mathbf{\Pi}. \tag{3.68}$$

Typically a simplified version of the viscous stress tensor is assumed in order to avoid the very complicated structure in (3.50); in this way $\mathbf{\Pi} = -\mu \mathbf{W}$, where μ is a single fluid viscosity (potentially a combination of parallel, perpendicular and gyro), which is assumed to be uniform constant. More discussion on the viscosity assumptions are developed in Chp. 5 and Chp. 8. Using the Einstein notation:

$$(\nabla \cdot \mathbf{\Pi})_j = -\mu\, (\nabla \cdot \mathbf{W})_j = -\mu \left(\frac{\partial^2 v_j}{\partial x_i^2} + \frac{1}{3} \frac{\partial^2 v_i}{\partial x_i \partial x_j} \right), \tag{3.69}$$

and, making the additional simplifying hypothesis $\nabla \cdot \mathbf{v} = 0$, the final form of the momentum conservation equation:

$$\rho \left(\frac{\partial \mathbf{v}}{\partial t} + (\mathbf{v} \cdot \nabla) \mathbf{v} \right) = \mathbf{j} \times \mathbf{B} - \nabla p + \mu \nabla^2 \mathbf{v}. \tag{3.70}$$

Thanks to the combination $m_e(3.24) - m_i(3.21)$ one finds a generalization of the Ohm's law. However, since the exact calculations give rise to a very complex equation, approximations are made in order to keep only the relevant physical terms and to simplify the equation as much as possible. Neglecting terms related to viscosity, the electron mass, assuming a constant current density $\mathbf{j}$ in time and a simplified form of the friction force $\mathbf{F}$, the equation one can get after some steps of algebra is:

$$\mathbf{E} + \mathbf{v} \times \mathbf{B} - \frac{\mathbf{j}}{\sigma} = \frac{1}{en} \left(\mathbf{j} \times \mathbf{B} - \nabla p_e \right), \tag{3.71}$$

that is commonly known as *generalized Ohm's law*. More complete forms of this equation can be found in Choudhuri [1998] and Fitzpatrick [2014], where less strict assumptions are made. Anyhow, for the vast majority of physical applications it is common to perform a further simplification by neglecting the right hand side of (3.71), and obtaining:

$$\mathbf{E} + \mathbf{v} \times \mathbf{B} = \eta \mathbf{j}. \tag{3.72}$$

The single fluid *energy balance equation* is obtained by the combination (3.22) + (3.25):

$$\frac{3}{2} \frac{dp}{dt} + \frac{5}{2} p \nabla \cdot \mathbf{v} + \mathbf{\Pi} : \nabla \mathbf{v} + \nabla \cdot \mathbf{q} = \eta j^2. \tag{3.73}$$

In this equation the heat sources are represented by the viscous heating term $\mathbf{\Pi} : \nabla \mathbf{v}$ and the ohmic heating term $\eta j^2 \simeq W_i + W_e$. If present, other sources of external heating have to be taken into account in the heat transport term $\nabla \cdot \mathbf{q}$. To guarantee the closure of the model, Maxwell's equations are added, remembering that no charge imbalance is contemplated in the model, resulting in the absence of the displacement current term in Faraday's law:

$$\nabla \cdot \mathbf{E} = 0, \qquad \nabla \cdot \mathbf{B} = 0, \qquad \nabla \times \mathbf{E} = -\frac{\partial \mathbf{B}}{\partial t}, \qquad \nabla \times \mathbf{B} = \mu_0 \mathbf{j}. \tag{3.74}$$

3.7 Visco-resistive MHD model

Once obtained the single fluid equations, the *visco-resistive MHD model* is obtained by simply rewriting them with some additional assumptions:

- negligible effect of a pressure gradient (often valid in case of low β plasmas and if current driven instabilities represent the focus of the model). We mention that the validity of this approximation has been questioned in Ref. Chahine and Bos [2018], where it is shown that the condition $\beta << 1$ is not enough to neglect the pressure gradient term $|\nabla p|$, which should be compared rigorously to the $|\mathbf{j} \times \mathbf{B}|$ term;
- time-constant and uniform in space mass density ρ,
- resistivity η and viscosity μ represent the only transport coefficients of the model,

getting the following set of equations:

$$\rho \left(\frac{\partial \mathbf{v}}{\partial t} + (\mathbf{v} \cdot \nabla) \mathbf{v} \right) = \mathbf{j} \times \mathbf{B} + \mu \nabla^2 \mathbf{v}, \tag{3.75}$$

$$\frac{\partial \mathbf{B}}{\partial t} = \nabla \times (\mathbf{v} \times \mathbf{B}) - \nabla \times (\eta \mathbf{j}) \,, \tag{3.76}$$

$$\nabla \cdot \mathbf{B} = 0, \tag{3.77}$$

$$\nabla \times \mathbf{B} = \mu_0 \mathbf{j}. \tag{3.78}$$

Then, the physical quantities appearing in the visco-resistive model are normalized with respect to their typical scale values. This procedure does not really add anything related to the physics of the system but it helps in understanding which are the mechanisms and the relative terms in the equation that drive the development of plasma dynamics.
The normalizations adopted are:

$$\rho = \rho_0 \tilde{\rho}, \qquad v = v_A \tilde{v}, \qquad t = \tau_A \tilde{t}, \qquad r = a\tilde{r}, \qquad B = B_0 \tilde{B}, \tag{3.79}$$

where $\rho_0 = m_i n$, v_A and τ_A are the Alfvén velocity and time respectively, which represent the velocity of propagation of hydromagnetic waves and time needed for these waves to travel along a macroscopic distance, conventionally chosen to be a, the minor radius of the toroidal device. B_0 is the on-axis toroidal magnetic field. Thanks to the linearization of MHD equations hydromagnetic waves can be treated, finding that:

$$v_A = \frac{B}{\sqrt{\mu_0 \rho_0}}, \qquad \tau_A = \frac{a\sqrt{\mu_0 \rho_0}}{B}. \tag{3.80}$$

To complete this scheme of normalization, the definition $\gamma = m_i/m_p$ is added. The normalizations in (3.79) also affect the derivatives and the other quantities appearing in the model:

$$\nabla = \frac{\tilde{\nabla}}{a}, \qquad \frac{\partial}{\partial t} = \frac{\partial}{\tau_A \partial \tilde{t}}, \qquad j = \frac{B_0}{\mu_0 a} \tilde{j}. \tag{3.81}$$

Replacing the normalization scheme (3.79) - (3.81) into the equations of the visco-resistive model (3.75)-(3.78), after basic algebra steps and the removal of the ˜ symbol the visco-resistive model equations become:

$$\frac{\partial \mathbf{v}}{\partial t} + (\mathbf{v} \cdot \nabla)\, \mathbf{v} = \mathbf{j} \times \mathbf{B} + \frac{\mu \tau_A}{a^2 \rho_0} \nabla^2 \mathbf{v}, \tag{3.82}$$

$$\frac{\partial \mathbf{B}}{\partial t} = \nabla \times (\mathbf{v} \times \mathbf{B}) - \nabla \times \left(\frac{\eta \tau_A}{\mu_0 a^2} \mathbf{j} \right), \tag{3.83}$$

$$\nabla \cdot \mathbf{B} = 0, \tag{3.84}$$

$$\nabla \times \mathbf{B} = \mathbf{j}, \tag{3.85}$$

in which also the normalization $\rho = 1$ is considered, since mass density is assumed to be constant. Once equations are written in the form (3.82) - (3.85), it is quite evident that there are two dimensionless groupings of coefficients that contain the all the physical parameters. It is expected those dimensionless combinations to describe the behaviour of the system.
In particular, defining resistive and viscous time τ_r and τ_μ as the time scales during which resistive and viscous phenomena take place:

$$\tau_r = \frac{a^2 \mu_0}{\eta}, \qquad \tau_\mu = \frac{a^2 n_i \gamma m_p}{\mu}, \tag{3.86}$$

it is possible to introduce two dimensionless fluid numbers that are the *viscous Lundquist number* M and the *Lundquist number* S, defined in terms of resistive, viscous and Alfvén times:

$$M := \frac{\tau_\mu}{\tau_A} = \frac{a^2\rho_0}{\mu\tau_A} \qquad S := \frac{\tau_r}{\tau_A} = \frac{a^2\mu_0}{\eta\tau_A}, \tag{3.87}$$

that, once replaced in equations (3.82) - (3.83), return:

$$\frac{\partial \mathbf{v}}{\partial t} + (\mathbf{v}\cdot\nabla)\,\mathbf{v} = \mathbf{j}\times\mathbf{B} + M^{-1}\nabla^2\mathbf{v}, \tag{3.88}$$

$$\frac{\partial \mathbf{B}}{\partial t} = \nabla\times(\mathbf{v}\times\mathbf{B}) - \nabla\times\left(S^{-1}\mathbf{j}\right), \tag{3.89}$$

that, with equations (3.84) and (3.85), constitute the final form of the visco-resistive model. The implementation of the visco-resitive model has been done in Padova, and the code bears the name SpeCyl, see Chp. 4. In this thesis a large use of outputs from the code SpeCyl is made.

3.7.1 The Hartmann number

In Sec. 3.7, we show that two dimensionless parameters (S and M) represent the modelling of transport in the simple visco-resistive model. To better investigate the physical insight of the model, it is more convenient to rewrite Eq. (3.88) - (3.89) by means of a proper change of coordinates, see Ref. Cappello and Escande [2000]:

$$t \to \bar{t} = \sqrt{\frac{M}{S}}t, \qquad v \to \bar{v} = \sqrt{\frac{S}{M}}v, \qquad \frac{\partial}{\partial t} \to \frac{\partial}{\partial \bar{t}} = \sqrt{\frac{S}{M}}\frac{\partial}{\partial t}. \tag{3.90}$$

In this way two additional fluid dimensionless parameters are introduced: the *magnetic Prandtl number* P and *Hartmann number* H, defined as follows:

$$P := \frac{\tau_r}{\tau_\mu} = \frac{S}{M} = \frac{\mu_0\mu}{\rho_0\eta}, \qquad H := \frac{\sqrt{\tau_r\tau_\mu}}{\tau_A} = \sqrt{SM} = \frac{aB}{\sqrt{\eta\mu}}. \tag{3.91}$$

The result of the change of coordinates for the visco-resistive model is a set of differential equations, valid for the normalized variables:

$$P^{-1}\left(\frac{\partial \mathbf{v}}{\partial t} + (\mathbf{v}\cdot\nabla)\,\mathbf{v}\right) = \mathbf{j}\times\mathbf{B} + H^{-1}\nabla^2\mathbf{v}, \tag{3.92}$$

$$\frac{\partial \mathbf{B}}{\partial t} = \nabla\times(\mathbf{v}\times\mathbf{B}) - \nabla\times\left(H^{-1}\mathbf{j}\right), \tag{3.93}$$

$$\nabla\cdot\mathbf{B} = 0, \qquad \nabla\times\mathbf{B} = \mathbf{j}, \tag{3.94}$$

where the couple of parameters (P, H) has replaced (S, M) in transport modelling. In particular, the Hartmann number plays a key role in the study of magnetohydrodynamic stability of plasmas (Ref. Montgomery [1992]). A fundamental contribution to visco-resistive MHD research consisted of the analytical study of the steady states (see Ref. Bates and Montgomery [1998], Ref. Kamp and Montgomery [2004], Ref. Shan and Montgomery [1993], Ref. Shan [1994]), highlighting the role of finite velocity fields in the force balance and of the toroidicity effect, see Ref. Morales et al. [2014]. The most important obstacle encountered in the previous papers concerns the estimate of the viscosity coefficient, which is often assumed to be of the same order of the Braginskii parallel viscosity. We will question and discuss this choice in Chp. 8, in the case of the RFP configuration.
Focusing on the non-linear dynamics of Eq. (3.92) - Eq. (3.94), if the inertia term in Eq. (3.92)

becomes negligible (e. g. studying the properties of the time averaged global quantities characterizing the RFP configurations), the dynamics of the visco-resistive model depends only on the Hartmann number, that turns out to be the model 'ruling parameter'. Further considerations on this topic are presented in Chp. 4.
To conclude, we remark that introducing the fluid numbers it is possible to describe plasma conditions which may differ a lot in terms of plasma physical parameters (although with the same dimensionless parameters) using the same rescaled equations. This represents the great advantage of this modelling approach.

3.8 Summary and final remarks

In this Chapter we have discussed the main MHD models used in plasma physics (Braginskii equations, single fluid model and visco-resistive model). In addition, also the basics of plasma physics transport have been introduced with reference to classical, neoclassical and turbulent theories. The most important results of this Chapter can be summarized in two points:

- The evaluation of the transport coefficients as function of the main plasma measurable parameters (formulas reported in App. B.1), following the formal mathematical derivation of the Chapmann-Enskog and Balescu closure procedure. These formulas are the starting points for the development of Chp. 5, 8 and 9. In particular, in Chp. 8, the different transport theories for the plasma viscosity will be compared on a wide database of RFX-mod shots.
- The introduction and the derivation of the fluid dimensionless numbers, with particular reference to the Hartmann number. Indeed, the latter represents (according to numerical simulations) the ruling parameter of RFP plasma dynamical regimes (see Chp. 4), while in Chp. 9 we will discussed the role of the Hartmann number in describing the density limit phenomenology, limited to the RFP configuration.

Part II

Numerical simulations studies

Chapter 4

SpeCyl & PIXIE3D numerical codes

This chapter is devoted to the introduction of the numerical codes SpeCyl and PIXIE3D for the simulation of 3D non-linear visco-resistive magnetohydrodynamics of fusion plasmas, focusing on: the domain of validity of the models simulated, the numerical scheme of solution adopted, the modelling results obtained so far.
In Sec. 4.1, the spectral SpeCyl code is introduced, with reference to the equations solved, the transport parameters included in the model (dimensionless resistivity and viscosity), and the boundary conditions adopted for the solution of the equations.
Sec. 4.2 concerns the PIXIE3D code. In this case some differences with respect to SpeCyl are highlighted: in particular the larger set of differential equations solved (including the energy balance), which allows the heat transport modelling and the different numerical scheme adopted (finite volume elements).
In Sec. 4.3 the results of the numerical modelling activity, related to RFP plasmas, are presented, describing the role of both transport dimensionless parameters and edge seed magnetic perturbations.
Starting with Sec. 4.4, the specific analyses carried on for this Thesis are described, with focus on the input parameters of the simulations composing the database analyzed.
In Sec. 4.5, the results of the analysis are summarized, as concerns the description of helical self-organized regimes rise, triggered by specific values of the transport dimensionless parameters and magnetic perturbations.
Summary and final remarks follow in Sec. 4.6.

4.1 The SpeCyl code

In the study of MHD models used to understand fusion plasma experimental features (e. g. plasma relaxation, Ref. Ortolani and Schnack [1993]) it is very common to deal with non-linear differential equations (see Ref. Biskamp [1993]), which necessarily require a numerical approach to be solved, relying on supercomputers computational power and numerical codes developments. The increase of the latter has encouraged the development of the numerical approach in the last decades. About that, several numerical codes devoted to the solution of MHD models have been developed: DEBS (see Ref. Schnack et al. [1987]), Nimrod (see Ref. Glasser et al. [1999]), XTOR (see Ref. Lütjens and Luciani [2008]) and M3D (see Ref. Park et al. [1999]). Moreover, it is worth mentioning the (more recent) rise and growth of international modelling and coding projects like JOREK (see Ref. Huysmans and Czarny [2007], Hoelzl et al. [2021]), a massively parallel fully implicit non-linear extended MHD code, managed by a collaboration of scientists from different institutes involved in the European fusion research program. In this work, we will focus on simpler codes for non-linear MHD modelling, called SpeCyl (in this Section) and PIXIE3D (Sec. 4.2).
The Specyl code is a numerical tool that performs 3D nonlinear visco-resistive MHD simulations. The code was introduced for the first time in Ref. Cappello and Biskamp [1996] to study magnetic reconnection phenomena in the RFP configuration, using properly a MHD approach. The code carries out the solution of the equations of the visco-resistive model, derived in Sec. 3.7, here rewritten for the sake of completeness (in dimensionless form), indicating with $\eta = S^{-1}$ and $\nu = M^{-1}$ the dimensionless resistivity and viscosity:

$$\frac{\partial \mathbf{v}}{\partial t} + (\mathbf{v} \cdot \nabla)\, \mathbf{v} = \mathbf{j} \times \mathbf{B} + \nu \nabla^2 \mathbf{v}, \tag{4.1}$$

$$\frac{\partial \mathbf{B}}{\partial t} = \nabla \times (\mathbf{v} \times \mathbf{B}) - \nabla \times (\eta \mathbf{j})\,. \tag{4.2}$$

$$\nabla \cdot \mathbf{B} = 0, \tag{4.3}$$

$$\nabla \times \mathbf{B} = \mathbf{j}. \tag{4.4}$$

We also recall the main hypothesis made to obtain the set of Eq. (4.1) - (4.4): the presence of a negligible pressure, constant mass density and viscosity and resistivity as effective transport coefficients.
SpeCyl adopts a semi-implicit temporal advance scheme and works in cylindrical geometry (r, θ, z), exploiting a spectral formulation in the periodic coordinates (azimuthal: $\theta \in [0, 2\pi]$ and axial $z \in [0, 2\pi R_0]$) and finite difference scheme (with a staggered mesh) for the normalized radial coordinate $r \in [0, 1]$. Naming m and n the poloidal and toroidal wave numbers, a generic function $f(r, \theta, z, t)$ can be rewritten in Fourier series as:

$$f(r, \theta, z, t) = \sum_{m=-\infty}^{+\infty} \sum_{n=-\infty}^{+\infty} f_{m,n}\,(r, t)\, e^{i\left(m\theta + \frac{n}{R_0} z\right)}, \tag{4.5}$$

where the expression z/R_0 (with R_0 major radius of the rectified torus) represents the toroidal angle ϕ. To guarantee the function f to be real, a condition on its transform $f_{m,n}$ has to be required:

$$f \in \mathbb{R} \quad \longrightarrow \quad f^*_{m,n} = f_{-m,-n}. \tag{4.6}$$

The prediction of the magnetic field Fourier spectrum is fundamental because it determines the plasma helical regime, depending on the ratio of the dominant and secondary modes contributions. In the numerical simulation only a finite number of Fourier modes is taken into account.

Those considered by the SpeCyl code, chosen after a convergence study described in Ref. Cappello and Biskamp [1996], are shown in Fig 4.1. It is worth noting that the high number of Fourier harmonics considered (including those with $m > 2$) is fundamental in order to guarantee the spectrum convergence. However, in the analysis made in this Chapter we will focus on the $m = 0$ and $m = 1$ modes, because they have a larger amplitude and because the modes with $m > 2$ are not experimentally measured.

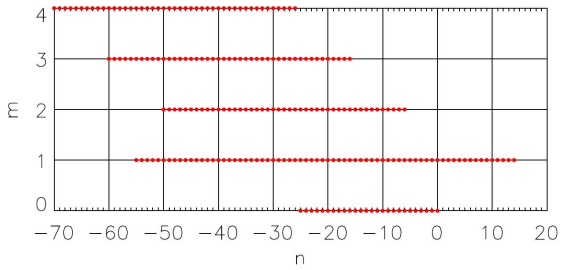

Figure 4.1: Fourier modes considered by the SpeCyl code (red dots), from Ref. Bonfiglio et al. [2010].

Working in the Fourier space greatly simplifies the solution of differential equations, transforming derivatives and integrals into linear algebra operations. Linear differential equations are transformed in algebraic equations that involve the same mode (the same m and n numbers) of different physical quantities in the Fourier space. On the contrary, non linearity is transformed into convolution of different Fourier modes. An exemplification of the last statement can be found in App. B.3.
Relatively to transport, the SpeCyl code takes into account only the resistivity and viscosity coefficients which depend, in principle, on time and space. The dependencies chosen in SpeCyl are simplified in order to allow the simulation to be made in a reasonable time and also because direct measurements (or indirect estimates) of the viscosity profile are extremely difficult. This will be matter of further discussion in Chp. 5 and 8. The coefficients assumed are a time constant and radially uniform viscosity and a time constant resistivity. The only non trivial dependence is the radial one of the resistivity:

$$\nu(r) = \nu_0, \qquad \eta(r) = \eta_0 \left(1 + A \left(\frac{r}{a}\right)^B\right), \qquad A = 20, \qquad B = 10. \tag{4.7}$$

The resistivity profile is chosen considering the typical experimental profiles of the temperature as function of the cylinder radius and the relations between resistivity and temperature, according to Eq. (3.36). The choice of these dependencies is absolutely non trivial, and the verification of the validity of this assumption is also matter of discussion of this work.
The initial condition imposed to solve the differential equations can be of two types: ideal shell or magnetic perturbation. The ideal shell boundary conditions consist of the absence of radial magnetic field and of poloidal electric field at the boundary:

$$b^r_{m,n}(a) = 0, \qquad E^\theta_{m,n}(a) = 0, \qquad \forall m, n. \tag{4.8}$$

Additional conditions are the presence of a constant toroidal electric field ($E_z = E_0$) to induce the plasma current and the no slip condition for two velocity components: $v_\theta(a) = 0$, $v_z(a) = 0$. On the contrary, magnetic perturbations (MPs) are obtained imposing the presence of a non-zero edge radial magnetic field for a specific mode ($b^r_{m,n}(a) \neq 0$). This type of simulations is particularly interesting for the RFP configuration because they can induce the transition to SH or QSH, as it will be explained in Sec. 4.3.2.
In Ref. Bonfiglio et al. [2010] a cross-benchmark non-linear verification of the SpeCyl and PIXIE3D codes is presented. Despite the different numerical methods exploited by the two

codes, the comparison has resulted in excellent results, in terms of agreement between SpeCyl and PIXIE3D simulation predictions in the common domain of applications of the two models, for both the tokamak and the RFP configurations. The latter result represents a key point in favour of the use of the two codes in numerical simulating fusion plasmas.

4.2 The PIXIE3D code

The second MHD code available for fusion plasmas numerical simulations used in this work (see Chp. 6) is PIXIE3D, developed at Los Alamos National Laboratory (LANL), New Mexico, USA. With respect to the SpeCyl code, PIXIE3D solves a wider set of differential equations, including the continuity equation and the energy balance equation, which allows heat transport modelling. PIXIE3D is a parallel, implicit, Newton-Krylov solver for the solution of the 3D nonlinear viscoresistive MHD, presented in Ref. Chacón [2008], exploiting a finite volume methods.
The numerical spatial discretization adopted works in an arbitrary curvilinear geometry. In particular, the finite volume scheme is conservative, which guarantees at each time step the condition $\nabla \cdot \mathbf{B} = 0$ and $\nabla \cdot \mathbf{j} = 0$ to be satisfied. This represents a fundamental feature to preserve numerical accuracy and avoid unphysical results, as explained in detail in Ref. Chacón [2004]. For the temporal advancement, a second order *Crank-Nicolson algorithm* is implied, producing a set of non linear algebraic equations, solved by means of the *Newton-Krylov method*. One of the most important feature of this code is the preconditioning strategy, which consists of reformulating the set of partial differential equations so that the Jacobian matrix (from the Newton-Krylov method) assumes a block-diagonal form, definitely much easier to be inverted and numerically stable. The preconditioner initially exploited the smallness of the plasma flow. However, the code has then been upgraded with the possibility of dealing with arbitrary plasma flows and including also the Hall effect terms in Eq. (4.11), Ref. Chacón [2008].
The equations solved by the code are the followings, here written in their conservative form and in dimensionless units:

$$\frac{\partial \rho}{\partial t} + \nabla \cdot (\rho \mathbf{v} - D \nabla \rho) = 0, \tag{4.9}$$

$$\frac{\partial \mathbf{B}}{\partial t} + \nabla \times \mathbf{E} = 0, \tag{4.10}$$

$$\mathbf{E} + \mathbf{v} \times \mathbf{B} = \eta \mathbf{j}, \tag{4.11}$$

$$\nabla \cdot \mathbf{B} = 0, \tag{4.12}$$

$$\mathbf{j} = \nabla \times \mathbf{B}, \tag{4.13}$$

$$\frac{\partial (\rho \mathbf{v})}{\partial t} + \nabla \cdot \left[\rho \mathbf{v}\mathbf{v} - \mathbf{B}\mathbf{B} + \mathbb{1} \left(p + \frac{B^2}{2} \right) - \rho \nu \nabla \mathbf{v} \right] = 0, \tag{4.14}$$

$$\frac{\partial T}{\partial t} + \mathbf{v} \cdot \nabla T + (\gamma - 1) \left[T \nabla \cdot \mathbf{v} - \frac{\kappa \nabla^2 T + Q}{\alpha_T \rho} \right] = 0, \tag{4.15}$$

where D represents the particle diffusivity which models cross-field particle diffusion, η and ν are respectively the dimensionless resistivity and viscosity, κ represents the thermal conductivity, $\alpha_T := T_i/T_e$ (with the kinetic pressure given by $p = nT_e(1 + \alpha_T)$), while Q represents the heat source in the energy balance equation accounting for the ohmic and viscous contributions: $Q = \eta j^2 + \rho \nu \nabla \mathbf{v} : \nabla \mathbf{v}$.
In the solution of the energy balance equation, one of the most challenging problems to be

overcome is the presence of a strong anistropy in the fusion plasmas heat transport ($\chi_\perp/\chi_\parallel << 1$), which has required the introduction of an asymptotic-preserving semi-Lagrangian algorithm (Ref. Chacón et al. [2014]). Interesting progress have been made in MHD modelling exploiting the PIXIE3D code, involving both the tokamak and the RFP configuration, Ref. Bonfiglio et al. [2013]. An interesting development which will be preliminary discussed in this work is the introduction of a Spitzer-like resistivity profile, self-consistently evolved according to the energy balance equation solution for the temperature profile (see Chp. 5 - 6) and its influence on the stability of MHD modes and helical self-organization process.

4.3 SpeCyl code in modelling RFP plasmas

Since the 90s the SpeCyl code has been used to perform 3D non linear magnetohydrodynamics simulations that turned out to be of fundamental importance in modelling the RFP configuration, reproducing or predicting experimental results coming from RFX and RFX-mod devices. In this Section, the main achievements in this research field are mentioned, pointing out the aspects that can be useful for this work. At the state of art of this research, the rise of helical self-organized state in RFP simulations results to be ruled jointly by the visco-resistive transport coefficients and the magnetic boundary conditions, as shown in Ref. Veranda et al. [2019].

4.3.1 The role of transport dimensionless parameters

The role played by the Hartmann number (representing the visco-resistive dissipation) emerged among the first results of numerical simulations. In Ref. Cappello and Escande [2000], the Eq. (4.1) - (4.4) are rewritten introducing properly the Hartmann and the Prandtl numbers, as done in Sec. 3.7.1, obtaining the set of Eq. (3.92) - (3.94), from which it is evident that the Hartmann number becomes the main plasma parameter when the inertia terms are negligible. Then, results of MHD numerical simulations are presented with $H \approx 10^2 - 10^4$, Fig. 4.2).

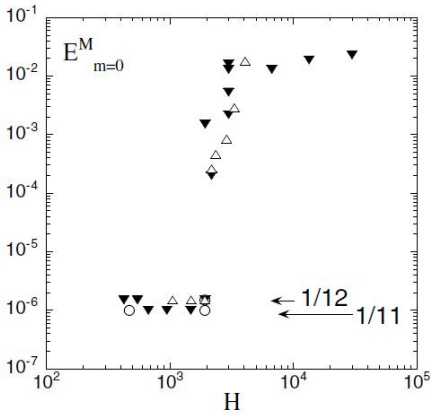

Figure 4.2: Magnetic energy of the $m = 0$ modes: a phase transition appears around $H \simeq 2500$. Below this threshold, the magnetic Fourier spectrum is dominated by $m = 1$ $n = -11$ or $n = -12$ mode, with very low magnetic energy of the $m = 0$ modes. Above this threshold, the energy of $m = 0$ is increased by orders of magnitude. Plot taken from Ref. Cappello and Escande [2000].

These simulations were made exploring a wide range of the initial parameters, compatibly with the computational power available in those years. In Fig. 4.2 the time averaged magnetic energy (in normalized units) associated with the $m = 0$ modes as function of the Hartmann number is plotted. Simulations properties considered are summarized in Tab. 4.1.

Symbol	Simulation settings
△	$S = 3.3 \times 10^3$, $P \in \left[\frac{2}{3}, 10\right]$
▾	$S = 3.0 \times 10^4$, $P \in [1, 5000]$
○	Slightly perturbed SH initial condition

Table 4.1: Simulations analyzed in Ref. Cappello and Escande [2000]. The simulations represented by a triangle are developed from a fully turbulent initial state.

The results found in Fig. 4.2 are: the independence on the Prandtl number and the presence of a phase transition between $H = 2000$ and $H = 3000$ that is pointed out by the discontinuity in the the value of the $m = 0$ magnetic energy. At low Hartmann values the magnetic energy related to the $m = 0$ modes is reduced by some orders of magnitude. In these cases with $H \lesssim 2500$, the energy associated to the modes with $m/n = 1/11$ or $m/n = 1/12$ represents the dominant contribution to the spectrum.
The threshold $H \simeq 2500$ "separates" the domain into two different regions in which the plasma is found into two different phases: SH below the Hartmann threshold value (in which the modes $m/n = 1/11$ and $m/n = 1/12$ dominate) and MH above the threshold value. The Hartmann number is thus a fundamental parameter to understand the transition from SH to MH, turning out as ruling parameter of visco-resistive magnetohydrodynamics. This behavior resembles the role played by the dimensionless Reynolds number ($\mathrm{Re} := \frac{Lv}{\nu}$, being L, v, ν the scale values of length, velocity and kinematic viscosity) in the case of incompressible isothermal fluid mechanics, described in Ref. Boussinesq [1877], where a critical threshold Re_{crit} is found to govern the transition from laminar $\mathrm{Re} << \mathrm{Re}_{crit}$ to turbulent regime $\mathrm{Re} >> \mathrm{Re}_{crit}$.

4.3.2 Edge seed magnetic perturbations (MP)

In more recent times the modeling activity has been aimed at understanding the role of boundary conditions. In particular, in Ref. Bonfiglio et al. [2013] and Ref. Veranda et al. [2013], simulations with seed magnetic perturbations (MPs) are presented: a radial magnetic field of a determined mode (typically the usual dominant mode $m = 1$, $n = -7$) of a relative magnitude of 2% with respect to the edge magnetic field is introduced as initial perturbation. These values are also the typical one that are involved in the experiment, as it happens in RFX-mod device. An important analogy between SpeCyl numerical simulations and the RFX-mod experiment is shown in Bonfiglio et al. [2013]: a QSH phase can be stimulated by means of an adequate initial boundary condition of the radial magnetic field.

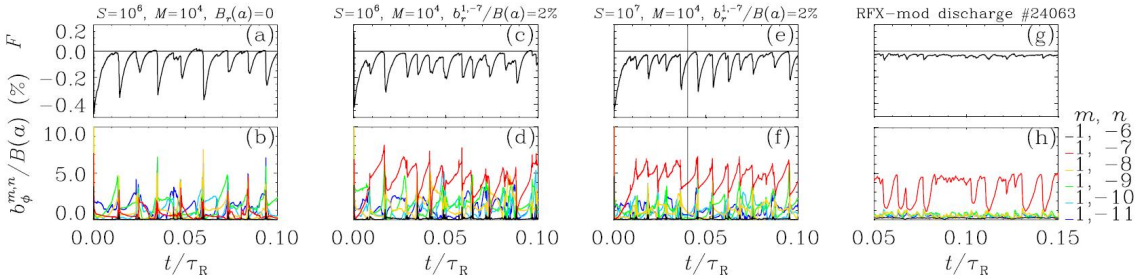

Figure 4.3: Comparison between three different simulations and an RFX-mod shot for the F factor and the toroidal magnetic field: The introduction of a non zero edge magnetic perturbation, stimulates the periodic emergence of the dominant mode, which reproduces the experimental RFP 'sawtooth' activity. Plot from Ref. Bonfiglio et al. [2013].

More precisely, in Fig. 4.3, quasi-periodic cycles in QSH phase are repeated: they are charac-

terized by the dominance of a Fourier mode of the magnetic field followed by a sudden crash in which the system returns in MH phase, resembling the experimental-like RFP sawtooth activity. This behaviour is shown for simulations with $H \approx 10^5$, and for RFX-mod # 24063 shot with $I_p \simeq 1.5\,\mathrm{MA}$, $n_e \simeq 2.8 \times 10^{19}\,\mathrm{m}^{-3}$ and $T_e \simeq 750\,\mathrm{eV}$.
The agreement between SpeCyl numerical simulations and RFX-mod experiments has found a further confirmation in Ref. Veranda et al. [2017]. In this article, visco-resistive MHD results predicted experimental measurements, in the case of seed magnetic perturbation application, possible thanks to the active-feedback control system with which RFX-mod device is equipped (see Sec. 7.1). The result is shown in Fig. 4.4: the introduction of the magnetic perturbations, allows for the modelling of helically self-organized states, even at low levels of the dissipation coefficients. In addition, the perturbation is able to impose its helical twist to the entire plasma column, resulting in the precise modelling of RFX-mod shots with external magnetic perturbation different in time.

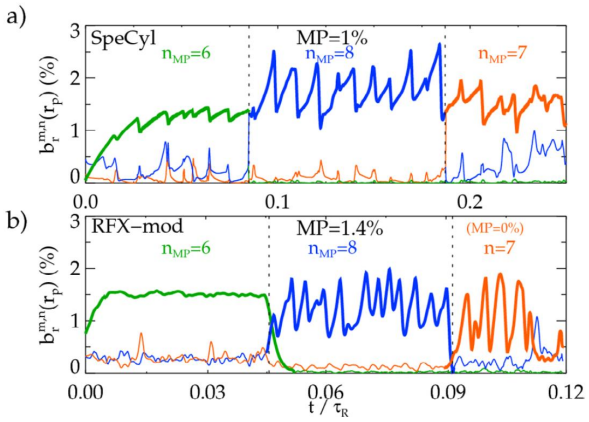

Figure 4.4: Comparison between a Specyl simulation with $S = 10^6$ (a) and an RFX-mod shot (#30932) with $I_p \sim 1.5\,\mathrm{MA}$ (b) with the same seed magnetic perturbation for the radial magnetic field. The position r_P represents $r_p = 0.9a$. Plot from Ref. Veranda et al. [2017].

The success obtained by the SpeCyl code in modelling the RFP physics justifies the use of the code and its future developments and it reveals the visco-resistive model to be the right theoretical framework for the purposes of this work.

4.4 SpeCyl simulations database description

In this work, a database composed by 95 numerical simulations made for previous studies (see Ref. Veranda et al. [2019]) are considered. The initial inputs for the central viscosity ν_0 and the central resistivity η_0 are chosen in order to cover a range for the Hartmann number as wide as possible that spans an interval of about four orders of magnitude, between 10^2 and 10^6.
Because of the strong uncertainty characterizing the experimental viscosity estimates in RFP plasmas, (discussed in Chp. 8), also other values of the Hartmann parameter would be of major interest (in particular $H \sim 10^6 - 10^8$). However, according to Eq. (3.92) and (3.93), where terms proportional to H^{-1} appear, the introduction of a high Hartmann number implies the coexistence (inside the same differential equation) of terms of order 0 and at least one term of order H^{-1} that causes a great increase in the computational time needed, making high Hartmann number simulations unsustainable by the present computational power. In addition, when decreasing dissipative coefficients, the model would require to be supplemented with at least the generalized Ohm's law terms, which remains a major effort altogether.
The aspect ratio is fixed: $R_0/a = 4$, the value of RFX-mod device.
In the database, different types of simulations are contained with respect to the initial magnetic

perturbations (MPs): some of them are devoid of the initial magnetic perturbations (**MP off**), while others are endowed with the initial magnetic perturbation, obtained imposing a non zero radial magnetic field at the radial position $r = a$ for a determined Fourier mode at the initial time (**MP on**). The modes stimulated in this second case are those that typically dominate the spectrum in the SH or QSH phases in RFX-mod device: $m = 1$, $-9 \leqslant n \leqslant -5$, $n = -1$. In particular, the most frequent stimulated mode is the one with $m = 1$, $n = -7$, because of the role played by the latter during RFX-mod QSH phase, although the mechanism by which this specific mode dominates is not fully understood yet. The intensity of the perturbation is usually expressed in terms of the perturbation normalized to the edge poloidal magnetic field ($B_\theta(a)$): the values considered in the simulations are 1.3%, 2%, 4%, 6%. The most reliable values (applied in the experiments) are between 2% and 4%. The histogram distribution of the simulations database is shown in Fig. 4.5 for the Hartmann number (a) and the magnetic perturbations (b), (c). The ranges of transport parameters are reported in Tab. 4.2.

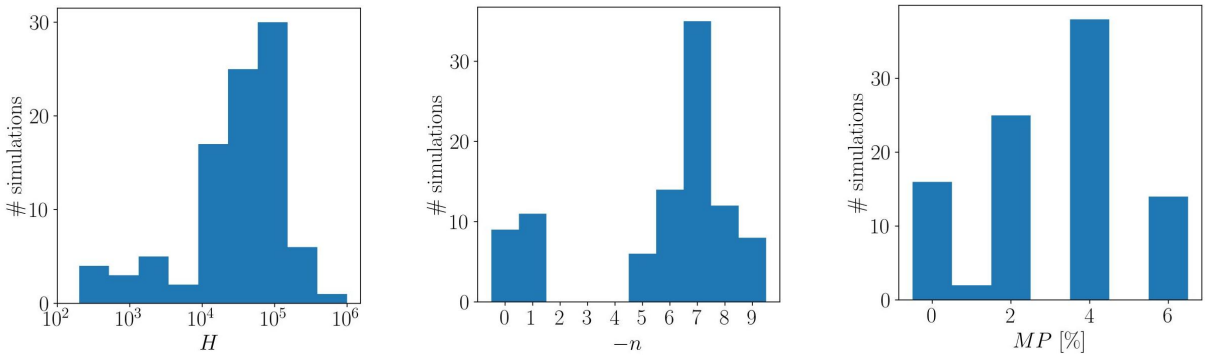

(a) (b) (c)

Figure 4.5: Database distribution of the inputs which determine the development of a SpeCyl simulation dynamics: visco-resistive dissipation (a), toroidal number of the input magnetic perturbations considered, with poloidal mode number $m = 1$ (the value $n = 0$ corresponds to the absence of stimulation) (b), intensity of the magnetic perturbation $b_r^{1,n}(a)/B_\theta(a)$ (c).

	SpeCyl simulations interval
Lundquist S	4×10^2 - 10^7
Visc. Lund. M	10 - 10^5
Mag. Prandtl P	1 - 10^5
Hartmann H	2×10^2 - 10^6

Table 4.2: Ranges of the dimensionless transport parameters in the database of SpeCyl simulations analyzed in this work.

The output of the simulations are the Fourier components of the magnetic **B** and velocity **v** fields (expressed in cylindrical coordinates), considered in Fig 4.1, for each time instant of the simulation. The magnetic and kinetic energy, are easily obtained integrating, over the plasma volume, B^2 and v^2. Detailed calculations are reported in App. B.4, for the case of the magnetic energy.
Since a great majority of the discharges simulations are characterized by periodic intervals of single mode dominance (QSH) separated by sudden crashes of magnetic chaos (MH), it is reasonable to calculate time averages only in the QSH phase time. This technique was proposed and used in Ref. Piovesan et al. [2009] to identify helical states in the experimental data analysis of RFX-mod shots. To reach this goal, the spectral index N_s is defined as:

$$N_s = \left[\sum_{n=-20}^{-7} \left(\frac{B_{1,n}^2}{\sum_{j=-20}^{-7} B_{1,j}^2} \right)^2 \right]^{-1}, \tag{4.16}$$

where $B_{1,n}$ is a generic harmonic of the magnetic field. The spectral index N_s was introduced for the first time in Ref. Ho et al. [1995]. A value of $N_s = 1$ implies the plasma to be in a pure SH. A threshold N_{th} for N_s below which the system is considered to be in QSH is usually chosen and, consequently, the time average is computed only for the instants during which the spectral index is below the threshold chosen. The choice of this threshold value clearly results to be arbitrary and, from now on, the time average below the threshold value will be indicated by the symbol $\langle\rangle_{t|N_s(t)<N_{th}}$. Reasonable values for N_{th} are in the interval $3-5$.
The quantities considered in the database analysis are here listed:

- Edge magnetic field related to the dominant and the secondaries modes, both for the cases $m = 0$ and $m = 1$ and for each of the three components radial B^r, poloidal B^θ and toroidal B^z:

$$\left\langle B_{0,dom}^r \left(r = 0.95a\right)\right\rangle_{t|N_s(t)<N_{th}}, \qquad \left\langle B_{0,dom}^{\theta,z} \left(r = a\right)\right\rangle_{t|N_s(t)<N_{th}}, \tag{4.17}$$

$$\left\langle B_{0,sec}^r \left(r = 0.95a\right)\right\rangle_{t|N_s(t)<N_{th}}, \qquad \left\langle B_{0,sec}^{\theta,z} \left(r = a\right)\right\rangle_{t|N_s(t)<N_{th}}, \tag{4.18}$$

$$\left\langle B_{1,dom}^r \left(r = 0.95a\right)\right\rangle_{t|N_s(t)<N_{th}}, \qquad \left\langle B_{1,dom}^{\theta,z} \left(r = a\right)\right\rangle_{t|N_s(t)<N_{th}}, \tag{4.19}$$

$$\left\langle B_{1,sec}^r \left(r = 0.95a\right)\right\rangle_{t|N_s(t)<N_{th}}, \qquad \left\langle B_{1,sec}^{\theta,z} \left(r = a\right)\right\rangle_{t|N_s(t)<N_{th}}. \tag{4.20}$$

  It is necessary to point out some details about calculations in formulas (4.17) - (4.20). The edge radial magnetic fields are evaluated at the radial position $r = 0.95a$ because, since zero resistivity boundary condition is assumed, the evaluation of the radial field at $r = a$ simply amounts to 0 and so its calculation is not of particular physical interest. To calculate the secondary modes contributions the following formula is applied (here written in the case of $m = 1$ modes):

$$B_{1,sec}^i = \sqrt{\sum_{\substack{j=-20,\\ j\neq n_{dom}}}^{-7} \left(B_{1,j}^i\right)^2}, \tag{4.21}$$

  where i can be r, θ, z. The dominant mode is calculated at each time step and, in principle, it can be different from time to time.

- The time averaged magnetic energy related to the dominant and secondary modes both for the case $m = 0$ and $m = 1$:

$$\left\langle W_{0,dom}^M \right\rangle_{t|N_s(t)<N_{th}}, \qquad \left\langle W_{0,sec}^M \right\rangle_{t|N_s(t)<N_{th}}, \tag{4.22}$$

$$\left\langle W_{1,dom}^M \right\rangle_{t|N_s(t)<N_{th}}, \qquad \left\langle W_{1,sec}^M \right\rangle_{t|N_s(t)<N_{th}}. \tag{4.23}$$

  In this case the energy of the secondary modes is found, simply summing all the secondary modes:

$$W^M_{1,sec} = \sum_{\substack{j=-20,\\ j\neq n_{dom}}}^{-7} W^M_{1,j}, \tag{4.24}$$

because, in the case of energy, all the contributions are positive.

The calculation of all the previous quantities is repeated for all the simulations in the database and are all dimensionless.

4.5 Simulations results: the role of the Hartmann number

4.5.1 Magnetic energy

In Fig. 4.6, the values of the time average magnetic energy values, calculated according to Eq. (4.22) - (4.24), are plot as function of the Hartmann number, for simulations selected from the database.
The subplots a) and b) concern the the magnetic energy of $m = 1$ modes. At low values of the Hartmann number, $H \sim 10^2 - 10^3$ and in absence off magnetic perturbation (MP off), Fig. 4.6, visco-resistive simulations display the rise of a single helicity phase, characterized by the emergence of modes with relatively high toroidal wave numbers (e. g. $m = 1$, $n = -11$) as dominant mode, in absence of magnetic perturbation. For higher values of the Hartmann parameter ($H \geqslant 2000$), the magnetic energy of $m = 1$ modes decreases for the dominant and the secondary modes. The plasma is in multiple helicity phase.

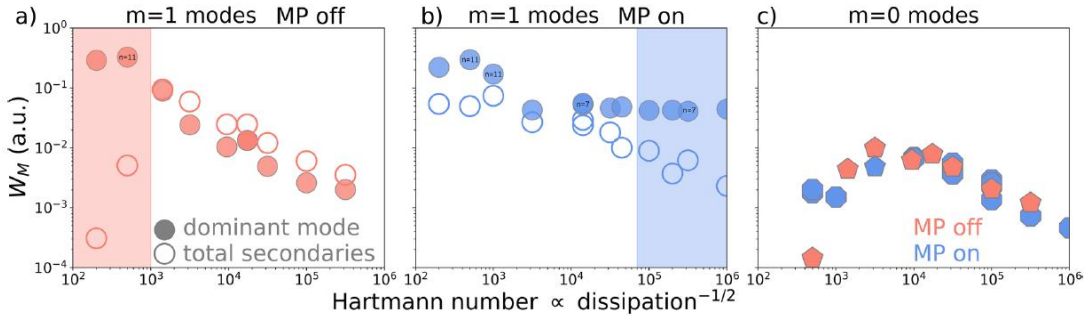

Figure 4.6: Plot of the magnetic energy W_M as function of the Hartmann number H, on the SpeCyl database simulation. The magnetic energy associated to the $m = 1$ modes is shown in plot a) for the case in absence of magnetic perturbation and in plot b) for the case with magnetic perturbation active. In plot c) the $m = 0$ modes are shown, for both (MP on and off) cases. Figure from Ref. Veranda et al. [2019].

In Fig. 4.6 b), the effect of the magnetic perturbations is highlighted. At low H, the edge boundary conditions (on the modes $m = 1$, $-9 \leqslant n \leqslant -5$) sustain the secondary modes. However, the most interesting range for this case is $H \sim 10^5 - 10^6$, in which the magnetic perturbations trigger the dominance of the $m = 1$, $n = -7$ mode, imposing the so called quasi-single helicity.
In Fig. 4.6 c), the focus is set on the magnetic energy of the $m = 0$ modes, distinguishing the cases with and without the magnetic perturbations. At low Hartmann ($H \sim 10^2 - 10^3$), the magnetic energy is low (corresponding to an ordered plasma phase), only in absence of magnetic perturbations. At intermediate Hartmann range $H \sim 10^3 - 10^4$ the $m = 0$ magnetic energy is high, corresponding to a disordered multiple helicity plasma phase, while at high Hartmann, $H \geqslant 10^5$, the magnetic energy is lowered again in correspondence of the quasi-single helicity phase, triggered by the magnetic perturbations.

4.5.2 Edge magnetic field

In this Section, the values of the magnetic field modes eigenvalues as function of the Hartamnn number are analyzed. In particular, we focus on the edge toroidal component, because this is the most suitable to experimental data the comparison, developed in Chp. 8. Moreover, in Chp. 9, the role played by edge radial $m = 0$ modes in triggering the density limit in RFP plasmas will be discussed. In Fig. 4.6, the secondary modes, calculated according to Eq. (4.18), (4.20) and (4.21) are plot as function of the Hartmann number, limiting, for reason of simplicity, the data shown to the simulations without magnetic perturbations or with a magnetic perturbation on the $m = 1$, $n = -7$ mode.

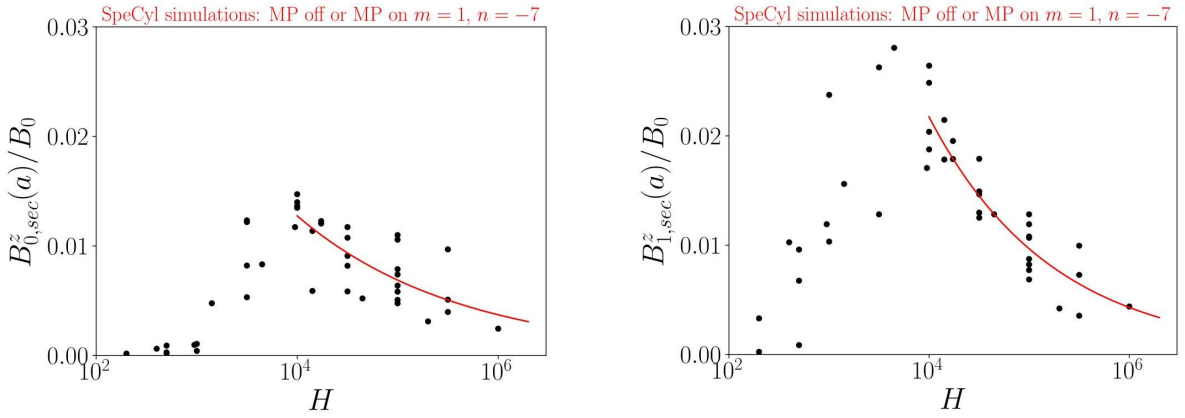

Figure 4.7: Edge toroidal magnetic field modes amplitude as function of the Hartmann number H, for the $m = 0$ modes (a) and the $m = 1$ modes (b). The simulations considered are limited to those with no magnetic perturbation, or magnetic perturbation with helical twist $m = 1$, $n = -7$, with variable intensity of the magnetic perturbation. The data points considered for the fit are in the region $H \geqslant 10^4$.

The results shown are in agreement with the trends highlighted analyzing the magnetic energy. In particular, two trends are clearly distinguished when analyzing the magnetic field eigen-modes as function of the Hartmann: an increasing trend for $H < 10^4$ and a decreasing one, for $H \geqslant 10^4$. This corresponds to the existence of three different phases: a single helicity regime, for $H < 2000$, characterized by low secondary eigen-modes, a multiple helicity regime at intermediate Hartmann values, characterized by high values of the secondary eigen-modes and a quasi-single helicity regime, for $H > 10^5$, with low secondary eigen-modes.
As shown in Sec. 2.6, in RFP plasmas a spontaneous transition to helical self-organized states spontaneously takes place, mainly triggered (in the experiment) by increasing values of the plasma current. Such a transition (from a multiple helicity regime to a quasi-single helicity regime), is observed in Fig. 4.7, for the high Hartmann interval $H \sim 10^4 - 10^6$. As consequence of it, the high Hartmann regime turns out to be the most relevant, according to an experimental point of view. In this domain, the decreasing trend of the secondary eigen-modes is fitted with a power law, according to the ordinary least squares (OLS) method:

$$B^z_{0,sec}(a)/B_0 = (0.15 \pm 0.07) \cdot H^{-0.27 \pm 0.05} \quad r = -0.76, \tag{4.25}$$

$$B^z_{1,sec}(a)/B_0 = (0.55 \pm 0.19) \cdot H^{-0.35 \pm 0.03} \quad r = -0.90. \tag{4.26}$$

These results by numerical simulations of the visco-resistive model, are going to be the basis of the comparison with the experimental data, in Chp. 8, 9.

4.6 Summary and final remarks

In this Chapter, the numerical codes used for the solution of 3D non-linear visco-resistive MHD models have been described in details. These numerical tools are the SpeCyl and the PIXIE3D codes, which have been used in the development of this work. Two main points deserve to be highlighted at this point:

- Numerical simulations of the visco-resistive model describe the rise of helically self-organized states in RFP plasmas, in agreement with the experimental observations. Two fundamental inputs are necessary for this result: the dimensionless transport parameters (resistivity and viscosity) and the edge seed magnetic perturbations.
- Analyzing a wide database of SpeCyl simulations, varying the visco-resistive dissipation parameters and the boundary conditions, a quantitative law to describe the relation between secondary modes and the Hartmann number (visco-resistive dissipation) is found, see Eq. (4.25) - (4.26) . This will be matter of the comparison to the experimental data in Chp. 8, 9.

Chapter 5

Transport coefficient studies in SpeCyl: radial profile and time evolution

This Chapter deals with the study of transport dimensionless coefficients in SpeCyl numerical simulations in RFP configuration plasmas with the aim of advancing the MHD modelling tool towards a self-consistent evolution of transport coefficients. In particular, the effect of the on-axis values of resistivity and viscosity is tested in helical geometry simulations, while in 3D simulations the focus is set on the resistivity and the viscosity profiles, since the effect of the on-axis value is already known by previous studies (see Chp. 4). As final step, preliminary time-dependent evolution of viscosity and resistivity is tested.
In Sec. 5.1, a database of 2D SpeCyl simulations is analyzed to study the effect of resistivity and viscosity in determining the mode growth rate. The results are then compared to the prediction of growth rate scaling in magnetic reconnection theories which include plasma viscosity effects.
Sec. 5.2 concerns the effect of the resistivity. In particular, we test flatter resistivity profiles with respect to the one inspired by the Spitzer formula application on typical experimental temperature profiles.
Sec. 5.3 deals with the study of viscosity profiles which resemble the radial dependence of the perpendicular Braginskii viscosity. Three different cases are considered: the effect on the growth rate of 2D simulations, the effect on the dynamics of 3D simulations in QSH regime (simulations with applied magnetic perturbation) and in MH regime (simulations with ideal boundary conditions). Appreciable effects are observed in the latter case.
In Sec. 5.4 we introduce a time dependence of the visco-resistive dissipation in two different cases: a time exponential decrease of the Hartmann number (which allows to model the progressive growth of secondary modes as the visco-resistive dissipation is increased) and a preliminary self-consistent time dependence which links the Hartmann number to the plasma helical order (which allows to reproduce a decrease of the dissipation during the ordered phase and an increase of the dissipation during the crashes).
Summary and final remarks follow in Sec. 5.5.

5.1 The effect of resistivity and viscosity coefficients in 2D numerical simulations

This Section is devoted to study the effects of dimensionless resistivity and viscosity coefficients in 2D SpeCyl numerical simulations, where we only consider twenty harmonics of a specific MHD mode. In these simulations, the equilibrium perturbation gives rise to the exponential growth of the resonant mode (characterized by a specific growth rate γ), until a saturation value is reached. After that, the MHD mode behaviour becomes stationary.
To perform this study, a database of 25 simulations (Fig. 5.1 (a)) has been produced perturbing the tearing mode $m = 1$, $n = -12$ and the harmonics $m = 2$, $n = -24$, ..., $m = 20$, $n = -240$, spanning the ranges $10^4 \leqslant S \leqslant 10^6$ and $10^2 \leqslant M \leqslant 10^4$ for the Lundquist and viscous Lundquist numbers, which we recall to be defined as $S = 1/\eta_0$ and $M = 1/\nu_0$, with η_0 and ν_0 dimensionless core resistivity and viscosity. The profiles considered for the latter are constant in time: $\eta = \eta_0 \left(1 + 20r^{10}\right)$ and $\nu = \nu_0$.
Computing for all the simulations in Fig. 5.1 (a), the magnetic energy of the mode, which is defined as:

$$W_M^{m,n}(t) = \int_V \left(\mathbf{B}^{m,n}(\mathbf{r}, t)\right)^2 dV, \tag{5.1}$$

for a mode with poloidal and toroidal wave numbers m and n, we observe that the main effect of the fluid dimensionless numbers affects the mode growth rate of W_M. In particular, in Fig. 5.1 (b) the growth rate dependence of the magnetic energy of the first harmonic $W_M^{1,-12}$ on S and M is analyzed in the simulation database.

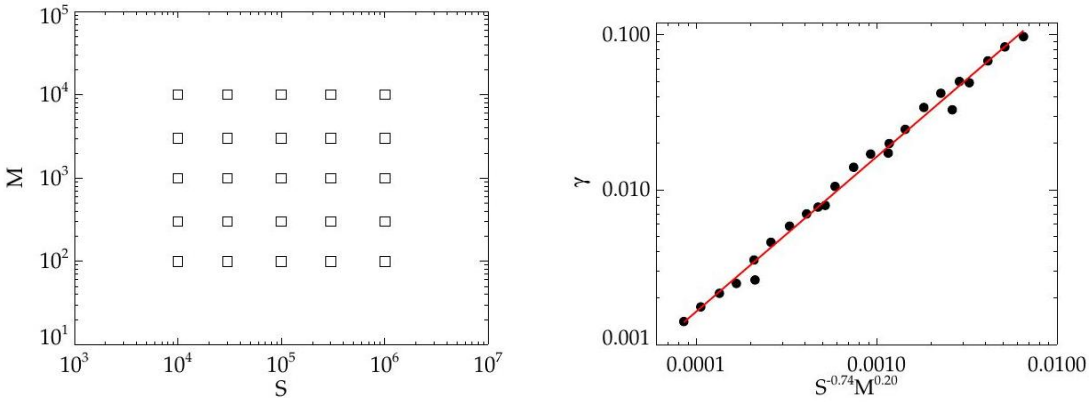

Figure 5.1: Analysis of 2D SpeCyl simulations with $m = 1$, $n = -12$. Input Lundquist and viscous Lundquist number in the simulations database (a), where each marker represents a simulation and scaling law for the growth rate of the magnetic energy of the mode $m = 1$, $n = -12$ as function of fluid dimensionless parameters, (b).

The dependence found has the following expression:

$$\gamma = (16.3 \pm 0.9) \cdot S^{-0.74 \pm 0.01} M^{0.20 \pm 0.01}, \qquad r = 0.996. \tag{5.2}$$

The latter shows that despite the major role played by the resistivity in determining the growth rate (studied by the pioneering works about magnetic reconnection in astrophysics, Ref. Parker [1957]: $\gamma \propto \eta^{1/2}$ and Ref. Petschek [1964]: $\gamma \propto \eta^0$), in visco-resistive MHD there is a non-negligible influence by the plasma viscosity, which was studied in Ref. Park et al. [1984] and Ref. Porcelli [1987], proposing analytical modifications to the reconnection growth rate scaling: $\gamma \propto \eta^{3/4}\nu^{-1/4}$ and $\gamma \propto \eta^{5/6}\nu^{-1/6}$ respectively. The result of the numerical analysis presented in

Eq. (5.2) displays a good quantitative agreement with both the studies. However, a justification of the quantitative result of the scaling based on analytical calculations about magnetic reconnection is beyond the scope of this work.

5.2 Resistivity profile studies

The most frequently used resistivity profile in SpeCyl simulations is $\eta_1(r) = \eta_0 \left(1 + 20r^{10}\right)$, representing a polinomial fit of Spitzer resistivity formula (see Ref. Spitzer [1956]) applied to the electron temperature profile experimental measurements on RFX. We will discuss more deeply the validity of this choice in Sec. 8.3.
In this Section, we present a brief sensitivity study on the resistivity profile of 3D SpeCyl numerical simulations (where all the Fourier modes shown in Fig. 4.1 are considered), inspired to Ref. Sätherblom et al. [1996], where different resistivity profile were tested on the basis of RFP device EXTRAP T1 experimental measurements. A similar work is presented in Ref. Futatani et al. [2015], where the role of non uniform transport coefficients is tested in both tokamak and RFP configuration, applying identical (polynomial) profiles for resistivity and viscosity. However, in this work we are going to test separately the effect of resistivity (in this Section) and viscosity (in Sec. 5.3) profiles.
We compare two SpeCyl simulations with the following fluid dimensionless number and magnetic boundary conditions:

$$S = 10^6, \qquad M = 10^4, \qquad P = 100, \qquad H = 10^5, \qquad b_r^{1,-7}(a)/B_\theta(a) = 3.5\%,$$

which correspond to the Quasi Single Helicity plasma regime. The two simulations have both the flat viscosity profile ($\nu(r) = \nu_0$) and they only differ for the resistivity profiles imposed:

$$\eta_1(r) = \eta_0 \left(1 + 20r^{10}\right), \qquad \eta_2(r) = \eta_0 \left(1 + 20r^{30}\right),$$

illustrated in Fig. 5.2 (a). $\eta_1(r)$ and $\eta_2(r)$ are almost equal in the central region ($r/a < 0.6$) but significantly differ in the edge ($r/a > 0.8$), where the resistivity realistic profile could deviate from the Spitzer formula, e. g. because of the impurity concentration effects. Even if it does not modify the equilibrium and the qualitative behaviour of the plasma dynamics evolution (both the profiles give rise to a QSH plasma regime), the resistivity profile influences the dominant $m = 1$ $n = -7$ mode amplitude (see Fig. 5.2 (b) and the time scale of the RFP sawtooth dynamics, i.e. quasi-periodic emergence of a dominant mode in the MHD spectrum.

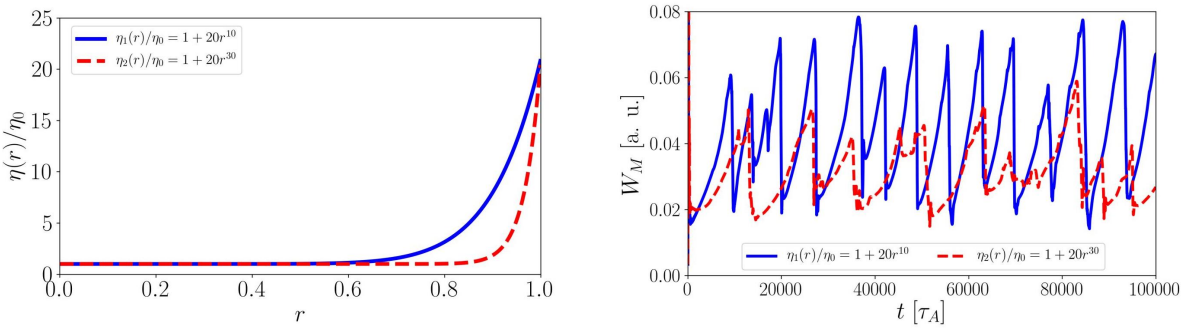

(a) (b)

Figure 5.2: Analysis of resistivity profile effects in SpeCyl simulations: resistivity profiles compared (a), time evolution of the magnetic energy of the dominant fluctuation $m = 1$, $n = -7$ (b). A moderate variation of the resistivity radial dependence can cause the variation of a factor 2 in the magnetic energy of the dominant mode.

In particular, the higher resistivity profile ($\eta_1(r)$) gives rise to a larger dominant magnetic field fluctuation by almost a factor two, in agreement with the results from Ref. Sätherblom et al. [1996]. Moreover, the sawtooth period τ_{saw}, representing the time interval between two maxima of the dominant mode, increases choosing a lower resistivity profile, qualitatively consistent with a previous study on SpeCyl simulations (see Ref. Veranda et al. [2020]), where a scaling of the τ_{saw} on resistivity and viscosity coefficients is performed and results in $\tau_{saw} \propto \eta^{-0.87}\nu^{0.11}$.

5.3 Viscosity profile studies

In this Section a sensitivity study related to the kinematic viscosity profile $\nu(r)$ is presented. A similar analysis was carried on in Ref. Futch et al. [2018], where the effects of identical resistivity and viscosity profiles with modified dissipation in the plasma region with $r/a > 0.6$ are studied, with specific focus on the $m = 0$, $n = 1$ mode and the effects on the crash dynamics.
In the following analysis only the viscosity profile is modified, keeping fixed the resistivity and focusing the analysis on the time-average of velocity and magnetic field spectral components. The case of viscosity profile resembling the functional dependence indicated by Braginskii for the perpendicular viscosity $\nu_\perp^{Brag}$ is here considered as reference, since the RFP dynamics is determined by magnetic instabilities and fluid convection, both perpendicular to the magnetic field. Five different viscosity profiles are analyzed (see Fig. 5.3):

- the flat profile $\nu_1(r)/\nu_0 = 1$, the most frequently used in SpeCyl simulations so far,
- the resistivity-like profile $\nu_2(r)/\nu_0 = 1 + 20r^{10}$, which keeps the Prandtl number constant over the whole plasma volume,
- the polynomial Braginskii fit $\nu_3(r)/\nu_0 = 1 + 5r^3$, a monotonous trend which resemble the Braginskii profile for $r/a < 0.65$,
- a 'Braginskii-like' profile $\nu_4(r)/\nu_0 = 1 + 20r^3\cos(1.6r)$, an analytical formula which roughly reproduces the Braginskii profile.
- the flat profile $\nu_5(r)/\nu_0 \approx 2.82$, with the same volume average viscosity of $\nu_4(r)$.

Four of them ($\nu_{1,\dots,4}(r)$) have the same on-axis value of the viscosity, while $\nu_5(r)$ has the same volume average of $\nu_4(r)$ and it is used only for additional comparison in the most significant case (3D simulations in Multiple Helicity regime).

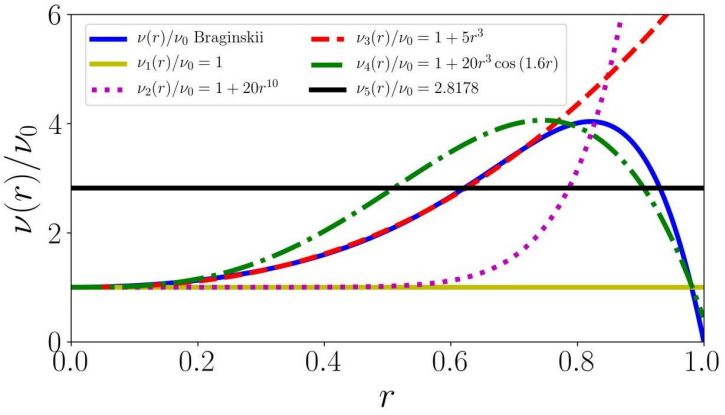

Figure 5.3: Kinematic viscosity profiles analyzed in this Section: Flat profile $\nu_1(r)$, resistivity-like profile $\nu_2(r)$, polynomial fit of Braginskii profile $\nu_3(r)$, Braginskii-like profile $\nu_4(r)$, flat profile with the same volume average value of the Braginskii-like viscosity profile $\nu_5(r)$.

5.3.1 2D simulations

As first test case we consider four 2D SpeCyl numerical simulations, with helicity $h = n/m = -12$, fixed resistivity profile $\eta(r) = \eta_0 \left(1 + 20r^{10}\right)$ and characterized by the following fluid dimensionless numbers:

$$S = 10^5, \qquad M = 10^2, \qquad P = 10^3, \qquad H = 3.16 \cdot 10^3, \tag{5.3}$$

distinct only by the viscosity profile $\nu_1(r)$, ..., $\nu_4(r)$. In Fig. 5.4, the evolution in time of the kinetic and the magnetic energy related to the first harmonic ($m = 1$, $n = -12$) is shown, comparing the viscosity profiles $\nu_1(r)$, ..., $\nu_4(r)$, during the exponential growth phase.

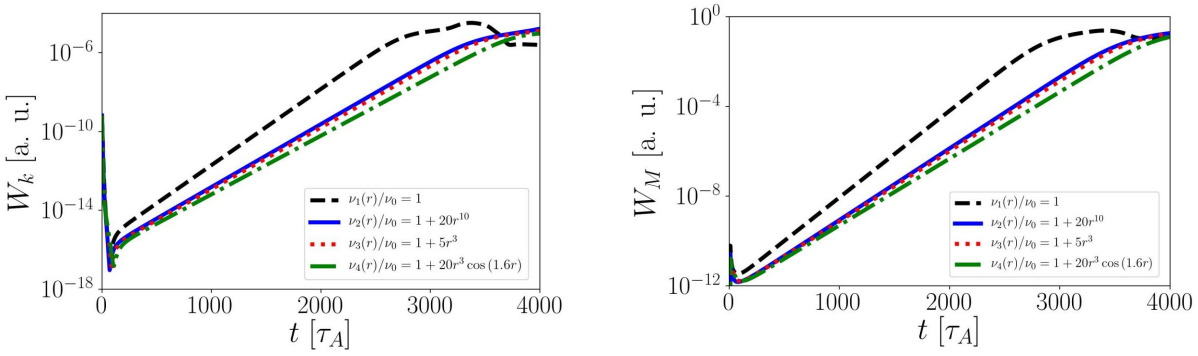

(a) (b)

Figure 5.4: Time evolution of the kinetic (a) and magnetic (b) energy related to the $m = 1$, $n = -12$ mode. The choice of different viscosity profiles changes the growth rate, which slightly decreases as the Braginskii viscosity profile is approached.

Although the viscosity profile has no significant effects on the mode saturation value, a slowdown in the growth of the mode is observed as we consider higher profiles for both the kinetic and the magnetic energy. In particular, for the latter, the growth rate decreases from the value of $\gamma\tau_A = 8.90 \cdot 10^{-3}$ for $\nu_1(r)$ to the value $\gamma\tau_A = 6.85 \cdot 10^{-3}$ for $\nu_4(r)$. This result points out a damping role of the viscosity profiles which are higher at the radial position correspondent to the resonant radius of the instability with the helical twist imposed in the 2D simulation.

5.3.2 3D simulations: Quasi Single Helicity regime

In 3D numerical simulations the viscosity profile modification results in very different effects depending on the presence/absence of the magnetic perturbation. In this Section, we show that the effect of an applied magnetic perturbation is largely dominant and that the helical twist imposed to the plasma column by the latter is not jeopardized by the viscosity profile.
We study a set of four numerical simulations with the following fluid dimensionless numbers and boundary conditions:

$$S = 10^6, \qquad M = 10^4, \qquad P = 10^2, \qquad H = 10^5, \qquad b_r^{1,-7}(a)/B_\theta(a) = 3.5\%, \tag{5.4}$$

distinguished only by the viscosity profile: $\nu_1(r)$, ..., $\nu_4(r)$.
In Fig. 5.5, the time average (during the QSH phase) value of the magnetic energy is compared for the four viscosity profiles, distinguishing the contributions of the dominant mode ($m = 1$, $n = -7$), the secondary $m = 1$ modes and the $m = 0$ modes. Despite a slight growth of the secondary $m = 1$ and $m = 0$ modes, the value of the $m = 1$ $n = -7$ mode is almost constant and remains considerably larger for all the profiles considered, conserving the helical order imposed by the boundary conditions.

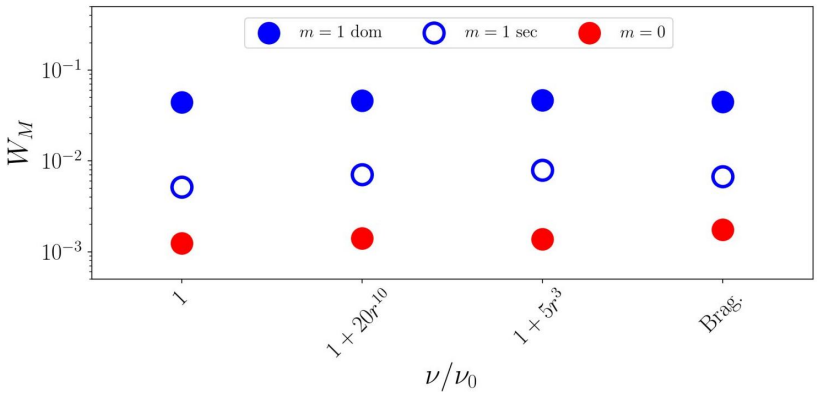

Figure 5.5: Magnetic energy of the $m = 1$ dominant mode, $m = 1$ secondary modes, $m = 0$ modes, testing the effect of the viscosity profiles $\nu_1(r)$, ..., $\nu_4(r)$: no significant modifications to helical self-organization are observed in the QSH regime.

5.3.3 3D simulations Multiple Helicity regime

In this study, we compare SpeCyl simulations with either flat ($\nu(r) = \nu_0$) (the most frequent setting in recent simulations studies, see Ref. Bonfiglio et al. [2013] and Ref. Veranda et al. [2017]) or Braginskii-like ($\nu/\nu_0 = 1 + 20r^3 \cos(1.6r)$) viscosity profiles respectively: the latter is larger by an average factor 2.8, and up to 4 in the edge region, Fig. 5.6 (a).
In the two simulations we set: $\eta_0 = 10^{-6}$, $\nu_0 = 10^{-4}$, ideal magnetic field boundary conditions $b_r(a) = 0$ and the same resistivity profile: $\eta(r) = \eta_0 \left(1 + 20r^{10}\right)$. The different viscosity profile setting does not significantly modify the axis-symmetric components of the magnetic field, Fig. 5.6 (b), (c).

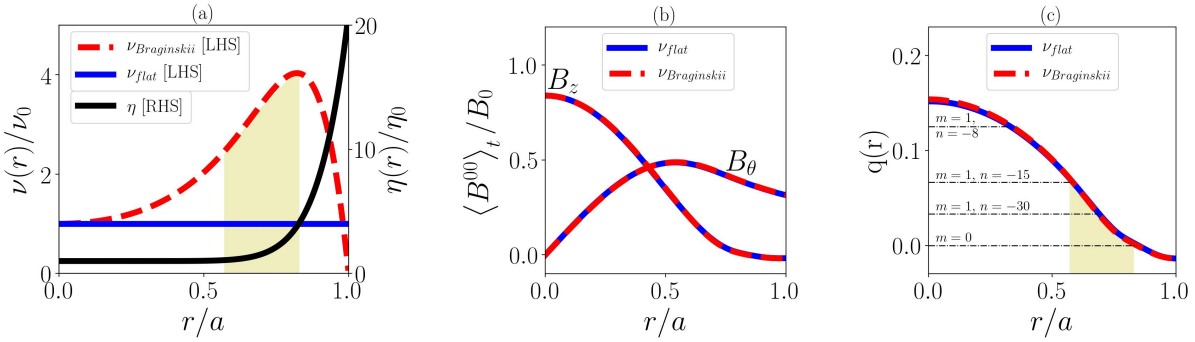

Figure 5.6: SpeCyl simulations settings for resistivity and viscosity (a), time average axisymmetric fields (b), safety factor (c) comparison for the flat and perpendicular Braginskii viscosity profile. The resonance of $m = 0$ and $m = 1$ secondary modes corresponds to the highlighted region where the Braginskii viscosity profile is larger than the flat one.

Comparing the time dependence of the kinetic $W_k(t)$ and the magnetic energy $W_M(t)$ of the $m = 1$ dominant and secondary modes shows that the basic RFP sawtoothing dynamics, is unchanged by the viscosity profiles, Fig. 5.7 (a) - (d). However, the time-average energy spectrum ratio (Fig. 5.8) highlights a moderate damp of the $m = 1$ and $m = 0$ velocity spectral components with respect to the simulations with a radially constant viscosity profile. In particular, the damp is greater for those components resonating in the spatial regions where the viscosity profile is higher. Furthermore, an increased MHD activity magnetic activity of the $m = 1$ spectral components is confirmed by the v_z and b_z eigen-functions radial profile, Fig. 5.7 (e) - (h). This is consistent with a simple picture of velocity and magnetic field interplay: the plasma flow counteracts the growth of magnetic perturbations and vice-versa Fitzpatrick [1998].

The case of the $m = 0$ modes magnetic energy is less clear (Fig. 5.8 (b)): although the majority of the $m = 0$ modes displays an increase of the magnetic energy, it is not possible to identify a precise trend. In this case, the flow 'reducing action' on the magnetic instabilities is less effective because at the reversal (the resonance region of $m = 0$ modes) the flow itself is small, being evaluated near the edge, where the no-slip boundary condition is assumed in this simulation ($v_z^{00}(a) = 0$). In addition, the modes non-linear interaction may possibly contribute to the $m = 0$ modes reduced enhancement.

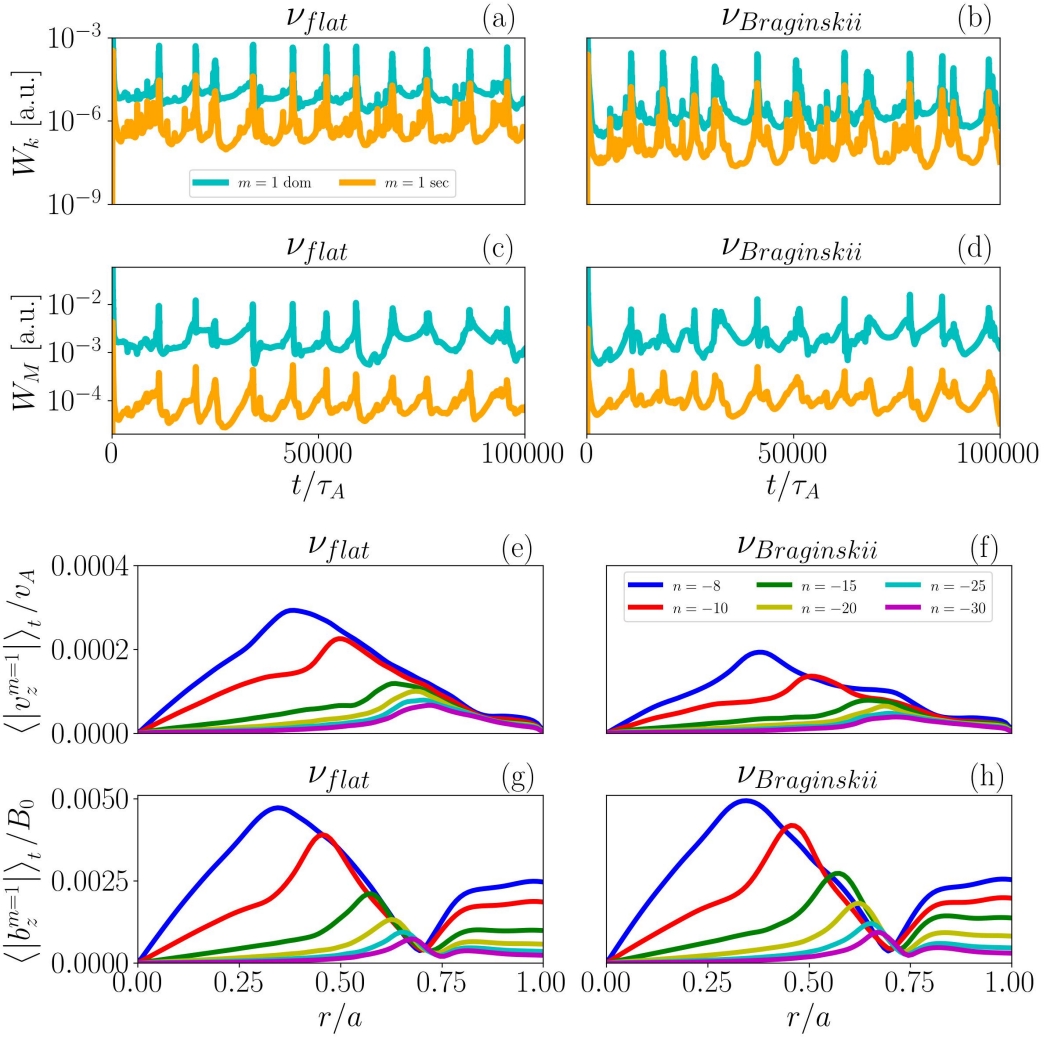

Figure 5.7: Viscosity profiles (ν_{flat} and $\nu_{Braginskii}$) effect comparison in SpeCyl simulations. The introduction of the Braginskii viscosity profile produces: a damp of $m = 1$ dominant and secondary modes kinetic energy W_k (a, b) and of $m = 1$ axial velocity eigen-functions $v_z^{m=1}$ (e, f) and a slight enhancement of magnetic energy W_M (c, d) and axial component magnetic field $v_z^{m=1}$ (g, h), more evident for $n \leqslant -15$ modes.

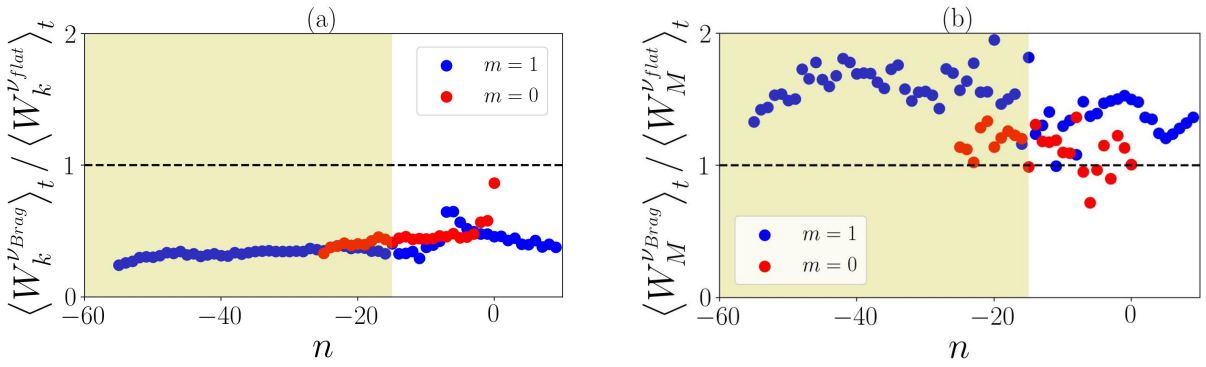

Figure 5.8: The time-average energy ratio between the Braginskii and uniform viscosity profile for each $m = 0$ (•) and $m = 1$ (•) spectral component shows: a damp of the kinetic energy, for both the $m = 1$ and the $m = 0$ modes (a) and a more noticeable enhancement of the magnetic energy for the $m = 1$, $n \leqslant -15$ secondary modes (blue markers highlighted in in the figure) (b). No definite trend is shown for the $m = 0$ modes, although the majority of them shows a magnetic energy enhancement.

5.4 Time dependent visco-resistive dissipation

This Section concerns the introduction of time-dependent visco-resistive dissipation coefficients in SpeCyl simulations. Although being a preliminary study, it represents an important step towards the self-consistent evolution of the transport coefficients, required in order to achieve a more realistic modelling of toroidal pinches.

5.4.1 Exponential time dependence: three regime continuous transition

The first study consists of varying in time the Hartmann number, according to the Eq. (5.5), illustrated in Fig. 5.9, in a 3D simulation with $b_r^{1,-7}(a)/B_\theta(a) = 3.5\%$ as initial boundary condition.

$$H(t) = \begin{cases} \sqrt{2} \cdot 10^5 = H_0 & t \leqslant 53000\tau_A \\ H_0 \cdot 10^{-2 \cdot 10^{-5}(t/\tau_A - 53000)} & t > 53000\tau_A. \end{cases} \tag{5.5}$$

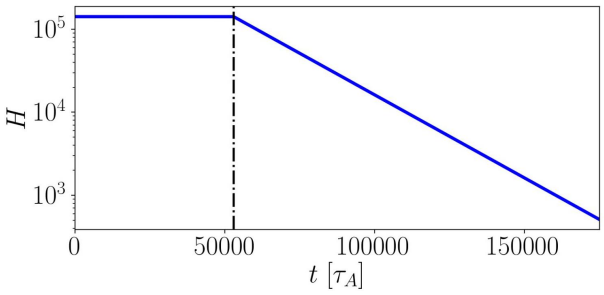

Figure 5.9: Hartmann number time dependence set as input: Constant during the first interval, the Hartmann number is then exponentially decreased according to Eq. (5.5).

The ratio between resistivity and viscosity is kept constant $P = 50$, as the ratio $E_0/\eta_0 = 4.2$ in order to guarantee the conservation of the RFP axisymmetric equilibrium during the simulation (see Ref. Delzanno et al. [2008]), properly modifying at each time iteration the value of the on-axis toroidal electric field E_0. The time dependence in Eq. (5.5) allows to model the three

regimes (Quasi Single Helicity, Multiple Helicity and Single Helicity) and the transition between them in a single simulation. Although not inspired by a specific experimental condition, the time dependence considered is of interest for the RFP modelling because, as it will be shown in Chp. 9, the decrease of the Hartmann number is linked to the RFP density limit phenomenology by means of the $m = 0$ modes growth, which is modelled in this simulation.
In Fig. 5.10, the evolution of the magnetic energy related to the $m = 1$ (a) and $m = 0$ (b) contributions is shown and the three helical regimes can be identified:

- For $t \leqslant 53000\tau_A$, the Hartmann number is constant ($H = H_0 = \sqrt{2} \cdot 10^5$) and because of the MP imposed, the standard QSH regime is displayed with the $m = 1$, $n = -7$ mode as dominant and low $m = 0$ modes. The RFP sawtooth oscillation is recovered, with constant period.
- During the interval $53000\tau_A < t \lesssim 140000\tau_A$, the Hartmann number undergoes a reduction of about two orders of magnitude. As consequence of it the $m = 0$ and the $m = 1$ secondary modes grow, while the RFP sawtooth activity becomes faster, being the τ_{saw} reduction qualitatively in agreement with Ref. Veranda et al. [2020]. For $t \geqslant 100000\tau_A$ the plasma can be considered in MH regime and the magnetic perturbations are softly switched off.
- For $t \gtrsim 140000\tau_A$, the SH regime is recovered, due to the low value of the Hartmann number achieved, consisting of a helical self-organized state with dominant mode $m = 1$, $n = -9$. All the other Fourier modes of the magnetic field are significantly smaller.

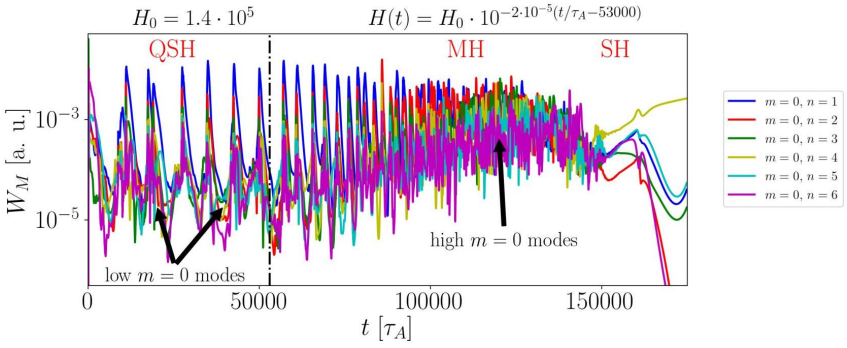

(a)

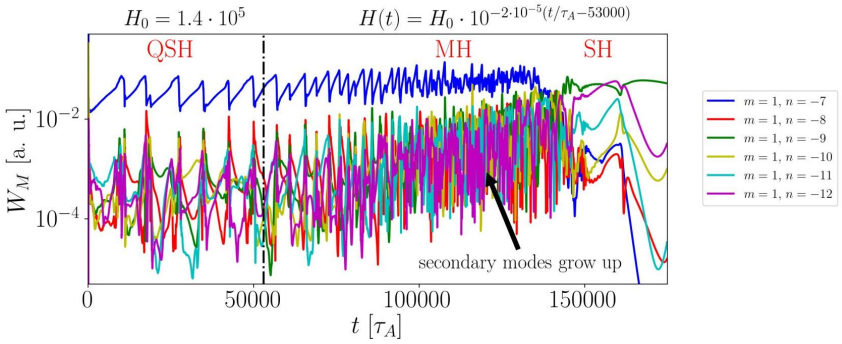

(b)

Figure 5.10: Magnetic energy time evolution of $m = 0$ (a) and $m = 1$ (b) modes: after the time dependence of Hartmann is switched on ($t/\tau_A > 53000$), the $m = 0$ and secondary $m = 1$ modes grow during the multiple helicity phase.

In conclusion, this simulation allows to study (in the experimentally relevant regime, $t \lesssim 140000\tau_A$) the QSH-MH transition and to show the progressive decrease of the helical order order as the Hartmann number is decreased.

5.4.2 Experimental-like time dependence: RFP sawtooth slow down

We finally evaluate the impact of a more realistic time dependent visco-resistive dissipation with uniform viscosity profile and resistivity profile $\eta = \eta_0 \left(1 + 20r^{10}\right)$. In particular, we present a 3D simulation with applied magnetic perturbation, fixed resistivity over viscosity ratio (Prandtl number), dissipation coefficients evolved according to the following relation:

$$\eta_0(t) = 1.75 \cdot 10^{-7} W_M(t)^{-1/2}, \qquad P = \nu_0/\eta_0 = 100, \qquad b_r^{1,-7}(a)/B_\theta(a) = 3.5\%. \tag{5.6}$$

This relation is motivated qualitatively by considering that high confinement and temperature (large magnetic energy of the dominant mode $W_M^{1,-7}$ in QSH) correspond to a low visco-resistive dissipation and vice-versa, according to the classical theory evaluation of transport coefficients, see App. B.1. In practice, considering a reference QSH shot of RFX-mod, like # 24063, shown in Fig. 2.11 a variation of 1.6 in T and 1.1 in n during QSH cycles in RFX-mod gives rise to a dissipation variation excursion of ~ 2.5, which is used here. This results in a preliminary attempt to get closer to a self-consistent evolution of the transport coefficients, whose on-axis value is updated after each time iteration, keeping the profile constant.
As shown in Fig. 5.11, the introduction of such dependence results in a time oscillation of the dissipation coefficients which are decreased on average. As consequence of it, a general slowdown of the RFP sawtooth activity is observed in the time evolution of the magnetic energy related to $m = 1$ dominant and secondary modes. In fact, the typical oscillation period τ_{saw} increases by 15%, from $7200\tau_A$ to $8200\tau_A$. This is ion qualitative agreement with the scaling s from Ref. Veranda et al. [2020].

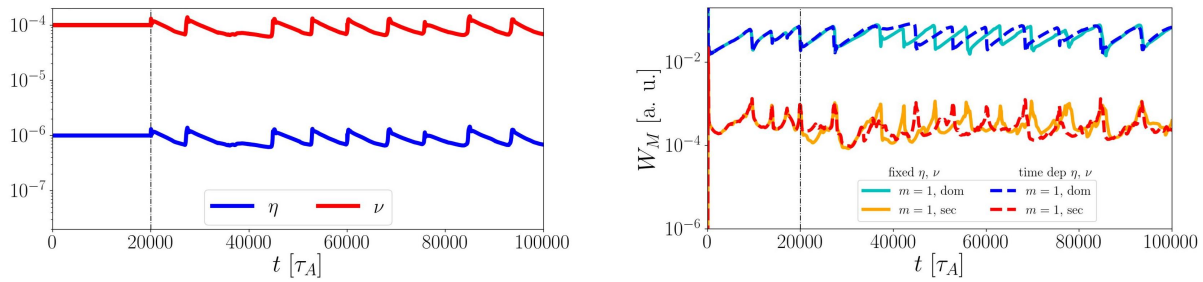

(a) (b)

Figure 5.11: Experimental-like time dependence of resistivity and viscosity (a). Magnetic energy of the dominant and secondary modes comparison with between constant and experimental-like time dependence of the dissipation. The average decrease of the dissipation causes a slow down of the sawtooth dynamics.

5.5 Summary and final remarks

In this Chapter, a sensitivity study about the effects of resistivity and viscosity profiles and time-dependence has been performed for 3D SpeCyl numerical simulations in RFP configuration. In addition, a smaller 2D study has been presented showing the role of the plasma viscosity in determining the mode growth rate.
The results of the study can be summarized in three points:

- Flatten resistivity profiles cause a decrease of the dominant mode and a slowdown of the RFP sawtooth activity.

- Braginskii-like viscosity profiles show the greatest effect in the Multiple Helicity regime, damping the velocity modes resonating where the viscosity profile is higher and allowing for a slight enhancement of the magnetic field corresponding modes.

- The tests of visco-resistive dissipation time dependence has allowed to model the progressive loss of the helical order as the visco-resistive dissipation is increased (exponential decrease of the Hartmann number) and to model a periodic oscillation of resistivity and viscosity in the core plasma, linking the dissipation coefficients to the helical order.
  The next step, in this research line, would aim at the introduction of a self-consistent evolution for the transport coefficients, allowing the resistivity and the viscosity to depend on all the spatial coordinates, to test whether this modification could have a positive feedback effect on the RFP helical self-organization.

Chapter 6

Tokamak sawtooth numerical simulations

In this Chapter, a preliminary study of the tokamak sawtooth oscillation is presented. Based on PIXIE3D simulations with helical symmetry ($h = -m/n = 1$), this study aims to be a test of the effect of transport dimensionless parameters on the tokamak sawtooth dynamics, not considering self-consistently evolved transport dimensionless parameters. As consequence of it, future improvements are predicted, discussed in the final part of the Chapter (Sec. 6.6) with the goal of introducing a self consistent resistivity evolution, by means of the Spitzer formula and of accounting for the fully 3D spectrum of the magnetic field. As long term development, also the comparison with the experimental data should be considered. in particular with circular tokamak discharges. as for example in RFX-mod.
In Sec. 6.1, a brief review of the sawtooth studies is provided, with specific focus on the pioneering studies which described the phenomenon and on the evolution of the numerical modelling.
In Sec. 6.2, we briefly describe the setup of PIXIE3D simulations presented in this Chapter.
In Sec. 6.3, we present basic results regarding the plasma initial axisymmetric equilibrium, analyzing the effects of a non negligible plasma pressure and of a Spitzer-like dependence of the resistivity.
Sec. 6.4 mainly describes the effects of the introduction in a PIXIE3D simulation of a non negligible pressure.
In Sec. 6.5, we describe the basic modelling of the sawtooth, achieved with the simulations, with specific reference to non-linear interaction between the core temperature and the $m = 1$, $n = -1$ magnetic instability. Finally, the role of transport coefficients (visco-resistive dissipation and heat conductivity) is analyzed in a database of simulations.
Summary and final remarks follow in Sec. 6.6.

6.1 Tokamak sawtooth oscillation: an historical introduction

Sawtooth oscillations represent an important phenomenon of tokamak core plasmas, observed for the first time almost fifty years ago, as described in Ref. von Goeler et al. [1974], but which still lacks a fully satisfying physical explanation. The main observed effect is the periodic growth (ramp up), followed by a sudden fall (crash) of the central plasma temperature; the opposite phenomenon is observed if the edge plasma temperature is taken into account, while a similar pattern is followed by the plasma density. The oscillation is linked to the MHD activity of the internal, marginally resonant $m = 1$, $n = -1$ resistive kink mode. This mechanism, which is also known as *magnetic flux pumping*, is responsible for the toroidal current density redistribution and for the consequent flattening of the safety factor profile in the central region, observed after the crash of the marginally resonant mode. Although non disruptive, the periodic loss of energy and particles from the plasma center, potentially limits the performance of future fusion devices, and future tokamak 'hybrid' scenarios aim to avoid it, achieving $q(0) > 1$, with low central safety factor shear.
To describe the tokamak sawtooth phenomenon, two main theories have been developed during the decades: the Kadomtsev model, presented in Ref. Kadomtsev [1975] and the Wesson model, presented in Ref. Wesson [1986]. The main difference between the two models involve the magnetic reconnection. In the Kadomtsev model, the temperature drop is caused by a fast magnetic reconnection event, while in the Wesson model, the $m = 1$, $n = -1$ mode is considered as a quasi-interchange instability, where the reconnection is not involved.
While being deeply studied from the experimental point of view, the focus of this Chapter is mainly on the numerical simulations modelling of the sawtooth instability. For this review we briefly mention the main results of previous numerical modelling works.
The first example of sawtooth modelling is found in Ref. Sykes and Wesson [1976], where a tokamak sawtooth oscillation with three modulations of decreasing amplitude is reproduced in a non-linear magnetohydrodynamics simulation. In successive studies, several 2D simulations have been performed, pointing out the role of plasma parameters. In Ref. Denton et al. [1986], the thermal conduction profile is found to influence the sawtooth shape, while in Ref. Denton et al. [1987], the thermal conduction and the β parameter are used to described the rise of two qualitatively different regimes of simulations: one characterized by the sawtooth and one by an $m = 1$ convective cell which damps the sawtooth. In these works, where a Spitzer-like resistivity coefficient is considered, the introduction of an anisotropic heat conduction is proved to be important in order to model the periodic repetition of the sawtooth oscillation.
Further developments have been achieved in Ref. Halpern et al. [2010] and Ref. Halpern et al. [2011], where three different regimes are identified and classified using the Lundquist number and the $\alpha := (\omega_{ci}\tau_A)^{-1}$ parameter: the non oscillating regime, a kink regime with resistive crashes and a sawtooth regime. A potential limit in this approach (and which affect also the work presented in this study) is represented by the computational power required in order to simulate realistic values of the Lundquist number S, amounting to $S \sim 10^8$ for typical tokamak discharge parameters. This limit is overcome in Ref. Günter et al. [2014] and in Ref. Yu et al. [2015], where magnetohydrodynamics simulations with realistic values of S are made, including two fluids effects which allow to reproduce some important experimental observations, like the fast sawtooth reconnection.
In Ref. Krebs et al. [2017] and Ref. Jardin et al. [2020]), a new model for the tokamak sawtooth has been developed supported by 3D MHD simulations, as a further development of the Wesson model. In this upgrade, the $m = 1$, $n = -1$ mode saturates and generates a dynamo electric field, which maintains the safety factor above one in the core. The origin of core temperature crash should be attribute to the higher order harmonics of the $m = 1$, $n = -1$ interchange mode, which increases the plasma core stochasticity and the consequent temperature drop.
For the sake of completeness, we mention that the flux pumping mechanism plays a key role

also in reversed field pinch configuration, where it is known as 'dynamo effect'. In this case, it represents a necessary contribution in the sustenance of the RFP discharge, see Ref. Bonfiglio et al. [2005], Ref. Cappello et al. [2006] and Ref. Piovesan et al. [2017], acting through the generation of a dynamo electric field and allowing the existence of a stationary configuration, with edge reversed toroidal field.

6.2 PIXIE3D simulations setup

In this Section we describe the settings of the simulation we study, to basically model the sawtooth instability with PIXIE3D, in Sec. 6.3 - 6.5.
As first step, we try to replicate the zero-pressure simulation 2D.TOK.S5, from Ref. Bonfiglio et al. [2010] (3D nonlinear verification of SpeCyl and PIXIE3D codes). In Tab. 6.1 the main settings of the simulation are represented; in particular the value $\gamma = 1$ is chosen, since a simulation without pressure is considered. In this 2D tokamak simulation the helicity $h = -1$ is considered, since we are interested in the mode $m = 1$, $n = -1$.

mesh points	Δt	t_{max}	η_0	ν_0	γ
$100 \times 64 \times 1$	2×10^{-3}	10000	10^{-5}	3×10^{-4}	1

Table 6.1: Main settings of the simulation, aimed at replicating the benchmark 2D.TOK.S5 simulation.

In addition, the Crank-Nicholson discretization scheme is chosen, and the convergence of the Newton algorithm is set according to a tolerance of 10^{-4}.
As second step, a simulation able to reproduce approximately the tokamak sawtooth activity is set up. In this case, all the settings made are kept as simple as possible, keeping anyway an enough detailed modeling in order to recover the typical sawtooth oscillation of the temperature in the plasma central region.
As in the previous case, a 2D tokamak simulation in helical geometry and with helicity $h = -1$ is considered. In Tab. 6.2, the simulation input parameters are shown: with respect to the previous one, the pressure is introduced (considering a non-zero initial β, a non-zero pressure at the wall and increasing γ up to 5/3). In this Chapter by mentioning the β parameter, we mean the on-axis value of β, if not differently specified.

mesh points	Δt	t_{max}	η_0	ν_0	$\chi_\parallel = \chi_\perp$	$p(r = a)$	γ
$128 \times 64 \times 1$	5×10^{-3}	10000	10^{-5}	3×10^{-4}	3.333×10^{-5}	10^{-5}	1.66667

Table 6.2: Main settings of the simulation aimed at a basic modeling of tokamak sawtooth oscillation.

To recover the sawtooth activity, also the heat transport is introduced by means of the thermal conduction $\chi = 3.33 \times 10^{-5}$. The anisotropy in the heat transport is avoided ($\chi_\parallel = \chi_\perp$) as well as the Spitzer resistivity dependence on temperature (η_0 is constant in time). In addition, small changes are made to the number of mesh points and the time step, without significantly affect the simulation results.

6.3 PIXIE3D simulations: 1D equilibrium

In this Section, studies of the axisymmetric equilibrium are presented, with particular reference to the effect generated by the introduction of a non zero pressure (and consequently heat transport) and of a Spitzer-like resistivity. Similar studies on the axisymmetric configuration were

also performed in Ref. Bonfiglio et al. [2013]. The detailed calculations of the pinch equilibrium for both the tokamak and the RFP configurations can be found in Ref. Delzanno et al. [2008]. Three simulations with the setup presented in Sec. 6.2 were considered:

$$S = 10^5, \qquad M = 3.33 \cdot 10^3, \qquad P = 30, \qquad H = 1.82 \cdot 10^4. \tag{6.1}$$

The first simulation has no pressure ($\beta = 0$), the second one has finite pressure and heat transport, being the heat conduction $\chi = 3.33 \cdot 10^{-5}$ (which correspond to $\beta \sim 2\%$), while the third one has, in addition, a Spitzer-like evolved resistivity according to $\eta_{Spitz} \propto T_e^{-3/2}$, instead of the fixed profile $\eta = \eta_0 \left(1 + 20 r^{10}\right)$, applied in the first two cases.
To study this simple 1D case the velocity perturbation which usually starts the simulation dynamics is switched off. The results are shown in Fig. 6.1 for the magnetic fields and in Fig. 6.2 for the temperature and the resistivity profile.

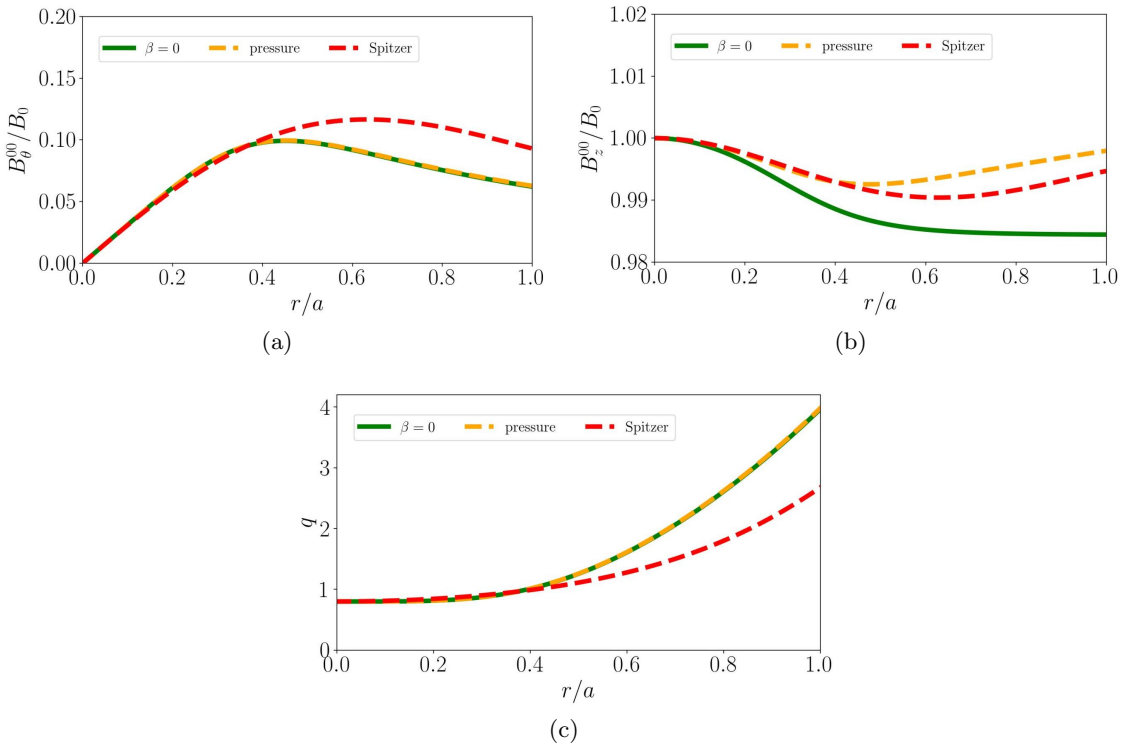

Figure 6.1: Comparison of the axisymmetric equilibrium of PIXIE3D simulations with the same visco-resistive coefficients in absence of kinetic pressure, $\beta = 0$ (solid green line), with pressure and imposed resistivity profile (yellow dashed line), with pressure and Spitzer-like resistivity (red dashed line), for: poloidal (a), toroidal (b) magnetic field components and cylindrical safety factor (c).

The introduction of a finite pressure (yellow dashed curve with respect to green one) does not have dramatic effects on the simulation equilibrium: the poloidal magnetic field is unaltered, while the toroidal field is slightly modified, without affecting the safety factor profile. Obviously the two resistivities are identical, because of the setup, while the comparison does not make sense for the temperature, being $T = 0$ in the pressure-less simulation.
The effects of a Spitzer-like resistivity (red lines with respect to the yellow lines) are more interesting: in fact, in this case, an important increase of the poloidal magnetic field and a consequent decrease of the safety factor profile take place. The temperature profile is increased by almost the 20% and the resistivity profile is largely modified in the external region, showing that the introduction of a Spitzer-like resistivity strongly modifies the axisymmetric equilibrium.

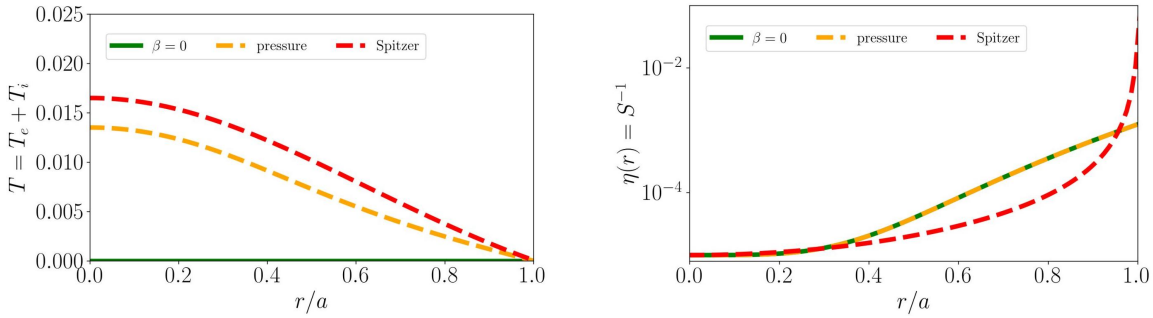

Figure 6.2: Comparison of the axisymmetric equilibrium of PIXIE3D simulations with the same visco-resistive coefficients in absence of kinetic pressure, $\beta = 0$, with pressure and imposed resistivity profile, with pressure and Spitzer-like resistivity, for: equilibrium temperature (a), dimensionless resistivity (b).

6.4 PIXIE3D tokamak simulations with helical $m = 1$, $n = -1$ geometry

In this Section, we comment about the time evolution of the axisymmetric configurations described in Sec. 6.3. This result was achieved only for simulations with a fixed resistivity profile and isotropic heat conductivity, while in the case of Spitzer-like resistivity, the algorithm convergence was not achieved. The reasons for the lack of convergence deserve additional studies and will be considered for future works, since the introduction of a self-consistently evolved resistivity represent an important step towards a more realistic modeling of the sawtooth instability. After observing the effect of a finite pressure introduction on the axisymmetric field, the focus is now set on the time evolution. In Fig. 6.3, the time evolution of the magnetic W_M of the main harmonics of the mode $m = 1$, $n = -1$ is shown.

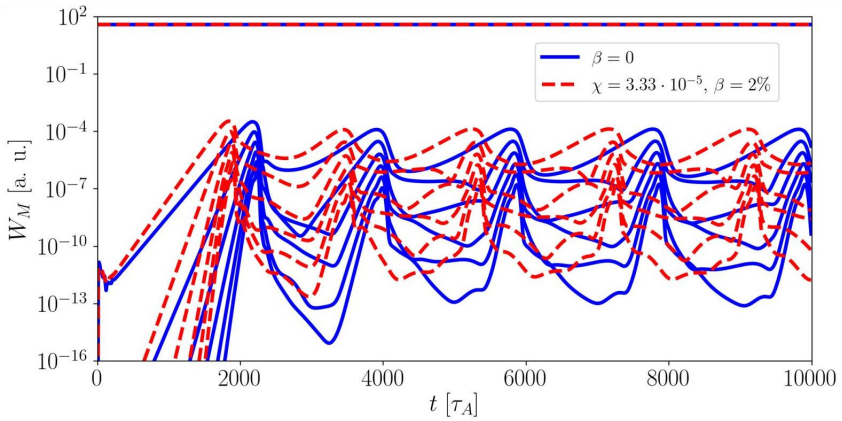

Figure 6.3: Magnetic energy as function of time, comparison between the pressure-less case and the non-zero pressure case, with $\chi = 3.33 \cdot 10^{-5}$, displaying a faster dynamics. From the top to the bottom each line represents: the axisymmetric component $m = 0$, $n = 0$, the first harmonic $m = 1$, $n = -1$, ..., the 6^{th} harmonic $m = 6$, $n = -6$.

For the $m = 0$, $n = 0$ no differences are highlighted. For the helical components, instead, the dynamics is significantly modified. In particular the introduction of the pressure and of a heat transport coefficient accelerate the dynamics both in the exponentially growing phase, then in the oscillatory phase. Performing simulations, varying the thermal conductivity χ it is easy to

notice that the dynamics accelerates as the χ is decreased (i. e. on-axis β is decreased).

6.5 Basic sawtooth modelling

In this Section, the basic features of the simulation are shown. Since pressure and heat transport have been introduced, the temperature evolution in time can be analysed, recovering (with this specific value of the transport coefficients) the typical sawtooth oscillation for the temperature of the center and the complementary oscillation, for the temperature in a peripheral plasma region.
In Fig. 6.4, the relationship between the central temperature and the magnetic energy of the $m = 1$ $n = -1$ mode is highlighted. In particular it is clear that the central temperature crashes happen concurrently with the $m = 1$, $n = -1$ instability peaks.

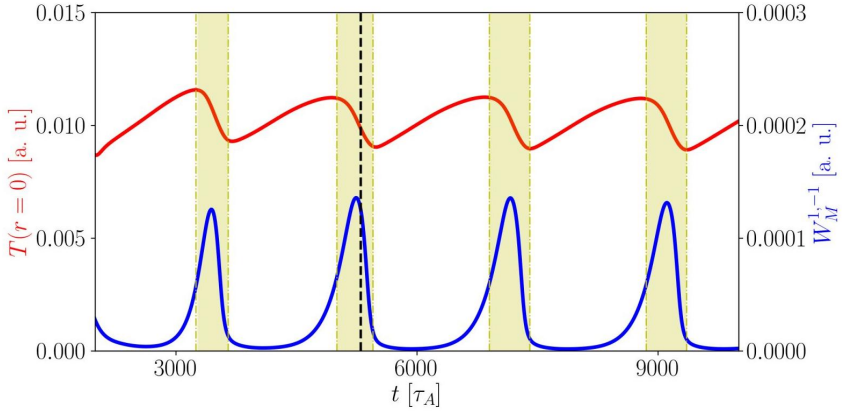

Figure 6.4: Time evolution of the core temperature (red line) and magnetic energy of the $m = 1$, $n = -1$ mode (blue line). Temperature crashes are associated with high $m = 1$, $n = -1$ MHD activity. The instant $t/\tau_A = 5300$ is highlighted, displaying temperature and helical flux function in Fig. 6.5.

We specify that the periodic behavior of the core temperature and of W_M^{1-1} observed in these simulations is due to the use of isotropic heat conductivity, with a fixed resistivity profile. The introduction of a Spitzer-like resistivity profile would require the introduction of the anisotropy heat conductivity to recover the periodic dynamical evolution. In order to get further information about thermal and magnetic data of the simulation, in Fig. 6.5 the temperature and the helical flux function χ_{hel} contour-plots are shown. The helical flux function χ_{hel} satisfies the relation: $\mathbf{B} \cdot \nabla \chi_{hel} = 0$. In this work, it is computed according to the following formula:

$$\chi(\mathbf{r}) = \int_0^r B_\theta^{0,0}(r')dr' + \frac{h}{R_0}\int_0^r r' B_z^{0,0}(r')dr' - \sum_{p=1}^{P} \frac{2r}{p}\left(\Re\left[B_r^{p,hp}(r)\right]\sin\star + \Im\left[B_r^{p,hp}(r)\right]\cos\star\right),$$

$$\star = m\theta + \frac{hpz}{R_0},$$

where the values of the helicity $h = m/n = -1$ and $P = 10$ are taken into account.
At the time instant considered a hot helical core is shown, and the temperature decreases as the plasma boundary is approached. On the other side, the helical flux function displays a slight departure from the axisymmetric case, since at $t = 5300\tau_A$ the intensity of the $m = 1$, $n = -1$ instability is low. We observe that the temperature contour-plot displays similar shapes to the helical flux-function, despite the isotropic heat transport hypothesis $\chi_\parallel = \chi_\perp$. In this case, the most significant terms on the momentum balance equation are $\mathbf{j} \times \mathbf{B}$ and ∇p, which imply $\mathbf{B} \cdot \nabla p \simeq 0$, so that the temperature can be considered as (almost) a flux function.

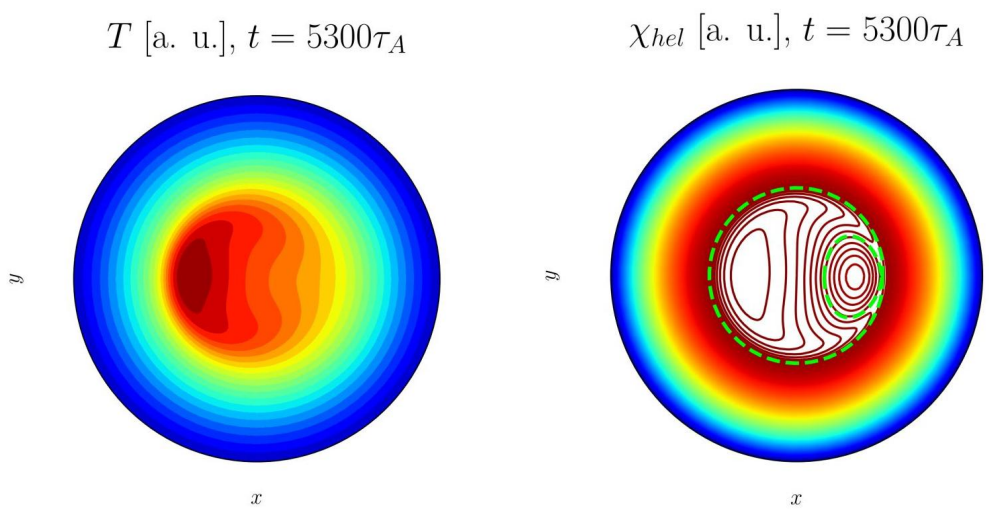

Figure 6.5: Contour plot at time instant $t/\tau_A = 5300$ for the temperature field (a) and the helical flux function (b), with the separatrix highlighted: both of them are affected by a similar helical shaping.

In Fig. 6.6 - 6.7 the time evolution of the sawtooth cycle is analyzed in details: six time instants are selected during the increasing and the decreasing temperature phase and, for each of them, the temperature and the safety factor profiles are plotted. In addition, the contour-plot of the temperature and the helical flux function is shown.
As the temperature $T(r = 0)$ grows, the safety factor profile tends to decrease around the $r \to 0$ region. The decrease of the safety factor below the value $q = 1$, allows the resonance of the $q = 1$ surface and the consequent growth of the $m = 1$, $n = -1$ instability. When the instability is sufficiently high, the central temperature decrease and the safety factor grows up to the value of $q = 1$. This cycle is repeated regularly during the whole simulation.
The contour-plots of the temperature and the helical flux display the presence of a strong non-linear interplay between between the $m = 1$, $n = -1$ magnetic field instability and the temperature field. However, the physical mechanism deserves further studies to be clarified.

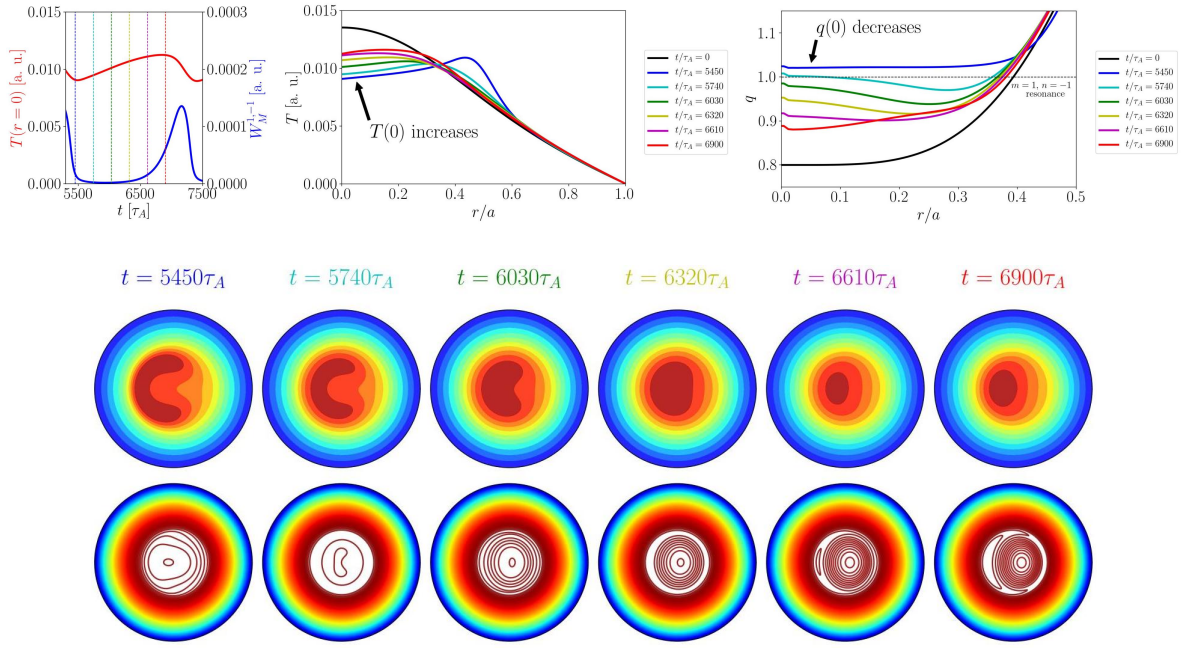

Figure 6.6: Sawtooth cycle: Temperature $T(r)$ and safety factor $q(r)$ profiles, during the ramp (growing phase of the central temperature). Six time frames are considered: for each of them the temperature (top) and the helical flux (bottom) contour-plots are shown.

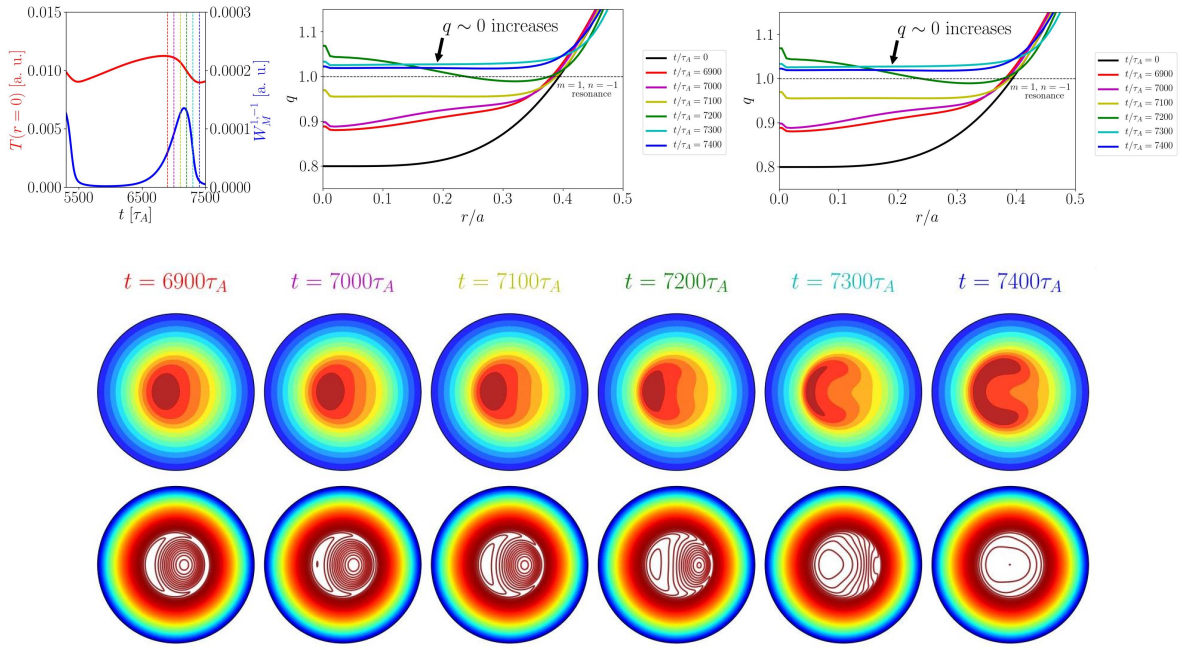

Figure 6.7: Sawtooth cycle: Temperature $T(r)$ and safety factor $q(r)$ profiles, during the 'crash' (decreasing phase of the central temperature). Six time frames are considered: for each of them the temperature (top) and the helical flux (bottom) contour-plots are shown.

6.5.1 The role of transport dimensionless parameters

To complete this study the database of simulations has been enlarged, including three systematic scans in the transport parameters:

- Fixed Prandtl, $P = 30$: $10^4 \leqslant S \leqslant 2 \cdot 10^5$, $10^{-6} \leqslant \chi \leqslant 2 \cdot 10^{-4}$, to evaluate the effect of resistivity and thermal conductivity.
- Low resistivity, $S = 10^5$: $P = 3, 10, 30, 100, 300, 1000$, $10^{-6} \leqslant \chi \leqslant 2 \cdot 10^{-4}$ to evaluate the effect of viscosity and thermal conductivity.
- High resistivity, $S = 3 \cdot 10^4$: $P = 3, 10, 30$, $10^{-6} \leqslant \chi \leqslant 2 \cdot 10^{-4}$ to evaluate the effect of viscosity and thermal conductivity.

Analyzing the core and peripheral temperature evolution in time, two main regimes have been identified: the sawtooth oscillations and the damped sawtooth, with an oscillation amplitude decreasing in time. Other minor regimes can be identified, being characterized mainly by the absence of the oscillation or by an average decreasing temperature.

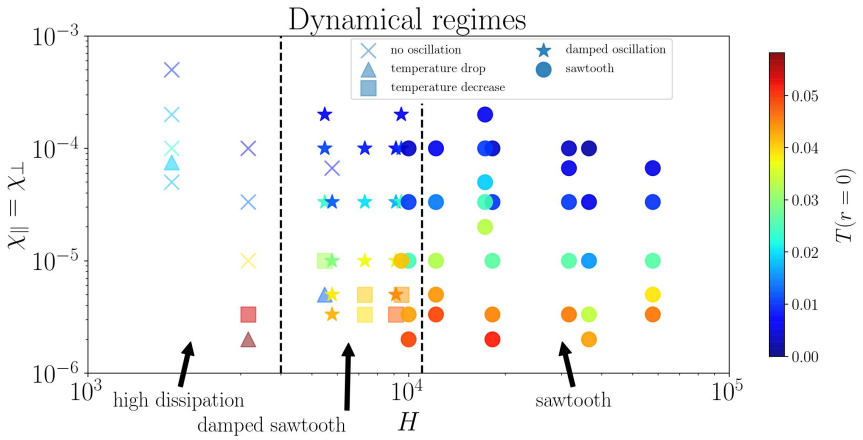

Figure 6.8: Database of PIXIE3D numerical simulations with finite β, fixed resistivity profile and isotropic heat conductivity: The Hartmann number rules the sawtooth regime, while the heat conductivity determines the core temperature value.

In Fig. 6.8, it is shown how the different regimes are ordered by the Hartmann number. In fact, at high visco-resistive dissipation, no oscillation is observed, at intermediate the damped sawtooth dominates, while at low dissipation, only the sawtooth is observed. We notice that this ordering property works better if the viscosity and the resistivity are jointly considered in a coefficient, instead of separately.
The colorbar is instead used to classify the points according to the core temperature (equivalent to the β parameter). It is observed that the core temperature decreases as the thermal conduction is increased, as expected by a basic picture according to which the transport increase causes the core plasma quantities to decrease.

6.6 Summary and future developments

In this Chapter a preliminary study of the tokamak sawtooth oscillation modelling was carried on, by means of PIXIE3D simulations with helical symmetry $m = 1$, $n = -1$. After a brief revision of the wide literature existing on this theme, we have shown that the basic characteristic of the sawtooth oscillations (in particular the core temperature time dependence) can be recovered in 2D simulations with finite pressure and fixed resistivity profile.

As further step, a database of numerical simulations has been constructed mainly varying the transport dimensionless parameters (resistivity, viscosity and isotropic heat conduction). Two different regimes emerged: sawtooth oscillations (at high Hartmann number) and damped sawtooth oscillations (at low Hartmann number). The isotropic heat conduction determines the core plasma temperature.
Since the ranges of transport dimensionless parameters explored in this work are still quite far from the observed experimental domain (at least for what concerns the Lundquist number), this study can be considered as a preliminary benchmark, which is in agreement the previous works, e. g. Ref. Denton et al. [1986]. Indeed, several improvements can be considered as future works, for example: the extension of the analysis to a fully 3D geometry, the introduction of a more realistic self consistent evolution of the plasma resistivity, according to the Spitzer formula, the introduction of anistropic heat conductivity $\chi_{\parallel} \neq \chi_{\perp}$ and the future comparison with experimental data (as a long term target).

Part III

Experimental data analyses

Chapter 7

Analysis of RFX-mod shots database

This Chapter presents the analysis of a wide RFX-mod shots database with the goal of achieving an experimental estimate of transport related dimensionless parameters, which are suggested to rule the MHD plasma dynamics, according to visco-resistive non-linear MHD simulations, Chp. 4. This requires the knowledge of transport coefficients formulas (developed in Chp. 3) and the assessment of plasma measurable quantities estimates on a wide statistical basis, able to represent the RFX-mod operational activity in the decade 2006 - 2016, before the ongoing shutdown.
In Sec. 7.1, the RFX-mod device, the largest RFP device in the world operated at Consorzio RFX in Padova, is introduced. The operational parameters and the state-of-the-art MHD control saddle coils system are mentioned.
In Sec. 7.2, the RFX-mod 2 upgrade is briefly presented, focusing on the effects preliminary predicted by the numerical simulations on the plasma self-organization, related to the vacuum vessel removal, which constitutes the main modification of the upgrade.
Sec. 7.3 introduces the database of RFX-mod shots analyzed in this work. For each subsets of shots we briefly summarize the scientific aim and plasma parameters ranges of the campaign.
Sec. 7.4 deals with the previous scaling studies performed on RFX-mod. The use of the Lundquist number and of the plasma current as independent variables in scaling studies is questioned, following the indications from SpeCyl numerical simulations which suggest a joint role of the visco-resistive coefficient and not of the resistivity only in ruling the MHD activity.
In Sec. 7.5, the fluid dimensionless numbers estimate (and, in particular, of the Hartmann number) is performed on the basis of the experimental data, temporarily limiting to the classical transport, choice discussed in Chp. 8. The numerical results are briefly discussed, focusing on the comparison with the values set as inputs in SpeCyl simulations.
In Sec. 7.6, the scaling relations between the Hartmann number, the Lundquist number and plasma current are discussed, representing the main independent variables used in RFP scaling studies.
Summary and final remarks follow in Sec. 7.7.

7.1 The RFX-mod device

RFX-mod (see Ref. Sonato et al. [2003]) is a medium size magnetic confinement fusion experiment, operating in Padova C.N.R. research area and managed by Consorzio RFX. It is a flexible device, able of operating both in tokamak and RFP configurations (more details can be found in Ref. Piovesan et al. [2013]). Since the experimental part of this work is focused on the study of phenomena in the case of reversed-field pinch, only the operational parameters in the RFP configuration (reported in Tab. 7.1) are analyzed.

Major radius, R_0	2.0 m
Minor radius, a	0.459 m
Plasma current, I_p	$\leqslant$ 2.0 MA
Toroidal field, B_ϕ	$\leqslant$ 0.7 T
Flat top time, Δt	$\simeq$ 250 ms

Table 7.1: RFX-mod device experimental features in RFP configuration.

Limiting to the reversed-field pinch configuration, RFX-mod is the largest device in operation and the main scientific results obtained in RFX (like helical self-organization, Sec. 2.6) proved to be of great interest in the fusion community, despite the resources spent in this research field are limited, if compared to tokamak or even stellarator configurations. Moreover, RFX-mod holds the highest plasma current record for an RFP device (2 MA), while the plasma on-axis magnetic field can reach a value of $B_0 \sim 2$ T, exploiting the phenomenon of helical self-organization. Fig. 7.1 illustrates the device during its operating phase.

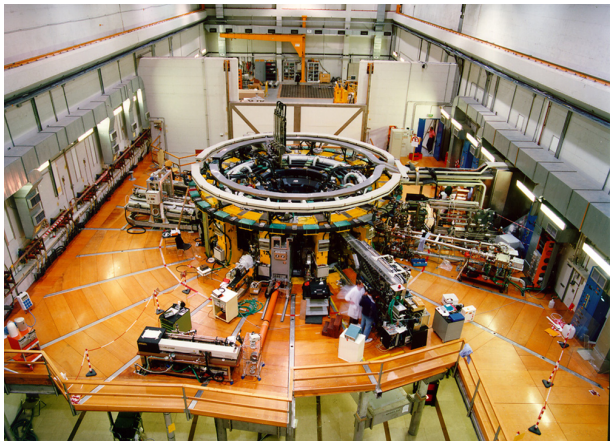

Figure 7.1: The RFX-mod device.

The toroidal device is composed by the toroidal vacuum vessel (aimed at containing the plasma), magnetic systems for producing plasma equilibrium and control, power supplies and diagnostics that surround the machine, Fig 7.1).
The internal wall that directly faces the plasma is composed by 2016 trapezoidal graphite tiles, only 1.8 cm thick (to maximize the plasma volume): the composition is chosen in order to sustain high thermal loads and to get low Z impurities. The vacuum vessel that allows reaching low pressures is composed by 72 wedge shaped elements that are sustained by the external mechanical structure.
The magnetic system is composed by 3 windings: the toroidal field coils (TF, 48 coils) for producing B_ϕ, the poloidal field coils (M, 20 coils) for inducing the plasma current I_p and associated B_θ field, and the vertical field coils ("field shaping" F, 16 coils), described in Ref. Stella et al. [1995]. The main aim of the latter system is to control, thanks to the generation of

magnetic field, the shape and position of the plasma.
The flagship of the RFX-mod experiment is a system of 192 saddle coils dedicated to plasma active control, (Fig. 7.2).

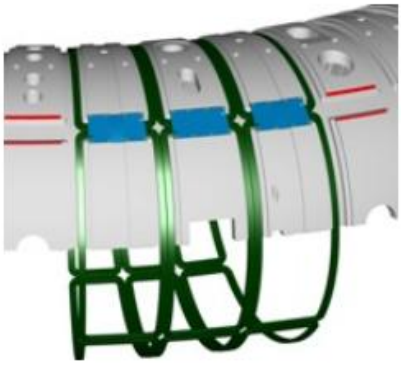

Figure 7.2: Representation of RFX-mod active control saddle coils.

These coils are installed both in poloidal and toroidal directions (like a saddle) but are used to generate a radial magnetic field of the order of some mT that can compensate the one generated by helical perturbations, resulting in the stabilization of resistive wall modes. To optimize the control, each coil has an independent control and power supply. The control system is one of the modification introduced in the upgrade of the 2000 - 2004 (from RFX to RFX-mod), described in Ref. Sonato et al. [2003].
The diagnostic apparatus is described, limited to the measurements that are of interest for this work in this Chapter, in Sec. 7.3.2.

7.2 The RFX-mod 2 upgrade

The RFX-mod device is now facing a shut down phase to allow the completion of its second upgrade RFX-mod 2 (whose details are referred in Ref. Marrelli et al. [2019]), which is currently predicted to terminate by the end of 2024, with the first RFX-mod 2 shot. The main aim of this upgrade consists of the resistence reduction of the device conductive boundaries to approach more ideal boundary conditions. According to current knowledge of RFP plasmas, this is expected to have beneficial effects on the tearing modes activity, resulting in an increase of the helical self-organization and confinement and in a reduced plasma-wall interaction.
From the design point of view (see Ref. Peruzzo et al. [2019]), the upgrade is realized by removing the vacuum vessel, made of Inconel, a material characterized by high resistivity. As consequence of it, the graphite tiles forming the first wall will be attached to the low resistivity copper stabilizing shell. In addition, the vacuum vessel removal has implied the re-design of the stainless steel support structure in order to make it vacuum tight.
The modification of the device boundaries allows to increase the plasma minor radius a and to consequently increase the plasma-shell proximity. Naming b the shell radius, the b/a ratio is expected to decrease from the value of $b/a = 1.11$ (for RFX-mod) to a value of $b/a = 1.04$ (for RFX-mod 2). The value $b/a = 1$ indicates ideal boundary conditions. In Ref. Bonfiglio et al. [2019], SpeCyl numerical simulations with a preliminary realistic modelling of the boundary predict the reduction of edge $m = 1$ magnetic field perturbations (of about 50%) and of the total magnetic energy associated to $m = 1$ secondary modes (of about 30%), for the RFX-mod 2 device, as shown in Fig. 7.3. The predicted reduction of $m = 1$ secondary modes amplitude is expected to improve the helical self-organization of the reversed-field pinch plasma and to reduce the edge plasma bulging due to the $m = 1$ modes phase locking.

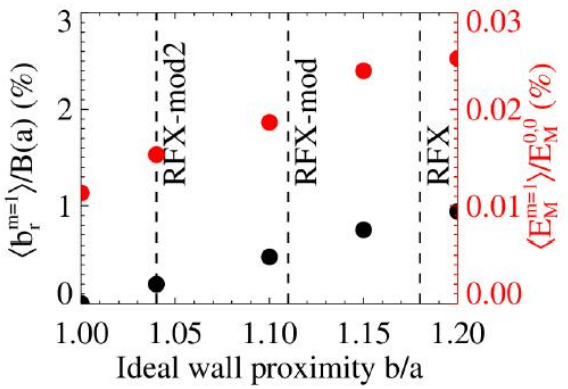

Figure 7.3: The increase of the plasma-shell proximity (decreasing the ration b/a) causes a significant reduction of $m = 1$ secondary modes, according to SpeCyl numerical simulations. Picture from Ref. Bonfiglio et al. [2019].

7.3 RFX-mod shots database description

7.3.1 Previous studies originating the database

The database of all the shots considered in this work is composed by six initial databases made up by RFX-mod shots (all in the RFP configuration) performed in different campaigns in between 2006 and 2016, before the shutdown phase. The discharges are chosen in order to scan a wide interval in the main plasma measurable quantities (to allow scaling studies, in Sec. 7.6, and viscosity evaluation in Chp. 8) and of Greenwald density ratio: $0.05 < n/n_G < 1$, in order to allow a study of the density limit on RFX-mod device, reported in Chp. 9.
The experimental data used in this Thesis, were collected and analyzed for previous studies that constitute the basis on which this work is developed. In particular, five different paths of research, to which they belong, can be identified:

- **Scaling studies**, devoted to the determination of empirical laws induced via a fitting procedure on the experimental data. This procedure has been widely applied on RFX-mod, to describe the helical self-organization as function of the plasma current and of the Lundquist number, but also to describe important plasma features (like density and temperature) as function of plasma parameters that be set directly in a shot (like the plasma current). A brief summary of the scaling results on RFX-mod is made in Sec. 7.4.

- Study of the **edge plasma physics in QSH phase**. This topic is of particular interest for density limit studies, due to the role played by edge magnetic field instabilities. The most recent study in this framework is Ref. Scarin et al. [2019], where the role of the $m = 1$ secondary modes is discussed with particular interest to plasma wall interactions. Defining $\Delta_{m,n}$ as a a plasma displacement associated to the radial magnetic field perturbation $b^r_{m,n}$, the ratio $\Delta_{1,sec}/\Delta_{1,-7}$ is proved to be an estimator of the strength of plasma wall interactions: the radiating power is found to be higher in the case of chaotic MH phase with respect to the well ordered SH phase. In addition, a comparison with SpeCyl numerical simulations and a prediction for the future RFX-mod2 experiment are made, envisaging a lower plasma wall interaction for the future experiment.

- Previous studies of the RFX-mod **density limit**, in which physical laws able to predict the behaviour of the ratio n/n_G are found. This will be described in Sec. 9.2, as they constitute the premise for understanding the interpretation of density limit phenomenon proposed in this Thesis.

- Study of the **confinement properties and transport barriers during the QSH**. This argument is of particular interest to optimize RFP fusion devices performance in terms of core density, temperature and confinement time, as already discussed in Sec. 2.6.
- Study of very **low current** shots physics, with particular reference to mode rotation and RFP density limit. These shots are particularly important for the database because they span the region of low temperature plasmas, and with high density and high Greenwald phenomenological ratio. This database is part of a wide review on RFX-mod scientific activity, Ref. Zuin et al. [2017].

In the next paragraphs the six databases are enumerated and briefly described:

1. The first database considered is composed by discharges # 35836 - #35851, #35883 - #35894 , #35902 - #35914 performed in year 2014. It was selected for a previous study regarding the density limit Spizzo et al. [2015] and it is a scan in the plasma current into three intervals: 600 kA, 800 kA, 1 MA, with a careful control of the $m = 0$, $n = -1$ mode via the feedback system.
2. The second database is composed by shots in the intervals: #19911 - #19960 and #26303 - #26351. The first ones are old 2006 stimulated discharges for the first studies on the density limit, Ref. Puiatti et al. [2009a], while the second were used in a subsequent campaign in 2009, also for density limit studies Spizzo et al. [2010]. These shots are characterized by high electron density.
3. The third database was considered in Scarin et al. [2019] and it is composed by QSH low density shots, useful to explore transport barriers in the region with $n/n_G \sim 0.15$ and palsma wall interaction effects on high-n mode locking.
4. The fourth database contains various discharges in the interval # 26352 - # 36059 aimed at studying scaling laws on RFX-mod, see Sec. 7.4. These shots were collected during the five years 2009 - 2014 of RFX-mod operations.
5. The fifth database contains shots for the study related to the $m = 0$ modes that include the following shots: # 35920 - # 35936, # 35937, # 35942, # 35943 and # 35959 - # 35976 These shots were also performed in the 2014 campaign, but were not included in publication Spizzo et al. [2015].
6. The sixth database includes many shots in range #37195 - #37281. They were collected during 2014 and studied in the context of the final overview of the RFX-mod scientific activity, Ref. Zuin et al. [2017]. The main feature of this shots is the extremely low plasma current $I_p \lesssim 200$ kA.

The overall database amounts to 263 shots, allowing a wide scan in plasma measurable parameters and also on plasma dimensionless transport parameters, which are going to be estimated in Sec 7.5. In Tab. 7.2, the main features of six databases of RFX-mod shots are summarized, highlighting the research framework of the campaign, the plasma current and reversal parameter ranges.

Database	Aim	Shots	year	Ref.	I_p	F
1st	Density limit	#35836 - #35851	2014	Spizzo et al. [2015]	500 - 600 kA	-0.1
		#35883 - #35894	2014	Spizzo et al. [2015]	800 kA	-0.1
		#35902 - #35914	2014	Spizzo et al. [2015]	1-1.2 MA	-0.1
2nd	Density limit	#19911 - #19960	2006	Puiatti et al. [2009a]	500 - 600 kA	-0.2
		#26303 - #26317	2009	Spizzo et al. [2010]	800 kA	-0.1
		#26321 - #26334	2009	Spizzo et al. [2010]	800 kA	-0.04 ÷ -0.05
		#26336 - #26351	2009	Spizzo et al. [2010]	1-1.2 MA	-0.04 ÷ -0.05
3d	QSH			Scarin et al. [2019]	$I_p > 1$ MA	
4th	Scaling laws	# 26352 ÷ # 36059 [range]	2009 2014	Sec. 7.4	200 kA − 2 MA	-0.01 ÷ -0.2
5th	Density limit	#35920 ÷ #35976 [range]	2014	Unpublished	400 - 600 kA	-0.05 ÷ -0.1
6th	Low current	#37195 ÷ #37281 [range]	2014	Zuin et al. [2017]	$\lesssim$ 200 kA	-0.01 ÷ -0.2

Table 7.2: RFX-mod database considered in this Thesis: all the shots are in RFP configuration. For each subset of shots the scientific motivation is highlighted, providing also the main reference in which the experimental campaign is described. The range of plasma current I_p and reversal parameter are also indicated.

7.3.2 Measured plasma quantities and related diagnostics

This section deals with the evaluation of the plasma parameters from the data directly collected by RFX-mod diagnostics. The parameters considered are: the plasma current I_p, the toroidal loop voltage V_{loop}, the on-axis magnetic field B_0, the electron density n_e, the electron temperature T_e, the edge radial and toroidal magnetic field instabilities. Only diagnostic signals during the flat top plasma current phase (during which I_p is approximately time constant) are taken into account.
From the point of view of radial dependence of the measured parameters, we consider only core or plasma core average quantities, while for the time dependence, all the quantities are measured in correspondence of the T_e Thomson scattering diagnostics measurements, repeated on RFX-mod at regular intervals of 25 ms (old shots) or 10 ms (new shots). This allows to obtain 2082 data points evaluation, for the 263 shots database. A brief itemize with the description of each plasma measurable quantity evaluation follows:

- Regarding the magnetic field, the toroidal on axis magnetic field is chosen, $B_0 = B_\phi(r = 0)$ because it is the reference value used in the codes, like SpeCyl. Since in many publications (see e. g. Ref. Terranova et al. [2000]) magnetic fluctuations are normalized to the edge poloidal field, $B_\theta(r = a)$, we recall here that in the Bessel function model the ratio $B_0/B_\theta(a) = 1/J_1(2\theta) \approx 3$ for a typical value of the pinch parameter $\Theta \approx 1.5$.

- The electron density n_e is evaluated in the core plasma, calculating the average in the region $-15\,\text{cm} \leqslant r \leqslant 15\,\text{cm}$ of the density profiles measured by a 16-chord CO_2 interferometer, described in Ref. Innocente et al. [1997]. For the ion density the quasi neutrality hypothesis is considered in this work, $n_i \approx n_e$.

- The electron temperature T_e is a profile average on the central region ($-15\,\text{cm} \leqslant r \leqslant 15\,\text{cm}$, as for the electron density). The temperature profiles are measured in 84 radial positions with 7 mm spatial resolution by a Thomson scattering diagnostic which uses a custom built Nd:YLF laser, described in Ref. Alfier and Pasqualotto [2007].

- No ion temperature T_i diagnostic is available on the RFX-mod device. Studies of the ion temperature behaviour are carried out, for example, on the MST device Dexter et al.

[1991] that is very similar to RFX-mod for the comparable dimensions and for operating in RFP configuration. MST is equipped with a charge exchange recombination spectroscopic system based on carbon impurities emission that allows for the evaluation of the ion temperature. The results are highlighted, for example, in Chapman et al. [2010], where it is shown that it is particularly difficult to model T_i in the RFP configuration. The ion temperature is of the same order of magnitude of the electron, but it is usually smaller, except for the instants in which the QSH phase is interrupted, in the so-called relaxation events: in these cases $T_i > T_e$. Since these time intervals are usually quite small, in this work the well accepted convention that $T_i = 0.5T_e$: this is confirmed also by a study on RFX-mod, with the a diagnostic for T_i measurements (the neutral particle analyzer), available for a limited number of shots (see Ref. Zuin et al. [2011]).

- The atomic number of the ions Z is replaced by the effective charge Z_{eff}, that takes into account the composition of the plasma. RFX-mod discharges are made with hydrogen or deuterium, with impurities that are mainly constitute by carbon. The conventional value chosen is $Z_{eff} = 1.5$. This value has been chosen on the basis of previous studies on RFX, where Z_{eff} varied in the range $1.2 \leqslant Z_{eff} \leqslant 2$ as a function of the loop voltage in the range $30\,\mathrm{V} \leqslant V_{loop} \leqslant 50\,\mathrm{V}$, see Ref. Carraro et al. [1995].

- The mass number $\gamma = m_i/m_p$ is easily obtained: $\gamma = 1$ (hydrogen), $\gamma = 2$ (deuterium). In this way, possible isotopic effects are fully taken into account in the present calculation.

- The minor radius a amounts to $a = 0.459\,\mathrm{m}$.

- The Coulomb logarithm $\ln\Lambda$ is treated as in Richardson [2019]: We recall here that Coulomb logarithm is defined as $\ln\Lambda := \ln(r_{max}/r_{min})$, being r_{max} and r_{min} the Debye length and the distance of closest approach during particle collisions at the average velocity.

- Edge radial and toroidal magnetic field perturbations are evaluated exploiting the NCT (NewComb Toroidal) algorithm, presented in Ref. Zanca and Terranova [2004]. This code performs the numerical solution of Newcomb equations, in toroidal domain, and it is able to determine the toroidal harmonics of the main MHD modes, using as boundary conditions magnetic flux measurements of RFX-mod pick-up coils.
  In this work, the modes considered are the dominant and main secondaries $m = 1$ and $m = 0$ modes: $m = 1$, $-20 \leqslant n \leqslant -7$, and $m = 0$, $-9 \leqslant n \leqslant -1$, with $n \neq -7$. The latter mode is excluded by the comparison with the cylindrical code SpeCyl, because originated from toroidal effects, in particular from the non linear interaction of the purely toroidal $m = 1$, $n = 0$, and the dominant $m = 1$, $n = -7$ modes.

These measurements constitute the starting point for the evaluation of transport coefficients, see Sec. 7.5 and Chp. 8 and especially of the Hartmann number, which will be applied to study the RFP density limit in Chp. 9.

7.3.3 Statistics of measured plasma quantities

In this Section, more details regarding the RFX-mod database analyzed in this work are provided. In particular, in Fig. 7.4, the probability distribution of the most important plasma measurable parameters is provided. It is worth noting that a wide range in plasma current ($105\,\mathrm{kA} \leqslant I_p \leqslant 1.96\,\mathrm{MA}$), on axis magnetic field ($0.12\,\mathrm{T} \leqslant B_0 \leqslant 1.99\,\mathrm{T}$), electron density ($3.45 \cdot 10^{18}\,\mathrm{m}^{-3} \leqslant n_e \leqslant 1.57 \cdot 10^{20}\,\mathrm{m}^{-3}$) and electron temperature ($33.9\,\mathrm{eV} \leqslant T_e \leqslant 1.13\,\mathrm{keV}$) is covered: for each quantity there is at least a factor of 20 between the minimum and the maximum value and all the intermediate values are represented, compatibly with the operational choices of RFX-mod.

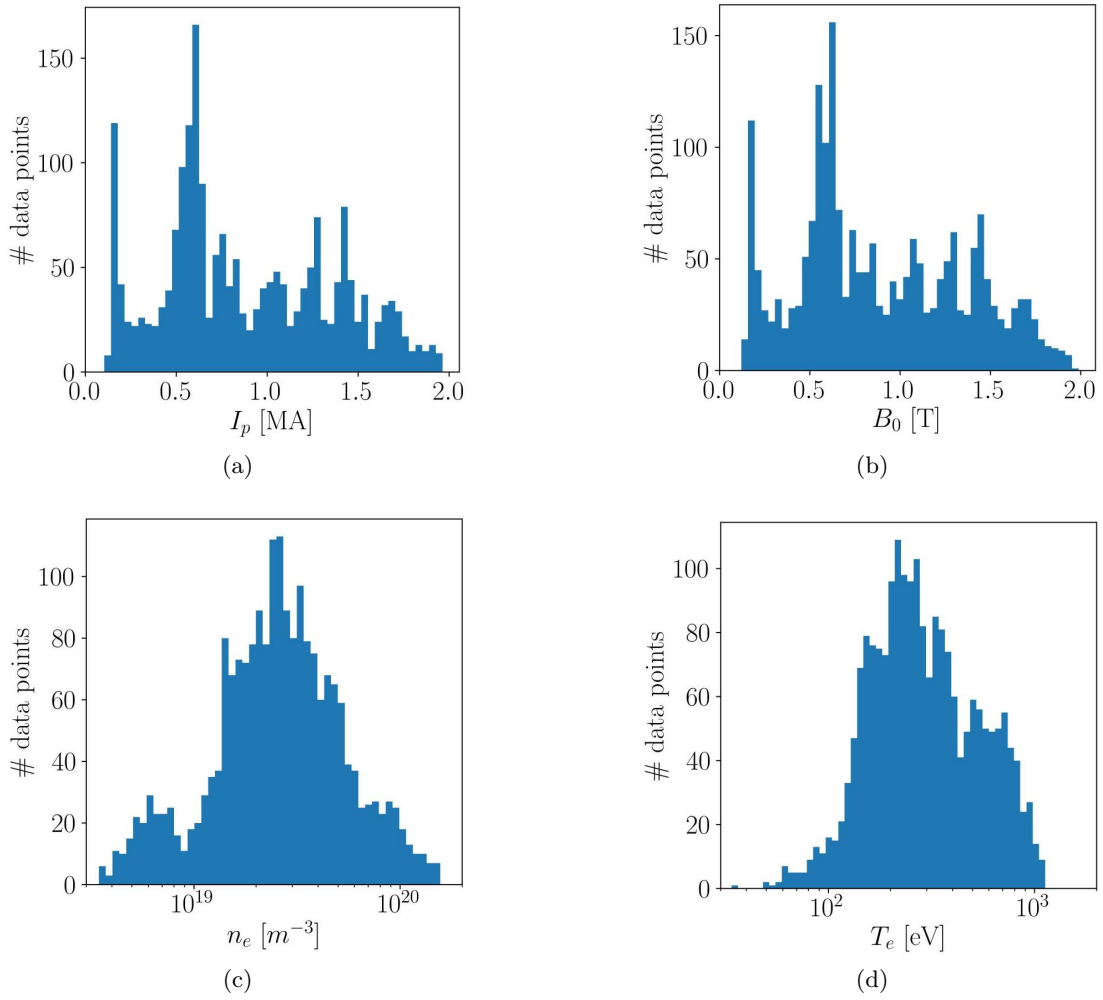

Figure 7.4: Histogram of the main plasma measurable quantities, in RFX-mod database analyzed for the plasma current (a), on axis magnetic field (b), electron density (c) and electron temperature (d).

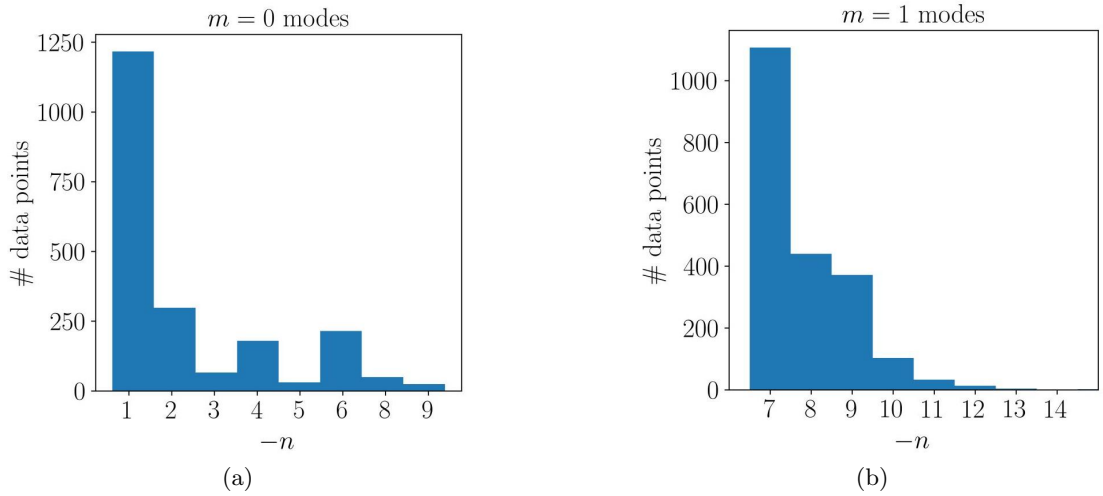

Figure 7.5: Toroidal wave number n of the dominant mode histogram for edge normalized toroidal magnetic field instabilities in the RFX-mod database analyzed: $m = 0$ (a) and $m = 1$ (b).

In Fig. 7.5 a statistic on the magnetic field eigenvalues instabilities is shown. In particular the two histograms show the toroidal wave number of dominant mode among the $m = 0$ (a) and the $m = 1$ (b) modes, respectively. It is worth noting that the most frequently dominant mode among the $m = 0$ is the $n = -1$, while for the $m = 1$ it is the $n = -7$ mode, in agreement with the past experimental findings on RFX-mod. Moreover, it is it is highly unlikely to find a dominant mode at high n.

7.4 Previous scaling studies on RFP plasmas

In the past research activity several scaling laws have been proposed for RFP plasmas, with the goal of describing the magnetic fluctuations ($\delta b/B_0$) trend and the transition from Multiple Helicity to Quasi Single Helicity regimes (with the consequent transport barrier formation and core temperature increase) as function of plasma parameters with an affordable experimental estimate. Despite the role of the Hartmann number in ruling magnetic field fluctuations, highlighted by numerical simulations (see Chp. 4), the latter has often been ignored in the past experimental scaling studies, mainly for the difficulties related to the viscosity estimate (see Chp. 8). This has favoured the use of the Lundquist number S and the plasma current in the scaling laws, paradigm that we want to question in this work.
One of the first magnetic fluctuations scaling as function of the Lundquist number $\left(\delta b/B_0 \propto S^{-1/3}\right)$ was proposed in Ref. Strauss [1986], mainly on the basis of analytical arguments. In Ref. Cappello and Biskamp [1996], a numerical study of SpeCyl MHD simulations shows the scaling of magnetic energy fluctuations $\delta W_m/W_m \propto S^{-0.44}$. This result was confirmed by an experimental scaling study presented in Ref. Terranova et al. [2000], in which a wide database of shots was considered, including standard shots, QSH shots and shots with particular initial condition to improve the confinement, in the old RFX machine, see Fig. 7.6. In this case Lundquist number S was evaluated by means of RFX diagnostics and using Spitzer resistivity and the normalized toroidal magnetic field fluctuations ($b_\phi/B_\theta(a)$) are obtained on the basis of experimental measurements.

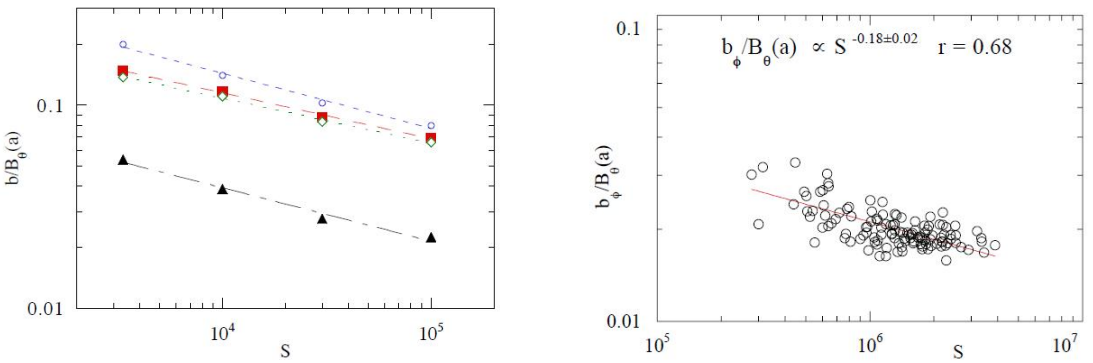

Figure 7.6: Normalized toroidal field fluctuations, as function of the Lundquist number S, for SpeCyl simulations (a) and RFX experimental data (b). In (a) different components of the toroidal field are analyzed. Plots taken from Ref. Terranova et al. [2000].

In Fig. 7.6, although the ranges of S analyzed in simulations and experimental data are different, the agreement of the two scaling laws is quite good, as it is the correlation coefficient. The agreement level, resulting from the fitting procedure, regards also the absolute values of the magnetic perturbations and not only the scaling laws slopes.
Other scaling laws for the magnetic perturbations were introduced in Ref. Terranova et al. [2000] involving the Prandtl number P or a multiple regression with plasma current I_p, electric

temperature T_e, density n and the effective charge Z_{eff}. This also implies the need for a viscosity coefficient estimate on the RFX experimental data. However in that work, the results did not significantly improve the previous one in terms of correlation value, partly because of a slight error in the evaluation of the experimental value of Prandtl. For this reason, at that time, the Lundquist number S turns out to be a good parameter that described the magnetic field perturbations, coherently with other works in the same years on MST (see Ref. Stoneking et al. [1998]) and on RFX (see Ref. Intravaia et al. [1999]). The results presented in Ref. Terranova et al. [2000] can be partially improved, since from Chp. 4 we know that visco-resistive simulations predict a better scaling with $H = \sqrt{SM}$.
The last scaling involving the Lundquist number is dated back to Ref. Piovesan et al. [2009], where the Lundquist number is used to describe the Multiple Helicity - Quasi Single Helicity transition. After that, directly measurable plasma parameters have been used independent variables of scaling laws. In particular the plasma current I_p has been used to describe the core plasma temperature in Ref. Innocente et al. [2007] and Innocente et al. [2009] where on a wide database of RFX-mod shots (in the ranges $0.2\,\mathrm{MA} < I_p < 1.6\,\mathrm{MA}$, $-0.045 < q(a) < 0$ and $0.1 < n/n_G < 1$) the following relation is shown:

$$T_e(r=0) \propto I_p^{1.09\pm0.01} \langle n_e \rangle^{-0.30\pm0.01} \left(b^{\phi}_{sec}(r=a) \right)^{-0.28\pm0.01}, \qquad r = 0.98. \tag{7.1}$$

The plasma current I_p is also used in Ref. Franz et al. [2013] to describe electron temperature gradients, while in Ref. Gobbin et al. [2015] the phenomenological ratio n/n_G is used to describe the core temperature.
Since aim of this work is the description of magnetic field fluctuations as function of the Hartmann evaluated on the experimental data, as suggested by SpeCyl simulations, the relation between the proposed parameter (Hartmann) and the previously used parameters (Lundquist number and plasma current) is going to be investigated in Sec. 7.6.

7.5 Experimental estimates of the transport related dimensionless parameters

In this Section, the fluid-dynamical numbers introduced in visco-resistive model Eq. (3.87) and (3.91) are calculated as function of the plasma parameters that can be experimentally measured. The basic algebra procedure simply consists of the replacement of the results reported in App. B.1 in the definition of the fluid-dynamical number. At the end an expression for each fluid number is obtained (see Ref. Veranda et al. [2014]), mainly depending on the basis of the transport model chosen to evaluate the viscosity. The resulting maths expressions are reported in App. B.2.
In the final Sections of the the Chapter we will use the perpendicular Braginskii viscosity, among the different viscosity evaluations available. This choice will be justified in Chp. 8. For simplicity reasons, only the formulas used in the next Sections are reported:

- Lundquist number S:

$$S_{\parallel} := \frac{a^2 \mu_0}{\eta_{\parallel} \tau_A} = 16.7 \pi^{3/2} \frac{\mu_0^{1/2} \epsilon_0^2}{m_p^{1/2} m_e^{1/2} e^2} \frac{a B T_e^{3/2}}{Z^{1/2} \gamma^{1/2} \ln \Lambda n_e^{1/2}}, \tag{7.2}$$

- viscous Lundquist number M:

$$M_{\perp} := \frac{a^2 \rho_0}{\mu^i_{\perp} \tau_A} = 44.5 \frac{\epsilon_0^2}{\mu_0^{1/2} m_p e^2} \frac{a B^3 T_i^{1/2}}{\gamma n_e^{3/2} Z^{1/2} \ln \Lambda}, \tag{7.3}$$

- Magnetic Prandtl number, P:

$$P_\perp := \frac{\mu_0 \mu_\perp^i}{\rho_0 \eta_\perp} = 4.08 \frac{\mu_0 m_p^{1/2}}{m_e^{1/2}} \frac{\gamma^{1/2} n_e T_e^{3/2}}{B^2 T_i^{1/2}} \propto \frac{nT}{B^2} \propto \beta(r=0). \tag{7.4}$$

  It is worth noting that the estimate of the magnetic Prandtl number, evaluated according to the Braginskii theory for the perpendicular viscosity is exactly proportional to the β plasma parameter, estimated in the core region.

- Hartmann number, H:

$$H_\perp := \frac{aB}{\sqrt{\eta_\perp \mu_\perp^i}} = 45.8 \frac{\epsilon_0^2}{m_e^{1/4} m_p^{3/4} e^2} \frac{aB^2 T_e^{3/4} T_i^{1/4}}{\gamma^{3/4} Z^{1/2} n_e \ln \Lambda}. \tag{7.5}$$

The previous equations are key formulas for the subsequent development of this work, because, they allow the evaluation in experimental conditions of the fluid-dynamical numbers that are expected (in particular the Hartmann number) to drive the physics of the RFP configuration plasmas, as it is suggested by visco-resistive MHD simulations.
The statistics of the four dimensionless parameters estimate is shown in Fig 7.7, while the numerical results of the evaluation are reported in Tab. 7.3, where the ranges of the estimated dimensionless parameters on the RFX-mod shots database are compared to the similar ranges which can be explored using SpeCyl MHD simulations, from Chp. 4.

	SpeCyl simulations range	Exp. data range
Lundquist S	4×10^2 - 10^7	10^5 - 2×10^8
Visc. Lund. M	10 - 10^5	8×10^4 - 2×10^9
Mag. Prandtl P	1 - 10^5	0.04 - 0.9
Hartmann H	2×10^2 - 10^6	8×10^4 - 3×10^8

Table 7.3: Ranges of the dimensionless transport parameters: in the database of SpeCyl simulations, from Tab. 4.2, (left column) and in the RFX-mod shots database (right column).

In Tab. 7.3, despite the partial overlap in the data and simulations ranges of transport parameters, there are some differences which deserve to be highlighted:

- S, M and H have larger values in the experimental data with respect to the simulations, which suggests a possible systematic underestimate of resistivity and viscosity by the classical Braginskii formula, while P is underestimated, suggesting that the underestimate mainly affects the viscosity coefficient, which represents the most difficult coefficient to evaluate.

- The magnetic Prandtl number has a very narrow range of variation in the experimental data with respect to the values considered in the simulations. This corresponds to an almost constant β parameter: $\beta_\theta \sim 3 - 4\%$, which confirms the hypothesis of constant β made in Ref. Connor and Taylor [1977], a dated study made to find a confinement scaling law for RFP devices.

The gap in the fluid dimensionless numbers estimates between data and simulations is not easily fixable, since the computational time of the simulations increases as the Hartmann number is increased, while experimental data points with lower $H_\perp$ would require high density, low plasma current and low temperature shots (see Eq. 7.5) beyond the RFX-mod operational limits.
For the sake of completeness, in Tab. 7.4 the values of the Hartmann number (in particular $H_\perp$) are calculated in the case of typical values of RFX-mod operations, for three example shots: the range spanned by $H_\perp$ is between 10^5 and 10^8.

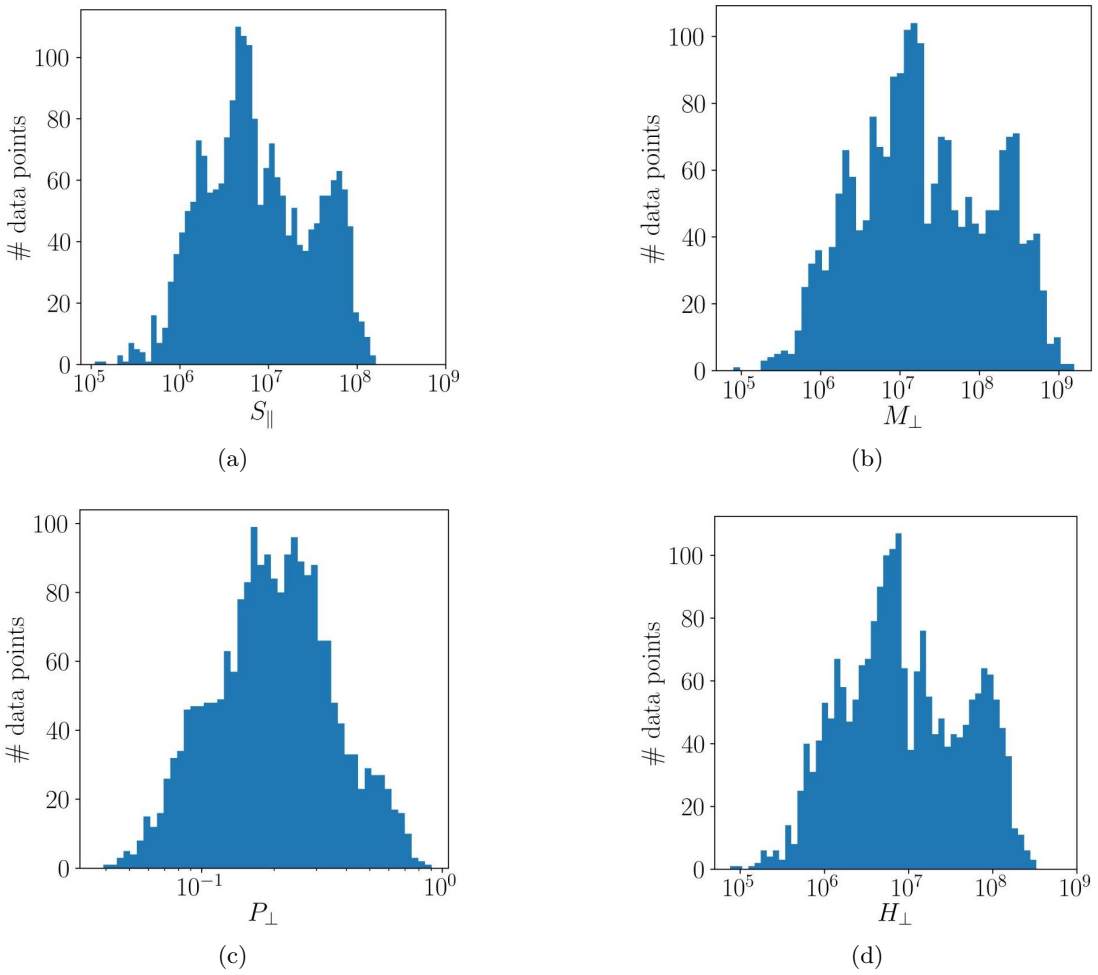

Figure 7.7: Transport related dimensionless parameters calculated using RFX-mod experimental data, using classical Braginskii theory of transport: parallel Lundquist number (a), viscous Lundquist number (b), perpendicular magnetic Prandtl number (c) and perpendicular Hartmann number (d).

shot	$B_0[T]$	T_e [eV]	γ	n_e $[10^{19}m^{-3}]$	$\ln\Lambda$	$H_\perp$	n/n_G
# 19956	0.427	110	1	4.84	14.3	7.95×10^5	0.739
# 26303	0.784	314	1	2.31	16.3	1.42×10^7	0.202
# 30775	1.69	664	1	2.35	17.4	1.27×10^8	0.093

Table 7.4: Perpendicular Hartmann number $H_\perp$ calculation examples for three representative RFX-mod shots.

7.6 Scaling laws on RFX-mod

This Section is devoted to the presentation of some scaling results on the RFX-mod database. In particular, we tested the relations of the Hartmann number $H_\perp$ (proposed as new parameter to order edge normalized magnetic fluctuations) with the Lundquist number and the plasma currents, used in previous scaling studies, Sec. 7.4. We consider ordinary least square fit of power law dependence.
As a first step, we show that the Lundquist number $S_\parallel$ and the plasma current display a good level of correlation on the RFX-mod database (See Fig. 7.8 and Eq. 7.6), in agreement with the previous RFX-mod scaling studies, where they have been mutually exchanged.

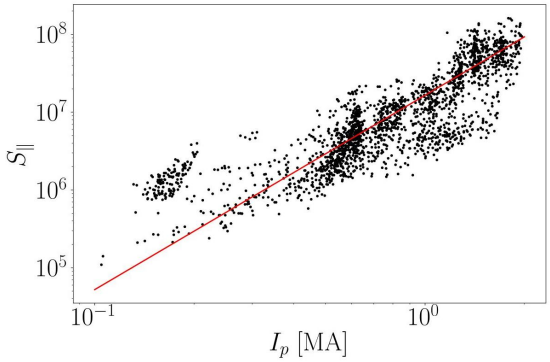

Figure 7.8: Parallel Lundquist number as function of the plasma current: a good correlation level is displayed.

$$S_\parallel = (1.65 \pm 0.05) \cdot 10^7 I_p^{2.50 \pm 0.06}, \quad [\text{MA}] \qquad r = 0.85. \tag{7.6}$$

In Fig. 7.9, the relation between the perpendicular Hartmann number $H_\perp$ and plasma current I_p (a), and the Lundquist $S_\parallel$ (b), is shown. Eq. 7.7 and 7.8 indicate the presence of a good correlation between $H_\perp$ and I_p and excellent correlation between $H_\perp$ and $S_\parallel$.

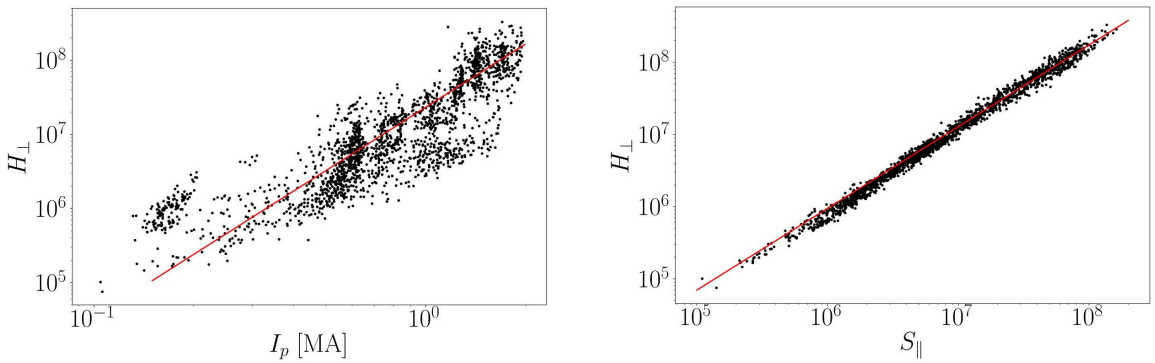

Figure 7.9: Perpendicular Braginskii Hartmann number as function of the plasma current with good correlation (a), Eq. 7.7 and the parallel Lundquist number with excellent correlation (b).

$$H_\perp = (23.2 \pm 0.9) \cdot 10^6 I_p^{2.84 \pm 0.08}, \quad [\text{MA}] \qquad r = 0.86, \tag{7.7}$$

$$H_\perp = (0.15 \pm 0.02) \cdot S_\parallel^{1.131 \pm 0.007}, \qquad r = 0.996. \tag{7.8}$$

If one addresses the high correlation of Eq. (7.8) by means of the relations (7.2) and (7.5), which represent the definitions of $S_{\parallel}$ and $H_{\perp}$, it is easily shown that $\gamma^{1/4} n^{1/2} T^{1/2}/B \propto const$, considering the assumption $T_i \propto T_e$. Neglecting the role of the mass number γ, the relation $nT/B^2 \propto const$ is found, which represents a confirmation of the narrow range of variation of the β parameter and of the magnetic Prandtl number, discussed in Sec. 7.5.
Moreover, the strong correlation between $S_{\parallel}$ and $H_{\perp}$ suggests:

- the possibility of studying interesting scaling laws with the perpendicular Hartmann number, without confuting the scaling with Lundquist number,
- the existence of an underlying correlation between transport dimensionless parameters, when they are evaluated on the RFX-mod database, according to classical Braginskii theory. This aspect is not seen in the numerical simulations, where the transport dimensionless parameter can be chosen with relative independence.

7.7 Summary and final remarks

In this Chapter the analysis of RFX-mod shots database has been presented aimed at the experimental evaluation of RFX-mod transport dimensionless parameters. The database is the result of several experimental campaigns made in the decade 2006-2016 on RFX-mod aimed at the study of the density limit, QSH regime, low plasma current regime and scaling laws. In this way the RFX-mod operational space is accurately represented.
The fluid dimensionless numbers are then evaluated, exploiting the formulas derived in Chp. 3 (temporarily limited to the classical Braginskii theory) and the measurements from the RFX-mod diagnostics. Three main points emerge from the statistical analysis of the results:

- The magnetic Prandtl number $P_{\perp}$ has a narrow range of variation. Being the latter directly proportional to the β plasma parameter, a confirmation that the β is almost constant in RFX-mod plasmas ($\beta_{\theta} \sim 3 - 4\%$) was given, in agreement with previous studies on RFP plasmas.
- The comparison of experimental fluid dimensionless number ranges with the SpeCyl simulation ranges show the existence of orders of magnitude differences, that are not easily fixable. This point requires a more detailed study on the plasma viscosity, which represent the major uncertainty plasma parameter of the model and it is addressed in Chp. 8.
- The existence of a hidden correlation between experimental fluid dimensionless numbers (not observed in input simulations parameters) is pointed out. In particular, the Lundquist number (used in the old scaling studies as independent variable) is highly correlated with the Hartmann number, which is shown to rule plasma helical regimes by MHD visco-resistive numerical simulations.

Chapter 8

Viscosity estimates on RFX-mod plasmas

Viscosity represents the transport coefficient which quantifies the rate of momentum transport. Despite the key role played by this coefficient in determining the dynamical regimes of reversed field pinch plasmas (through the dimensionless Hartmann number) in the framework of visco-resistive non-linear modelling (see Chp. 4), its experimental determination is still a wide open problem, Ref. Montgomery [1992]. Indeed, different transport theories exist, whose estimates differ by order of magnitude, making the viscosity the most uncertainty coefficient, deserving further studies.

In Sec. 8.1, the previous studies on plasma viscosity in reversed field pinch plasmas are presented, showing the presence of an important anomaly between the viscosity estimates

In Sec. 8.2, the kinematic viscosity coefficient is estimated according to classical (Braginskii) and turbulent (Ion Temperature Gradient, Finn) theories of transport, exploiting the RFX-mod data, from Chp. 7.

Such estimates are used in Sec. 8.3, to experimentally estimate the Hartmann number on RFX-mod shots, using the Spitzer formula for the resistivity, laying the groundwork for the comparison with SpeCyl numerical simulations, where the dimensionless Hartmann number represents an input parameter.

In Sec. 8.4, a first comparison (between simulations and experimental data) of the scaling relations linking the magnetic field instabilities and the RFP crash time to the Hartmann number is presented.

In Sec. 8.5, we present a preliminary analysis of the experimental data based on Bayesian data analysis techniques, which as pert of the visiting period at Ghent University and could be subject of future development of this work.

Summary and final remarks follow in Sec. 8.6.

8.1 Previous studies on RFP plasma viscosity

In this Section, we summarize the studies related to plasma viscosity experimental measurements, performed in the last decade in reversed field pinch devices.
As a first point, we state that these measurements are based on the study of plasma flow damping, consequent to the momentum injection by means of: a probe (biased electrode) or Resonant Magnetic Perturbations (RMP). In these experiments, the toroidal flow v_ϕ is usually measured by means of two methods: the Doppler effect spectroscopy to measure the impurity plasma flow and magnetic coils array to the measure the resonant tearing modes rotation velocity. The joint information from the two diagnostics allows to reconstruct the plasma flow profile $v_\phi(r)$. When the momentum injection is switched off, the plasma flow relaxes towards a stationary state, because of the viscous damping action. The same happens for the tearing modes rotation velocity, giving rise to the so called modes braking, which is modeled according to Ref. Fitzpatrick et al. [1999]. By means of a fitting procedure, the momentum slowing down time τ_{sd} can be inferred from the data, the kinematic perpendicular viscosity is consequently estimated as $\nu_\perp \sim \Delta r^2/\tau_{sd}$, being Δr the radial extension of the region considered. The main result of these studies is the evidence of an important viscosity anomaly δ, with respect to the estimates of the perpendicular viscosity according to the classical transport theory by Braginskii. The anomaly is defined as $\delta := \nu_\perp^{\text{meas}}/\nu_\perp^{Brag}$ and amounts up to some hundreds.
The results of the studied described are summarized in Tab. 8.1.

Ref.	# shots	Anomaly	Visc Estimate	Method	Device
Almagri et al. [1998]	20	$\delta \sim 92$	$\nu_\perp \approx 55\,\text{m}^2/\text{s}$	Probe	MST
Chapman et al. [2004]	18		$\tau_M \approx 1.3 - 2.1\,\text{ms}$	shell eddy currents	MST
Frassinetti et al. [2012]	4		$\nu_\perp \approx 2 - 40\,\text{m}^2/\text{s}$	RMP	EXTRAP T2R
Fridström et al. [2018]	9	$\delta \sim 4 - 340$	$\nu_\perp \approx 0.6 - 55\,\text{m}^2/\text{s}$	Probe, RMP	MST
Zanca et al. [2019]	2	$\delta \sim 150 - 500$	$\nu_\perp \approx 100\,\text{m}^2/\text{s}$	Braking exp.	RFX-mod

Table 8.1: Summary of the previous main studies related to plasma viscosity in RFP plasmas. We report the study reference paper, the number of shots, the viscosity anomaly, the viscosity estimate range and the method adopted and the RFP device considered.

The majority of the studies are related to the MST device: in Ref. Almagri et al. [1998], by means of biased electrode a viscosity of $\nu_\perp \sim 55\,\text{m}^2/\text{s}$ is estimated for 20 shots, corresponding to an almost two orders of magnitude anomaly. In Ref. Chapman et al. [2004], the global momentum confinement time τ_M is estimated evaluating the tearing modes braking due to eddy currents induced in the conducting shell. In Ref. Fridström et al. [2018] a detailed study based on both biased electrode and resonant magnetic perturbation is considered. It is shown that the viscosity scales as of the square amplitude of magnetic field fluctuations, which would confirm the dependence predicted by Finn, see Ref. Finn et al. [1992a]. In this case a The viscosity is estimated in the range $\nu_\perp \sim 0.6 - 55\,\text{m}^2/\text{s}$, which corresponds to a viscosity anomaly in the range $\delta \sim 4 - 340$. It is worth noting that the anomaly is non constant and it strongly depends on the plasma current.
On EXTRAP T2R, the kinematic viscosity spans the range $\nu_\perp \sim 2 - 40\,\text{m}^2/\text{s}$ as measured by means of resonant magnetic perturbations in Ref. Frassinetti et al. [2012].
On Ref. Zanca et al. [2019], a study on RFX-mod is presented, showing the viscosity $\nu_\perp \sim 100\,\text{m}^2/\text{s}$ and a large viscosity anomaly $\delta \sim 150 - 500$, on the base of RFX-mod modes braking. While studies in Ref. Almagri et al. [1998] and Ref. Fridström et al. [2018] show kinematic viscosity values compatible with the Finn estimate, in Ref. Craig et al. [2019] this compatibility is not found, even though observing an important anomaly with respect to the classical estimate. About this, a recent study in Ref. Chen et al. [2021] has questioned the hypothesis of quasi-linear response to magnetic field perturbation for fusion plasmas, putting in doubt the role of sound waves in fusion plasmas momentum transport (hypothesized by Finn theory), role mainly

played by the electrostatic turbulence.

8.2 Viscosity estimates on RFX-mod data

This Section deals with the estimate of plasma viscosity, on the RFX-mod database presented in Sec. 7.3, based on the transport theories presented in Chp. 3, used to model momentum transport in RFP: classical Braginskii (parallel, perpendicular and gyro), ITG theory, based on Ion Temperature Gradient and Finn theory, valid in presence of magnetic field stochasticity.
Since RFX-mod is not endowed with a diagnostic to measure the viscosity, we should rely on indirect estimates, based on transport theories and plasma parameters measurements.
To estimate the kinematic viscosity coefficient on RFX-mod, formulas in App. B.1 are exploited. For reasons of simplicity, we will evaluate the value of the viscosity in the core plasma, as we did for the plasma measurable parameters in Chp. 7, for each instant of detection of the Thomson scattering diagnostic.
The only additional hypothesis needed to the estimates are: the choice of the typical decay length of temperature and magnetic field $a_T = 0.2\,\mathrm{m}$ and $a_B = 0.8\,\mathrm{m}$ (see Ref. Guo et al. [1994]), in the ITG viscosity estimate and the strongly simplifying choice of the constant auto-correlation length in the Finn viscosity estimate, evaluated as: $L_c = 1.4\,\mathrm{m}$ according to Ref. Ciaccio et al. [2013].
The results of the viscosity ranges are shown in Fig. 8.1.

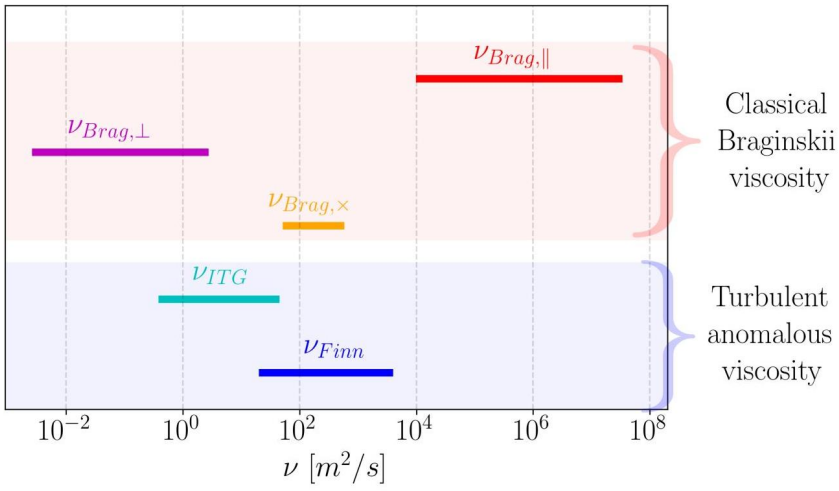

Figure 8.1: Kinematic viscosity range, evaluated on RFX-mod experimental database, according to the classical Braginskii (parallel, perpendicular, gyro) and turbulent (ITG, Finn) theory. Orders of magnitude differences are displayed by the different evaluations.

Orders of magnitude differences are displayed by the different estimates (Fig. 8.1). In particular, we preliminary notice that the parallel Braginskii viscosity $\nu_{\parallel}$ interval values have no overlap with any of the other estimates. On the contrary, the perpendicular viscosity $\nu_{\perp}$ overlaps with the ITG viscosity interval ν_{ITG}, while the gyro-viscosity, the ITG viscosity ν_{ITG} the Finn viscosity ν_{Finn} have comparable orders on the RFX-mod database.
This makes it difficult to make a comparison based solely on the viscosity absolute value and stimulates the search for a comparison method that takes into account also the functional dependencies of the viscosity coefficients. The line followed in this work, is based on the comparison of the scaling relations involving the Hartmann number between SpeCyl numerical simulations (see Sec. 4.5) and experimental data, elaborated in Sec. 8.4, as suggested in Ref. Bonfiglio et al. [2014].

8.3 Hartmann number estimates on RFX-mod data

This Section is devoted to the estimate of the Hartmann number, on the basis of RFX-mod experimental data. Since the dimensionless Hartmann number is jointly determined by resistivity and viscosity by means of the formula $H := aB_0/\sqrt{\eta\mu}$, an estimate of both the transport coefficients is required.
To estimate the plasma resistivity, we use the Spitzer resistivity formula, reported in App. B.1. This choice is still matter of discussion because a recent work has pointed out in Ref. Saad and Brunsell [2022] the need for an order of magnitude anomaly of the resistivity in order to obtain a quantitative agreement between the linear resistive MHD model predictions and resonant modes growth rate measurements on the EXTRAP T2R reversed-field pinch device. On the contrary, in Ref. Trintchouk et al. [2003] and Ref. Kuritsyn et al. [2006] a remarkable agreement is shown between the Spitzer estimate and the experimental measurements of the resistivity during magnetic reconnection experiments in collisional regime.
The five different estimates developed in Sec. 8.2 are used as plasma viscosity estimates and gives rise to five different estimates of the Hartmann number, whose range are reported in Fig. 8.2, next to the values of the Hartmann number used as input for SpeCyl simulations.

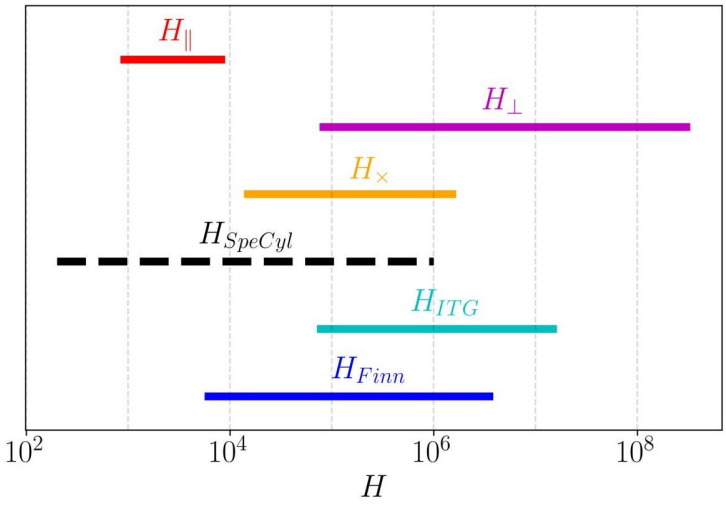

Figure 8.2: Hartmann number ranges: as input parameter of the SpeCyl code (dashed line), evaluated on RFX-mod experimental database (continuous line), using Spitzer resistivity and the viscosity evaluations from Fig. 8.1.

Comparing the different Hartmann number estimates we notice that they all partially overlap the range of the input SpeCyl simulations values, but none of them exactly overlaps, making necessary a more refined comparison method.

8.4 SpeCyl MHD simulations and experimental data comparison

This section aims at preliminary figuring out the model for viscosity with the highest adherence to experimental data. To reach this goal, the Hartmann number estimates from Sec. 8.3 are considered, we compute the power-law scaling ($y = CX^\alpha$, with ordinary least square method fit), of the normalized temporal scales of reconnection events $\bar{\tau}_{crash}$ and of $m = 0$, $m = 1$ secondary modes as function of the Hartmann number, which rules the MHD dynamics.
For the first scaling, we consider the normalization $\bar{\tau}_{crash} := \sqrt{\eta/\nu}\,\tau_{crash}$: the normalization factor comes from the change of coordinates described in Ref. Cappello and Escande [2000] and it is required to evaluate the scaling on the Hartmann number. We estimate the reconnection

time τ_{crash} as the interval between the maximum and the minimum value of the edge axial magnetic field, during a reconnection event Veranda et al. [2020]. For the second and the third scalings, we consider the following quantities to represent the secondary modes:

$$B^z_{0,sec}(a) := \sqrt{\sum_{\substack{-9\leqslant n\leqslant -1 \\ n\neq -7}} B^z_{0,n}(a)^2}, \qquad B^z_{1,sec}(a) := \sqrt{\sum_{-20\leqslant n\leqslant -8} B^z_{1,n}(a)^2},$$

where the $m = 0$, $n = -7$ mode is excluded to avoid considering toroidal effects, in the comparison with the cylindrical code SpeCyl, as did in Sec. 4.5. In Fig. 8.3, the plots of $\bar{\tau}_{crash}$, $m = 0$ and $m = 1$ secondary modes as function of the five different evaluations of the Hartmann number are shown. The same scalings are computed also for a wide database of SpeCyl simulations (with flat viscosity profile), varying both the absolute values of the dimensionless transport coefficients and the intensity of non-ideal magnetic field boundary conditions Veranda et al. [2019]. In this case the Hartmann number is determined by the input central values of dimensionless resistivity η_0 and viscosity ν_0: $H_{SpeCyl} := 1/\sqrt{\eta_0\nu_0}$. The fit coefficient of variation r and the scaling slope α values are shown in Tab. 8.2, referring to both simulations and experimental data.

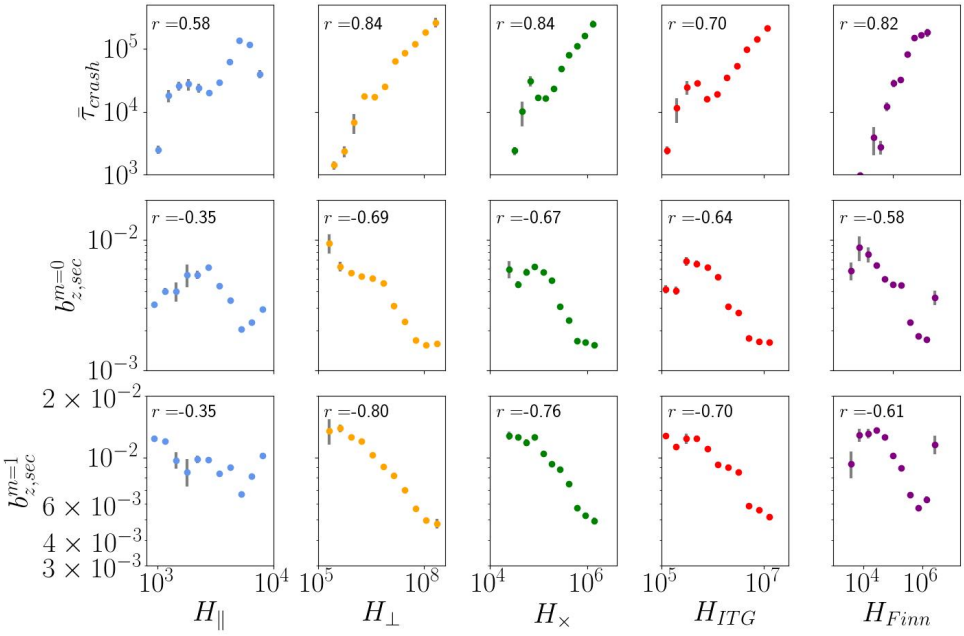

Figure 8.3: Plot of reconnection events time scale, $m = 0$ and $m = 1$ secondary modes as function of the Hartmann number, evaluating the kinematic viscosity according to the momentum transport theories, described in Chp. 3. For each plot the scaling regression coefficient r is reported. Data are averaged over equal logarithmic intervals of the Hartmann number.

Analyzing the values of the correlation coefficient r we notice that: $H_\parallel$ has little correlation with the secondary modes, while the ITG and Finn estimates of the viscosity produce a correlation coefficient lower than the remaining cases, so these estimates do not represent the best possible choice for the viscosity coefficient evaluation. In support of this, we list some drawbacks related to the Finn viscosity estimate. The coefficient of variation values of the scalings involving $m = 0$ and $m = 1$ secondary modes are lower than in the other cases, despite the definition of the viscosity as function of the secondary modes itself. The hypothesis of quasi-linear response to magnetic field perturbation is rarely satisfied Chen et al. [2021], as the hypothesis of uniformly chaotic transport Rechester and Rosenbluth [1978], since more recent studies have shown the non-uniformly chaotic and sub-diffusive nature of transport in RFP plasmas Spizzo et al. [2009],

	α			r		
	$\bar{\tau}_{crash}$	$b^z_{0,sec}(a)/B_0$	$b^z_{1,sec}(a)/B_0$	$\bar{\tau}_{crash}$	$b^z_{0,sec}(a)/B_0$	$b^z_{1,sec}(a)/B_0$
H_{SpeCyl}	0.72 ± 0.05	-0.27 ± 0.05	-0.35 ± 0.03	0.84	-0.76	-0.90
$H_\perp$	0.74 ± 0.02	-0.240 ± 0.009	-0.204 ± 0.004	0.84	-0.69	-0.80
$H_\times$	1.21 ± 0.03	-0.34 ± 0.01	-0.300 ± 0.006	0.84	-0.67	-0.76
$H_\parallel$	1.68 ± 0.09	-	-	0.58	-0.35	-0.35
H_{ITG}	0.95 ± 0.03	-0.24 ± 0.01	-0.218 ± 0.005	0.70	-0.64	-0.70
H_{Finn}	1.14 ± 0.05	-0.33 ± 0.01	-0.271 ± 0.007	0.82	-0.58	-0.61

Table 8.2: Scaling slope (with uncertainty) and coefficient of variation for the power-law fit of normalized temporal scales of reconnection events and secondary ($m = 0$ and $m = 1$) modes as function of the Hartmann number for both SpeCyl simulations and experimental data evaluation. The highest coefficients of variation and the scaling slope with the best agreement with the simulations are highlighted.

Auriemma et al. [2015].
We observe that the estimate $\nu_\perp$ maximizes the correlation of all quantities, followed by $\nu_\times$. In addition, $\nu_\perp^{Brag}$ and $\nu_\times^{Brag}$ display a good level of adherence for the scaling slope (α) of the reconnection events temporal scale $\bar{\tau}_{crash}$ and $m = 1$ secondary modes respectively. The quantitative comparison between simulations and experimental data (Fig. 8.4) shows that the experimental data match quite well the decreasing trend (at high Hartmann) of the simulations, however displaying a non monotonous trend of $m = 0$ modes for the $\nu_\times$ (Fig. 8.4 (a)) and the existence of an offset in the scaling involving $\nu_\perp$ (Fig. 8.4 (b), (d)). A comparison of the power-law fitting regression coefficients showed that the offset corresponds to a multiplicative factor $\delta \sim 250$ for the perpendicular Braginskii viscosity. Furthermore, we observe that the anomaly factor δ shows a slight variation in the $m = 0$ and $m = 1$ secondary modes scaling, as the Hartmann number is varied.
In the case of the perpendicular viscosity even the domains in the Hartmann number of SpeCyl simulations and experimental data differ significantly. To overcome this difference is a hard task, since the computational time of the simulations increases as the Hartmann number is increased, while experimental data points with lower $H_\perp$ would require high density, low plasma current and low temperature shots, see Eq. (7.5), beyond the RFX-mod operational limits.

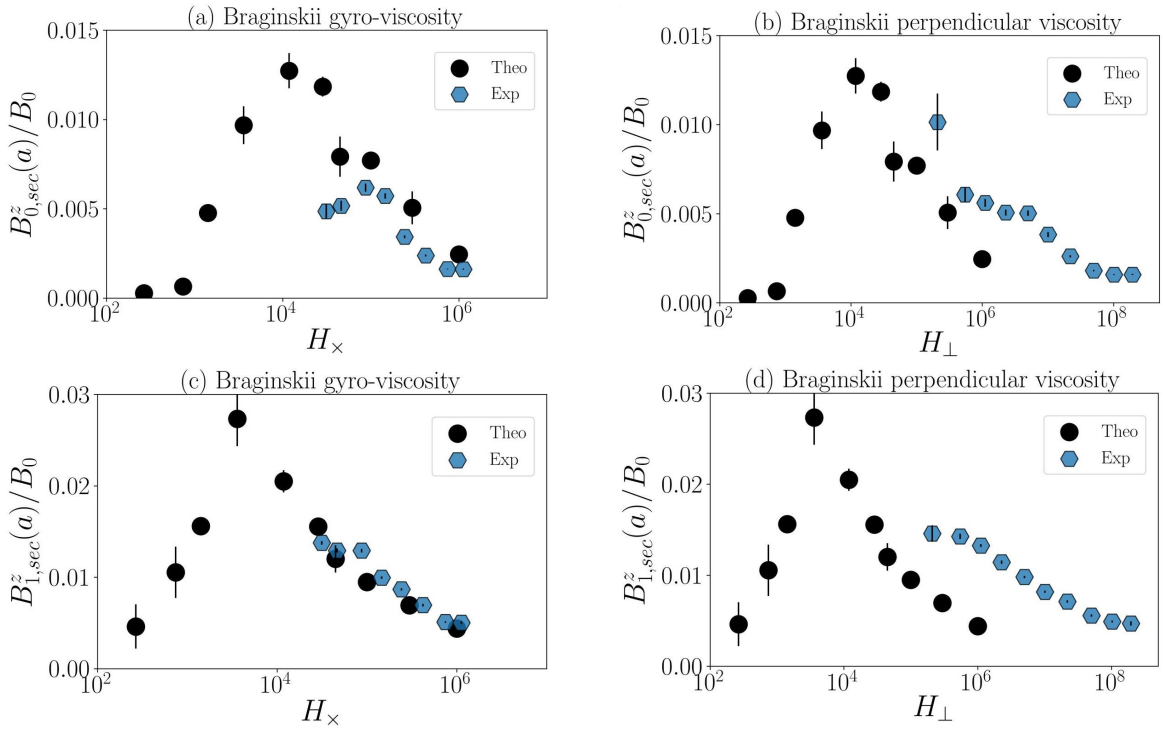

Figure 8.4: Plot of $m = 0$ and $m = 1$ secondary modes as function of the Hartmann number, evaluated considering perpendicular (b), (d) and gyro (a), (c) Braginskii viscosity, comparing SpeCyl simulations and experimental data. Simulations and data are averaged over equal logarithmic intervals.

8.5 Applications of Bayes' theorem in RFX-mod data analysis

This Section summarizes a preliminary work carried out in collaboration with Ghent University (De Rycke et al. [2022]) aiming to establish which among the five viscosity estimates provides the major contribution in maximizing the agreement between SpeCyl numerical simulations and RFX-mod data, exploiting advanced Bayesian data analysis methods.
Bayes' theorem represents a powerful tool in advanced data analysis, with applications to model comparison and robust regression (Ref. Bishop [2006]). In particular, bayesian data analysis plays a key role in fusion Science research, see Ref. Verdoolaege et al. [2021]. In the next paragraphs, we briefly introduce the fundamentals of Bayes' theorem, before discussing the potential applications to this work.
A necessary first premise is that Bayes' theorem always involve conditional probability: $P(A|B)$ (i. e. probability of A 'given' B), defined by the relation: $P(A|B) = P(A \cap B)/P(B)$, being A, B two events with respectively probabilities $P(A)$ and $P(B)$. In the framework of discrete probability Bayes' theorem is written as follows:

$$P\left(A|B\right) = \frac{P\left(B|A\right)P\left(A\right)}{P\left(B\right)}, \tag{8.1}$$

where the following naming is usually adopted: *conditioning* or *posterior*: $P(A|B)$, *likelihood*: $P(B|A)$, *prior*: $P(A)$ and *marginal*: $P(B)$.
The most interesting applications in advanced data analysis involve continuous probability distributions. Indeed, in bayesian analysis, probability is used to quantify the uncertainty and, for this reason, each variable is defined by a probability distribution function. In this case, if one chooses $\mathbf{w}$ as a parameter to estimate (e. g. models fitting parameters in a regression problem) and $P(\mathbf{w})$ its probability distribution, the Bayes' theorem writes as follows:

$$P(\mathbf{w}) = \frac{L(\mathbf{w})\pi(\mathbf{w})}{Z}, \tag{8.2}$$

where the four terms represent the following quantities:

- *posterior*: $P(\mathbf{w})$ represents the Bayesian solution of the regression problem. Distribution probability of the fitting parameters, given the data points.
- *likelihood*: $L(\mathbf{w})$ represents the discrepancy or misfit between the data and the model function
- *prior*: $\pi(\mathbf{w})$ describes the background knowledge
- *evidence*: Z it's a normalizing constant and does not depend on $\mathbf{w}$

In the next two subsections two applications of the Bayes theorem to the RFX-mod database are presented.

8.5.1 Bayesian model comparison of the viscosity estimates

The Bayes' theorem represents a useful tool in comparing the description of a set of experimental data $\mathcal{D}$ according to different models $\mathcal{M}_k$.
In the case in analysis, the set of the data is represented by the RFX-mod measurements data: $\mathcal{D} = (n, T_e, T_i, B_0, \gamma, Z_{eff}; b_\phi^{0,sec}(a), b_\phi^{1,sec}(a))$. While the five different models to be compared are the power laws scaling of edge magnetic field $m = 0$ and $m = 1$ modes as function of the five Hartmann numbers, depending on the viscosity theory used to estimate them: $\mathcal{M}_k$, $(b_\phi^{0,sec}(a), b_\phi^{1,sec}(a), \tau_{saw}) = CH^\alpha$, where H can be $H_\parallel$, $H_\perp$, $H_\times$, H_{ITG}, H_{Finn}, depending on the k model considered. The Bayes' theorem is so written, considering mutually exclusive models, aiming at the determination of $p(\mathcal{M}_k|\mathcal{D})$, which represents the probability of the k^{th} model, given the data-set:

$$p(\mathcal{M}_k|\mathcal{D}) = \frac{p(\mathcal{D}|\mathcal{M}_k)p(\mathcal{M}_k)}{p(\mathcal{D})} \propto p(\mathcal{D}|\mathcal{M}_k)p(\mathcal{M}_k) \propto p(\mathcal{D}|\mathcal{M}_k), \tag{8.3}$$

where, we consider $p(\mathcal{D})$ to be a constant, not depending on the model choice and we make the additional hypothesis that $p(\mathcal{M}_k)$ is equal for all the models. Finally, only the *evidence* $p(\mathcal{D}|\mathcal{M}_k)$ remains. This term is usually computed by means of the following integral:

$$p(\mathcal{D}|\mathcal{M}_k) = \int p(\mathbf{f}|\mathcal{M}_k)p(\mathcal{D}|\mathbf{f}, \mathcal{M}_k)d\mathbf{f}, \tag{8.4}$$

where $\mathbf{f}$ represents the vector made with the fitting coefficients, parameters of the regression problem, see Sec. 8.5.2. There are specifically devoted Python routines (e. g. `dynesty` and `pymc3`) to compute the integral in $d\mathbf{f}$ and the so called *Bayes' factor* $Z_{i,j}$ between two models i, j:

$$Z_{i,j} = \frac{p(\mathcal{M}_i|\mathcal{D})}{p(\mathcal{M}_j|\mathcal{D})}, \tag{8.5}$$

allowing the order of the five viscosity theories, according to their probability of describing the power-law scaling of the secondary modes as function of the Hartmann number. The final classification of the models is the following (from the most probable to the less probable): $\nu_\perp$ $\nu_\times$, ν_{ITG}, ν_{Finn}, $\nu_\parallel$.
This is agreement, with the less refined comparison made in Sec. 8.4.

8.5.2 Bayesian regression of edge magnetic field instabilities as function of the Hartmann number

Advanced regression techniques are widely used in fusion science research. In particular, their role is fundamental in experimental scaling representing the only reliable method to predict some fundamental physical quantities (e. g. the energy confinement τ_E), see Ref. Verdoolaege et al. [2021]. In this subsection, we present the bayesian regression method application to the fit of edge magnetic field modes as function of the Hartmann, which basically confirms the results we get in Sec. 8.4. As for the model comparison problem, the main variables to write the problem are:

- the dataset: $\mathcal{D} = (n, T_e, T_i, B_0, \gamma, Z_{eff}; b_\phi^{0,sec}(a), b_\phi^{1,sec}(a), \tau_{saw})$
- a model (i. e. the fitting law): $\mathcal{M}_k$, $(b_\phi^{0,sec}(a), b_\phi^{1,sec}(a), \tau_{saw}) = CH^\alpha$, where H can be $H_\parallel$, $H_\perp$, $H_\times$, H_{ITG}, H_{Finn}, depending on the k model
- the fitting parameters: $\mathbf{f} = (C, \alpha)$, which represent the quantities to be determined.

The regression parameter distribution function can be rewritten by means of the Bayes' theorem:

$$p(\mathbf{f}|\mathcal{D}, \mathcal{M}_k) = \frac{p(\mathbf{f}|\mathcal{M}_k)p(\mathcal{D}|\mathbf{f}, \mathcal{M}_k)}{p(\mathcal{D}|\mathcal{M}_k)}, \tag{8.6}$$

where $p(\mathbf{f}|\mathcal{M}_k)$ represents the prior, which we set as a uniform distribution for the coefficient $C \sim \mathcal{U}(0, 1)$ and as a Gauss distribution for the slope α with the mean and the standard deviation given by SpeCyl simulations fit (see Sec. 4.5), $p(\mathcal{D}|\mathbf{f}, \mathcal{M}_k)$ represents the likelihood and $p(\mathcal{D}|\mathcal{M}_k)$ represents the evidence and it acts as normalization. The likelihood is computed by means of `pymc3` routines and exploiting the formula:

$$p\left(\mathcal{D}|C_k, \alpha_k, H_k^*\right) = p\left(\mathcal{D}|C_k, \alpha_k, H_k(n^*, T_e^*, T_i^*, B_0^*, \gamma^*, Z_{eff}^*, ...)\right), \tag{8.7}$$

Where the * represents the true value of the quantity.
In Fig. 8.5 and 8.6 the Bayesian fit result is superimposed to ordinary least square prediction, showing a high level of agreement.

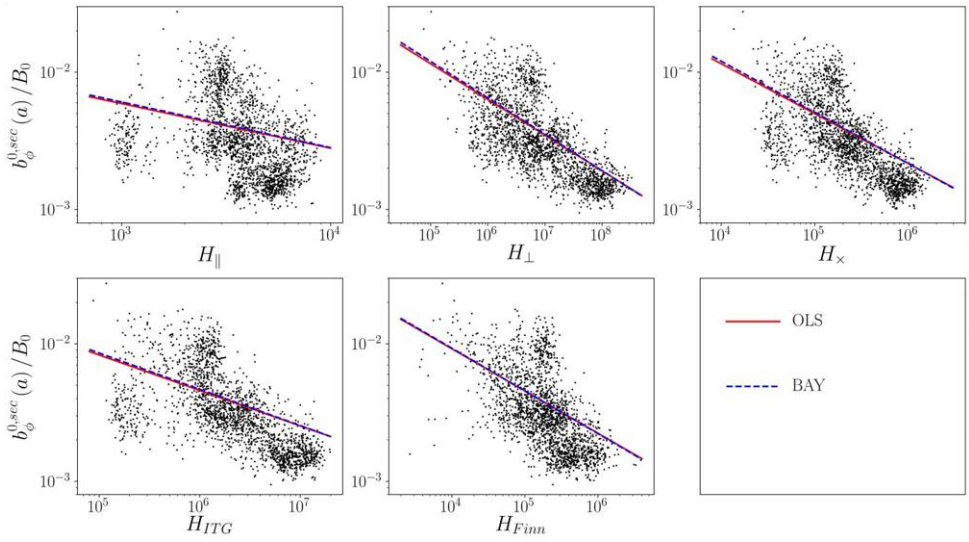

Figure 8.5: Fit of $m = 0$ magnetic field instabilities as function of the Hartmann number, evaluated according to five different theories. The Ordinary least square fit (OLS) and the Bayesian method described in this section (BAY), gives comparable results.

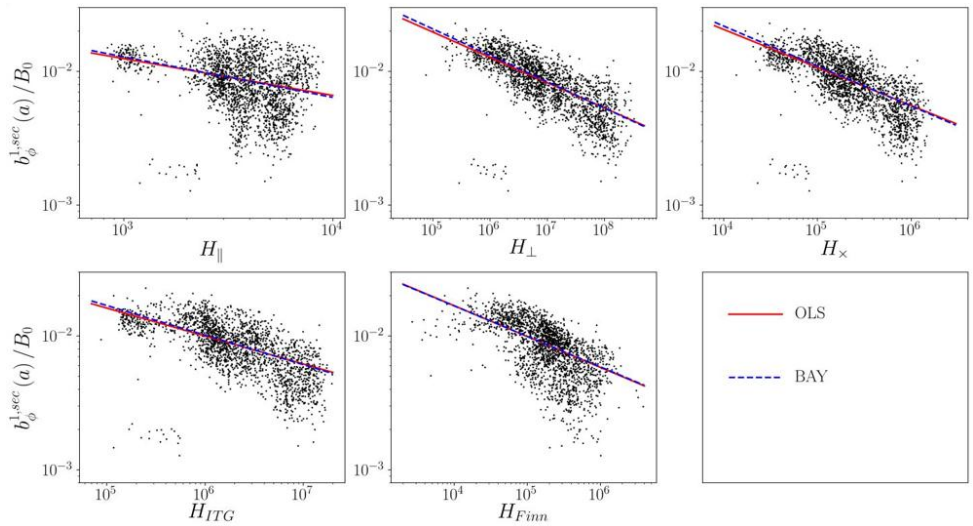

Figure 8.6: Fit of $m = 1$ magnetic field instabilities as function of the Hartmann number, evaluated according to five different theories. The Ordinary least square fit (OLS) and the Bayesian method described in this section (BAY), gives comparable results.

8.6 Summary and final remarks

In this Chapter, we analyze the problem of the viscosity estimate in Reversed Field Pinch plasmas. The previous studies, mainly consisting of measurements based on plasma flow perturbation, have shown the presence of an important viscosity anomaly (between the measured viscosity and the Braginskii estimate). Even if the Finn viscosity estimate matches the experimental data quite well, there are studies which questions the role of sound waves in momentum propagation and the uniformly chaotic nature of the magnetic field, making the estimate of RFP plasma viscosity still an open problem.
To figure out a viscosity estimate for RFX-mod plasmas, the kinematic viscosity has been evaluated according to different theories of transport (classical Braginskii, ITG and Finn) on the RFX-mod database shots. Using the Spitzer resistivity formula, also the Hartmann number has been evaluated, according to different theories of transport. Important differences in the ranges are highlighted for both the kinematic viscosity and the Hartmann number, making necessary a refined comparison to select the viscosity estimate which maximizes the agreement between SpeCyl simulations and experimental data.
Comparing the scaling laws of edge magnetic field $m = 0$ and $m = 1$ modes and average crash times as function of the Hartmann number, it was possible to show that the agreement (in terms of coefficients of variation and slope scaling fit) is maximized by the perpendicular Braginskii viscosity (followed by the Barginskii gyro-viscosity), despite showing an important offset in the Hartmann which is translated in viscosity anomaly $\delta \sim 250$. This result is confirmed by a preliminary study based on Bayesian model comparison, which will be matter of further analysis in the future. In fact, according to the preliminary result, the perpendicular Braginskii viscosity maximizes the Bayes factor, followed by the Braginskii gyro-viscosity.
Several future developments could be considered for this work: to calculate the uncertainties propagation from the plasma measured quantities to the Hartmann number, to test whether the resistivity is anomalous too and to consider the possibility of joint contributions from distinct theories to the viscosity.

Chapter 9

Magneto-fluid origin of the RFP density limit

This Chapter represents the arrival point of this work. Indeed, the estimate of transport dimensionless parameters, developed in Chp. 7, and refined in Chp. 8 is applied to better understand the reversed field pinch density limit. The latter is a non-disruptive limit which restricts the operational space of RFP devices. Since experimental analysis show that $m = 0$ geometry instabilities play a key role in determining the density limit, we will link the onset of the latter to the $m = 0$ secondary modes ruling parameter in visco-resistive MHD simulations, i. e. the Hartmann number, see Chp. 4.
Sec. 9.1 deals with the problem of the density limit in fusion plasmas. In particular, a simple picture of fusion science research in this field is sketched out, from the Greenwald phenomenological parameter to the theories which try to explain the density limit on the basis of turbulence, MHD and power-balance.
Sec. 9.2 presents the density limit studies focused on the RFP configuration, performed in Padova on both the RFX and the RFX-mod devices in the past decades.
In Sec. 9.3, the MARFE phenomenology is described. In the reversed field pinch, this is a high density, highly radiative plasma ring with poloidal symmetry, that is triggered by the growth of $m = 0$ magnetic islands. This radiative phenomenon is identified as a potential cause of the high density discharge discharge termination.
In Sec. 9.4, the relation between the MARFE onset and the experimentally estimated Hartmann number is investigated. In particular a specific threshold in H is found, below which the MARFE represents the dominant radiative phenomenon. Exploiting the Hartmann definition, the latter threshold can be rewritten as a density threshold (which scales as B^2T), above which the MARFE is most frequently detected.
In Sec. 9.5, the RFP plasma phenomenology is analyzed as the Hartmann number is decreased, comparing SpeCyl numerical simulations and the RFX-mod experimental data. The main effect observed is the progressive growth of secondary (both $m = 0$ and $m = 1$) modes which give rise to the main phenomena characterizing the reversed-field pinch plasmas. In fact, common thresholds for the QSH-MH transition, the MARFE onset and the high density limit (above which no shots are performed) are identified on both RFX-mod data and SpeCyl simulations.
Summary and final remarks follow in Sec. 9.6.

9.1 Framework of density limit research

In this Section we provide a brief summary of the studies on the density limit in fusion plasmas research, without claiming of carrying out the subject in an exhaustive way, but with the aim of framing the original work done in this Thesis.
As anticipated in Sec. 1.7, the density limit is an operational limit which severely restricts the operational space of fusion devices and it represents a key topic to be understood in view of the future fusion experiments and reactors. In the next subsections, the Greenwald phenomenological parameter, frequently used to describe the density limit, is introduced, followed by the theories most frequently used to described this phenomenon grouped on the basis of the explanation framework given (based on turbulence and zonal flows or on magnetohydrodynamics and magnetic island formations or power balance).

9.1.1 Greenwald phenomenological parameter

One of the first work which systematically studies the density limit is found in Ref. Murakami et al. [1976], where the maximum achievable density in tokamak plasmas is shown to be related to the plasma current. In particular, the operating parameters were firstly parameterized by the ratio I/N, being I the plasma current and N the number of particles per unit toroidal length. In Ref. Greenwald et al. [1988] and Ref. Greenwald [2002] wide databases of density limit relevant shots collected from different devices for both the tokamak and the reversed field pinch configurations are studied. These studies have brought to the definition of a phenomenological parameters, quantifying the maximum achievable line average density, the so called *Greenwald density* n_G:

$$\bar{n}\left(10^{20}\,\mathrm{m}^{-3}\right) < \frac{I\,(\mathrm{MA})}{\pi a^2\,(\mathrm{m}^2)} =: n_G\left(10^{20}\,\mathrm{m}^{-3}\right). \tag{9.1}$$

This parameter is widely used in fusion science research because it provides an effective rule of thumb to describe the density limit and it is expressed as function of easily measurable input parameters of the shot and it is derived on the basis of the a multi-machine database. The main problem related to the Greenwald scaling is the absence of first principle derivation, that inserts the Greenwald parameter into a solid theoretical construction (see Ref. Hawryluk and Zohm [2019] and Ref. Sarazin et al. [2019]). This explanation could pertain to radiation, transport or turbulence physics and still represents an open problem in fusion plasma physics.
Despite with a different outcome, the Greenwald scaling involves both tokamak (disruptive limit) and reversed field pinch (discharge termination). Differently, the stellarators have a different phenomenology (see Ref. Sudo et al. [1990]), which involves an important dependence on the input power. The critical density is defined by the so called *Sudo limit*:

$$n_c\left(10^{20}\,\mathrm{m}^{-3}\right) = 0.25\frac{P^{0.5}\,(\mathrm{MW})\,B_0^{0.5}\,(\mathrm{T})}{a\,(\mathrm{m})\,R_0^{0.5}\,(\mathrm{m})}, \tag{9.2}$$

being P the absorbed power by the plasma, B_0 the on-axis magnetic field, a, R_0 the minor a and major radius R_0.

9.1.2 Turbulence based theories

There is a wide range of studies aimed at investigating the role of turbulence in determining the density limit phenomena.
Zonal flows are plasma flows in the poloidal direction, constant on the magnetic surface, but strongly varying in the radial direction. This flow is originated by the $\mathbf{E}\times\mathbf{B}$ interaction between the perturbation of the toroidal electric field in the radial direction and the toroidal magnetic field. More details on zonal flows can be found in Ref. Diamond et al. [2005]. The strong

variation in the radial direction gives rise to a shear layer, mainly localized in the edge region. In Ref. Singh and Diamond [2021a], the Greenwald limit is shown to be linked to the edge shear layer collapse. In particular, the dimensionless parameter which describes the shear layer collapse is computed: $\rho_s/\sqrt{\rho_{sc}L_n}$, being ρ_s, ρ_{sc} and L_n, respectively the ion sound radius, the zonal flow screening length and the equilibrium density scale length. A critical value for the edge density (which scales with the plasma current) is found to determine the edge shear layer collapse.
In Ref. Singh and Diamond [2021b] the theory based on zonal flows is also extended to other important phenomenology of tokamak plasmas, like the L-H transition between the low and the high confinement phase.

9.1.3 Magnetohydrodynamics theories

This approach relates the density limit instability to the plasma magnetohydrodynamics activity, often related to tearing modes.
A first work belonging to this research line is found in Ref. Granetz [1982], where it is shown that relevant magnetohydrodynamics activity is found only if a certain line-averaged density threshold $\bar{n}_c$ is overcome. Analyzing data from Alcator C this threshold is found to depend on the on-axis magnetic field B_0 according to: $n_c \propto B_0^2$. It is worth noticing that a similar scaling is found in Ref. Pucella et al. [2017], studying FTU shots and also in Ref. Carati et al. [2012], on the basis of a perturbation approach to evaluate the density threshold above which chaos arises in the electron (single particle) gyro-motion.
The origin of the MHD activity is often associated to thermal destabilization (see Ref. Rebut and Hugon [1985]), which it is found to favour the growth of the $m = 3$, $n = -1$ and $m = 4$, $n = -1$ magnetic islands Ref. Suttrop et al. [1997]. In Ref. Gates and Delgado-Aparicio [2012] and Ref. White et al. [2015], the thermal island destabilization mechanism is compatible with the Greenwald scaling describing the density limit.
In Ref. Chang et al. [2019], it is shown that the island can also be the cause of destabilization (and not only a consequence) by means of ambipolar potential and related plasma flows near the separatrix X-point.

9.1.4 Power-balance theories

A first interpretation of the fusion devices density limit in terms of power balance can be found in Ref. Wesson and Campbell [2011]. This approach is based on the study of the energy balance equation in a 1D cylindrical model (see Ref. Zanca et al. [2017]), where each quantity depends on the plasma radius r, typically including: heat conduction input power contribution (due to both Ohmic heating and auxiliary heating systems) and radiation losses by light impurities. The limiting density is found imposing in the solution of the magneto-thermal equilibrium a realistic temperature profile, resulting in a Sudo-like scaling for the stellator, a modified Greenwald-scaling $\propto I_p^{8/9}$ for the RFP and the Ohmic tokamak and a mixed scaling $\propto I_p^{4/9} P^{4/9}$, bringing to light a long-neglected power dependency of the density limit (see Ref. Zanca et al. [2019]).
The model has been refined, also exploiting additional experimental data available (Ref. Zanca et al. [2022]). A further upgrade of the model is presented in Ref. Escande et al. [2021] accounting for a delay between the radiation of power and the production of radiating impurities on the divertor. This phenomenon is known as Plasma-Wall Self Organization (PWSO) and points out the role of radiation in the density limit which can take place also for value of the radiated power which equalizes only half of the input power. A possibility to relax such limit is found in reducing the impurity production during the start up, goal that can be achieved using electron cyclotron resonance heating system during the ramp-up phase of the discharge.

9.2 Density limit studies on RFX and RFX-mod devices

This Section is devoted to summarize the studies about the reversed field pinch density limit on the RFX and RFX-mod devices. This is necessary because the original part of this Chapter can be considered as the next step after the mentioned studies. It is useful to recall that, although non disruptive, the high density limit represents a strong bound to RFP performance devices, because shots with $n > n_G$ are not observed in RFX-mod, except for very low plasma current values.
A first study of RFP density limit is found in Ref. Ortolani and Rostagni [1983], where the critical density density is shown to scale with I/N on ETA-BETA II. The phenomenology of the reversed field pinch density limit has been analyzed also on RFX (Ref. Valisa et al. [2005]) and RFX-mod (Ref. Valisa et al. [2006]). In particular, it is shown that the description given by the Greenwald parameter is matched fairly well in the ranges of current analyzed. In addition, it is shown that a plausible cause of the soft discharge termination is the presence of a toroidally localized and poloidally symmetric radiation which cools the plasma core. It is also observed that the local radiation takes place at values of global radiated power well below the total Ohmic input. In Ref. Puiatti et al. [2009b], Ref. Puiatti et al. [2009a] and Ref. Spizzo et al. [2010] the relation between the poloidal symmetric radiation ($m = 0$ geometry) and the density limit is investigated, showing a preliminary relation between $m = 0$ topology magnetic field instabilities and the approach to the density limit, shown in Fig. 9.1, consisting of the growth of $m = 0$ edge magnetic field instabilities as the phenomenological ratio n/n_G is increased.

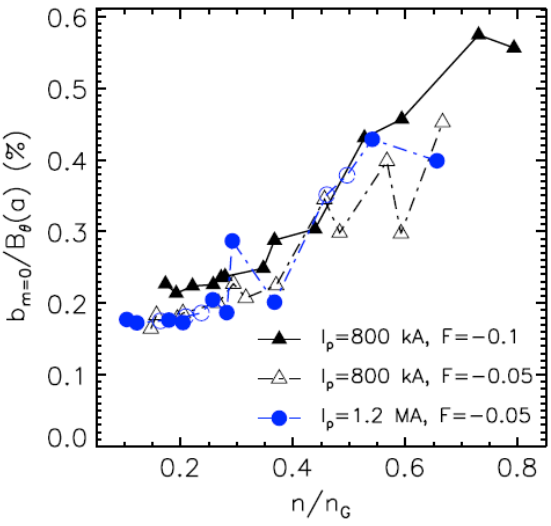

Figure 9.1: Plot of the $m = 0$, $-6 \leqslant n \leqslant -1$ modes normalized magnetic field perturbation as function of the ratio n/n_G: the entity of such modes grows approaching the density limit. Picture adapted from Ref. Spizzo et al. [2010].

The mechanism linking the edge magnetic field instabilities to the poloidally symmetric radiation, named MARFE (Multifaceted Radiation From the Edge) has been furthered investigated during the years, enlarging the RFX-mod database, in Ref. Spizzo et al. [2014] and Ref. Spizzo et al. [2015]. The data points are shown in Fig. 9.2 in the so called 'Greenwald plane', showing the low density (side of the runaway electrons) and high density (side of the Greenwald limit, $n = n_G$). We will not discuss further the MARFE onset mechanism because it is argument of the next Section. The high density is also proved to have important effects on the edge turbulence, for density values $n/n_G > 0.4 - 0.5$, see Ref. Agostini and Scarin [2019]

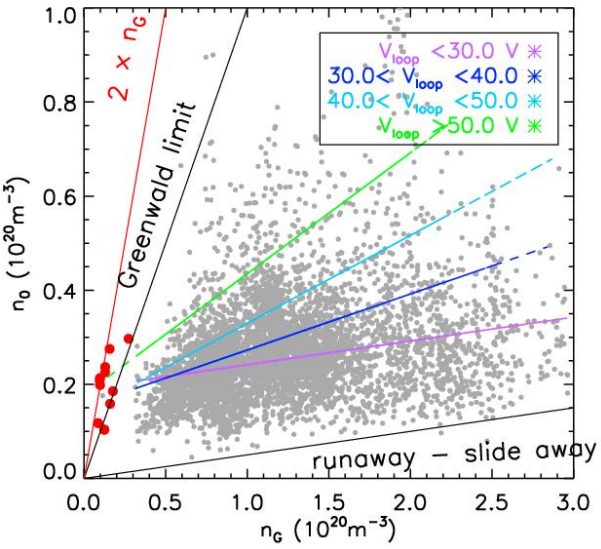

Figure 9.2: Operational space of RFX-mod in the Greenwald plane: straight lines are interpolation of points grouped according to values of loop voltage, which is proportional to the ohmic input power. Red points are discharges at low current and $n_0 \sim n_G$. Picture adapted from Ref. Spizzo et al. [2015].

9.3 The role of MARFE and edge magnetic field instabilities in triggering the RFP density limit

This Section is devoted to the MARFE (Multifaceted Asymmetric Radiation From the Edge) phenomenon, which is reviewed in Ref. Lipschultz [1987] and Ref. Tokar et al. [1999], for the tokamak configuration. A first clarification is necessary: the MARFE in tokamak and RFP configurations have completely different geometry, as shown in Fig. 9.3.

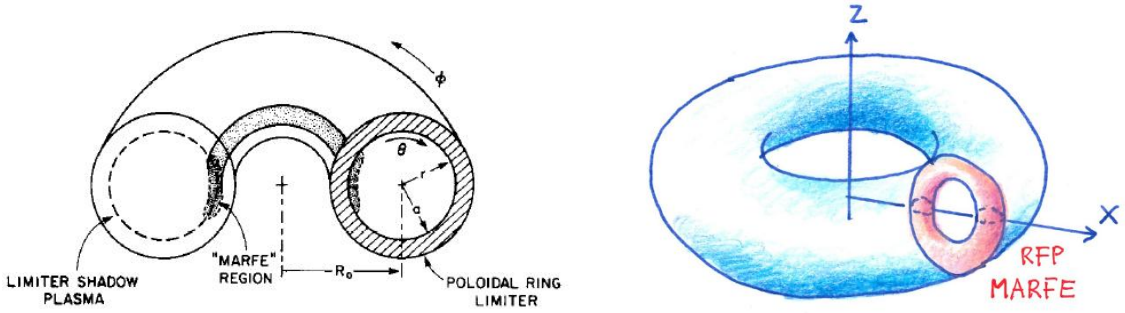

(a) (b)

Figure 9.3: Schematic comparison between the MARFEs: in tokamak, toroidal symmetry, poloidally localized, $n = 0$ geometry (a), from Ref. Lipschultz [1987] and in RFP, poloidal symmetry, toroidally localized, $m = 0$ geometry (b), from Ref. Spizzo et al. [2022].

In particular, in the tokamak configuration, the radiative phenomenon is toroidally symmetric and localized at the edge (on the high file side) with limited extension in the poloidal angle ($\sim 30°$), while in the RFP configuration, the MARFE is toroidally localized and has poloidal symmetry. The localization at specific toroidal angle, makes the RFP MARFE a very difficult phenomenon to detect. For both tokamak and RFP configuration the MARFE appears in correspondence of $n/n_G \gtrsim 0.5$, and the strong edge radiation is claimed to play a key role in

triggering the density limit.
In the RFP a key role for the MARFE development is played by the $m = 0$ magnetic islands, as shown in Ref. Spizzo et al. [2015]. The Poincaré plot of the $m = 0$, $n = -1$ island, shown in Fig. 9.4 for three different shots at different values of the edge magnetic field instability, has the O-point and the X-point localized at the reversal and increases its width according to $\sqrt{B^r_{0,1}(r_{rev})}$. At critical values of the edge magnetic field instability the island separatrix intersects the wall, Fig. 9.4 (d).

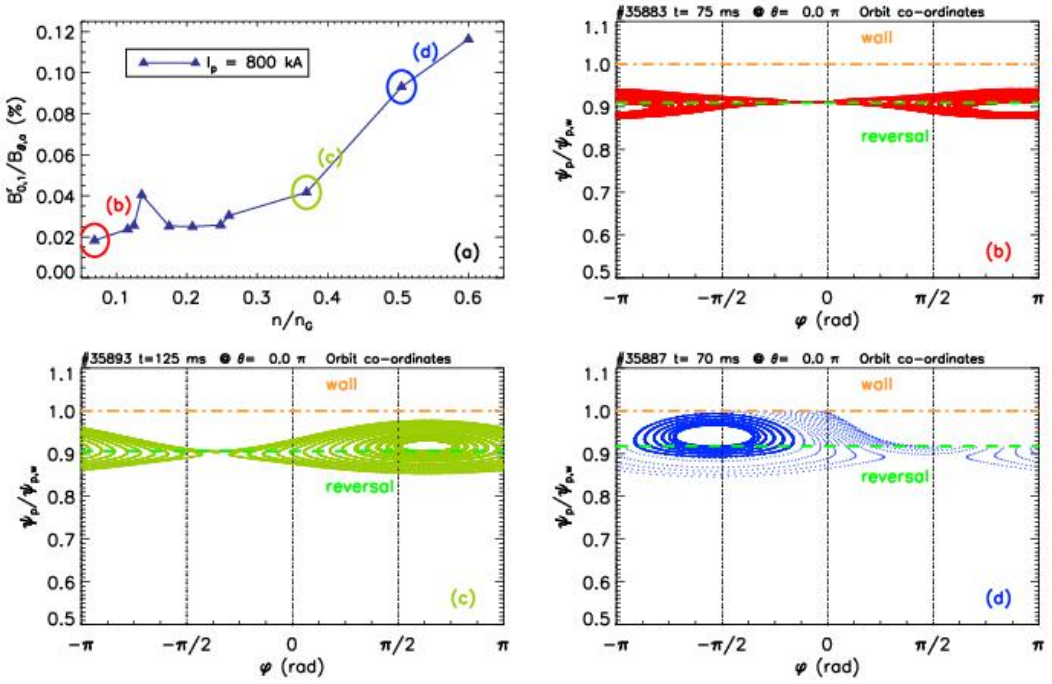

Figure 9.4: Plot of the $m = 0$, $n = -1$ mode normalized radial magnetic field as function of the ratio n/n_G: the entity of such mode grows approaching the density limit; (b) - (d) Magnetic topology of the $m = 0$, $n = -1$ island, for three discharges marked as circles in frame (a). The critical size of the island is reached when the flux surfaces intercept the first wall. Picture adapted from Ref. Spizzo et al. [2015].

The island formation highly perturb the edge plasma: in fact, the slow down of the electrons near the island X-point generates an electric field to restore the local quasi-neutrality which gives rise to planar flow $\mathbf{E} \times \mathbf{B}$ (in r, ϕ direction), increasing as the island size grows. When the island separatrix intersects the wall a stagnation point of the flow is generated in correspondence of the island X-point. This generated a toroidally localized accumulation of particles and impurities, resulting in a peaked density and edge radiation (the so called MARFE).
The localization of the MARFE in correspondence of the island X-point is pointed out in Fig. 9.5, where the Poincaré plot of the magnetic island, reconstructed with the guiding center code ORBIT (Ref. White and Chance [1984]) is superimposed to the radiation contour-plot, obtained from the RFX-mod tomographic diagnostic Franz et al. [2001], in the r, ϕ plane. In this plot, a poloidal flux normalized coordinate ψ_p is used as radial coordinate, while $u_{0,1}$ is the toroidal angle evaluated in reference frame co-rotating with the 0,1 island.
The link observed between edge $m = 0$ instabilities and MARFE phenomenon suggests the possibility of describing the MARFE onset by means of the Hartmann number, which we have shown to rule edge magnetic field modes in Chp. 4 and we can now evaluate according to the viscosity evaluation method developed from Chp. 8.

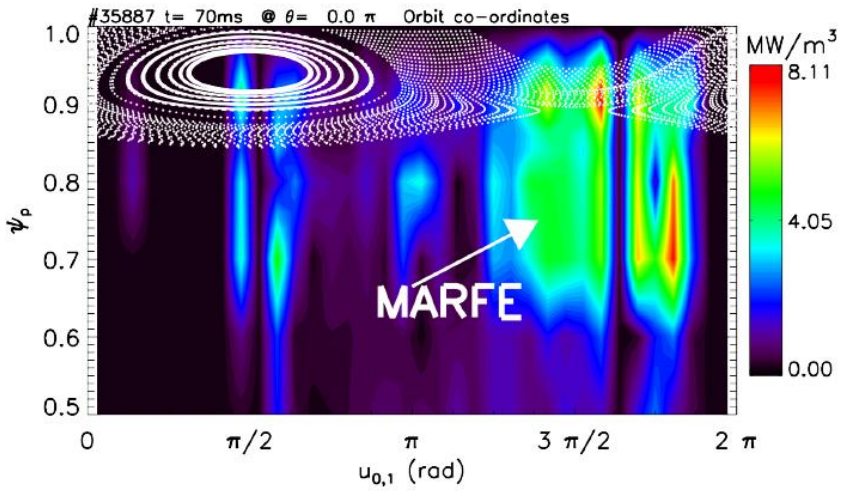

Figure 9.5: Reconstruction of the $m = 0$ $n = -1$ magnetic field island, superimposed to the plasma radiation contourplot. The edge radiation peak (MARFE) is localized in correspondence of the island X-point. Picture adapted from Ref. Spizzo et al. [2022].

9.4 The role of the Hartmann in triggering the rise of the MARFE

To test the relation between the Hartmann number (ruling parameter of the visco-resistive MHD) and the MARFE detection, a subset of the database described in Sec. 7.3 was considered. The reduction of the shots considered is to be attributed to the difficulty in detecting the radiation by means of the bolometric diagnostic. For this reason, only the shots with the global radiation contour-plot available are considered in this Section.
Among these shots, only two different 'geometries' of the radiation are identified: the $m = 1$ geometry, which is attributed to the locking (a phenomenon consisting on the bulging of the plasma column due to a precise relation between the phases of the different $m = 1$ modes, see Ref. Zanca [2008]) and the $m = 0$ geometry which is attributed to the MARFE. The two geometries are highlighted in Fig. 9.6. According to the shape of the radiation observed during the discharge, the shots are classified as 'locking' or 'MARFE'.

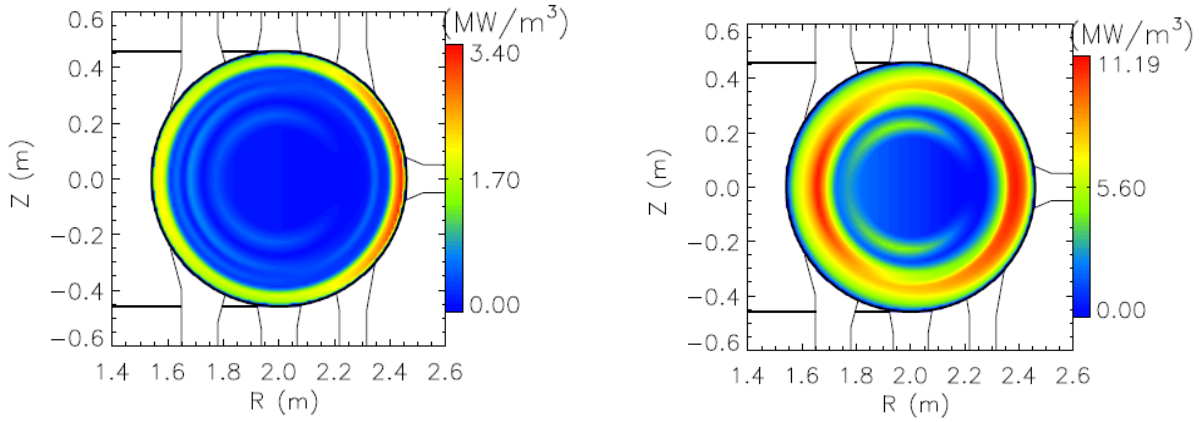

(a) (b)

Figure 9.6: Reconstruction of the radiation in RFX-mod shots: poloidal projection at a fixed toroidal angle. Different geometries of the radiation are highlighted: $m = 1$, classified as locking (a) and $m = 0$ geometry, classified as MARFE (b), from Ref. Puiatti et al. [2009b].

In the next paragraphs, we will discuss how to identify the MARFE from an operative point of view in a RFX-mod shot with the emissivity map available.
As first step, the angle of maximum emissivity is identified and expressed in the $u_{0,1}$ toroidal coordinate. The local radiated power, $P_{rad,loc}$, is calculated by means of a Gaussian fit of the radiated power per toroidal length and integrating the latter over a one standard deviation wide interval $[-\sigma, +\sigma]$, along the toroidal direction. As second step, the topology of the $m = 0$ $n = -1$ island is reconstructed: this allows the introduction of the angular coordinates $u_{0,1}$, defined in such a way that the island O-point corresponds to $u_{0,1} = \pi/2$, while the island X-point corresponds to $u_{0,1} = 3\pi/2$.
In Fig. 9.7, the helical angle of the maximum radiation is plot as function of the perpendicular Hartmann number. Data points are colored according to the value of local radiation $P_{rad,loc}$, while the size of the points corresponds to the Greenwald phenomenological ratio.

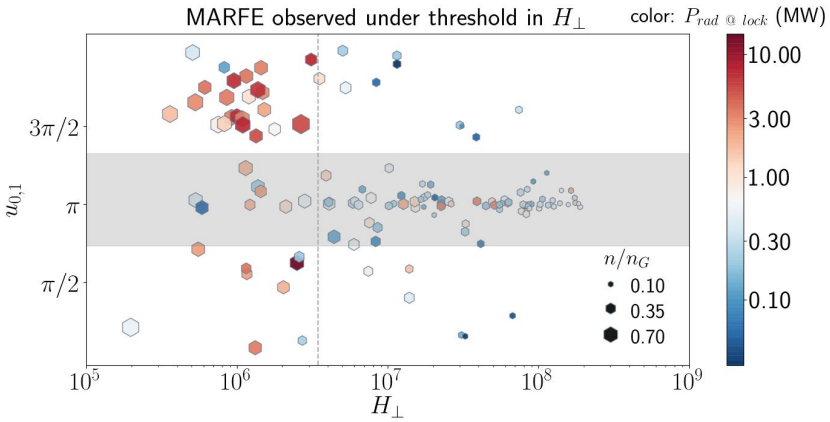

Figure 9.7: Helical angle of maximum emissivity as a function of the Hartmann number $H_\perp$ in the RFX-mod database. Color coding refers to the local radiated power around the maximum (in MW), the size of the dots corresponds to the value of the Greenwald parameter n/n_G. They gray band corresponds to the 'locking' cases, while the points outside the band are considered as 'MARFE'.

Two different clusters of data-points can be approximately identified, corresponding to two qualitatively different radiation pattern, radiated power and n/n_G ratio:

- The 'locking' shots (highlighted by the grey bend in Fig. 9.7) which have a peak of the radiation far from both the island O and X-points: $u_{0,1} \sim \pi$, meaning that the radiation has no specific phase relationship with the island topology. The local radiation of these shots is generally low: $P_{rad,loc} \lesssim 1\,\mathrm{MW}$, as the phenomenological ratio: $n/n_G \lesssim 0.3$.

- the 'MARFE' shots (data-points outside the grey band in Fig. 9.7), which have a radiation peak around $u_{0,1} \sim 3\pi/2$ (the island X-point), triggered by the magnetic island topology, through the formation of a convective cell, as explained in Sec. 9.3. These shots have large local radiated power: $P_{rad,loc} \sim 10\,\mathrm{MW}$ and high Greenwald ratio: $n/n_G \sim 0.7$.

It is worth noting that the 'MARFE' shots are mainly localized at low values of the perpendicular Hartmann number, which stimulates a further analysis to better understand the relation between the MARFE rise and the Hartmann number.
To reach this goal, for each shot also the Hartmann number H^* is calculated. This is a modified estimate of the perpendicular Hartmann which includes a corrective multiplicative factor in the plasma viscosity $\delta \sim 250$, $\nu^* := \delta\nu_\perp$, introduced to accommodate the offset between the experimental data and the simulations, discussed in the final part of Sec. 8.4. Being the correction only a multiplicative factor, H^* maintains all the scaling relations observed for $H_\perp$.

The estimate of H^* for the shot is made considering the time average of the plasma measurable parameters, during the flat top phase.
Before continuing, it could be useful to revise the main steps (From the previous Chapters), that we follow in order to achieve an effective Hartmann evaluations on RFX-mod valid to describe the rise of the MARFE:

- The Hartmann number has been identified as ruling parameters of the visco-resistive MHD (Chp. 4).
- The transport dimensionless coefficients have been experimentally evaluated on RFX-mod database, according to the main transport theories (Chp. 7).
- The perpendicular Braginskii viscosity has been selected to evaluate the Hartmann number (Chp. 8) as the viscosity estimates maximizing the agreement between the RFX-mod experimental data and the SpeCyl simulations.
- In Sec. 8.4, we have introduced the corrective factor, to accommodate the viscosity anomaly, but keeping the functional dependence of the perpendicular Hartmann.

The statistics of the geometry radiation classification is shown in Fig. 9.8, where the Hartmann number emerges as good parameter to split the data in the two categories. Moreover, a threshold in the Hartmann number H^*_{c1} is highlighted, separating the regions with prevalence of $m = 0$ radiation (for $H^* < H^*_{c1}$) and prevalence of $m = 1$ radiation (for $H^* > H^*_{c1}$), being: $H^*_{c1} = (2.2 \pm 0.5) \cdot 10^5$, with the uncertainty determined by the binning of the histogram.

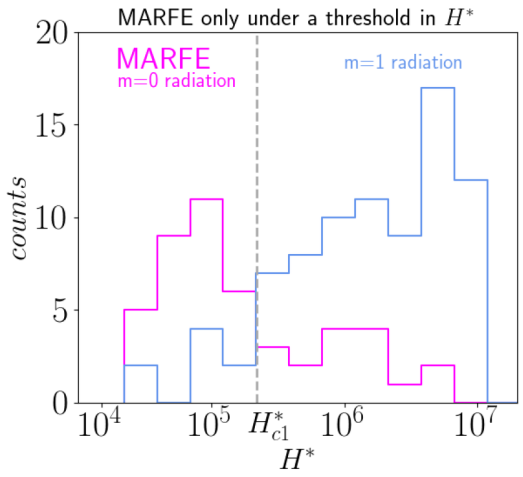

Figure 9.8: Statistics of shots with bolometric map available as function of the Hartmann number H^*, classified in 'locking' and 'MARFE'. A threshold in Hartmann, below which the MARFE phenomenon is dominant, is plot. Picture from Ref. Veranda et al. [2021].

Inverting the relation expressing the Hartmann number (Eq. 7.5), for H^*_{c1}, an expression of the critical density n_{MARFE} for the MARFE onset is found:

$$n_{\mathrm{MARFE}} \left[10^{20}\,\mathrm{m}^{-3}\right] \simeq \frac{1}{4} \frac{a[\mathrm{m}]\, B^2[\mathrm{T}]\, T[\mathrm{eV}]}{Z^{1/2} m_i^{3/4} \ln \Lambda}. \tag{9.3}$$

It is worth noting that the scaling of the critical density as function of the magnetic field: $n_c \propto B^2$ coincides with that predicted by MHD based theories for the density limit, see Ref. Granetz [1982]. Eq. (9.3) is proposed as a relation for the critical density over which the onset of the MARFE phenomenon in the RFP happens: it comes from experimental observations of the relation between MARFE onset and m=0 magnetic islands and from the numerical result that the dimensionless Hartmann number is the only quantity ruling the physics of those islands.

9.5 MHD description of the RFP density limit based on the first-principle Hartmann number

In this Section, we analyze the behaviour of RFX-mod plasmas, varying the Hartmann number, with reference to the edge toroidal magnetic field instabilities, which determines the helical self-organization, trigger the offset of the MARFE and the approach to the density limit. In addition, the experimental data (from the entire database presented in Sec. 7.3) are compared to the SpeCyl simulations (from the database presented in Sec. 4.4).
Since the number of points involved in this analysis is very high for both experimental data and numerical simulations, the average over equal logarithmic intervals in the Hartmann number H^* is considered. The uncertainties on the y-axis are computed evaluating the uncertainty of the average of the points belonging to the corresponding logarithmic interval. The plots of $m = 0$ and $m = 1$ modes are shown in Fig. 9.9 and Fig. 9.10, respectively. The experimental points are colored according to the average value of the Greenwald phenomenological parameter n/n_G.

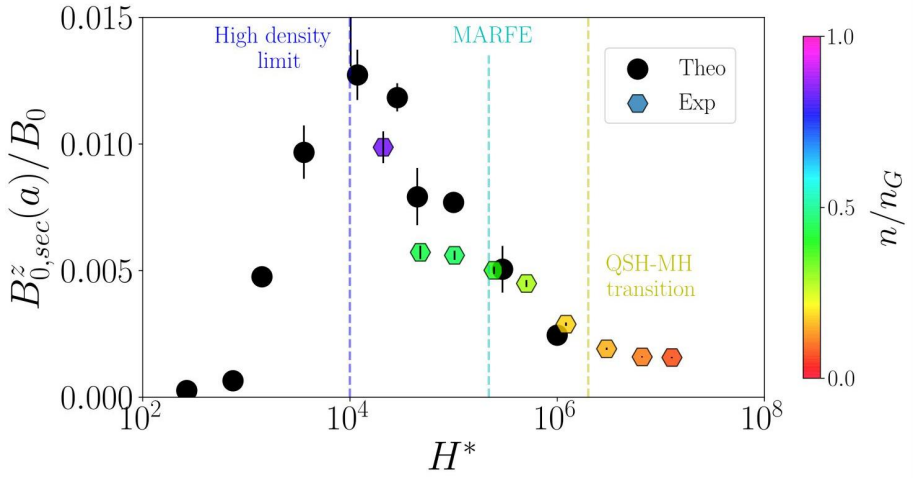

Figure 9.9: Edge toroidal magnetic field $m = 0$ secondary modes: comparison between SpeCyl numerical simulations and RFX-mod experimental data, both averaged over equal logarithmic intervals. Three threshold are highlighted corresponding to the QSH-MH transition, the MARFE onset, the high density limit, beyond which no shots are observed. The experimental points are colored according to their average n/n_G phenomenological ratio.

We analyze the trend of the edge magnetic field instabilities as the Hartmann number H^* is decreased from $H^* \sim 10^7$, to $H^* \sim 10^4$.
At high Hartmann $H^* \sim 10^6 - 10^8$ the plasma is found for both experimental data and simulations in a so called Quasi-Single Helicity, characterized by the low values of (both $m = 0$ and $m = 1$) secondary modes. Decreasing H^*, the secondary modes increase, corresponding to a progressive loss of the helical order. Also, an average increase of the n/nG phenomenological ratio is observed in experimental data. This causes the transition to the turbulent Multiple Helicity regime.
At $H^* \sim 2.2 \cdot 10^5$ the threshold for the MARFE onset is found, the phenomenological Greenwald ratio amounts to $n/n_G \sim 0.5$. $H^* \sim 10^4$ is the threshold beyond which no experimental points are observed, amounting the average of the Greenwald ratio to $n/n_G \sim 0.8$. At this value also the maximum of the secondary modes (both $m = 0$ and $m = 1$) in the simulations is observed and for $H^* < 10^4$ only simulations are observed, corresponding to the Single Helicity regime. In other words, H^* is identified: by simulations as the threshold for the dynamical transition MH-SH and by the experimental data as the point of maximum of the $m = 0$ instabilities, corresponding to the maximum possible extension of the $m = 0$ magnetic island. This suggest considering $H^* \sim 10^4$ as the threshold for the RFP high density limit.

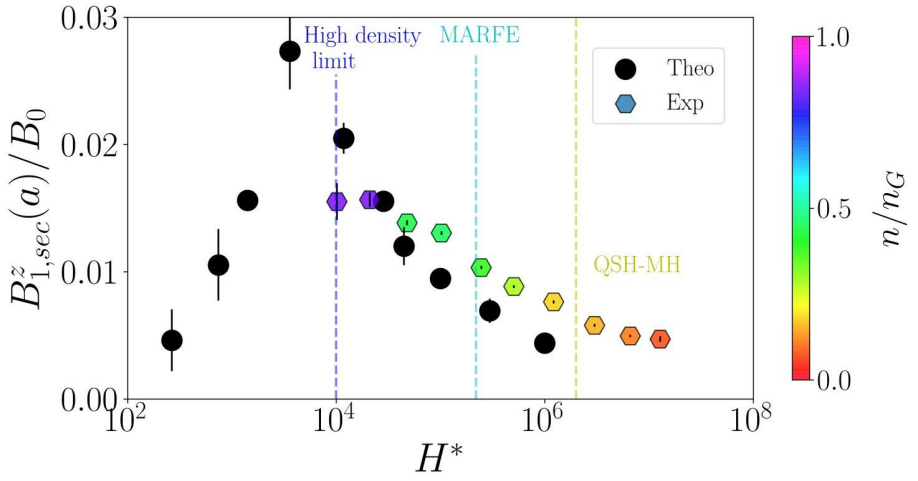

Figure 9.10: Edge toroidal magnetic field $m = 1$ secondary modes: comparison between SpeCyl numerical simulations and RFX-mod experimental data, both average over equal logarithmic intervals. Three threshold are highlighted corresponding to the QSH-MH transition, the MARFE onset, the high density limit, beyond which no shots are observed. The experimental points are colored according to their average n/n_G phenomenological ratio.

9.6 Summary and final remarks

In this Chapter, the reversed field pinch density limit has been studied, by means of a magneto-fluid approach. After revising the basic phenomenology of the density limit and the main theory frameworks developed to better understand the phenomenon, the focus is set on the RFP density limit.
Limited to this configuration, a key role in determining the density limit onset is played by the so-called MARFE that is a high density, highly radiative plasma ring with poloidal symmetry, which is triggered by the growth of $m = 0$ magnetic islands. We remark that the MARFE is a well known precursor of the density limit also in the tokamak. The relation between MARFE and "amplitude" of m=0 islands opens the way to link the density limit phenomenology to the the dimensionless Hartmann number, which is known to rule the trend of $m = 0$ secondary modes, from MHD visco-resistive simulations.
The main results of this Chapter are:

- The derivation of a critical threshold for the density n_{MARFE} scaling as $\propto B^2 T$ above which the MARFE is identified as the most frequent radiative phenomenon. This result is based on both: the relation between the Hartmann and the $m = 0$ modes amplitude and on the statistical analysis of the radiation observed.

- The description for both simulations and experimental data, by means of the dimensionless Hartmann number, of the secondary modes (both $m = 0$ and $m = 1$) trends which cause RFP dynamical transition (i.e. qualitative change of the plasma helical order level) and triggers the onset of the MARFE and the density limit. In particular, we observed in correspondence of the threshold $H^* \sim 10^4$, the maximum amplitude of $m = 0$ secondary modes, corresponding to the maximum possible extension of the $m = 0$ $n = -1$ magnetic island, beyond which the plasma single helicity phase is observed (only in numerical simulations). This suggests to identify it as the RFP high density limit threshold.

Part IV

Conclusions

Conclusions

The aim of this Thesis consisted on improving the description of the reversed field pinch dynamical transitions and related density limit by means of a better understanding of transport dimensionless parameters role and their experimental in toroidal self-organized pinches. To achieve this aim three intermediate steps have been considered: to improve the understanding of transport dimensionless parameters in 3D non-linear MHD simulations, to assess a kinematic viscosity estimate in RFP fusion plasmas and, finally, to understand the role of transport dimensionless in the MHD description of reversed field pinch fusion plasmas, with particular reference to the density limit.
In the next paragraphs we recall the Conclusions developed at end of each chapter, which are here presented in a summarized, compact text. Possible future developments are presented in the final paragraph.

Transport coefficient studies in 3D non-linear MHD simulations
SpeCyl simulations (RFP configuration) Since the role of the Hartmann number (which represents the visco-resistive dissipation) as ruling parameter of the visco-resistive MHD is a well consolidated result (Ref. Cappello and Escande [2000], and Ref. Veranda et al. [2019]), in this work, a 'more realistic' modelling of the viscosity and resistivity coefficients was attempted. In particular, a sensitivity study about the effects of resistivity and viscosity profiles and time-dependence has been performed for 3D SpeCyl numerical simulations in RFP configuration.
This study has shown that flatten resistivity profiles cause a decrease of the dominant mode and a slowdown of the RFP sawtooth activity, while Braginskii-like viscosity profiles, damp the velocity modes resonating where the viscosity profile is higher and allow for a slight enhancement of the magnetic field corresponding modes.
The tests of visco-resistive dissipation time dependence has allowed to model the progressive loss of the helical order as the visco-resistive dissipation is increased (exponential decrease of the Hartmann number) and to model a periodic oscillation of resistivity and viscosity in the core plasma, linking the dissipation coefficients to the helical order. This result constitutes a first step towards a self-consistent modelling of transport coefficients in MHD simulations.

PIXIE3D simulations (Tokamak configuration) A set of finite pressure PIXIE3D numerical simulations with helical symmetry ($h = m/n = -1$) was performed, systematically varying the dimensionless transport coefficients (resistivity, viscosity and isotropic heat conductivity), with the aim of studying the tokamak sawtooth activity. This has allowed the identification of two regimes: sawtooth oscillations (at low visco-resistive dissipation) and damped sawtooth oscillations (at high visco-resistive dissipation). The description in terms of joint viscosity and resistive dissipation has proven to be more effective than a description based on a single coefficient only. Moreover, the isotropic heat conductivity is shown to determine the plasma core temperature.

Assessment of the kinematic viscosity coefficient in RFP plasmas

Analyzing a wide database of RFX-mod shots in RFP configuration, the kinematic viscosity coefficient was evaluated according to the main theories of transport known in RFP research (classical Braginskii, Ion Temperature Gradient and Finn).
The main contribution to the viscosity term able to maximize the agreement between visco-resistive magnetohydrodynamics numerical simulations and experimental data is shown to be related to the perpendicular Braginskii viscosity. This conclusion is drawn exploiting: transport physics based considerations, comparison of the regression coefficients (between simulations and experimental data) and preliminary Bayesian model comparison studies.
This result allows selecting a specific evaluation of transport dimensionless parameters (and in particular of the Hartmann number) on the experimental data and consequently to use them in the description of RFP plasmas physical phenomena, like the density limit.

MHD description of the RFP density limit

A description of the RFP density limit is developed in the context of nonlinear magnetohydrodynamics, highlighting the role of the Hartmann number in triggering the growth of edge $m = 0$ instabilities and in the MARFE (Multifaceted Asymmetric Radiation From the Edge) onset. In reversed-field pinch configuration, the latter is constituted by a toroidally localized and poloidally symmetric highly radiative ring, whose formation is triggered by the growth of the $m = 0$ magnetic islands and that is a precursor of the discharge termination, as shown in Ref. Spizzo et al. [2015].
In conclusion, the Hartmann number finally results as a fluid dimensionless number, derived from first principle equations able to describe the growth of the poloidally symmetric magnetic field instabilities and radiation, identified as precursor of the reversed field pinch density limit.

Future developments

Different future developments can be considered for this work, which are presented organizing them in two categories: numerical simulations and experimental data analysis.

- **Numerical simulations**. A desirable future development in this research field consists of further improving the modelling towards self-consistent time evolution. We suggest two possibilities for RFP and tokamak configuration.
  RFP configuration: PIXIE3D simulations with finite pressure including Spitzer-like self-consistently evolved resistivity could be considered, to see if the resistivity dependence on temperature has a positive feedback effect on the RFP self-organization process.
  Tokamak configuration: Future studies are programmed to exploit a Spitzer-like self-consistently evolved resistivity in 2D simulations with fixed helicity $h = m/n = -1$, so far considered in this work only for basic 1D axisymmetric simulations. A future extension of the analysis to 3D simulations is definitely on schedule. These steps would help to improve the preliminary modelling of the sawtooth instability made in this work, making interesting the comparison with the experimental data.

- **Experimental data**. A future development deserving additional studies could aim at estimating the uncertainty on transport dimensionless parameters on the basis of plasma measurable parameters uncertainties and at deepening the Bayesian model comparison applied to select the transport model, according to which the plasma viscosity should be estimated.
  As long term future development, the extension of this work to the tokamak configuration can be considered. This would require to investigate the role of the viscosity in tokamak plasmas and eventually to estimate it on the basis of tokamak shots experimental data. As consequence of it, the role of the Hartmann number could be investigated in the theories which speculate an MHD origin of the tokamak density limit.

Appendix A

Proofs of theorems

A.1 Woltjer's theorems

First Woltjer's theorem. *If a magneto-fluid has zero resistivity ($\eta = 0$), then helicity $\mathcal{H}$ is conserved in time:*

$$\frac{d\mathcal{H}}{dt} = 0. \tag{A.1}$$

Proof. The proof of this theorem simply consists in the evaluation of the rate of change in time of the helicity:

$$\frac{d\mathcal{H}}{dt} = \int \frac{\partial}{\partial t}\left(\mathbf{A}\cdot\mathbf{B}\right) dV = \int \frac{\partial \mathbf{A}}{\partial t}\cdot\mathbf{B} dV + \int \mathbf{A}\cdot\frac{\partial \mathbf{B}}{\partial t} dV. \tag{A.2}$$

In case of zero resistivity the diffusive term in the induction equation is absent and this determines the time variation of $\mathbf{B}$ and considering that $\mathbf{B} = \nabla\times\mathbf{A}$ also the time variation of the vector potential $\mathbf{A}$ is determined:

$$\frac{\partial \mathbf{B}}{\partial t} = \nabla\times\left(\mathbf{v}\times\mathbf{B}\right), \qquad \frac{\partial \mathbf{A}}{\partial t} = \mathbf{v}\times\mathbf{B}. \tag{A.3}$$

Replacing equations (A.3) in equation (A.2), a null term is obtained because $(\mathbf{v}\times\mathbf{B})\cdot\mathbf{B} = 0$, while the remaining term can be evaluated by means of the following vector identity $\nabla\cdot(\mathbf{V}\times\mathbf{W}) = \mathbf{W}\cdot(\nabla\times\mathbf{V}) - \mathbf{V}\cdot(\nabla\times\mathbf{W})$ (that holds for any couple of vectors), obtaining:

$$\frac{d\mathcal{H}}{dt} = \int \mathbf{A}\cdot\nabla\times\left(\mathbf{v}\times\mathbf{B}\right) dV = \int \nabla\cdot\left[\left(\mathbf{v}\times\mathbf{B}\right)\times\mathbf{A}\right] dV + \int \left(\mathbf{v}\times\mathbf{B}\right)\cdot\left(\nabla\times\mathbf{A}\right) dV. \tag{A.4}$$

In equation (A.4) the second term in the sum is zero, while the first can be evaluated using the Gauss theorem:

$$\frac{d\mathcal{H}}{dt} = \oint_{\partial V}\left[\left(\mathbf{v}\times\mathbf{B}\right)\times\mathbf{A}\right]\cdot d\mathbf{S}, \tag{A.5}$$

Here ∂V represents the surface of the magneto-fluid system and $d\mathbf{S}$ is a vector element perpendicular to the surface differential element dS. Since $\mathbf{v}$ and $\mathbf{B}$ are parallel to the boundary of the magneto-fluid, the whole integrand has zero component perpendicular to the surface and so the total integral contribution is zero, thus proving the theorem. □

Second Woltjer's theorem. *In a system in which the magnetic helicity $\mathcal{H}$ is kept constant, the minimization of the magnetic energy $W = \int B^2/2\mu_0 dV$ is obtained for a force-free field defined by the condition:*

$$\nabla \times \boldsymbol{B} = \mu \boldsymbol{B}, \tag{A.6}$$

with μ = constant.

Proof. To find the minimum of the magnetic energy in presence of constant helicity constraint the Lagrange multipliers method is applied. It consists in solving the following equation:

$$\delta W - \frac{\mu}{2\mu_0}\delta\mathcal{H} = 0, \tag{A.7}$$

where the constant $\mu/2\mu_0$ is chosen as Lagrange multiplier. Replacing the definitions of magnetic and helicity one can get:

$$\delta W - \frac{\mu}{2\mu_0}\delta\mathcal{H} = \int \left(\frac{\mathbf{B}\cdot\delta\mathbf{B}}{\mu_0} - \mu\frac{\delta\mathbf{A}\cdot\mathbf{B}}{2\mu_0} - \mu\frac{\mathbf{A}\cdot\delta\mathbf{B}}{2\mu_0} \right) dV. \tag{A.8}$$

The last term in the sum in (A.8) can be rewritten, remembering that $\delta\mathbf{B} = \nabla\times\delta\mathbf{A}$, and making use of the vector identity $\nabla\cdot(\mathbf{V}\times\mathbf{W}) = \mathbf{W}\cdot(\nabla\times\mathbf{V}) - \mathbf{V}\cdot(\nabla\times\mathbf{W})$ that has already been met:

$$\int \frac{\mathbf{A}\cdot\delta\mathbf{B}}{2\mu_0} dV = \int \frac{\mathbf{A}\cdot(\nabla\times\delta\mathbf{A})}{2\mu_0} dV = \int \left[\frac{\nabla\cdot(\delta\mathbf{A}\times\mathbf{A})}{2\mu_0} + \frac{\delta\mathbf{A}\cdot(\nabla\times\mathbf{A})}{2\mu_0} \right] dV. \tag{A.9}$$

The first term in the sum is evaluated by means of the Gauss theorem as surface integral on the magneto-fluid boundary, where variations are expected to be exactly zero. Therefore, the only surviving term is the second:

$$\int \frac{\mathbf{A}\cdot\delta\mathbf{B}}{2\mu_0} dV = \int \frac{\delta\mathbf{A}\cdot\mathbf{B}}{2\mu_0} dV. \tag{A.10}$$

Replacing the previous result in (A.8) the proof is obtained. In fact:

$$0 = \delta W - \frac{\mu}{2\mu_0}\delta\mathcal{H} = \int \frac{B}{2\mu_0} \left(\delta\mathbf{B} - \mu\delta\mathbf{A}\right) dV \quad \Longleftrightarrow \quad \mathbf{B} = \mu\mathbf{A}. \tag{A.11}$$

After taking the curl on both sides, (A.11) exactly becomes: $\nabla\times\mathbf{B} = \mu\mathbf{B}$, the condition that defines force free fields. □

Appendix B

MHD equations

B.1 Transport coefficients formulas

In this Section, the main transport coefficient formulas are listed, as derived in Chp. 3

B.1.1 Spitzer resistivity

$$\eta_{\parallel} = \frac{0.06}{\pi^{3/2}} \frac{m_e^{1/2} e^2}{\epsilon_0^2} \frac{Z \ln \Lambda}{T_e^{3/2}} \qquad \eta_{\perp} = \frac{0.118}{\pi^{3/2}} \frac{m_e^{1/2} e^2}{\epsilon_0^2} \frac{Z \ln \Lambda}{T_e^{3/2}} \tag{B.1}$$

B.1.2 Braginskii kinematic viscosity

$$\nu_{\parallel} = 34.6 \pi^{3/2} \frac{\epsilon_0^2}{e^4 m_p^{1/2}} \frac{T_i^{5/2}}{Z^4 \ln \Lambda \gamma^{1/2} n_i} \tag{B.2}$$

$$\nu_{\perp} = \frac{1}{8\pi^{3/2}} \frac{m_p^{1/2} e^2}{\epsilon_0^2} \frac{\gamma^{1/2} n_e \ln \Lambda}{T_i^{1/2} B^2} \tag{B.3}$$

$$\nu_{\times} = 1.25 \frac{1}{e} \frac{T_i}{ZB} \tag{B.4}$$

B.1.3 Turbulent estimates of the viscosity

$$\nu_{ITG} = 1.08 \times 10^{-4} e^{-3/2} \frac{\gamma^{1/2} T_e T_i^{1/2}}{Z a_T^{3/4} a_B^{1/4} B^2} \tag{B.5}$$

$$\nu_{Finn} = c_s L_C \sum_{m,n} \left(\frac{b_{m,n}^r}{B} \right)^2 \tag{B.6}$$

evaluating the sound speed $c_s = \sqrt{\frac{\gamma_e Z T_e + \gamma_i T_i}{M_i}}$ with $\gamma_e = 1$, $\gamma_i = 3$ and with L_c representing the auto-correlation length.

B.1.4 Classical heat diffusivity

$$\chi_{\parallel}^e = 27.2 \pi^{3/2} \frac{\epsilon_0^2}{m_e^{1/2} e^4} \frac{T_e^{5/2}}{Z \ln \Lambda n_e} \tag{B.7}$$

$$\chi_{\parallel}^{i} = 46.8\pi^{3/2}\frac{\epsilon_0^2}{m_p^{1/2}e^4}\frac{T_i^{5/2}}{Z^4\gamma^{1/2}\ln\Lambda n_i} \tag{B.8}$$

$$\chi_{\perp}^{e} = \frac{0.544}{\pi^{3/2}}\frac{m_e^{1/2}e^2}{\epsilon_0^2}\frac{Z^3 n_i \ln\Lambda}{T_e^{1/2}B^2} \tag{B.9}$$

$$\chi_{\perp}^{i} = \frac{0.167}{\pi^{3/2}}\frac{m_p^{1/2}e^2}{\epsilon_0^2}\frac{\gamma^{1/2}Z^2 n_i \ln\Lambda}{T_i^{1/2}B^2} \tag{B.10}$$

$$\chi_{\times}^{e} = 2.5\frac{1}{e}\frac{T_e}{B} \tag{B.11}$$

$$\chi_{\times}^{i} = 2.5\frac{1}{e}\frac{T_i}{ZB} \tag{B.12}$$

B.2 Dimensionless transport related parameters formulas

In this Section, the main formulas to compute transport related dimensionless parameters are listed, as they are used in Chp. 7.

B.2.1 Lundquist number

$$S_{\parallel} := \frac{a^2\mu_0}{\eta_{\parallel}\tau_A} = 16.7\pi^{3/2}\frac{\mu_0^{1/2}\epsilon_0^2}{m_p^{1/2}m_e^{1/2}e^2}\frac{aBT_e^{3/2}}{Z^{1/2}\gamma^{1/2}\ln\Lambda n_e^{1/2}} \tag{B.13}$$

$$S_{\perp} := \frac{a^2\mu_0}{\eta_{\perp}\tau_A} = \frac{a^2\mu_0}{1.96\eta_{\parallel}\tau_A} = 0.51 S_{\parallel} \tag{B.14}$$

B.2.2 Viscous Lundquist number

$$M_{\parallel} := \frac{a^2\rho_0}{\mu_{\parallel}^{i}\tau_A} = 5.3\times10^{-3}\frac{e^4}{\mu_0^{1/2}\epsilon_0^2}\frac{n_e^{1/2}Z^{7/2}aB\ln\Lambda}{T_i^{5/2}} \tag{B.15}$$

$$M_{\perp} := \frac{a^2\rho_0}{\mu_{\perp}^{i}\tau_A} = 44.5\frac{\epsilon_0^2}{\mu_0^{1/2}m_p e^2}\frac{aB^3T_i^{1/2}}{\gamma n_e^{3/2}Z^{1/2}\ln\Lambda} \tag{B.16}$$

$$M_{\times} := \frac{a^2\rho_0}{\mu_{\times}^{i}\tau_A} = 0.8\frac{e}{m_e^{1/2}m_p^{1/2}}\frac{Z^{3/2}aB^2}{\gamma^{1/2}n_e^{1/2}T_i} \tag{B.17}$$

B.2.3 Magnetic Prandtl number

$$P_{\parallel} := \frac{\mu_0\mu_{\parallel}^{i}}{\rho_0\eta_{\parallel}} = 576\pi^3\frac{\epsilon_0^4\mu_0}{m_p^{1/2}m_e^{1/2}e^6}\frac{T_i^{5/2}T_e^{3/2}}{\gamma^{1/2}Z^4 n_e(\ln\Lambda)^2} \tag{B.18}$$

$$P_{\perp} := \frac{\mu_0\mu_{\perp}^{i}}{\rho_0\eta_{\perp}} = 4.08\frac{\mu_0 m_p^{1/2}}{m_e^{1/2}}\frac{\gamma^{1/2}n_e T_e^{3/2}}{B^2T_i^{1/2}} \tag{B.19}$$

$$P_{\times} := \frac{\mu_0\mu_{\times}^{i}}{\rho_0\eta_{\parallel}} = 20.8\pi^{3/2}\frac{\mu_0\epsilon_0^2}{m_e^{1/2}e^3}\frac{T_iT_e^{3/2}}{Z^2B\ln\Lambda} \tag{B.20}$$

B.2.4 Hartmann number

$$H_{\parallel} := \frac{aB}{\sqrt{\eta_{\parallel}\mu^{i}_{\parallel}}} = 0.69\frac{e}{m_e^{1/4}m_p^{1/4}}\frac{Z^{3/2}aBT_e^{3/4}}{\gamma^{1/4}T_i^{5/4}} \tag{B.21}$$

$$H_{\perp} := \frac{aB}{\sqrt{\eta_{\perp}\mu^{i}_{\perp}}} = 45.8\frac{\epsilon_0^2}{m_e^{1/4}m_p^{3/4}e^2}\frac{aB^2T_e^{3/4}T_i^{1/4}}{\gamma^{3/4}Z^{1/2}n_e\ln\Lambda} \tag{B.22}$$

$$H_{\times} := \frac{aB}{\sqrt{\eta_{\parallel}\mu^{i}_{\times}}} = 8.61\frac{\epsilon_0}{m_e^{1/4}m_p^{1/2}e^{1/2}}\frac{aB^{3/2}T_e^{3/4}}{Z^{1/2}\gamma^{1/2}n_e^{1/2}T_i^{1/2}\left(\ln\Lambda\right)^{1/2}} \tag{B.23}$$

B.3 MHD visco-resistive equations in Fourier space

The aim of this section is to explain how the differential equations of the magnetohydrodynamics are commuted passing to the Fourier space. The entire section is performed in cylindrical geometry with periodic boundary conditions.

Linearity in the real space. A linear differential equation is transformed, in the Fourier space, in an algebraic equation that involves relationship only between the same Fourier mode.

This can be evident analyzing, as example, the Ampère-Maxwell that in the last form is reduced to:

$$\nabla \times \mathbf{B} = \mathbf{j}. \tag{B.24}$$

In the Fourier space, the fields $\mathbf{B}$ and $\mathbf{j}$ are rewritten as:

$$\mathbf{B}(r,\theta,z,t) = \sum_{m=-N_\theta}^{+N_\theta} \sum_{n=-N_z}^{+N_z} \mathbf{B}_{m,n}(r,t)\, e^{i\left(m\theta + \frac{n}{R_0}z\right)}, \tag{B.25}$$

$$\mathbf{J}(r,\theta,z,t) = \sum_{m'=-N_\theta}^{+N_\theta} \sum_{n'=-N_z}^{+N_z} \mathbf{J}_{m',n'}(r,t)\, e^{i\left(m'\theta + \frac{n'}{R_0}z\right)}. \tag{B.26}$$

Using the well known expression for the curl in cylindrical coordinates and calculating the derivatives an equation about the modes is obtained since the exponential function is not altered by the derivations, unless the addition of multiplicative constants:

$$\mathbf{j}_{m,n}(r,t) = \begin{pmatrix} \frac{im}{r} B^\theta_{m,n}(r,t) - \frac{inz}{R_0} B^z_{m,n}(r,t) \\ \frac{inz}{R_0} B^r_{m,n}(r,t) - \frac{\partial}{\partial r} B^z_{m,n}(r,t) \\ \frac{B^\theta_{m,n}(r,t)}{r} + \frac{\partial B^\theta_{m,n}(r,t)}{\partial r} - \frac{im}{r} B^r_{m,n}(r,t) \end{pmatrix}. \tag{B.27}$$

Non linearity in the real space. A non linear differential equation is transformed, in the Fourier space, in an algebraic equations that involves relationship only between different Fourier modes.

To exemplify this concept it's enough to evaluate a typical term of the MHD equations: $\mathbf{j} \times \mathbf{B}$. Since $\mathbf{j} \times \mathbf{B} = (\nabla \times \mathbf{B}) \times \mathbf{B}$, the calculation can be carried out in cylindrical coordinates:

$$\mathbf{j} \times \mathbf{B} = \begin{pmatrix} B_z j_\theta - B_\theta j_z \\ B_r j_z - j_r B_z \\ B_\theta j_r - B_r j_\theta. \end{pmatrix} \tag{B.28}$$

If the previous result for j is replaced, interaction terms between different modes arise as it can be seen calculating, for example, the radial component:

$$\begin{aligned} (\mathbf{j} \times \mathbf{B})_r = &\sum_{m,n} \sum_{m',n'} B^z_{m,n}(r,t) \left(\frac{in'z}{R_0} B^r_{m',n'}(r,t) - \frac{\partial B^z_{m',n'}(r,t)}{\partial r} \right) e^{i\left(m\theta + \frac{n}{R_0}z\right)} e^{i\left(m'\theta + \frac{n'}{R_0}z\right)} + \\ &- \sum_{m,n} \sum_{m',n'} B^\theta_{m,n}(r,t) \left(\frac{B^\theta_{m',n'}(r,t)}{r} + \frac{\partial B^\theta_{m',n'}(r,t)}{\partial r} - \frac{im'}{r} B^r_{m',n'}(r,t) \right) e^{i\left(m\theta + \frac{n}{R_0}z\right)} e^{i\left(m'\theta + \frac{n'}{R_0}z\right)}. \end{aligned} \tag{B.29}$$

Fourier series of the product of two physical quantities in the real space. The Fourier mode of the product of two physical quantities can be written as convolution of different modes in the real space. In formulas:

$$\left[B^i B^j\,(r,t)\right]_{\tilde{m},\tilde{n}} = \sum_{m,n} B^i_{m,n}(r,t)\left(B^j_{m-\tilde{m},n-\tilde{n}}(r,t)\right)^* e^{i\left(\tilde{m}\theta+\frac{\tilde{n}}{R_0}z\right)}, \tag{B.30}$$

where i, j are two general dimensions in cylindrical coordinates and the magnetic field is chosen, without loss of generality.

Proof. Rewriting the product of magnetic field in Fourier series:

$$B^i B^j = \sum_{m,n}\sum_{m',n'} B^i_{m,n}(r,t)B^j_{m',n'}(r,t)e^{i(m+m')\theta}e^{i\frac{n+n'}{R_0}z}. \tag{B.31}$$

To prove the thesis the following identities about the Kronecker δ are used:

$$e^{i(m+m')\theta} = \sum_{\tilde{m}} e^{i\tilde{m}\theta}\delta_{\tilde{m},m+m'}, \qquad e^{i\frac{n+n'}{R_0}z} = \sum_{\tilde{n}} e^{i\frac{\tilde{n}}{R_0}z}\delta_{\tilde{n},n+n'}, \tag{B.32}$$

that, once replaced in (B.31), gives the following equation obtained using the Kronecker δ properties:

$$B^i B^j = \sum_{\tilde{m},\tilde{n}}\left[\sum_{m,n} B^i_{m,n}(r,t)B^j_{\tilde{m}-m,\tilde{n}-n'}(r,t)e^{i\tilde{m}\theta}e^{i\frac{\tilde{n}}{R_0}z}\right] e^{i\left(\tilde{m}\theta+\frac{\tilde{n}}{R_0}z\right)}. \tag{B.33}$$

Subsequently, using the condition for reality $B_{-m,-n} = B^*_{m,n}$, to match the definition of the Fourier series one can get the thesis:

$$\left[B^i B^j\,(r,t)\right]_{\tilde{m},\tilde{n}} = \sum_{m,n} B^i_{m,n}(r,t)\left(B^j_{m-\tilde{m},n-\tilde{n}}(r,t)\right)^* e^{i\left(\tilde{m}\theta+\frac{\tilde{n}}{R_0}z\right)}. \tag{B.34}$$

□

B.4 Magnetic energy computation

In this section we briefly summarize the computation of the magnetic energy applied in the IDL post-processing routine `energy_compute_pix.pro`. Considering a cylindrical geometry and dimensionless units (B is normalized to the on axis magnetic field B_0 and the energy to the value $B_0^2 a^3/\mu_0$), the magnetic energy is expressed as:

$$W_M(t) = \int \frac{\mathbf{B}\left(\mathbf{r},t\right)^2}{2} dV = \frac{1}{2}\int B_r^2\left(\mathbf{r},t\right) + B_\theta^2\left(\mathbf{r},t\right) + B_z^2\left(\mathbf{r},t\right) dV. \tag{B.35}$$

In addition, each component of the magnetic field (in cylindrical geometry) can be rewritten, accounting for the Fourier series, as sum over the poloidal m and toroidal n wave numbers of the magnetic field modes $B_i^{m,n}\left(r,t\right)$ multiplied by the relative harmonics. Being complex numbers, the trivial identity (B.37) holds for each of the Fourier modes:

$$B_i\left(\mathbf{r},t\right) = \sum_{m,n} B_i^{m,n}\left(r,t\right) e^{i(m\theta+n\phi)}, \tag{B.36}$$

$$B_i^{m,n}\left(r,t\right) = \Re[B_i^{m,n}\left(r,t\right)] + i\Im[B_i^{m,n}\left(r,t\right)], \tag{B.37}$$

$$B_i^2\left(\mathbf{r},t\right) = \sum_{m',n'}\sum_{m,n}\left(B_i^{m',n'}\left(r,t\right)\right)^* B_i^{m,n}\left(r,t\right) e^{i(m-m')\theta} e^{i(n-n')\phi}, \tag{B.38}$$

being $-M \leqslant m, m' \leqslant M$ and $-N \leqslant n, n' \leqslant N$. The integral is written in cylindrical coordinates:

$$\begin{aligned}
\int B_i^2\left(\mathbf{r},t\right) dV &= \int \sum_{m',n'}\sum_{m,n}\left(B_i^{m',n'}\left(r,t\right)\right)^* B_i^{m,n}\left(r,t\right) e^{i(m-m')\theta} e^{i(n-n')\phi} dV = \\
&= \int_0^1\int_0^{2\pi}\int_0^{2\pi} \sum_{m',n'}\sum_{m,n}\left(B_i^{m',n'}\left(r,t\right)\right)^* B_i^{m,n}\left(r,t\right) e^{i(m-m')\theta} e^{i(n-n')\phi} R_0 d\phi d\theta r dr = \\
&= \int_0^1 \sum_{m',n'}\sum_{m,n}\left(B_i^{m',n'}\left(r,t\right)\right)^* B_i^{m,n}\left(r,t\right) \int_0^{2\pi} e^{i(m-m')\theta} d\theta \int_0^{2\pi} e^{i(n-n')\phi} d\phi R_0 r dr.
\end{aligned}$$

For the integrals in the angular coordinates (θ, ϕ) the following identity holds:

$$\int_0^{2\pi} e^{ikx} dx = \begin{cases} \int_0^{2\pi} 1 dx = 2\pi, & k = 0, \\ \int_0^{2\pi} \left[\cos\left(kx\right) + i\sin\left(kx\right)\right] dx = 0, & k \neq 0, \quad k \in \mathbb{Z}, \end{cases} \qquad \int_0^{2\pi} e^{ikx} dx = 2\pi\delta_{k0}. \tag{B.39}$$

Using identity (B.39):

$$\int_0^{2\pi} e^{i(m-m')\theta} d\theta = 2\pi\delta_{mm'}, \qquad \int_0^{2\pi} e^{i(n-n')\phi} d\phi = 2\pi\delta_{nn'}.$$

The integral computation becomes:

$$\begin{aligned}
\int B_i^2\left(\mathbf{r},t\right) dV &= \int_0^1 \sum_{m',n'}\sum_{m,n}\left(B_i^{m',n'}\left(r,t\right)\right)^* B_i^{m,n}\left(r,t\right) 2\pi\delta_{mm'} 2\pi\delta_{nn'} R_0 r dr = \\
&4\pi^2 R_0 \int_0^1 \sum_{m,n} |B_i^{m,n}\left(r,t\right)|^2 r dr = 4\pi^2 R_0 \sum_{m,n}\int_0^1 \left(\Re[B_i^{m,n}\left(r,t\right)]^2 + \Im[B_i^{m,n}\left(r,t\right)]^2\right) r dr,
\end{aligned}$$

that, once replaced in (B.35), gives:

$$W_M(t) = 2\pi^2 R_0 \sum_{m=-M}^{M} \sum_{n=-N}^{N} \left(\int_0^1 r\Re[B_r^{m,n}(r,t)]^2 dr + \int_0^1 r\Im[B_r^{m,n}(r,t)]^2 dr + \right.$$
$$+ \int_0^1 r\Re\left[B_\theta^{m,n}(r,t)\right]^2 dr + \int_0^1 r\Im\left[B_\theta^{m,n}(r,t)\right]^2 dr +$$
$$\left. + \int_0^1 r\Re[B_z^{m,n}(r,t)]^2 dr + \int_0^1 r\Im[B_z^{m,n}(r,t)]^2 dr \right). \quad \text{(B.40)}$$

Making explicit the equilibrium ($m = 0$, $n = 0$) term from the sum, and recalling the following property: $B^*_{m,n} = B_{-m,-n}$, that holds for the Fourier harmonics of a real quantity (B):

$$W_M(t) = 2\pi^2 R_0 \left(\int_0^1 r\Re\left[B_r^{0,0}(r,t)\right]^2 dr + \int_0^1 r\Im\left[B_r^{0,0}(r,t)\right]^2 dr + \right.$$
$$+ \int_0^1 r\Re\left[B_\theta^{0,0}(r,t)\right]^2 dr + \int_0^1 r\Im\left[B_\theta^{0,0}(r,t)\right]^2 dr + \int_0^1 r\Re\left[B_z^{0,0}(r,t)\right]^2 dr + \int_0^1 r\Im\left[B_z^{0,0}(r,t)\right]^2 dr \Big) +$$
$$+ 4\pi^2 R_0 \sum_{m=1}^{M} \sum_{n=1}^{N} \left(\int_0^1 r\Re[B_r^{m,n}(r,t)]^2 dr + \int_0^1 r\Im[B_r^{m,n}(r,t)]^2 dr + \right.$$
$$\left. + \int_0^1 r\Re\left[B_\theta^{m,n}(r,t)\right]^2 dr + \int_0^1 r\Im\left[B_\theta^{m,n}(r,t)\right]^2 dr + \int_0^1 r\Re[B_z^{m,n}(r,t)]^2 dr + \int_0^1 r\Im[B_z^{m,n}(r,t)]^2 dr \right), \quad \text{(B.41)}$$

which is exactly the computation made by the routine `energy_compute_pix.pro`. The magnetic energy related to a specific mode $W_M^{m,n}$ is also defined. It is calculated, accounting for each mode contribution separately:

$$W_M^{m,n}(t) = 2\pi^2 R_0 \left(\int_0^1 r\Re[B_r^{m,n}(r,t)]^2 dr + \int_0^1 r\Im[B_r^{m,n}(r,t)]^2 dr + \right.$$
$$+ \int_0^1 r\Re\left[B_\theta^{m,n}(r,t)\right]^2 dr + \int_0^1 r\Im\left[B_\theta^{m,n}(r,t)\right]^2 dr +$$
$$\left. + \int_0^1 r\Re[B_z^{m,n}(r,t)]^2 dr + \int_0^1 r\Im[B_z^{m,n}(r,t)]^2 dr \right). \quad \text{(B.42)}$$

For a non equilibrium mode ($m \neq 0$, $n \neq 0$), the magnetic energy of the mode is usually defined considering also the harmonic with opposite wave numbers, that gives an additional factor 2.

$$\bar{W}_M^{m,n}(t) = 4\pi^2 R_0 \left(\int_0^1 r\Re[B_r^{m,n}(r,t)]^2 dr + \int_0^1 r\Im[B_r^{m,n}(r,t)]^2 dr + \right.$$
$$+ \int_0^1 r\Re\left[B_\theta^{m,n}(r,t)\right]^2 dr + \int_0^1 r\Im\left[B_\theta^{m,n}(r,t)\right]^2 dr +$$
$$\left. + \int_0^1 r\Re[B_z^{m,n}(r,t)]^2 dr + \int_0^1 r\Im[B_z^{m,n}(r,t)]^2 dr \right),$$

$$W_M(t) = W_M^{0,0}(t) + \sum_{m=1}^{M} \sum_{n=1}^{N} \bar{W}_M^{m,n}(t). \quad \text{(B.43)}$$

Bibliography

M. Agostini and P. Scarin. Edge turbulence approaching the density limit in RFX-mod experiment. *Plasma Physics and Controlled Fusion*, 62(2):025009, Nov 2019. doi: 10.1088/1361-6587/ab53b6. URL https://doi.org/10.1088/1361-6587/ab53b6.

R. Albanese and all. DTT: a divertor tokamak test facility for the study of the power exhaust issues in view of DEMO. *Nuclear Fusion*, 57(1):016010, Oct 2016. doi: 10.1088/0029-5515/57/1/016010. URL https://doi.org/10.1088/0029-5515/57/1/016010.

A. Alfier and R. Pasqualotto. New Thomson scattering diagnostic on RFX-mod. *Review of Scientific Instruments*, 78(1):013505, 2007. doi: 10.1063/1.2431769. URL https://doi.org/10.1063/1.2431769.

A. F. Almagri, J. T. Chapman, C. S. Chiang, D. Craig, D. J. Den Hartog, C. C. Hegna, and S. C. Prager. Momentum transport and flow damping in the reversed-field pinch plasma. *Physics of Plasmas*, 5(11):3982–3985, 1998. doi: 10.1063/1.873118. URL https://doi.org/10.1063/1.873118.

V. Antoni and S. Ortolani. Characteristics of the magnetic field fluctuations in the ETA-BETA II reversed field pinch experiment. *Plasma Physics*, 25(7):799, Jul 1983. doi: 10.1088/0032-1028/25/7/009. URL https://dx.doi.org/10.1088/0032-1028/25/7/009.

S. Atzeni and J. Meyer-ter Vehn. *The Physics of Inertial Fusion: Beam Plasma Interaction, Hydrodynamics, Hot Dense Matter*. International Series of Monographs on Physics. OUP Oxford, 2004. ISBN 9780191524059. URL https://books.google.be/books?id=HiaQDwAAQBAJ.

F. Auriemma, R. Lorenzini, M. Agostini, L. Carraro, G. D. Masi, A. Fassina, M. Gobbin, E. Martines, P. Innocente, P. Scarin, W. Schneider, and M. Zuin. Characterization of particle confinement properties in RFX-mod at a high plasma current. *Nuclear Fusion*, 55(4):043010, Mar 2015. doi: 10.1088/0029-5515/55/4/043010. URL https://doi.org/10.1088/0029-5515/55/4/043010.

R. Balescu. *Transport Processes in Plasmas*, volume 1 of *Transport Processes in Plasmas*. North-Holland, 1988a. ISBN 9780444870933. URL https://books.google.be/books?id=Y7Y5cgAACAAJ.

R. Balescu. *Transport Processes in Plasmas*, volume 2 of *Transport Processes in Plasmas*. North-Holland, 1988b. ISBN 9780444870919. URL https://books.google.be/books?id=NZgiAQAAIAAJ.

R. Balescu. Stochastic transport in plasmas. *European Journal of Physics*, 21(4):279, Jul 2000. doi: 10.1088/0143-0807/21/4/301. URL https://dx.doi.org/10.1088/0143-0807/21/4/301.

M. Banks. JET smashes fusion energy record. *Physics World*, 35(3):11–11, Aug 2022. doi: 10.1088/2058-7058/35/03/10. URL https://doi.org/10.1088/2058-7058/35/03/10.

M. Barbarino. A brief history of nuclear fusion. *Nature Physics*, 16:890–893, 2020. doi: 10.1038/s41567-020-0966-x. URL https://doi.org/10.1038/s41567-020-0966-x.

J. W. Bates and D. C. Montgomery. Toroidal visco-resistive magnetohydrodynamic steady states contain vortices. *Physics of Plasmas*, 5(7):2649–2653, 1998. doi: 10.1063/1.872952. URL https://doi.org/10.1063/1.872952.

M. G. Bell, K. M. McGuire, V. Arunasalam, C. W. Barnes, S. H. Batha, G. Bateman, M. A. Beer, R. E. Bell, M. Bitter, N. L. Bretz, R. V. Budny, C. E. Bush, S. R. Cauffman, Z. Chang, C.-S. Chang, C. Z. Cheng, D. S. Darrow, R. O. Dendy, W. Dorland, H. H. Duong, R. D. Durst, P. C. Efthimion, D. Ernst, H. Evenson, N. J. Fisch, R. K. Fisher, R. J. Fonck, E. D. Fredrickson, G. Y. Fu, H. P. Furth, N. N. Gorelenkov, B. Grek, L. R. Grisham, G. W. Hammett, G. R. Hanson, R. J. Hawryluk, W. W. Heidbrink, H. W. Herrmann, K. W. Hill, J. C. Hosea, H. Hsuan, M. H. Hughes, R. A. Hulse, A. C. Janos, D. L. Jassby, F. C. Jobes, D. W. Johnson, L. C. Johnson, J. Kesner, H. W. Kugel, N. T. Lam, B. Leblanc, F. M. Levinton, J. Machuzak, R. Majeski, D. K. Mansfield, E. Mazzucato, M. E. Mauel, J. M. McChesney, D. C. McCune, G. McKee, D. M. Meade, S. S. Medley, D. R. Mikkelsen, S. V. Mirnov, D. Mueller, G. A. Navratil, R. Nazikian, D. K. Owens, H. K. Park, W. Park, P. B. Parks, S. F. Paul, M. P. Petrov, C. K. Phillips, M. W. Phillips, C. S. Pitcher, A. T. Ramsey, M. H. Redi, G. Rewoldt, D. R. Roberts, J. H. Rogers, E. Ruskov, S. A. Sabbagh, M. Sasao, G. Schilling, J. F. Schivell, G. L. Schmidt, S. D. Scott, I. Semenov, S. Sesnic, C. H. Skinner, B. C. Stratton, J. D. Strachan, W. Stodiek, E. J. Synakowski, H. Takahashi, W. M. Tang, G. Taylor, J. L. Terry, M. E. Thompson, W. Tighe, S. V. Goeler, R. B. White, R. M. Wieland, J. R. Wilson, K.-L. Wong, P. Woskov, G. A. Wurden, M. Yamada, K. M. Young, M. C. Zarnstorff, and S. J. Zweben. Overview of DT results from TFTR. *Nuclear Fusion*, 35(12):1429–1436, Dec 1995. doi: 10.1088/0029-5515/35/12/i02. URL https://doi.org/10.1088/0029-5515/35/12/i02.

I. B. Bernstein, E. A. Frieman, M. D. Kruskal, R. M. Kulsrud, and S. Chandrasekhar. An energy principle for hydromagnetic stability problems. *Proceedings of the Royal Society of London. Series A. Mathematical and Physical Sciences*, 244(1236):17–40, 1958. doi: 10.1098/rspa.1958.0023. URL https://royalsocietypublishing.org/doi/abs/10.1098/rspa.1958.0023.

B. Bigot. ITER assembly phase: Progress toward first plasma. *Fusion Engineering and Design*, 164:112207, 2021. ISSN 0920-3796. doi: https://doi.org/10.1016/j.fusengdes.2020.112207. URL https://www.sciencedirect.com/science/article/pii/S0920379620307559.

C. Bishop. *Pattern Recognition and Machine Learning*. Information Science and Statistics. Springer, 2006. ISBN 9780387310732. URL https://books.google.it/books?id=kTNoQgAACAAJ.

D. Biskamp. *Nonlinear Magnetohydrodynamics*. Cambridge Monographs on Plasma Physics. Cambridge University Press, 1993. ISBN 9780521599184. URL https://books.google.be/books?id=OzFNhaVKA48C.

H. A. B. Bodin. Evolution of the RFP. *Plasma Physics and Controlled Fusion*, 30(14):2021–2029, Dec 1988. doi: 10.1088/0741-3335/30/14/006. URL https://doi.org/10.1088/0741-3335/30/14/006.

H. A. B. Bodin. The reversed field pinch. *Nuclear Fusion*, 30(9):1717–1737, Sep 1990. doi: 10.1088/0029-5515/30/9/005. URL https://doi.org/10.1088/0029-5515/30/9/005.

H. A. B. Bodin and A. A. Newton. Reversed-field-pinch research. *Nuclear Fusion*, 20(10): 1255–1324, Oct 1980. doi: 10.1088/0029-5515/20/10/006. URL https://doi.org/10.1088/0029-5515/20/10/006.

D. Bonfiglio, S. Cappello, and D. F. Escande. Dominant Electrostatic Nature of the Reversed Field Pinch Dynamo. *Phys. Rev. Lett.*, 94:145001, Apr 2005. doi: 10.1103/PhysRevLett.94.145001. URL https://link.aps.org/doi/10.1103/PhysRevLett.94.145001.

D. Bonfiglio, L. Chacón, and S. Cappello. Nonlinear three-dimensional verification of the SPECYL and PIXIE3D magnetohydrodynamics codes for fusion plasmas. *Physics of Plasmas*, 17(8):082501, 2010. doi: 10.1063/1.3462908. URL https://doi.org/10.1063/1.3462908.

D. Bonfiglio, S. Cappello, M. Veranda, L. Chacón, and D. F. Escande. Progress in nonlinear 3D MHD modeling of fusion plasmas with the PIXIE3D code. In *APS Division of Plasma Physics Meeting Abstracts*, volume 2013 of *APS Meeting Abstracts*, page CP8.078, Oct. 2013. URL https://ui.adsabs.harvard.edu/abs/2013APS..DPPCP8078B.

D. Bonfiglio, M. Veranda, S. Cappello, D. F. Escande, and L. Chacón. Experimental-like Helical Self-Organization in Reversed-Field Pinch Modeling. *Phys. Rev. Lett.*, 111:085002, Aug 2013. doi: 10.1103/PhysRevLett.111.085002. URL http://link.aps.org/doi/10.1103/PhysRevLett.111.085002.

D. Bonfiglio, S. Cappello, D. F. Escande, G. Di Giannatale, A. Kryzhanovskyy, V. Veranda, L. Marrelli, and P. Zanca. Effect of a realistic boundary on the helical self-organization of the RFP. In *Proc. of the 46$^{\text{th}}$ EPS Conference on Plasma Physics*, volume 43C, Milan, IT, 8 - 12 July 2019. European Physical Society. URL http://ocs.ciemat.es/EPS2019PAP/pdf/P1.1049.pdf.

D. Bonfiglio et al. 3D MHD contribution, Tavola rotonda viscosità. In *RFX-mod Scientific and Operation Meetings*, 2014.

H.-S. Bosch and G. Hale. Improved formulas for fusion cross-sections and thermal reactivities. *Nuclear Fusion*, 32(4):611–631, Apr 1992. doi: 10.1088/0029-5515/32/4/i07. URL https://doi.org/10.1088/0029-5515/32/4/i07.

J. Boussinesq. *Essai sur la théorie des eaux courantes*. Impr. nationale, 1877.

S. I. Braginskii. *Transport processes in a plasma*, volume 1. Consultants Bureau, New York, 1965.

B. N. Breizman, P. Aleynikov, E. M. Hollmann, and M. Lehnen. Physics of runaway electrons in tokamaks. *Nuclear Fusion*, 59(8):083001, Jun 2019. doi: 10.1088/1741-4326/ab1822. URL https://dx.doi.org/10.1088/1741-4326/ab1822.

P. R. Brunsell, H. Bergsåker, M. Cecconello, J. R. Drake, R. M. Gravestijn, A. Hedqvist, and J.-A. Malmberg. Initial results from the rebuilt EXTRAP T2R RFP device. *Plasma Physics and Controlled Fusion*, 43(11):1457, Oct 2001. doi: 10.1088/0741-3335/43/11/303. URL https://dx.doi.org/10.1088/0741-3335/43/11/303.

A. Buffa, S. Costa, L. Fellin, G. Malesani, P. Mondino, G. Nalesso, S. Ortolani, G. Rostagni, and A. Stella. Reverse-field-pinch experiments in the ETA-BETA device. *Plasma Physics and Fusion Technology*, 1975. URL https://inis.iaea.org/search/search.aspx?orig_q=RN:6216345.

C. Bustreo, P. Agostinetti, P. Bettini, R. Casagrande, R. Cavazzana, D. Escande, M. Osipenko, F. Panza, R. Piovan, M. E. Puiatti, G. Ricco, M. Ripani, M. Valisa, G. Zollino, and

M. Zuin. RFP based Fusion-Fission Hybrid reactor model for nuclear applications. *Fusion Engineering and Design*, 146:2725–2728, 2019. ISSN 0920-3796. doi: https://doi.org/10.1016/j.fusengdes.2019.05.006. URL https://www.sciencedirect.com/science/article/pii/S092037961930643X. SI:SOFT-30.

S. Cappello and D. Biskamp. Reconnection processes and scaling laws in reversed field pinch magnetohydrodynamics. *Nuclear Fusion*, 36(5):571, 1996. URL https://iopscience.iop.org/article/10.1088/0029-5515/36/5/I05.

S. Cappello and D. F. Escande. Bifurcation in Viscoresistive MHD: The Hartmann Number and the Reversed Field Pinch. *Phys. Rev. Lett.*, 85:3838–3841, Oct 2000. doi: 10.1103/PhysRevLett.85.3838. URL https://link.aps.org/doi/10.1103/PhysRevLett.85.3838.

S. Cappello and R. Paccagnella. Nonlinear plasma evolution and sustainment in the reversed field pinch. *Physics of Fluids B: Plasma Physics*, 4(3):611–618, 1992. doi: 10.1063/1.860471. URL https://doi.org/10.1063/1.860471.

S. Cappello, D. Bonfiglio, and D. F. Escande. Magnetohydrodynamic dynamo in reversed field pinch plasmas: Electrostatic drift nature of the dynamo velocity field. *Physics of Plasmas*, 13 (5):056102, 2006. doi: 10.1063/1.2177198. URL https://doi.org/10.1063/1.2177198.

S. Cappello, D. Bonfiglio, D. F. Escande, S. C. Guo, A. Alfier, and R. Lorenzini. The Reversed Field Pinch toward magnetic order: a genuine self-organization. *AIP Conference Proceedings*, 1069(1):27–39, 2008. doi: 10.1063/1.3033714. URL https://aip.scitation.org/doi/abs/10.1063/1.3033714.

A. Carati, M. Zuin, A. Maiocchi, M. Marino, E. Martines, and L. Galgani. Transition from order to chaos, and density limit, in magnetized plasmas. *Chaos: An Interdisciplinary Journal of Nonlinear Science*, 22(3):033124, 2012. doi: 10.1063/1.4745851. URL https://doi.org/10.1063/1.4745851.

L. Carraro, P. Innocente, M. E. Puiatti, F. Sattin, P. Scarin, and M. Valisa. Effects of the impurities on the loop voltage in RFX. In *Proc. of the 22nd EPS Conference on Plasma Physics*, volume 19C, pages 161–164, Bournemouth, UK, 3 - 7 July 1995. European Physical Society (Petit Lancy).

P. J. Catto. Practical gyrokinetics. *Journal of Plasma Physics*, 85(3):925850301, 2019. doi: 10.1017/S002237781900031X. URL https://www.cambridge.org/core/journals/journal-of-plasma-physics/article/practical-gyrokinetics/D8576F75C08B2A5DB3797F5673AE578F.

L. Chacón. Scalable parallel implicit solvers for 3d magnetohydrodynamics. *Journal of Physics: Conference Series*, 125:012041, Jul 2008. doi: 10.1088/1742-6596/125/1/012041. URL https://doi.org/10.1088/1742-6596/125/1/012041.

L. Chacón. A non-staggered, conservative, $\nabla \cdot \vec{B} = 0$, finite-volume scheme for 3D implicit extended magnetohydrodynamics in curvilinear geometries. *Computer Physics Communications*, 163(3):143–171, 2004. ISSN 0010-4655. doi: https://doi.org/10.1016/j.cpc.2004.08.005. URL https://www.sciencedirect.com/science/article/pii/S0010465504004369.

L. Chacón. An optimal, parallel, fully implicit Newton–Krylov solver for three-dimensional viscoresistive magnetohydrodynamics. *Physics of Plasmas*, 15(5):056103, 2008. doi: 10.1063/1.2838244. URL https://doi.org/10.1063/1.2838244.

L. Chacón, D. del Castillo-Negrete, and C. D. Hauck. An asymptotic-preserving semi-Lagrangian algorithm for the time-dependent anisotropic heat transport equation. *Journal of Computational Physics*, 272:719–746, 2014. ISSN 0021-9991. doi: https://doi.org/10.1016/j.jcp.2014.04.049. URL https://www.sciencedirect.com/science/article/pii/S0021999114003258.

R. Chahine and W. J. T. Bos. On the role and value of β in incompressible mhd simulations. *Physics of Plasmas*, 25(4):042115, 2018. doi: 10.1063/1.5018666. URL https://doi.org/10.1063/1.5018666.

C. S. Chang, S. Ku, and R. M. Churchill. X-point ion orbit physics in scrape-off layer and generation of a localized electrostatic potential perturbation around X-point. *Physics of Plasmas*, 26(1):014504, 2019. doi: 10.1063/1.5072795. URL https://doi.org/10.1063/1.5072795.

B. E. Chapman, R. Fitzpatrick, D. Craig, P. Martin, and G. Spizzo. Observation of tearing mode deceleration and locking due to eddy currents induced in a conducting shell. *Physics of Plasmas*, 11(5):2156–2171, 2004. doi: 10.1063/1.1689353. URL https://doi.org/10.1063/1.1689353.

B. E. Chapman, A. F. Almagri, J. K. Anderson, D. L. Brower, K. J. Caspary, D. J. Clayton, D. Craig, D. J. D. Hartog, W. X. Ding, D. A. Ennis, G. Fiksel, S. Gangadhara, S. Kumar, R. M. Magee, R. O'Connell, E. Parke, S. C. Prager, J. A. Reusch, J. S. Sarff, H. D. Stephens, and Y. M. Yang. Generation and confinement of hot ions and electrons in a reversed-field pinch plasma. *Plasma Physics and Controlled Fusion*, 52(12):124048, Nov 2010. doi: 10.1088/0741-3335/52/12/124048. URL https://doi.org/10.1088/0741-3335/52/12/124048.

S. Chapman, T. Cowling, D. Burnett, and C. Cercignani. *The Mathematical Theory of Non-uniform Gases: An Account of the Kinetic Theory of Viscosity, Thermal Conduction and Diffusion in Gases*. Cambridge Mathematical Library. Cambridge University Press, 1990. ISBN 9780521408448. URL https://books.google.be/books?id=JcjHpiJPKeIC.

C.-C. Chen, P. H. Diamond, and S. M. Tobias. Ion heat and parallel momentum transport by stochastic magnetic fields and turbulence. *Plasma Physics and Controlled Fusion*, 64(1):015006, Dec 2021. doi: 10.1088/1361-6587/ac38b2. URL https://dx.doi.org/10.1088/1361-6587/ac38b2.

A. R. Choudhuri. *The Physics of Fluids and Plasmas: An Introduction for Astrophysicists*. Cambridge University Press, 1998. ISBN 9780521555432. URL https://books.google.be/books?id=pcmyNUuob_AC.

G. Ciaccio, M. Veranda, D. Bonfiglio, S. Cappello, G. Spizzo, L. Chacón, and R. B. White. Numerical verification of orbit and nemato codes for magnetic topology diagnosis. *Physics of Plasmas*, 20(6):062505, 2013. doi: 10.1063/1.4811380. URL https://doi.org/10.1063/1.4811380.

J. W. Connor and J. B. Taylor. Scaling laws for plasma confinement. *Nuclear Fusion*, 17(5):1047–1055, Oct 1977. doi: 10.1088/0029-5515/17/5/015. URL https://doi.org/10.1088/0029-5515/17/5/015.

D. Craig, E. H. Tan, B. Schott, J. K. Anderson, J. Boguski, D. J. Den Hartog, T. Nishizawa, M. D. Nornberg, and Z. A. Xing. Intrinsic flow and tearing mode rotation in the RFP during improved confinement. *Physics of Plasmas*, 26(7):072503, 2019. doi: 10.1063/1.5095620. URL https://doi.org/10.1063/1.5095620.

A. J. Creely, M. J. Greenwald, S. B. Ballinger, D. Brunner, J. Canik, J. Doody, T. Fülöp, D. T. Garnier, R. Granetz, T. K. Gray, and et al. Overview of the SPARC tokamak. *Journal of Plasma Physics*, 86(5):865860502, 2020. doi: 10.1017/S0022377820001257. URL https://www.cambridge.org/core/journals/journal-of-plasma-physics/article/overview-of-the-sparc-tokamak/DD3C44ECD26F5EACC554811764EF9FF0.

J. De Rycke, G. Verdoolaege, J. Hall, and H. Wu. Kinematic viscosity estimates in RFP fusion plasmas: a Bayesian approach, 2022.

G. L. Delzanno, L. Chacón, and J. M. Finn. Electrostatic mode associated with the pinch velocity in reversed field pinch simulations. *Physics of Plasmas*, 15(12):122102, 2008. doi: 10.1063/1.3026714. URL https://doi.org/10.1063/1.3026714.

R. E. Denton, J. F. Drake, R. G. Kleva, and D. A. Boyd. Skin currents and compound sawteeth in tokamaks. *Phys. Rev. Lett.*, 56:2477–2480, Jun 1986. doi: 10.1103/PhysRevLett.56.2477. URL https://link.aps.org/doi/10.1103/PhysRevLett.56.2477.

R. E. Denton, J. F. Drake, and R. G. Kleva. The m=1 convection cell and sawteeth in tokamaks. *The Physics of Fluids*, 30(5):1448–1451, 1987. doi: 10.1063/1.866258. URL https://aip.scitation.org/doi/abs/10.1063/1.866258.

R. N. Dexter, D. W. Kerst, T. W. Lovell, S. C. Prager, and J. C. Sprott. The madison symmetric torus. *Fusion Technology*, 19(1):131–139, 1991. doi: 10.13182/FST91-A29322. URL https://doi.org/10.13182/FST91-A29322.

P. H. Diamond, S.-I. Itoh, K. Itoh, and T. S. Hahm. Zonal flows in plasma - a review. *Plasma Physics and Controlled Fusion*, 47(5):R35, Apr 2005. doi: 10.1088/0741-3335/47/5/R01. URL https://dx.doi.org/10.1088/0741-3335/47/5/R01.

D. Escande, F. Sattin, and P. Zanca. Plasma-wall self-organization in magnetic fusion. *Nuclear Fusion*, 62(2):026001, Dec 2021. doi: 10.1088/1741-4326/ac3c87. URL https://dx.doi.org/10.1088/1741-4326/ac3c87.

D. F. Escande, S. Cappello, F. D'Angelo, P. Martin, S. Ortolani, and R. Paccagnella. Single helicity: a new paradigm for the reversed-field pinch. *Plasma Physics and Controlled Fusion*, 42:B243, 2000.

EUROfusion Consortium. European Research Roadmap to the Realisation of Fusion Energy. *Eurofusion*, 2018. URL https://www.euro-fusion.org/eurofusion/roadmap/.

E. Fermi. The Development of the First Chain Reacting Pile. *Proceedings of the American Philosophical Society*, 90(1):20–24, 1946. ISSN 0003049X. URL http://www.jstor.org/stable/3301034.

J. M. Finn, P. N. Guzdar, and A. A. Chernikov. Particle transport and rotation damping due to stochastic magnetic field lines. *Physics of Fluids B: Plasma Physics*, 4(5):1152–1155, 1992a. doi: 10.1063/1.860123. URL https://doi.org/10.1063/1.860123.

J. M. Finn, R. Nebel, and C. Bathke. Single and multiple helicity ohmic states in reversed-field pinches. *Physics of Fluids B: Plasma Physics*, 4(5):1262–1279, 1992b. doi: 10.1063/1.860082. URL https://doi.org/10.1063/1.860082.

R. Fitzpatrick. Bifurcated states of a rotating tokamak plasma in the presence of a static error-field. *Physics of Plasmas*, 5(9):3325–3341, 1998. doi: 10.1063/1.873000. URL https://doi.org/10.1063/1.873000.

R. Fitzpatrick. *Plasma Physics: An Introduction*. CRC Press, 2014. ISBN 9781466594272. URL https://books.google.be/books?id=5HbSBQAAQBAJ.

R. Fitzpatrick, S. C. Guo, D. J. Den Hartog, and C. C. Hegna. Effect of a resistive vacuum vessel on dynamo mode rotation in reversed field pinches. *Physics of Plasmas*, 6(10):3878–3889, 1999. doi: 10.1063/1.873650. URL https://doi.org/10.1063/1.873650.

P. Franz, L. Marrelli, A. Murari, G. Spizzo, and P. Martin. Soft x ray tomographic imaging in the RFX reversed field pinch. *Nuclear Fusion*, 41(6):695–709, Jun 2001. doi: 10.1088/0029-5515/41/6/304. URL https://doi.org/10.1088/0029-5515/41/6/304.

P. Franz, M. Gobbin, L. Marrelli, A. Ruzzon, F. Bonomo, A. Fassina, E. Martines, and G. Spizzo. Experimental investigation of electron temperature dynamics of helical states in the RFX-mod reversed field pinch. *Nuclear Fusion*, 53(5):053011, Apr 2013. doi: 10.1088/0029-5515/53/5/053011. URL https://doi.org/10.1088/0029-5515/53/5/053011.

L. Frassinetti, S. Menmuir, K. E. J. Olofsson, P. R. Brunsell, and J. R. Drake. Tearing mode velocity braking due to resonant magnetic perturbations. *Nuclear Fusion*, 52(10):103014, Sep 2012. doi: 10.1088/0029-5515/52/10/103014. URL https://doi.org/10.1088/0029-5515/52/10/103014.

J. Freidberg. *Plasma Physics and Fusion Energy*. Cambridge University Press, 2007. ISBN 9780521851077. URL https://books.google.be/books?id=ZGU-ngEACAAJ.

R. Fridström, B. E. Chapman, A. F. Almagri, L. Frassinetti, P. R. Brunsell, T. Nishizawa, and J. S. Sarff. Dependence of Perpendicular Viscosity on Magnetic Fluctuations in a Stochastic Topology. *Phys. Rev. Lett.*, 120:225002, May 2018. doi: 10.1103/PhysRevLett.120.225002. URL https://link.aps.org/doi/10.1103/PhysRevLett.120.225002.

S. Futatani, J. A. Morales, and W. J. T. Bos. Dynamic equilibria and magnetohydrodynamic instabilities in toroidal plasmas with non-uniform transport coefficients. *Physics of Plasmas*, 22(5):052503, 2015. doi: 10.1063/1.4919960. URL https://aip.scitation.org/doi/abs/10.1063/1.4919960.

A. M. Futch, D. Craig, R. Hesse, and C. M. Jacobson. Role of resistivity and viscosity in the excitation of stable m=0 modes during the RFP sawtooth crash. *Physics of Plasmas*, 25(11):112506, 2018. doi: 10.1063/1.5054578. URL https://doi.org/10.1063/1.5054578.

D. A. Gates and L. Delgado-Aparicio. Origin of Tokamak Density Limit Scalings. *Phys. Rev. Lett.*, 108:165004, Apr 2012. doi: 10.1103/PhysRevLett.108.165004. URL http://link.aps.org/doi/10.1103/PhysRevLett.108.165004.

A. H. Glasser, C. R. Sovinec, R. A. Nebel, T. A. Gianakon, S. J. Plimpton, M. S. Chu, D. D. Schnack, and the NIMROD Team. The nimrod code: a new approach to numerical plasma physics. *Plasma Physics and Controlled Fusion*, 41(3A):A747, mar 1999. doi: 10.1088/0741-3335/41/3A/067. URL https://dx.doi.org/10.1088/0741-3335/41/3A/067.

M. Gobbin, P. Franz, F. Auriemma, R. Lorenzini, and L. Marrelli. Spontaneous versus induced hydrogen and deuterium helical shaped plasmas with electron internal transport barriers. *Plasma Physics and Controlled Fusion*, 57(9):095004, Jul 2015. doi: 10.1088/0741-3335/57/9/095004. URL https://doi.org/10.1088/0741-3335/57/9/095004.

H. Goedbloed, R. Keppens, and S. Poedts. *Magnetohydrodynamics: Of Laboratory and Astrophysical Plasmas*. Cambridge University Press, 2019. ISBN 9781107123922. URL https://books.google.be/books?id=Wqh7DwAAQBAJ.

R. Goldston and P. Rutherford. *Introduction to Plasma Physics*. IOP Publishing, 1995. ISBN 9780750301831. URL https://books.google.be/books/about/Introduction_to_Plasma_Physics.html?id=7kM7yEFUGnAC&redir_esc=y.

R. S. Granetz. Density Threshold for Magnetohydrodynamic Activity in Alcator *C*. *Phys. Rev. Lett.*, 49:658–661, Aug 1982. doi: 10.1103/PhysRevLett.49.658. URL http://link.aps.org/doi/10.1103/PhysRevLett.49.658.

M. Greenwald. Density limits in toroidal plasmas. *Plasma Physics and Controlled Fusion*, 44 (8):R27–R53, 2002. URL http://stacks.iop.org/0741-3335/44/R27.

M. Greenwald, J. L. Terry, S. M. Wolfe, S. Ejima, M. G. Bell, S. M. Kaye, and G. H. Neilson. A new look at density limits in tokamaks. *Nuclear Fusion*, 28(12):2199, 1988. URL https://iopscience.iop.org/article/10.1088/0029-5515/28/12/009.

S. C. Guo, R. Paccagnella, and F. Romanelli. Ion-temperature-gradient-driven instability and anomalous ion heating in reversed-field pinches. *Physics of Plasmas*, 1(8):2741–2747, 1994. doi: 10.1063/1.870509. URL https://doi.org/10.1063/1.870509.

S. Günter, Q. Yu, K. Lackner, A. Bhattacharjee, and Y.-M. Huang. Fast sawtooth reconnection at realistic Lundquist numbers. *Plasma Physics and Controlled Fusion*, 57(1):014017, Nov 2014. doi: 10.1088/0741-3335/57/1/014017. URL https://dx.doi.org/10.1088/0741-3335/57/1/014017.

F. D. Halpern, D. Leblond, H. Lütjens, and J.-F. Luciani. Oscillation regimes of the internal kink mode in tokamak plasmas. *Plasma Physics and Controlled Fusion*, 53(1):015011, Nov 2010. doi: 10.1088/0741-3335/53/1/015011. URL https://doi.org/10.1088/0741-3335/53/1/015011.

F. D. Halpern, H. Lütjens, and J.-F. Luciani. Diamagnetic thresholds for sawtooth cycling in tokamak plasmas. *Physics of Plasmas*, 18(10):102501, 2011. doi: 10.1063/1.3646305. URL https://doi.org/10.1063/1.3646305.

R. Hawryluk and H. Zohm. The challenge and promise of studying burning plasmas. *Physics Today*, 72(12):34–40, 2019. doi: 10.1063/PT.3.4363. URL https://doi.org/10.1063/PT.3.4363.

Y. L. Ho, D. D. Schnack, P. Nordlund, S. Mazur, H. Satherblom, J. Scheffel, and J. R. Drake. Effect of aspect ratio on magnetic field fluctuations in the reversed-field pinch. *Physics of Plasmas*, 2(9):3407–3411, 1995. doi: 10.1063/1.871122. URL https://doi.org/10.1063/1.871122.

M. Hoelzl, G. Huijsmans, S. Pamela, M. Becoulet, E. Nardon, F. J. Artola, B. Nkonga, C. Atanasiu, V. Bandaru, A. Bhole, D. Bonfiglio, A. Cathey, O. Czarny, A. Dvornova, T. Feher, A. Fil, E. Franck, S. Futatani, M. Gruca, H. Guillard, J. W. Haverkort, I. Holod, D. Hu, S. Kim, S. Q. Korving, L. Kos, I. Krebs, L. Kripner, G. Latu, F. Liu, P. Merkel, D. Meshcheriakov, V. Mitterauer, S. Mochalskyy, J. Morales, R. Nies, N. Nikulsin, F. Orain, D. Penko, J. Pratt, R. Ramasamy, P. Ramet, C. Reux, K. Särkimäki, N. Schwarz, P. S. Verma, S. F. Smith, C. Sommariva, E. Strumberger, D. van Vugt, M. Verbeek, E. Westerhof, F. Wieschollek, and J. Zielinski. The JOREK non-linear extended MHD code and applications to large-scale instabilities and their control in magnetically confined fusion plasmas. *Nuclear Fusion*, Apr 2021. doi: 10.1088/1741-4326/abf99f. URL https://doi.org/10.1088/1741-4326/abf99f.

K. Huang. *Statistical Mechanics, 2^{nd} Ed.* Wiley, 2008. ISBN 9788126518494. URL https://books.google.be/books?id=ZHl8HLk-K3AC.

G. T. A. Huysmans and O. Czarny. MHD stability in X-point geometry: simulation of ELMs. *Nuclear Fusion*, 47(7):659–666, Jun 2007. doi: 10.1088/0029-5515/47/7/016. URL https://doi.org/10.1088/0029-5515/47/7/016.

IEA (International Energy Agency). Energy technology perspectives 2020. *IEA*, 2020. URL https://www.iea.org/reports/energy-technology-perspectives-2020.

C. Iliadis. *Nuclear Physics of Stars*. Wiley, 2015. ISBN 9783527336517. URL https://books.google.be/books?id=kLZNCAAAQBAJ.

P. Innocente, S. Martini, A. Canton, and L. Tasinato. Upgrade of the RFX CO_2 interferometer using in-vessel optics for extended edge resolution. *Review of Scientific Instruments*, 68(1): 694–697, 1997. doi: 10.1063/1.1147677. URL https://doi.org/10.1063/1.1147677.

P. Innocente, A. Alfier, L. Carraro, R. Lorenzini, R. Pasqualotto, D. Terranova, and the RFX Team. Transport and confinement studies in the RFX-mod reversed-field pinch experiment. *Nuclear Fusion*, 47(9):1092–1100, Aug 2007. doi: 10.1088/0029-5515/47/9/004. URL https://doi.org/10.1088/0029-5515/47/9/004.

P. Innocente, A. Alfier, A. Canton, and R. Pasqualotto. Plasma performance and scaling laws in the RFX-mod reversed-field pinch experiment. *Nuclear Fusion*, 49(11):115022, Sep 2009. doi: 10.1088/0029-5515/49/11/115022. URL https://doi.org/10.1088/0029-5515/49/11/115022.

A. Intravaia, L. Marrelli, P. Martin, R. Pasqualotto, P. Franz, A. Murari, G. Spizzo, T. Bolzonella, A. Canton, P. Innocente, S. Martini, M. E. Puiatti, P. Scarin, D. Terranova, and M. Valisa. Scaling of local core transport with lundquist number in the reversed field pinch. *Phys. Rev. Lett.*, 83:5499–5502, Dec 1999. doi: 10.1103/PhysRevLett.83.5499. URL https://link.aps.org/doi/10.1103/PhysRevLett.83.5499.

S. C. Jardin, I. Krebs, and N. Ferraro. A new explanation of the sawtooth phenomena in tokamaks. *Physics of Plasmas*, 27(3):032509, 2020. doi: 10.1063/1.5140968. URL https://doi.org/10.1063/1.5140968.

B. B. Kadomtsev. Disruptive instability in tokamaks. *Sov. Tech. Phys. Lett. (Engl. Transl.); (United States)*, 1:5, 1 1975. URL https://www.osti.gov/biblio/7147025.

Y. Kamada, E. D. Pietro, M. Hanada, P. Barabaschi, S. Ide, S. Davis, M. Yoshida, G. Giruzzi, C. Sozzi, and the JT-60SA Integrated Project Team. Completion of JT-60SA construction and contribution to ITER. *Nuclear Fusion*, 62(4):042002, Mar 2022. doi: 10.1088/1741-4326/ac10e7. URL https://doi.org/10.1088/1741-4326/ac10e7.

L. P. J. Kamp and D. C. Montgomery. Toroidal steady states in visco-resistive magnetohydrodynamics. *Journal of Plasma Physics*, 70(2):113–142, 2004. doi: 10.1017/S0022377803002629.

M. Keilhacker, A. Gibson, C. Gormezano, P. J. Lomas, P. R. Thomas, M. L. Watkins, P. Andrew, B. Balet, D. Borba, C. D. Challis, I. Coffey, G. A. Cottrell, H. P. L. D. Esch, N. Deliyanakis, A. Fasoli, C. W. Gowers, H. Y. Guo, G. T. A. Huysmans, T. T. C. Jones, W. Kerner, R. W. T. König, M. J. Loughlin, A. Maas, F. B. Marcus, M. F. F. Nave, F. G. Rimini, G. J. Sadler, S. E. Sharapov, G. Sips, P. Smeulders, F. X. Söldner, A. Taroni, B. J. D. Tubbing, M. G. von Hellermann, D. J. Ward, and J. Team. High fusion performance from deuterium-tritium plasmas in JET. *Nuclear Fusion*, 39(2):209–234, Feb 1999. doi: 10.1088/0029-5515/39/2/306. URL https://doi.org/10.1088/0029-5515/39/2/306.

M. Kikuchi, K. Lackner, and M. Q. Tran. *Fusion Physics*. Non-serial Publications. INTERNATIONAL ATOMIC ENERGY AGENCY, Vienna, 2012. ISBN 978-92-0-130410-0. URL https://www.iaea.org/publications/8879/fusion-physics.

T. Klinger, T. Andreeva, S. Bozhenkov, C. Brandt, R. Burhenn, B. Buttenschön, G. Fuchert, B. Geiger, O. Grulke, H. Laqua, N. Pablant, K. Rahbarnia, T. Stange, A. von Stechow, N. Tamura, H. Thomsen, Y. Turkin, T. Wegner, I. Abramovic, S. Äkäslompolo, J. Alcuson, P. Aleynikov, K. Aleynikova, A. Ali, A. Alonso, G. Anda, E. Ascasibar, J. P. Bähner, S. G. Baek, M. Balden, J. Baldzuhn, M. Banduch, T. Barbui, W. Behr, C. Beidler, A. Benndorf, C. Biedermann, W. Biel, B. Blackwell, E. Blanco, M. Blatzheim, S. Ballinger, T. Bluhm, D. Böckenhoff, B. Böswirth, L.-G. Böttger, M. Borchardt, V. Borsuk, J. Boscary, H.-S. Bosch, M. Beurskens, R. Brakel, H. Brand, T. Bräuer, H. Braune, S. Brezinsek, K.-J. Brunner, R. Bussiahn, V. Bykov, J. Cai, I. Calvo, B. Cannas, A. Cappa, A. Carls, D. Carralero, L. Carraro, B. Carvalho, F. Castejon, A. Charl, N. Chaudhary, D. Chauvin, F. Chernyshev, M. Cianciosa, R. Citarella, G. Claps, J. Coenen, M. Cole, M. Cole, F. Cordella, G. Cseh, A. Czarnecka, K. Czerski, M. Czerwinski, G. Czymek, A. da Molin, A. da Silva, H. Damm, A. de la Pena, S. Degenkolbe, C. Dhard, M. Dibon, A. Dinklage, T. Dittmar, M. Drevlak, P. Drewelow, P. Drews, F. Durodie, E. Edlund, P. van Eeten, F. Effenberg, G. Ehrke, S. Elgeti, M. Endler, D. Ennis, H. Esteban, T. Estrada, J. Fellinger, Y. Feng, E. Flom, H. Fernandes, W. H. Fietz, W. Figacz, J. Fontdecaba, O. Ford, T. Fornal, H. Frerichs, A. Freund, T. Funaba, A. Galkowski, G. Gantenbein, Y. Gao, J. G. Regaña, D. Gates, J. Geiger, V. Giannella, A. Gogoleva, B. Goncalves, A. Goriaev, D. Gradic, M. Grahl, J. Green, H. Greuner, A. Grosman, H. Grote, M. Gruca, C. Guerard, P. Hacker, X. Han, J. Harris, D. Hartmann, D. Hathiramani, B. Hein, B. Heinemann, P. Helander, S. Henneberg, M. Henkel, J. H. Sanchez, C. Hidalgo, M. Hirsch, K. Hollfeld, U. Höfel, A. Hölting, D. Höschen, M. Houry, J. Howard, X. Huang, Z. Huang, M. Hubeny, M. Huber, H. Hunger, K. Ida, T. Ilkei, S. Illy, B. Israeli, S. Jablonski, M. Jakubowski, J. Jelonnek, H. Jenzsch, T. Jesche, M. Jia, P. Junghanns, J. Kacmarczyk, J.-P. Kallmeyer, U. Kamionka, H. Kasahara, W. Kasparek, Y. Kazakov, N. Kenmochi, C. Killer, A. Kirschner, R. Kleiber, J. Knauer, M. Knaup, A. Knieps, T. Kobarg, G. Kocsis, F. Köchl, Y. Kolesnichenko, A. Könies, R. König, P. Kornejew, J.-P. Koschinsky, F. Köster, M. Krämer, R. Krampitz, A. Krämer-Flecken, N. Krawczyk, T. Kremeyer, J. Krom, M. Krychowiak, I. Ksiazek, M. Kubkowska, G. Kühner, T. Kurki-Suonio, P. Kurz, S. Kwak, M. Landreman, P. Lang, R. Lang, A. Langenberg, S. Langish, H. Laqua, R. Laube, S. Lazerson, C. Lechte, M. Lennartz, W. Leonhardt, C. Li, C. Li, Y. Li, Y. Liang, C. Linsmeier, S. Liu, J.-F. Lobsien, D. Loesser, J. L. Cisquella, J. Lore, A. Lorenz, M. Losert, A. Lücke, A. Lumsdaine, V. Lutsenko, H. Maaßberg, O. Marchuk, J. Matthew, S. Marsen, M. Marushchenko, S. Masuzaki, D. Maurer, M. Mayer, K. McCarthy, P. McNeely, A. Meier, D. Mellein, B. Mendelevitch, P. Mertens, D. Mikkelsen, A. Mishchenko, B. Missal, J. Mittelstaedt, T. Mizuuchi, A. Mollen, V. Moncada, T. Mönnich, T. Morisaki, D. Moseev, S. Murakami, G. Náfrádi, M. Nagel, D. Naujoks, H. Neilson, R. Neu, O. Neubauer, U. Neuner, T. Ngo, D. Nicolai, S. Nielsen, H. Niemann, T. Nishizawa, R. Nocentini, C. Nührenberg, J. Nührenberg, S. Obermayer, G. Offermanns, K. Ogawa, J. Ölmanns, J. Ongena, J. W. Oosterbeek, G. Orozco, M. Otte, L. P. Rodriguez, N. Panadero, N. P. Alvarez, D. Papenfuß, S. Paqay, E. Pasch, A. Pavone, E. Pawelec, T. S. Pedersen, G. Pelka, V. Perseo, B. Peterson, D. Pilopp, S. Pingel, F. Pisano, B. Plaum, G. Plunk, P. Pölöskei, M. Porkolab, J. Proll, M.-E. Puiatti, A. P. Sitjes, F. Purps, M. Rack, S. Récsei, A. Reiman, F. Reimold, D. Reiter, F. Remppel, S. Renard, R. Riedl, J. Riemann, K. Risse, V. Rohde, H. Röhlinger, M. Romé, D. Rondeshagen, P. Rong, B. Roth, L. Rudischhauser, K. Rummel, T. Rummel, A. Runov, N. Rust, L. Ryc, S. Ryosuke, R. Sakamoto, M. Salewski, A. Samartsev, E. Sanchez, F. Sano, S. Satake, J. Schacht, G. Satheeswaran, F. Schauer, T. Scherer, J. Schilling, A. Schlaich, G. Schlisio, F. Schluck, K.-H. Schlüter, J. Schmitt, H. Schmitz, O. Schmitz, S. Schmuck, M. Schneider, W. Schneider, P. Scholz, R. Schrittwieser, M. Schröder, T. Schröder, R. Schroeder, H. Schumacher, B. Schweer, E. Scott, S. Sereda, B. Shanahan, M. Sibilia, P. Sinha, S. Sipliä, C. Slaby, M. Sleczka, H. Smith, W. Spiess, D. Spong, A. Spring, R. Stadler, M. Stejner, L. Stephey, U. Stridde, C. Suzuki, J. Svensson, V. Szabó, T. Szabolics,

T. Szepesi, Z. Szökefalvi-Nagy, A. Tancetti, J. Terry, J. Thomas, M. Thumm, J. Travere, P. Traverso, J. Tretter, H. T. Mora, H. Tsuchiya, T. Tsujimura, S. Tulipán, B. Unterberg, I. Vakulchyk, S. Valet, L. Vano, B. van Milligen, A. J. van Vuuren, L. Vela, J.-L. Velasco, M. Vergote, M. Vervier, N. Vianello, H. Viebke, R. Vilbrandt, A. Vorköper, S. Wadle, F. Wagner, E. Wang, N. Wang, Z. Wang, F. Warmer, T. Wauters, L. Wegener, J. Weggen, Y. Wei, G. Weir, J. Wendorf, U. Wenzel, A. Werner, A. White, B. Wiegel, F. Wilde, T. Windisch, M. Winkler, A. Winter, V. Winters, S. Wolf, R. Wolf, A. Wright, G. Wurden, P. Xanthopoulos, H. Yamada, I. Yamada, R. Yasuhara, M. Yokoyama, M. Zanini, M. Zarnstorff, A. Zeitler, D. Zhang, H. Zhang, J. Zhu, M. Zilker, A. Zocco, S. Zoletnik, and M. Zuin. Overview of first Wendelstein 7-X high-performance operation. *Nuclear Fusion*, 59(11):112004, Jun 2019. doi: 10.1088/1741-4326/ab03a7. URL https://doi.org/10.1088/1741-4326/ab03a7.

H. Koguchi, H. Sakakita, S. Kiyama, K. Yambe, T. Asai, Y. Hirano, F. Auriemma, D. Terranova, and P. Innocente. High Beta and High Density Operation in TPE-RX. *Plasma and Fusion Research*, 4:022–022, 2009. doi: 10.1585/pfr.4.022. URL https://www.jstage.jst.go.jp/article/pfr/4/0/4_0_022/_article.

I. Krebs, S. C. Jardin, S. Günter, K. Lackner, M. Hoelzl, E. Strumberger, and N. Ferraro. Magnetic flux pumping in 3D nonlinear magnetohydrodynamic simulations. *Physics of Plasmas*, 24(10):102511, 2017. doi: 10.1063/1.4990704. URL https://doi.org/10.1063/1.4990704.

A. Kuritsyn, M. Yamada, S. Gerhardt, H. Ji, R. Kulsrud, and Y. Ren. Measurements of the parallel and transverse Spitzer resistivities during collisional magnetic reconnection. *Physics of Plasmas*, 13(5):055703, 2006. doi: 10.1063/1.2179416. URL https://doi.org/10.1063/1.2179416.

L. D. Landau. The transport equation in the case of Coulomb interaction. *J. Exp. Theor. Phys.*, 7:203, 1937.

I. Langmuir. Oscillations in Ionized Gases. *Proc Natl Acad Sci USA*, 14(8):627–37, Aug 1928. URL https://www.ncbi.nlm.nih.gov/pmc/articles/PMC1085653/.

J. D. Lawson. Some criteria for a power producing thermonuclear reactor. *Proceedings of the Physical Society. Section B*, 70(1):6–10, Jan 1957. doi: 10.1088/0370-1301/70/1/303. URL https://doi.org/10.1088/0370-1301/70/1/303.

B. Lipschultz. Review of MARFE phenomena in tokamaks. *Journal of Nuclear Materials*, 145-147:15 – 25, 1987. ISSN 0022-3115. doi: https://doi.org/10.1016/0022-3115(87)90306-0. URL http://www.sciencedirect.com/science/article/pii/0022311587903060.

W. Liu, W. Mao, T. Lan, G. Zhuang, J. Zheng, P. Yuan, H. Li, J. Xie, A. Liu, Z. Wu, Z. Liu, S. Wan, H. Wang, X. Wen, H. Zhou, Z. Wei, W. You, C. Tu, M. Tan, Z. Li, Y. Adil, H. Xu, T. Deng, J. Zhu, C. Chen, S. Zhang, J. Wu, Y. Zu, B. Luo, C. Xiao, and W. Ding. An overview of diagnostic upgrade and experimental progress in the KTX. *Nuclear Fusion*, 59 (11):112013, Jul 2019. doi: 10.1088/1741-4326/ab168c. URL https://doi.org/10.1088/1741-4326/ab168c.

R. Lorenzini, M. Agostini, A. Alfier, V. Antoni, L. Apolloni, F. Auriemma, O. Barana, M. Baruzzo, P. Bettini, D. Bonfiglio, T. Bolzonella, F. Bonomo, M. Brombin, A. Buffa, A. Canton, S. Cappello, L. Carraro, R. Cavazzana, G. Chitarin, S. Dal Bello, A. De Lorenzi, G. De Masi, D. F. Escande, A. Fassina, P. Franz, E. Gaio, E. Gazza, L. Giudicotti, F. Gnesotto, M. Gobbin, L. Grando, S. C. Guo, P. Innocente, A. Luchetta, G. Manduchi, G. Marchiori, D. Marcuzzi, L. Marrelli, P. Martin, S. Martini, E. Martines, F. Milani, M. Moresco, L. Novello, S. Ortolani, R. Paccagnella, R. Pasqualotto, S. Peruzzo, R. Piovan, P. Piovesan, L. Piron, A. Pizzimenti, N. Pomaro, I. Predebon, M. E. Puiatti, G. Rostagni, F. Sattin,

P. Scarin, G. Serianni, P. Sonato, E. Spada, A. Soppelsa, S. Spagnolo, G. Spizzo, M. Spolaore, C. Taliercio, D. Terranova, V. Toigo, M. Valisa, P. Veltri, N. Vianello, P. Zaccaria, B. Zaniol, L. Zanotto, E. Zilli, and M. Zuin. Improvement of the magnetic configuration in the reversed field pinch through successive bifurcations. *Physics of Plasmas*, 16(5):056109, 2009a. doi: 10.1063/1.3082821. URL https://doi.org/10.1063/1.3082821.

R. Lorenzini, E. Martines, P. Piovesan, D. Terranova, P. Zanca, M. Zuin, A. Alfier, D. Bonfiglio, F. Bonomo, A. Canton, S. Cappello, L. Carraro, R. Cavazzana, D. F. Escande, A. Fassina, P. Franz, M. Gobbin, P. Innocente, L. Marrelli, R. Pasqualotto, M. E. Puiatti, M. Spolaore, M. Valisa, N. Vianello, P. Martin, and RFX-mod team and collaborators. Self-organized helical equilibria as a new paradigm for ohmically heated fusion plasmas. *Nature Physics*, 5: 570–574, 2009b. doi: 10.1038/nphys1308. URL https://doi.org/10.1038/nphys1308.

H. Lütjens and J.-F. Luciani. The xtor code for nonlinear 3d simulations of mhd instabilities in tokamak plasmas. *Journal of Computational Physics*, 227(14):6944–6966, 2008. ISSN 0021-9991. doi: https://doi.org/10.1016/j.jcp.2008.04.003. URL https://www.sciencedirect.com/science/article/pii/S0021999108002064.

D. Maisonnier, D. Campbell, I. Cook, L. D. Pace, L. Giancarli, J. Hayward, A. L. Puma, M. Medrano, P. Norajitra, M. Roccella, P. Sardain, M. Q. Tran, and D. Ward. Power plant conceptual studies in Europe. *Nuclear Fusion*, 47(11):1524–1532, Oct 2007. doi: 10.1088/0029-5515/47/11/014. URL https://doi.org/10.1088/0029-5515/47/11/014.

L. Marrelli, R. Cavazzana, D. Bonfiglio, M. Gobbin, G. Marchiori, S. Peruzzo, M. Puiatti, G. Spizzo, D. Voltolina, P. Zanca, M. Zuin, G. Berton, P. Bettini, T. Bolzonella, A. Canton, S. Cappello, L. Carraro, L. Cordaro, S. D. Bello, M. D. Palma, G. D. Masi, A. Fassina, F. Gnesotto, L. Grando, P. Innocente, F. Lunardon, G. Manduchi, D. Marcuzzi, N. Marconato, R. Piovan, N. Pomaro, A. Rigoni, A. Rizzolo, P. Scarin, M. Siragusa, P. Sonato, S. Spagnolo, M. Spolaore, and D. T. and. Upgrades of the RFX-mod reversed field pinch and expected scenario improvements. *Nuclear Fusion*, 59(7):076027, Jun 2019. doi: 10.1088/1741-4326/ab1c6a. URL https://doi.org/10.1088/1741-4326/ab1c6a.

L. Marrelli, P. Martin, M. E. Puiatti, J. S. Sarff, B. E. Chapman, J. R. Drake, D. F. Escande, and S. Masamune. The reversed field pinch. *Nuclear Fusion*, 61(2):023001, 2021. doi: 10.1088/1741-4326/abc06c. URL https://doi.org/10.1088/1741-4326/abc06c.

S. Masamune, A. Sanpei, R. Ikezoe, T. Onchi, K.-I. Murata, K. Oki, H. Shimazu, T. Yamashita, and H. Himura. Characterization of Initial Low-Aspect Ratio RFP Plasmas in "RELAX". *Journal of the Physical Society of Japan*, 76(12):123501, 2007. doi: 10.1143/JPSJ.76.123501. URL https://doi.org/10.1143/JPSJ.76.123501.

V. Masson-Delmotte, P. Zhai, H.-O. Pörtner, D. Roberts, J. Skea, P. R. Shukla, A. Pirani, W. Moufouma-Okia, C. Péan, R. Pidcock, S. Connors, J. B. R. Matthews, Y. Chen, X. Zhou, M. I. Gomis, E. Lonnoy, T. Maycock, M. Tignor, and T. Waterfield. IPCC, 2018: Global Warming of 1.5°C. An IPCC Special Report on the impacts of global warming of 1.5°C above pre-industrial levels and related global greenhouse gas emission pathways, in the context of strengthening the global response to the threat of climate change, sustainable development, and efforts to eradicate poverty, 2018. URL https://www.ipcc.ch/sr15/.

A. Molodyk, S. Samoilenkov, A. Markelov, P. Degtyarenko, S. Lee, V. Petrykin, M. Gaifullin, A. Mankevich, A. Vavilov, B. Sorbom, J. Cheng, S. Garberg, L. Kesler, Z. Hartwig, S. Gavrilkin, A. Tsvetkov, T. Okada, S. Awaji, D. Abraimov, A. Francis, G. Bradford, D. Larbalestier, C. Senatore, M. Bonura, A. E. Pantoja, S. C. Wimbush, N. M. Strickland, and A. Vasiliev. Development and large volume production of extremely high current density

$YBa_2Cu_3O_7$ superconducting wires for fusion. *Nature Scientific Reports*, 11:2084, 2021. doi: 10.1038/s41598-021-81559-z. URL https://doi.org/10.1038/s41598-021-81559-z.

D. Montgomery. Magnetohydrodynamic stability thresholds as a function of Hartmann number and pinch ratio. *Plasma Physics and Controlled Fusion*, 34(6):1157–1162, Jun 1992. doi: 10.1088/0741-3335/34/6/016. URL https://doi.org/10.1088/0741-3335/34/6/016.

J. A. Morales, W. J. T. Bos, K. Schneider, and D. C. Montgomery. The effect of toroidicity on reversed field pinch dynamics. *Plasma Physics and Controlled Fusion*, 56(9):095024, aug 2014. doi: 10.1088/0741-3335/56/9/095024. URL https://dx.doi.org/10.1088/0741-3335/56/9/095024.

M. Murakami, J. D. Callen, and L. A. Berry. Some observations on maximum densities in tokamak experiments. *Nuclear Fusion*, 16:347, Apr. 1976. URL https://ui.adsabs.harvard.edu/abs/1976NucFu..16..347M.

J. Ongena, R. Koch, R. Wolf, and H. Zohm. Magnetic-confinement fusion. *Nature Physics*, 12(5): 398–410, May 2016. doi: 10.1038/nphys3745. URL https://doi.org/10.1038/nphys3745.

S. Ortolani. Equilibrium and stability properties of reversed field pinch configurations. In *Proceedings of the International School of Plasma Physics, Course on Mirror-based and Field-reversed Approaches to Magnetic Fusion, Varenna, Italy*, 1983.

S. Ortolani and G. Rostagni. Density limits and scaling laws in reversed field pinches. *Nuclear Instruments and Methods in Physics Research*, 207(1):35 – 48, 1983. ISSN 0167-5087. doi: https://doi.org/10.1016/0167-5087(83)90221-1. URL http://www.sciencedirect.com/science/article/pii/0167508783902211.

S. Ortolani and D. D. Schnack. *Magnetohydrodynamics of Plasma Relaxation*. WORLD SCIENTIFIC, 1993. doi: 10.1142/1564. URL https://www.worldscientific.com/doi/abs/10.1142/1564.

W. Park, D. A. Monticello, and R. B. White. Reconnection rates of magnetic fields including the effects of viscosity. *The Physics of Fluids*, 27(1):137–149, 1984. doi: 10.1063/1.864502. URL https://aip.scitation.org/doi/abs/10.1063/1.864502.

W. Park, E. V. Belova, G. Y. Fu, X. Z. Tang, H. R. Strauss, and L. E. Sugiyama. Plasma simulation studies using multilevel physics models. *Physics of Plasmas*, 6(5):1796–1803, 1999. doi: 10.1063/1.873437. URL https://doi.org/10.1063/1.873437.

E. N. Parker. Sweet's mechanism for merging magnetic fields in conducting fluids. *Journal of Geophysical Research (1896-1977)*, 62(4):509–520, 1957. doi: 10.1029/JZ062i004p00509. URL https://agupubs.onlinelibrary.wiley.com/doi/abs/10.1029/JZ062i004p00509.

N. J. Peacock, D. C. Robinson, M. J. Forrest, P. D. Wilcock, and V. V. Sannikov. Measurement of the Electron Temperature by Thomson Scattering in Tokamak T3. *Nature*, 224:488–490, 1969. doi: 10.1038/224488a0. URL https://doi.org/10.1038/224488a0.

S. Peruzzo, M. Bernardi, G. Berton, R. Cavazzana, S. Dal Bello, M. Dalla Palma, L. Grando, M. Iafrati, D. Marcuzzi, D. Rizzetto, A. Rizzolo, F. Rossetto, M. Siragusa, M. Spolaore, L. Trevisan, M. Utili, and M. Zuin. Technological challenges for the design of the RFX-mod2 experiment. *Fusion Engineering and Design*, 146:692–696, 2019. ISSN 0920-3796. doi: https://doi.org/10.1016/j.fusengdes.2019.01.057. URL https://www.sciencedirect.com/science/article/pii/S0920379619300651. SI:SOFT-30.

H. E. Petschek. MAGNETIC FIELD ANNIHILATION. In *AAS-NASA Symposium on the Physics of Solar Flares: Proceedings of a Symposium Held at the Goddard Space Flight Center, Greenbelt, Maryland, October 28-30, 1963*, volume 50, page 425. Scientific and Technical Information Division, National Aeronautics and Space Administration, 1964. URL https://books.google.be/books?hl=it&lr=&id=pTwstsb8KRMC&oi=fnd&pg=PA425&ots=1X6fmdg69K&sig=Hvw0D3Ce0ARCtBYEgbxfkLgNOpI&redir_esc=y#v=onepage&q&f=false.

R. Piovan, P. Agostinetti, C. Bustreo, R. Cavazzana, D. F. Escande, E. Gaio, F. Lunardon, A. Maistrello, M. Puiatti, M. Valisa, G. Zollino, and M. Zuin. Status and Perspectives of a Reversed Field Pinch as a Pilot Neutron Source. *IEEE Transactions on Plasma Science*, 48(6):1708–1714, 2020. doi: 10.1109/TPS.2019.2957888. URL https://ieeexplore.ieee.org/abstract/document/8948014?casa_token=-GUJ8oumI7YAAAAA:jkhPW_UbktpzR5QoYbK5gq_Sl4-8zm5a-0pgp1HgUjfEk-tRqg63VB-gGhA7keo_A2LN3PkNPQA.

P. Piovesan, M. Zuin, A. Alfier, D. Bonfiglio, F. Bonomo, A. Canton, S. Cappello, L. Carraro, R. Cavazzana, D. F. Escande, A. Fassina, M. Gobbin, R. Lorenzini, L. Marrelli, P. Martin, E. Martines, R. Pasqualotto, M. E. Puiatti, M. Spolaore, M. Valisa, N. Vianello, P. Zanca, and the RFX-mod Team. Magnetic order and confinement improvement in high-current regimes of RFX-mod with MHD feedback control. *Nuclear Fusion*, 49(8):085036, Jul 2009. doi: 10.1088/0029-5515/49/8/085036. URL https://doi.org/10.1088/0029-5515/49/8/085036.

P. Piovesan, D. Bonfiglio, F. Auriemma, F. Bonomo, L. Carraro, R. Cavazzana, G. De Masi, A. Fassina, P. Franz, M. Gobbin, L. Marrelli, P. Martin, E. Martines, B. Momo, L. Piron, M. Valisa, M. Veranda, N. Vianello, B. Zaniol, M. Agostini, M. Baruzzo, T. Bolzonella, A. Canton, S. Cappello, L. Chacón, G. Ciaccio, D. F. Escande, P. Innocente, R. Lorenzini, R. Paccagnella, M. E. Puiatti, P. Scarin, A. Soppelsa, G. Spizzo, M. Spolaore, D. Terranova, P. Zanca, L. Zanotto, and M. Zuin. RFX-mod: A multi-configuration fusion facility for three-dimensional physics studies. *Physics of Plasmas*, 20(5):056112, 2013. doi: 10.1063/1.4806765. URL https://doi.org/10.1063/1.4806765.

P. Piovesan, D. Bonfiglio, M. Cianciosa, T. C. Luce, N. Z. Taylor, D. Terranova, F. Turco, R. S. Wilcox, A. Wingen, S. Cappello, C. Chrystal, D. F. Escande, C. T. Holcomb, L. Marrelli, C. Paz-Soldan, L. Piron, I. Predebon, B. Zaniol, and The DIII-D and RFX-mod Teams. Role of a continuous MHD dynamo in the formation of 3D equilibria in fusion plasmas. *Nuclear Fusion*, 57(7):076014, May 2017. doi: 10.1088/1741-4326/aa700b. URL https://doi.org/10.1088/1741-4326/aa700b.

F. Porcelli. Viscous resistive magnetic reconnection. *The Physics of Fluids*, 30(6):1734–1742, 1987. doi: 10.1063/1.866240. URL https://aip.scitation.org/doi/abs/10.1063/1.866240.

R. Post. The magnetic mirror approach to fusion. *Nuclear Fusion*, 27(10):1579–1739, Oct 1987. doi: 10.1088/0029-5515/27/10/001. URL https://doi.org/10.1088/0029-5515/27/10/001.

G. Pucella, O. D'Arcangelo, O. Tudisco, F. Belli, W. Bin, A. Botrugno, P. Buratti, G. Calabrò, B. Esposito, E. Giovannozzi, D. Marocco, G. Ramogida, F. Sattin, G. Spizzo, P. Zanca, and M. Zuin. Analytical relation between peripheral and central density limit on FTU. *Plasma Physics and Controlled Fusion*, 59(8):085011, Jun 2017. doi: 10.1088/1361-6587/aa717e. URL https://doi.org/10.1088/1361-6587/aa717e.

M. E. Puiatti, P. Scarin, G. Spizzo, M. Valisa, M. Agostini, A. Alfier, A. Canton, L. Carraro, E. Gazza, R. Lorenzini, R. Paccagnella, I. Predebon, D. Terranova, D. Bonfiglio, S. Cappello, R. Cavazzana, S. Dal Bello, P. Innocente, L. Marrelli, R. Piovan, P. Piovesan, F. Sattin,

and P. Zanca. High density physics in reversed field pinches: comparison with tokamaks and stellarators. *Nuclear Fusion*, 49(4):045012 (9pp), 2009a. URL http://stacks.iop.org/0029-5515/49/045012.

M. E. Puiatti, P. Scarin, G. Spizzo, M. Valisa, R. Paccagnella, I. Predebon, M. Agostini, A. Alfier, A. Canton, S. Cappello, L. Carraro, E. Gazza, P. Innocente, R. Lorenzini, L. Marrelli, and D. Terranova. High density limit in reversed field pinches. *Physics of Plasmas*, 16(1): 012505, 2009b. doi: 10.1063/1.3063060. URL https://doi.org/10.1063/1.3063060.

J. J. Ramos. General expression of the gyroviscous force. *Physics of Plasmas*, 12(11):112301, 2005. doi: 10.1063/1.2114747. URL https://doi.org/10.1063/1.2114747.

P. Rebut and M. Hugon. Thermal instability and disruptions in a tokamak. In *Proceedings of the 10th International Atomic Energy Agency (IAEA) conference*, 1985. URL http://inis.iaea.org/search/search.aspx?orig_q=RN:16055814.

A. B. Rechester and M. N. Rosenbluth. Electron heat transport in a tokamak with destroyed magnetic surfaces. *Phys. Rev. Lett.*, 40(1):38–41, Jan 1978. URL https://www.taylorfrancis.com/chapters/edit/10.1201/9781003069515-48/electron-heat-transport-tokamak-destroyed-magnetic-surfaces-rechester-rosenbluth.

A. S. Richardson. *NRL PLASMA FORMULARY*. Naval research laboratory, 2019. URL https://www.nrl.navy.mil/News-Media/Publications/NRL-Plasma-Formulary/.

D. C. Robinson and R. E. King. Factors influencing the period of improved stability in zeta. *Plasma Physics and Controlled Nuclear Fusion Research*, 1(14):263, 1969. URL https://inis.iaea.org/search/search.aspx?orig_q=RN:44064045.

G. Rostagni. Rfx: an expected step in rfp research. *Fusion Engineering and Design*, 25(4): 301–313, 1995. ISSN 0920-3796. doi: https://doi.org/10.1016/0920-3796(94)00362-B. URL https://www.sciencedirect.com/science/article/pii/092037969400362B.

E. A. Saad and P. R. Brunsell. Experimental characterization and modelling of the resistive wall mode response in a reversed field pinch. *Plasma Physics and Controlled Fusion*, 64(5):055011, apr 2022. doi: 10.1088/1361-6587/ac5cf9. URL https://dx.doi.org/10.1088/1361-6587/ac5cf9.

A. D. Sakharov. Theory of the magnetic thermonuclear reactor, part II. *Soviet Physics Uspekhi*, 34(5):378–382, 1958. doi: 10.1070/pu1991v034n05abeh002493. URL https://doi.org/10.1070/pu1991v034n05abeh002493.

Y. Sarazin, J. Hillairet, J.-L. Duchateau, K. Gaudimont, R. Varennes, X. Garbet, P. Ghendrih, R. Guirlet, B. Pégourié, and A. Torre. Impact of scaling laws on tokamak reactor dimensioning. *Nuclear Fusion*, 60(1):016010, Oct 2019. doi: 10.1088/1741-4326/ab48a5. URL https://doi.org/10.1088/1741-4326/ab48a5.

J. Sarff. Perspective on Reversed Field Pinch (RFP) Fusion Research. In *Fusion Power Associates, 32nd Annual Meeting and Symposium*, 2011. URL https://fire.pppl.gov/fpa11_Sarff_RFP.pdf.

H. Sätherblom, S. Mazur, and P. Nordlund. Resistivity profile effects in numerical magnetohydrodynamic simulations of the reversed-field pinch. *Plasma Physics and Controlled Fusion*, 38(12):2205, 1996. URL https://iopscience.iop.org/article/10.1088/0741-3335/38/12/012.

P. Scarin, M. Agostini, G. Spizzo, M. Veranda, P. Zanca, and the RFX-mod Team. Helical plasma-wall interaction in the RFX-mod: effects of high-n mode locking. *Nuclear Fusion*, 59(8):086008, Jun 2019. doi: 10.1088/1741-4326/ab2071. URL https://doi.org/10.1088/1741-4326/ab2071.

D. Schnack, D. Barnes, Z. Mikic, D. S. Harned, and E. Caramana. Semi-implicit magnetohydrodynamic calculations. *Journal of Computational Physics*, 70(2):330–354, 1987. ISSN 0021-9991. doi: https://doi.org/10.1016/0021-9991(87)90186-0. URL https://www.sciencedirect.com/science/article/pii/0021999187901860.

X. Shan. Toroidal resistive MHD equilibria. *Comments on Plasma Physics and Controlled Fusion*, 15(6):315–320, 1994.

X. Shan and D. Montgomery. Global searches of Hartmann-number-dependent stability boundaries. *Plasma Physics and Controlled Fusion*, 35(8):1019, Aug 1993. doi: 10.1088/0741-3335/35/8/009. URL https://dx.doi.org/10.1088/0741-3335/35/8/009.

R. Singh and P. H. Diamond. Bounds on edge shear layer persistence while approaching the density limit. *Nuclear Fusion*, 61(7):076009, Jun 2021a. doi: 10.1088/1741-4326/abfadb. URL https://doi.org/10.1088/1741-4326/abfadb.

R. Singh and P. H. Diamond. A unified theory of zonal flow shears and density corrugations in drift wave turbulence. *Plasma Physics and Controlled Fusion*, 63(3):035015, Jan 2021b. doi: 10.1088/1361-6587/abd618. URL https://doi.org/10.1088/1361-6587/abd618.

P. Sonato, G. Chitarin, P. Zaccaria, F. Gnesotto, S. Ortolani, A. Buffa, M. Bagatin, W. R. Baker, S. Dal Bello, P. Fiorentin, L. Grando, G. Marchiori, D. Marcuzzi, A. Masiello, S. Peruzzo, N. Pomaro, and G. Serianni. Machine modification for active MHD control in RFX. *Fusion Engineering and Design*, 66-68:161–168, 2003. ISSN 0920-3796. doi: https://doi.org/10.1016/S0920-3796(03)00177-7. URL https://www.sciencedirect.com/science/article/pii/S0920379603001777. 22nd Symposium on Fusion Technology.

L. Spitzer. *Physics of Fully Ionized Gases*. Dover Books on Physics. Dover Publications, 1956. ISBN 9780486449821. URL https://books.google.be/books?id=Vn31DAAAQBAJ.

L. Spitzer. The Stellarator Concept. *The Physics of Fluids*, 1(4):253–264, 1958. doi: 10.1063/1.1705883. URL https://aip.scitation.org/doi/abs/10.1063/1.1705883.

G. Spizzo, R. B. White, S. Cappello, and L. Marrelli. Nonlocal transport in the reversed field pinch. *Plasma Physics and Controlled Fusion*, 51(12):124026, Nov 2009. doi: 10.1088/0741-3335/51/12/124026. URL https://doi.org/10.1088/0741-3335/51/12/124026.

G. Spizzo, P. Scarin, M. Agostini, A. Alfier, F. Auriemma, D. Bonfiglio, S. Cappello, A. Fassina, P. Franz, L. Piron, P. Piovesan, M. E. Puiatti, M. Valisa, and N. Vianello. Investigation on the relation between edge radial electric field asymmetries in rfx-mod and density limit. *Plasma Physics and Controlled Fusion*, 52(9):095011, 2010. URL http://stacks.iop.org/0741-3335/52/i=9/a=095011.

G. Spizzo, M. Agostini, P. Scarin, N. Vianello, R. B. White, S. Cappello, M. E. Puiatti, M. Valisa, and the RFX-mod Team. Edge topology and flows in the reversed-field pinch. *Nuclear Fusion*, 52(5):054015, May 2012. doi: 10.1088/0029-5515/52/5/054015. URL https://dx.doi.org/10.1088/0029-5515/52/5/054015.

G. Spizzo, N. Vianello, R. B. White, S. S. Abdullaev, M. Agostini, R. Cavazzana, G. Ciaccio, M. Puiatti, P. Scarin, O. Schmitz, M. Spolaore, and D. Terranova. Edge ambipolar potential in toroidal fusion plasmas. *Physics of Plasmas*, 21(5):056102, 2014. doi: 10.1063/1.4872173. URL https://doi.org/10.1063/1.4872173.

G. Spizzo, G. Pucella, O. Tudisco, M. Zuin, M. Agostini, E. Alessi, F. Auriemma, W. Bin, P. Buratti, L. Carraro, R. Cavazzana, G. Ciaccio, G. De Masi, B. Esposito, C. Galperti, S. Garavaglia, G. Granucci, M. Marinucci, L. Marrelli, E. Martines, C. Mazzotta, D. Minelli, A. Moro, M. E. Puiatti, P. Scarin, C. Sozzi, M. Spolaore, O. Schmitz, N. Vianello, and R. White. Density limit studies in the tokamak and the reversed-field pinch. *Nuclear Fusion*, 55(4):043007, 2015. doi: 10.1088/0029-5515/55/4/043007. URL http://stacks.iop.org/0029-5515/55/i=4/a=043007.

G. Spizzo, M. Veranda, N. Vivenzi, M. Agostini, D. Bonfiglio, S. Cappello, L. Carraro, M. E. Puiatti, P. Scarin, D. Terranova, M. Valisa, and M. Zuin. MHD origin of the density limit. *Bulletin of the American Physical Society*, 2022. URL https://meetings.aps.org/Meeting/DPP22/Session/UO03.1.

A. Stella, M. Guarnieri, F. Bellina, P. P. Campostrini, G. Chitarin, F. Trevisan, and P. Zaccaria. The RFX magnet system. *Fusion Engineering and Design*, 25(4):373–399, 1995. ISSN 0920-3796. doi: https://doi.org/10.1016/0920-3796(94)00281-B. URL https://www.sciencedirect.com/science/article/pii/092037969400281B.

M. R. Stoneking, J. T. Chapman, D. J. Den Hartog, S. C. Prager, and S. J. S. Experimental scaling of fluctuations and confinement with Lundquist number in the reversed-field pinch. *Physics of Plasmas*, 5(4):1004–1014, Apr 1998. doi: 10.1063/1.872670. URL https://doi.org/10.1063/1.872670.

H. R. Strauss. Hyper-resistivity produced by tearing mode turbulence. *The Physics of Fluids*, 29(11):3668–3671, Nov 1986. doi: 10.1063/1.865798. URL https://doi.org/10.1063/1.865798.

S. Sudo, Y. Takeiri, H. Zushi, F. Sano, K. Itoh, K. Kondo, and A. Iiyoshi. Scalings of energy confinement and density limit in stellarator/heliotron devices. *Nuclear Fusion*, 30(1):11–21, Jan 1990. doi: 10.1088/0029-5515/30/1/002. URL https://doi.org/10.1088/0029-5515/30/1/002.

W. Suttrop, K. Buchl, J. Fuchs, M. Kaufmann, K. Lackner, M. Maraschek, V. Mertens, R..Neu, M. Schittenhelm, M. Sokoll, and H. Zohm. Tearing mode formation and radiative edge cooling prior to density limit disruptions in ASDEX upgrade. *Nuclear Fusion*, 37(1):119–125, Jan 1997. doi: 10.1088/0029-5515/37/1/i09. URL https://doi.org/10.1088/0029-5515/37/1/i09.

A. Sykes and J. A. Wesson. Relaxation instability in tokamaks. *Phys. Rev. Lett.*, 37:140–143, Jul 1976. doi: 10.1103/PhysRevLett.37.140. URL https://link.aps.org/doi/10.1103/PhysRevLett.37.140.

I. E. Tamm. Theory of the magnetic thermonuclear reactor, part I. In *Plasma Physics and the Problem of Controlled Thermonuclear Reactions (Proceedings of the 1957 Geneva Conference on Peaceful Applications of Atomic Energy)*. Vienna: IAEA, 1957.

J. B. Taylor. Relaxation of toroidal plasma and generation of reverse magnetic fields. *Phys. Rev. Lett.*, 33:1139–1141, Nov 1974. doi: 10.1103/PhysRevLett.33.1139. URL https://link.aps.org/doi/10.1103/PhysRevLett.33.1139.

D. Terranova, T. Bolzonella, S. Cappello, P. Innocente, L. Marrelli, and R. Pasqualotto. Study of the scaling of magnetic fluctuations in the RFX reversed field pinch. *Plasma Physics and Controlled Fusion*, 42(7):843–854, Jun 2000. doi: 10.1088/0741-3335/42/7/307. URL https://doi.org/10.1088/0741-3335/42/7/307.

M. Z. Tokar, J. Rapp, D. Reiser, U. Samm, F. C. Schüller, G. Sergienko, and P. C. de Vries. Localized recycling as a trigger of MARFE. *Journal of Nuclear Materials*, 266–269:958–962, 1999. ISSN 0022-3115. doi: 10.1016/S0022-3115(98)00680-1. URL http://www.sciencedirect.com/science/article/B6TXN-3X6SKP6-5K/2/ca2429fb0a8aa0c42c698a81a5e22cac. Proc. 13th Int. Conf. on Plasma-Surface Interactions in Controlled Fusion Devices (PSI-13), San Diego (USA) 1998.

F. Trintchouk, M. Yamada, H. Ji, R. M. Kulsrud, and T. A. Carter. Measurement of the transverse Spitzer resistivity during collisional magnetic reconnection. *Physics of Plasmas*, 10 (1):319–322, 2003. doi: 10.1063/1.1528612. URL https://doi.org/10.1063/1.1528612.

F. Troyon, R. Gruber, H. Saurenmann, S. Semenzato, and S. Succi. MHD-Limits to Plasma Confinement. *Plasma Physics and Controlled Fusion*, 26(1A):209–215, Jan 1984. doi: 10.1088/0741-3335/26/1a/319. URL https://doi.org/10.1088/0741-3335/26/1a/319.

UNDP (United Nations Development Programme). Human development report 1990. *UNDP (United Nations Development Programme)*, 1990. URL https://hdr.undp.org/reports-and-publications.

M. Valisa, F. Auriemma, and A. Canton. The Greenwald density limit in the reversed field pinch, Jan 2005. URL https://www.osti.gov/etdeweb/biblio/20635044.

M. Valisa, L. Frassinetti, R. Paccagnella, M. E. Puiatti, F. Sattin, P. Scarin, G. Spizzo, M. Spolaore, N. Vianello, and the RFX team. Edge transport properties of RFX-mod approaching the Greenwald density limit. In *Fusion Energy Conference (Proc. 21st Int. Conf. Chengdu, People's Republic of China, 10–21 October 2006)*, pages CD–ROM file EX/P3–17. Vienna: IAEA, 2006. URL http://www-naweb.iaea.org/napc/physics/FEC/FEC2006/papers/ex_p3-17.pdf.

M. Veranda, D. Bonfiglio, S. Cappello, L. Chacón, and D. F. Escande. Impact of helical boundary conditions on nonlinear 3d magnetohydrodynamic simulations of reversed-field pinch. *Plasma Physics and Controlled Fusion*, 55(7):074015, jun 2013. doi: 10.1088/0741-3335/55/7/074015. URL https://dx.doi.org/10.1088/0741-3335/55/7/074015.

M. Veranda, D. Bonfiglio, S. Cappello, and P. Scarin. Viscosity and resistivity in fluid plasma theory: definition and scaling with plasma parameters. *Technical report Consorzio RFX*, 2014. URL https://portal.igi.cnr.it/diskr/note_interne/note_interne/gruppo_ft/FT-NT-04.pdf.

M. Veranda, D. Bonfiglio, S. Cappello, D. F. Escande, F. Auriemma, D. Borgogno, L. Chacón, A. Fassina, P. Franz, M. Gobbin, D. Grasso, and M. E. Puiatti. Magnetohydrodynamics modelling successfully predicts new helical states in reversed-field pinch fusion plasmas. *Nuclear Fusion*, 57(11):116029, Aug 2017. doi: 10.1088/1741-4326/aa7f46. URL https://doi.org/10.1088/1741-4326/aa7f46.

M. Veranda, D. Bonfiglio, S. Cappello, G. di Giannatale, and D. F. Escande. Helically self-organized pinches: dynamical regimes and magnetic chaos healing. *Nuclear Fusion*, 60 (1):016007, Oct 2019. doi: 10.1088/1741-4326/ab4863. URL https://doi.org/10.1088/1741-4326/ab4863.

M. Veranda, S. Cappello, D. Bonfiglio, D. F. Escande, and A. Kryzhanovskyy. Magnetic reconnection in three-dimensional quasi-helical pinches. *Rendiconti Lincei. Scienze Fisiche e Naturali*, 31:963–984, Dec 2020. doi: 10.1007/s12210-020-00944-4. URL https://doi.org/10.1007/s12210-020-00944-4.

M. Veranda, G. Spizzo, N. Vivenzi, M. Agostini, D. Bonfiglio, M. E. Puiatti, P. Scarin, D. Terranova, M. Zuin, and S. Cappello. The Greenwald density limit as a convective cell and radiative phenomenon in Reversed Field Pinch, 2021. URL http://aappsdpp.org/DPP2021/F/5148.pdf.

G. Verdoolaege, S. Kaye, C. Angioni, O. Kardaun, M. Maslov, M. Romanelli, F. Ryter, K. Thomsen, the ASDEX Upgrade Team, the EUROfusion MST1 Team, and J. Contributors. The updated ITPA global H-mode confinement database: description and analysis. *Nuclear Fusion*, 61(7):076006, May 2021. doi: 10.1088/1741-4326/abdb91. URL https://dx.doi.org/10.1088/1741-4326/abdb91.

S. von Goeler, W. Stodiek, and N. Sauthoff. Studies of Internal Disruptions and $m = 1$ Oscillations in Tokamak Discharges with Soft—X-Ray Tecniques. *Phys. Rev. Lett.*, 33:1201–1203, Nov 1974. doi: 10.1103/PhysRevLett.33.1201. URL https://link.aps.org/doi/10.1103/PhysRevLett.33.1201.

M. Wakatani. *Stellarator and Heliotron Devices*. Oxford University Press, 1998.

J. Wesson. Hydromagnetic stability of tokamaks. *Nuclear Fusion*, 18(1):87, Jan 1978. doi: 10.1088/0029-5515/18/1/010. URL https://dx.doi.org/10.1088/0029-5515/18/1/010.

J. Wesson and D. Campbell. *Tokamaks*. International Series of Monographs on Physics. OUP Oxford, 2011. ISBN 9780199592234. URL https://books.google.be/books?id=XJssMXjHUr0C.

J. A. Wesson. Sawtooth oscillations. *Plasma Physics and Controlled Fusion*, 28(1A):243–248, Jan 1986. doi: 10.1088/0741-3335/28/1a/022. URL https://doi.org/10.1088/0741-3335/28/1a/022.

J. A. Wesson, R. D. Gill, M. Hugon, F. C. Schüller, J. A. Snipes, D. J. Ward, D. V. Bartlett, D. J. Campbell, P. A. Duperrex, A. W. Edwards, R. S. Granetz, N. A. O. Gottardi, T. C. Hender, E. Lazzaro, P. J. Lomas, N. L. Cardozo, K. F. Mast, M. F. F. Nave, N. A. Salmon, P. Smeulders, P. R. Thomas, B. J. D. Tubbing, M. F. Turner, and A. Weller. Disruptions in JET. *Nuclear Fusion*, 29(4):641–666, Apr 1989. doi: 10.1088/0029-5515/29/4/009. URL https://doi.org/10.1088/0029-5515/29/4/009.

R. White, D. Gates, and D. Brennan. Thermal island destabilization and the Greenwald limit. *Physics of Plasmas*, 22(2):022514, 2015. doi: 10.1063/1.4913433. URL https://doi.org/10.1063/1.4913433.

R. B. White and M. S. Chance. Hamiltonian guiding center drift orbit calculation for plasmas of arbitrary cross section. *The Physics of Fluids*, 27(10):2455–2467, 1984. doi: 10.1063/1.864527. URL https://aip.scitation.org/doi/abs/10.1063/1.864527.

L. Woltjer. A THEOREM ON FORCE-FREE MAGNETIC FIELDS. *Proceedings of the National Academy of Sciences*, 44(6):489–491, 1958. doi: 10.1073/pnas.44.6.489. URL https://www.pnas.org/doi/abs/10.1073/pnas.44.6.489.

M. Yamada, R. Kulsrud, and H. Ji. Magnetic reconnection. *Rev. Mod. Phys.*, 82:603–664, Mar 2010. doi: 10.1103/RevModPhys.82.603. URL https://link.aps.org/doi/10.1103/RevModPhys.82.603.

Q. Yu, S. Günter, and K. Lackner. Numerical modelling of sawtooth crash using two-fluid equations. *Nuclear Fusion*, 55(11):113008, Sep 2015. doi: 10.1088/0029-5515/55/11/113008. URL https://dx.doi.org/10.1088/0029-5515/55/11/113008.

P. Zanca. Avoidance of tearing modes wall-locking in a reversed field pinch with active feedback coils. *Plasma Physics and Controlled Fusion*, 51(1):015006, Dec 2008. doi: 10.1088/0741-3335/51/1/015006. URL https://dx.doi.org/10.1088/0741-3335/51/1/015006.

P. Zanca and D. Terranova. Reconstruction of the magnetic perturbation in a toroidal reversed field pinch. *Plasma Physics and Controlled Fusion*, 46(7):1115–1141, Jun 2004. doi: 10.1088/0741-3335/46/7/011. URL https://doi.org/10.1088/0741-3335/46/7/011.

P. Zanca, F. Sattin, D. Escande, G. Pucella, and O. Tudisco. A unified model of density limit in fusion plasmas. *Nuclear Fusion*, 57(5):056010, Mar 2017. doi: 10.1088/1741-4326/aa6230. URL https://dx.doi.org/10.1088/1741-4326/aa6230.

P. Zanca, F. Sattin, D. F. Escande, and J. Contributors. A power-balance model of the density limit in fusion plasmas: application to the L-mode tokamak. *Nuclear Fusion*, 59(12):126011, Sep 2019. doi: 10.1088/1741-4326/ab3b31. URL https://doi.org/10.1088/1741-4326/ab3b31.

P. Zanca, F. Sattin, D. F. Escande, F. Auriemma, and J. Contributors. A power-balance model for the l-mode radiative density limit in fusion plasmas. *Plasma Physics and Controlled Fusion*, 64(5):054006, Mar 2022. doi: 10.1088/1361-6587/ac57cc. URL https://dx.doi.org/10.1088/1361-6587/ac57cc.

H. Zohm. Edge localized modes (ELMs). *Plasma Physics and Controlled Fusion*, 38(2):105–128, Feb 1996. doi: 10.1088/0741-3335/38/2/001. URL https://doi.org/10.1088/0741-3335/38/2/001.

H. Zohm. *Magnetohydrodynamic Stability of Tokamaks*. John Wiley & Sons, Ltd, 2014. ISBN 9783527677375. doi: https://doi.org/10.1002/9783527677375.fmatter. URL https://onlinelibrary.wiley.com/doi/abs/10.1002/9783527677375.

M. Zuin, W. Schneider, A. Barzon, R. Cavazzana, P. Franz, E. Martines, M. E. Puiatti, P. Scarin, and E. Zampiva. Ion temperature measurements by means of a neutral particle analyzer in RFX-mod plasmas. In A. Bécoulet, T. Hoang, and U. Stroth, editors, *Proc. of the 38$^{\text{th}}$ EPS Conference on Plasma Physics*, volume 35G, page PD2.10, Strasbourg, France, June 27 – July 1 2011. European Physical Society (Petit Lancy). URL http://ocs.ciemat.es/EPS2011PAP/pdf/PD2.10.pdf.

M. Zuin, S. D. Bello, L. Marrelli, M. Puiatti, P. Agostinetti, M. Agostini, V. Antoni, F. Auriemma, M. Barbisan, T. Barbui, M. Baruzzo, F. Belli, P. Bettini, M. Bigi, R. Bilel, M. Boldrin, T. Bolzonella, D. Bonfiglio, M. Brombin, A. Buffa, C. Bustreo, A. Canton, S. Cappello, L. Carraro, R. Cavazzana, D. Cester, L. Chacon, G. Chitarin, W. Cooper, L. Cordaro, M. D. Palma, S. Deambrosis, R. Delogu, A. D. Lorenzi, G. D. Masi, J. Dong, D. Escande, A. Fassina, F. Felici, A. Ferro, C. Finotti, P. Franz, L. Frassinetti, E. Gaio, F. Ghezzi, L. Giudicotti, F. Gnesotto, M. Gobbin, W. Gonzalez, L. Grando, S. Guo, J. Hanson, S. Hirshman, P. Innocente, J. Jackson, S. Kiyama, M. Komm, O. Kudlacek, L. Laguardia, C. Li, B. Liu, S. Liu, Y. Liu, D. López-Bruna, R. Lorenzini, T. Luce, A. Luchetta, A. Maistrello, G. Manduchi, D. Mansfield, G. Marchiori, N. Marconato, D. Marcuzzi, P. Martin, E. Martines, S. Martini, G. Mazzitelli, O. McCormack, E. Miorin, B. Momo, M. Moresco, Y. Narushima, M. Okabayashi, R. Paccagnella, N. Patel, M. Pavei, S. Peruzzo, N. Pilan, L. Pigatto, R. Piovan, P. Piovesan, C. Piron, L. Piron, I. Predebon, G. Pucella, C. Rea, M. Recchia, A. Rizzolo, G. Rostagni, C. Ruset, L. Sajò-Bohus, H. Sakakita, R. Sanchez, J. Sarff, F. Sattin, P. Scarin, O. Schmitz, W. Schneider, M. Siragusa, P. Sonato, E. Spada, S. Spagnolo, M. Spolaore, D. Spong, G. Spizzo, L. Stevanato, Y. Suzuki, C. Taliercio, D. Terranova, O. Tudisco, G. Urso, M. Valente, M. Valisa, M. Vallar, M. Veranda, N. Vianello, F. Villone, P. Vincenzi, N. Visonà, R. White, P. Xanthopoulos, X. Xu, V. Yanovskiy, A. Zamengo, P. Zanca,

B. Zaniol, L. Zanotto, Y. Zhang, and E. Zilli. Overview of the rfx-mod fusion science activity. *Nuclear Fusion*, 57(10):102012, Jun 2017. doi: 10.1088/1741-4326/aa61cc. URL https://dx.doi.org/10.1088/1741-4326/aa61cc.

A. B. Zylstra, A. L. Kritcher, O. A. Hurricane, D. A. Callahan, J. E. Ralph, D. T. Casey, A. Pak, O. L. Landen, B. Bachmann, K. L. Baker, L. Berzak Hopkins, S. D. Bhandarkar, J. Biener, R. M. Bionta, N. W. Birge, T. Braun, T. M. Briggs, P. M. Celliers, H. Chen, C. Choate, D. S. Clark, L. Divol, T. Döppner, D. Fittinghoff, M. J. Edwards, M. Gatu Johnson, N. Gharibyan, S. Haan, K. D. Hahn, E. Hartouni, D. E. Hinkel, D. D. Ho, M. Hohenberger, J. P. Holder, H. Huang, N. Izumi, J. Jeet, O. Jones, S. M. Kerr, S. F. Khan, H. Geppert Kleinrath, V. Geppert Kleinrath, C. Kong, K. M. Lamb, S. Le Pape, N. C. Lemos, J. D. Lindl, B. J. MacGowan, A. J. Mackinnon, A. G. MacPhee, E. V. Marley, K. Meaney, M. Millot, A. S. Moore, K. Newman, J.-M. G. Di Nicola, A. Nikroo, R. Nora, P. K. Patel, N. G. Rice, M. S. Rubery, J. Sater, D. J. Schlossberg, S. M. Sepke, K. Sequoia, S. J. Shin, M. Stadermann, S. Stoupin, D. J. Strozzi, C. A. Thomas, R. Tommasini, C. Trosseille, E. R. Tubman, P. L. Volegov, C. R. Weber, C. Wild, D. T. Woods, S. T. Yang, and C. V. Young. Experimental achievement and signatures of ignition at the National Ignition Facility. *Phys. Rev. E*, 106: 025202, Aug 2022. doi: 10.1103/PhysRevE.106.025202. URL https://link.aps.org/doi/10.1103/PhysRevE.106.025202.

Publications

- N. Vivenzi, M. Veranda, D. Bonfiglio, S. Cappello, Viscosity impact on 3D non-linear MHD simulations of RFP fusion plasmas, submitted to *Physics of Plasmas*, March 2023.
- N. Vivenzi, G. Spizzo, M. Veranda, D. Bonfiglio, S. Cappello, RFX-mod Team. Kinematic viscosity estimates in reversed-field pinch fusion plasmas, *Journal of Physics: Conference Series*, 2397 012010, Dec 2022. doi: 10.1088/1742-6596/2397/1/012010, URL https://dx.doi.org/10.1088/1742-6596/2397/1/012010.
- N. Vivenzi, M. Veranda, D. Bonfiglio and S. Cappello. Non-linear visco-resistive MHD modelling of reversed-field pinch fusion plasmas: viscosity coefficient studies, 2022, 48^{th} *EPS conference on Plasma Physics*, URL http://ocs.ciemat.es/EPS2022PAP/pdf/P4b.110.pdf.
- M. Veranda, G. Spizzo, N. Vivenzi, M. Agostini, D. Bonfiglio, M. E. Puiatti, P. Scarin, D. Terranova, M. Zuin, and S. Cappello. The Greenwald density limit as a convective cell and radiative phenomenon in Reversed Field Pinch, 2021, *Proceeding of* 5^{th} *Asia-Pacific conference on Plasma Physics* URL http://aappsdpp.org/DPP2021/F/5148.pdf.
- G. Spizzo, M. Veranda, N. Vivenzi, M. Agostini, D. Bonfiglio, S. Cappello, L. Carraro, M. E. Puiatti, P. Scarin, D. Terranova, M. Valisa, and M. Zuin. MHD origin of the density limit. *Bulletin of the American Physical Society*, 2022. URL https://meetings.aps.org/Meeting/DPP22/Session/UO03.1.
- S. Cappello, D. Bonfiglio, D. F. Escande, M. Veranda, A. Kryzhanovskyy, L. Spinicci, N. Vivenzi, RFX Team, L. Chacón, D. Grasso, D. Borgogno, F. Pegoraro. Structures in Reversed Field Pinch Magnetic Self-Organization: Insights and Prospects from 3D Nonlinear MHD, 20^{th} *International Congress on Plasma Physics*, 2022.
- D. Bonfiglio, D. F. Escande, L. Chacón, M. Veranda, N. Vivenzi, S. Cappello. The MHD dynamo effect in reversed-field pinch and tokamak plasmas: indications from nonlinear 3D MHD simulations. 19^{th} *European Fusion Theory Conference, Poster # 22*, 2021. URL https://indico.cern.ch/event/934747/book-of-abstracts.pdf
- S. Cappello, D. Bonfiglio, G. Di Giannatale, A. Kryzhanovskyy, G. Manduchi, A. Rigoni Garola, F. Sattin, L. Spinicci, G. Spizzo, M. Veranda, N. Vivenzi, D. F. Escande, L. Chacón, D. Grasso, M. V. Falessi, F. Pegoraro. Modelling of Basic Physics Issues in Toroidal Pinches and Tools for Performance Control, *2020* 28^{th} *IAEA Fusion Energy*, 2021. URL https://nucleus.iaea.org/sites/fusionportal/Shared%20Documents/FEC%202020/fec2020-preprints/preprint1047.pdf